



TECHNISCHE  
UNIVERSITÄT  
WIEN

## DISSERTATION

# Investigations of the reaction kinetics of thermochemical energy storage materials

ausgeführt zum Zwecke der Erlangung des akademischen Grades eines  
Doktors der technischen Wissenschaften unter der Leitung von

Priv.-Doz. Dr. Peter Weinberger

Institut für Angewandte Synthesechemie

und

Ass.Prof. Dr. Michael Harasek

Institut für Verfahrenstechnik, Umwelttechnik und Technische Biowissenschaften

eingereicht an der Technischen Universität Wien

Fakultät für Technische Chemie

von

Dipl.-Ing. Christian Knoll BSc

00825136

Fernkorngasse 9-13/2/4/20

1100 Wien

Wien, am

Christian Knoll

# 1. ACKNOWLEDGEMENT

The present work was accomplished between 09/2015 and 11/2017 at the Institute of Applied Synthetic Chemistry and the Institute of Chemical, Environmental & Biological Engineering, TU Wien, Austria.

First, I would like to express my gratitude to my supervisors Priv.-Doz. Dr. Peter Weinberger and Ass.Prof. Dr. Michael Harasek, for the interesting and challenging research program and on the other hand for the freedom in choosing the direction of this work but also the very helpful support whenever needed.

Furthermore, I want to sincerely thank Dr. Danny Müller for our long-lasting friendship and the best and most fruitful collaboration I can imagine, the accomplished work and publications would not have been possible without the cooperation.

Also, my colleagues in our working group Dipl.-Ing. Marco Seifried and Georg Gravogl, MSc ensured a very pleasant working atmosphere and shall be acknowledged for their always helpful pieces of advice. Furthermore, I am very grateful for sharing lots of conference and holiday experiences with them.

Special thanks to Dr. Klaudia Hradil and Dipl.-Ing Werner Artner from the X-Ray Center, TU Wien for providing nearly endless measuring time at ambient and non-ambient conditions for powder diffraction experiments and besides that for providing an always open toolbox, spare parts and advice, which were extremely helpful and enabled many experiments on short notice even outside of business opening hours. Thanks to Prof. Hermann Kronberger and Prof. Gernot Friedbacher for providing access to the SEM and Udo Starzacher and Elisabeth Eitenberger for technical assistance and measurements.

The whole team of the TVT division shall be thanked, especially, Dipl.-Ing Christian Jordan, and Mag. Sylvia Zibuschka for their support and the always very friendly working environment and the colleagues of the SolidHeat Consortium, especially Dr. Markus Deutsch. Thanks also to the colleagues of the AG Kirchner for some scientific discussions and the interesting social evenings.

Finally, I would like to thank my family for all the support and the possibility to carry out my studies and my friends for the joint years during our studies and work.

This work was financed by the Austrian Research Promotion Agency (Österreichische Forschungsförderungsgesellschaft FFG), project SolidHeat Kinetics, project number 848876.

## 2. ABSTRACT

Global warming and reduction of extensive emissions of greenhouse gases to the atmosphere are the major challenges of the global energy system nowadays. The widely discussed solutions are the promotion of renewable energy sources and enhancing the efficiency of existing energy converting processes to reach a dramatical reduction of fossil fuel usage. One key to efficiency enhancement is the utilization and storage of waste heat for later usage.

This thesis deals with the investigation of possible materials and systems for thermochemical energy storage. Key features of interest for suitable materials are the completeness of the chemical reaction, the reversibility, the cycle stability and the kinetic parameters.

The focus for this investigation lies on reactions between solid heat storage materials and reactive gases because of the relative ease of phase separation and its storage possibility. As storage materials different kinds of inorganic salts and salt hydrates as well as transition metal oxides and transition metal salts are investigated. The chosen reactive gases are water vapor, oxygen, ammonia and carbon dioxide.

The reactions were investigated using different independent analytical methods for example thermogravimetry / differential scanning calorimetry and *in situ* powder X-ray diffraction. The materials were characterized via different spectroscopic methods like X-ray fluorescence spectroscopy, and imaging techniques such as microscopy and scanning electron microscopy, as well as specific surface area measurements using Brunauer-Emmett-Teller theory (BET).

### 3. KURZFASSUNG

Globale Erwärmung und die Verringerung der umfangreichen Treibhausgasemissionen in die Atmosphäre sind heutzutage die größten Herausforderungen des globalen Energiesystems. Die viel diskutierten Lösungen sind die Förderung erneuerbarer Energiequellen und die Verbesserung der Effizienz bestehender Energieumwandlungsprozesse, um eine drastische Reduzierung des Verbrauchs fossiler Brennstoffe zu erreichen. Ein Schlüssel zur Effizienzsteigerung ist die Nutzung und Speicherung von Abwärme für die spätere Nutzung.

Diese Arbeit beschäftigt sich mit der Untersuchung möglicher Materialien und Systeme für die thermochemische Energiespeicherung. Von Interesse für geeignete Materialien sind die Vollständigkeit der chemischen Reaktion, die Reversibilität, die Zyklenstabilität und die kinetischen Parameter.

Der Fokus für diese Untersuchung liegt auf Reaktionen zwischen festen Wärmespeichermaterialien und reaktiven Gasen aufgrund der relativ einfachen Phasentrennung und der getrennten Speichermöglichkeit. Als Speichermaterialien werden verschiedene Arten anorganischer Salze und Salzhydrate sowie Übergangsmetalloxide und Übergangsmetallsalze untersucht. Die gewählten reaktiven Gase sind Wasserdampf, Sauerstoff und Ammoniak sowie Kohlendioxid.

Die Reaktionen wurden mit verschiedenen unabhängigen analytischen Methoden untersucht, zum Beispiel simultane thermische Analyse und *in-situ* Pulver-Röntgenbeugung. Die Materialien wurden durch verschiedene spektroskopische Methoden wie Röntgenfluoreszenzspektroskopie und bildgebende Verfahren wie Mikroskopie und Rasterelektronenmikroskopie sowie spezifische Oberflächenmessungen mit der Brunauer-Emmett-Teller-Theorie (BET) charakterisiert.



## 4. TABLE OF CONTENTS

1. Acknowledgement.....	2
2. Abstract .....	3
3. Kurzfassung.....	4
4. Table of contents .....	5
5. Introduction .....	7
5.1. Aim of the work.....	7
5.2. State of the Art for Thermal Energy Storage (TES).....	7
5.2.1. Sensible Heat Storage.....	7
5.2.2. Latent Heat Storage .....	8
5.2.3. Thermo-chemical Energy Storage.....	9
5.3. Kinetics of chemical reactions.....	12
5.4. Used analytical methods and measurement techniques.....	13
5.4.1. In-situ powder X-Ray diffraction (p-XRD) for hydration reactions .....	13
5.4.2. In-situ p-XRD of ammonization reactions .....	14
5.4.3. In-situ p-XRD O <sub>2</sub> /air of redox reactions .....	14
5.4.4. TG / DSC of rehydration reactions .....	14
5.4.5. TG / DSC of ammonization and redox reactions .....	15
5.4.6. TG / DSC of decomposition reactions .....	15
5.4.7. Brunauer, Emmett and Teller (BET) Specific surface area calculation.....	15
5.4.8. Scanning Electron Microscope (SEM).....	15
5.4.9. Data Evaluation and Plotting.....	16
5.5. Remark on the thesis.....	16
6. Published Journal Articles.....	17
6.1. Probing cycle stability and reversibility in thermochemical energy storage – CaC <sub>2</sub> O <sub>4</sub> ·H <sub>2</sub> O as perfect match?.....	17

6.2.	Combining in-situ X-ray diffraction with thermogravimetry and differential scanning calorimetry – An investigation of $\text{Co}_3\text{O}_4$ , $\text{MnO}_2$ and $\text{PbO}_2$ for thermochemical energy storage	17
6.3.	High-Temperature Energy Storage: Kinetic Investigations of the $\text{CuO}/\text{Cu}_2\text{O}$ Reaction Cycle	18
6.4.	An extension of the NPK method to include the pressure dependency of solid state reactions .....	19
7.	Submitted Journal Articles .....	20
7.1.	Calcium Doping Facilitates Water Dissociation in Magnesium Oxide.....	20
7.2.	An in-situ powder X-Ray diffraction study on the rehydration-reactivity of low temperature calcined $\text{Mg}(\text{OH})_2$ .....	20
7.3.	Influence of the Particle Morphology on Cycle Stability and Hydration Behavior of Magnesium Oxide .....	21
7.4.	Magnesium oxide from natural magnesite samples as thermochemical energy storage material.....	22
7.5.	Metal oxides for thermochemical energy storage – From gas-triggered isothermal cycling to low-temperature applications with increased $\text{O}_2$ pressure.....	22
7.6.	Transition metal ammoniates for thermochemical energy storage.....	23
7.7.	Lab-scale demonstration of thermochemical energy storage with $\text{NH}_3$ and impregnated-loaded zeolites.....	24
8.	References .....	25
9.	List of Publications.....	194
10.	Curriculum Vitae.....	200

# 5. INTRODUCTION

## 5.1. Aim of the work

The aim of this work is to investigate thermochemical energy storage (TCES) materials identified in a systematic database search<sup>1</sup> regarding their feasibility to be used in TCES systems. The important considerations concerning suitability for TCES materials are completeness of the chemical reaction, the reversibility, the cycle stability and the kinetic parameters, as well as costs and environmental sustainability. The work deals with experimental setups and measurements of these identified important properties, as well as kinetic investigations of the underlying chemical reactions.

## 5.2. State of the Art for Thermal Energy Storage (TES)

On a global scale, heat is the most abundant energy form used. The primary usage of all fossil fuels is heat, including electricity producing power plants or industrial processes and of course any form of domestic or industrial heating.<sup>2</sup> To fulfil the international agreements on reducing the worldwide carbon footprint and to reduce the dangerous long-term consequences of global warming effects, the Kyoto protocol<sup>3</sup> and the climate goals defined in the Paris-agreement,<sup>4</sup> the use of fossil fuels and the accompanying emission of greenhouse gases must be dramatically decreased. A second major part after the reduction of the used primary energy, which is by far less promoted in the international discussion, is the increase of the efficiency of all energy converting processes. One possible option of increasing the overall-efficiency is to store the heat for later use, instead of releasing the waste heat to the environment and use afterwards again primary energy.<sup>5,6</sup> In 2011, the International Energy Agency (IEA) estimated in a report entitled “Solutions for a low-carbon energy future” that global energy loss through waste heat accounts for 2/3 of the overall energy production.<sup>7</sup> Therefore, methods suitable for a reutilization of waste heat could contribute significantly to a more sustainable energy management.<sup>8-10</sup> There are several different approaches of thermal energy storage to this challenge, which will be discussed in this chapter.

### 5.2.1. Sensible Heat Storage

Thermal energy in sensible heat storage systems is stored either in a solid or in a liquid material by raising the temperature of the storage medium. Therefore, it is necessary for a useful storage

material to have a high specific heat capacity, long term stability under thermal cycling, compatibility with its containment and in the best case also low cost. Sensible heat storage can be classified as *Liquid media storage* (like water, oil based fluids, molten salts etc.) and *Solid media storage* (like rocks, metals and others).<sup>8</sup> One very prominent example for liquid media storage is the use of water for heat storage. At rather low temperatures water is the best storage medium, as it has a higher specific heat than most other materials, is cheap and widely available. Water can be used over the wide range of temperature of about 25 - 90 °C. For a 60 °C temperature change water can store about 250 kJ/kg. However, due to its vapor pressure, it requires thermal insulation and containment. For applications above the boiling point pressure withstanding containment, which increases costs is necessary. Water can be used either as a storage or as a transport medium for energy, for example, in solar energy systems. Consequently, it is the most widely used liquid storage medium today for solar based warm water and space heating applications.<sup>11</sup>

For high temperature thermal energy storage solid media storage can be an option, where materials such as rocks, metals, concrete, sand, bricks etc., can be used. In this case, the energy can be stored at any temperature level below the decomposition temperature, since the materials will not undergo a phase change. One of the materials with the highest energy density in the list of solid materials for sensible heat storage is cast iron, which exceeds the energy density level of water storage<sup>12</sup>. However, cast iron is more expensive than stone or brick. Pebble beds or rock piles are generally preferred as the storage material due to their low cost.<sup>8</sup> The major drawback of solid materials as sensible heat storage is the conception of the charging or discharging process where the use of an energy carrier is necessary which again will lead to thermal heat flow losses.

The biggest issue for sensible heat storage is the need of thermal insulation and the impossibility to perform long term storage, since heat will be lost constantly.<sup>13</sup>

### 5.2.2. Latent Heat Storage

In comparison to pure sensible heat storage concepts, latent heat storage is a more attractive technique, since there is a remarkable increase of storage density. There is the possibility to store heat as latent heat of fusion at the constant temperature of the phase transition of phase change materials (PCMs). For example, water requires around 80 times more energy to melt 1 kg of ice than to increase the temperature of 1 kg by 1 °C. This means that a much smaller weight and volume of material is needed to store the same amount of energy.

PCMs can undergo solid–solid, liquid–gas, and solid–liquid phase transformations. Solid–solid phase changes most commonly are not suitable for thermal storage applications due to their very low enthalpy of fusion. Liquid–gas PCMs usually have high heats of transformations, but the concomitant large volume change during transformation prevents practical applications.

Solid–liquid PCMs are useful because they store a relatively large quantity of heat over a narrow temperature range, without corresponding large volume changes. An example design for a solar heat storage could consist of the PCM placed in long thin tubes stacked in a container as heat exchanger. During the charging cycle the collected solar heat from the collector is circulated through the heat exchanger melting the PCM. Thus the PCM is storing the heat as sensible heat as well as latent heat of fusion. During the discharging cycle, the circulation of low temperature air would transport the heat from the PCM to the heat load. Therefore, the latent heat storage units utilize the latent heat due to a phase change during melting or freezing of the storage medium and, additionally, the sensible heat in the solid and liquid phases.

PCMs can be classified into the following major categories: inorganic compounds, organic compounds and eutectics of inorganic and/or organic compounds. Inorganic compounds include salt hydrates, salts, metals and alloys, whereas organic compounds are comprised of paraffins, non-paraffins and polyalcohols.<sup>8</sup>

The advantage of latent heat storage systems is their increased storage density, and their in comparison to sensible heat storage systems usually perfect cycle stability because of the non-degrading physical processes. On the other hand the heat can only be stored at the fixed temperature of the melting point of the chosen substance and the need of insulation is the same as above, otherwise the sensible part of the heat storage would be lost.<sup>13</sup>

### 5.2.3. Thermo-chemical Energy Storage

A newly developing technology which can overcome the drawbacks in latent and sensible heat storage is thermo-chemical energy storage (TCES). There can be two groups of thermo-chemical storage technologies distinguished. On the one hand thermo-chemical reactions and on the other hand sorption processes, both of which require thermal energy for the charging process, which is most commonly the separation between the storage material and the reactive component.<sup>14</sup>

Sorption storage systems include both adsorption and absorption.<sup>15</sup> Absorption is the phenomenon that occurs when a liquid or gas enters another material and is taken up by its

volume. In storage applications, absorption usually involves a gas entering a liquid,<sup>13</sup> adsorption involves the binding of a gas or liquid on the surface of a solid or porous material.

The focus of the investigations carried out in this work are thermochemical reactions between a solid storage material and a gaseous reactive component, because of the relative ease of separation and its storage possibility. In TCES, energy is stored through a reaction and recovered when the reaction is reversed. Many thermo-chemical storage systems have much higher energy densities than the other thermal energy storage technologies mentioned previously. High energy densities allow large amounts of energy to be stored in smaller volumes, making it more suitable for residential or mobile applications, or for any implementation where a small volume or a small weight is necessary. One major advantage of storing energy in thermo-chemical systems is that the heat is stored as a chemical potential and is not lost over time during storage. This allows for long-term storage, as thermo-chemical energy can theoretically be stored indefinitely at near ambient temperature without need of expensive insulation, which makes this technology very attractive.<sup>2</sup> Due to the high energy densities which can be obtained from the reactions of various TCES materials the contribution of sensible heat is negligible in contrast to the amount of heat stored in the reaction enthalpy. Possible materials include salts and salt hydrates as well as transition metal oxides at different oxidation states. The highest energy densities can be obtained from reactions of transition metal salts with ammonia.<sup>16</sup>

If release of the stored heat is required, the discharging reaction can be simply initiated by combining the storage material with the reactive compound.<sup>6, 15, 17, 18</sup> Depending on the reactive compound this cycle can either be carried out in an open system, for example oxidation with oxygen or air, and reduction under nitrogen atmosphere, or in a closed system which would be applicable for any reaction with ammonia.

The second big advantage of thermochemical energy storage systems is the possibility to change the operational charging and discharging temperatures by simply changing the partial pressure of the reactive gas component and therefore shifting the chemical equilibrium in the desired direction. This allows for the development of a chemical heat pump (CHP) system which consists of a solid-gas reactor coupled with a condenser/evaporator. The working principle is illustrated in fig. 1 in a Clausius–Clapeyron's diagram, wherein the solid-gas (S/G) and liquid-gas (L/G) equilibrium lines are given by the equation:<sup>2</sup>

$$\ln(P_{eq}) = \frac{\Delta H}{RT} + \frac{\Delta S}{R}$$

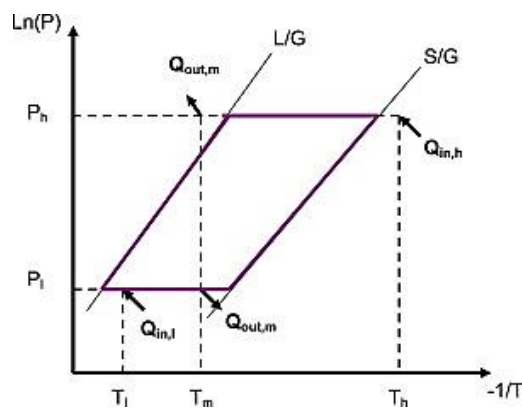


Figure 1: Working principle of a chemical heat pump.<sup>2</sup>

The chemical heat pump system can operate in two successive phases (thermal conversion) or with a time gap (thermal storage mode): charging phase (regeneration, decomposition or desorption) and discharging phase (production, synthesis or sorption). The charging phase occurs at high pressure ( $P_h$ ). Heat at high temperature ( $T_h$ ) is supplied to the reactor and the solid (S) decomposes starting at point  $Q_{in,h}$  in fig. 1. The gas (G) released from the decomposition reaction is condensed by rejecting heat from the condenser at medium temperature ( $T_m$ ) following the line of equal pressure towards  $Q_{out,m}$ . The discharging phase occurs at low pressure ( $P_l$ ). The liquid evaporates by absorbing heat at low temperature ( $T_l$ ) and the stored heat is released at  $T_m$  following the line of equal pressure from  $Q_{in,l}$  to  $Q_{out,m}$ . The charging and discharging occurs when the storage material is disturbed in its equilibrium of temperature (equilibrium temperature change,  $\Delta T$ ) and pressure (equilibrium pressure change,  $\Delta P$ ) for heat and mass transfer.<sup>19-22</sup>

For example, in the case of the dehydration and rehydration reaction of calcium oxalate monohydrate ( $\text{CaC}_2\text{O}_4 \cdot \text{H}_2\text{O} / \text{CaC}_2\text{O}_4$ ) the thermal analysis of the isothermal reaction upon the changed water vapor partial pressure reveals this phenomenon very clearly. The charging reaction is faster at higher temperatures and the discharging reaction is faster at lower temperatures. Nevertheless, both reaction pathways are accessible at different temperature levels as shown in fig 2.

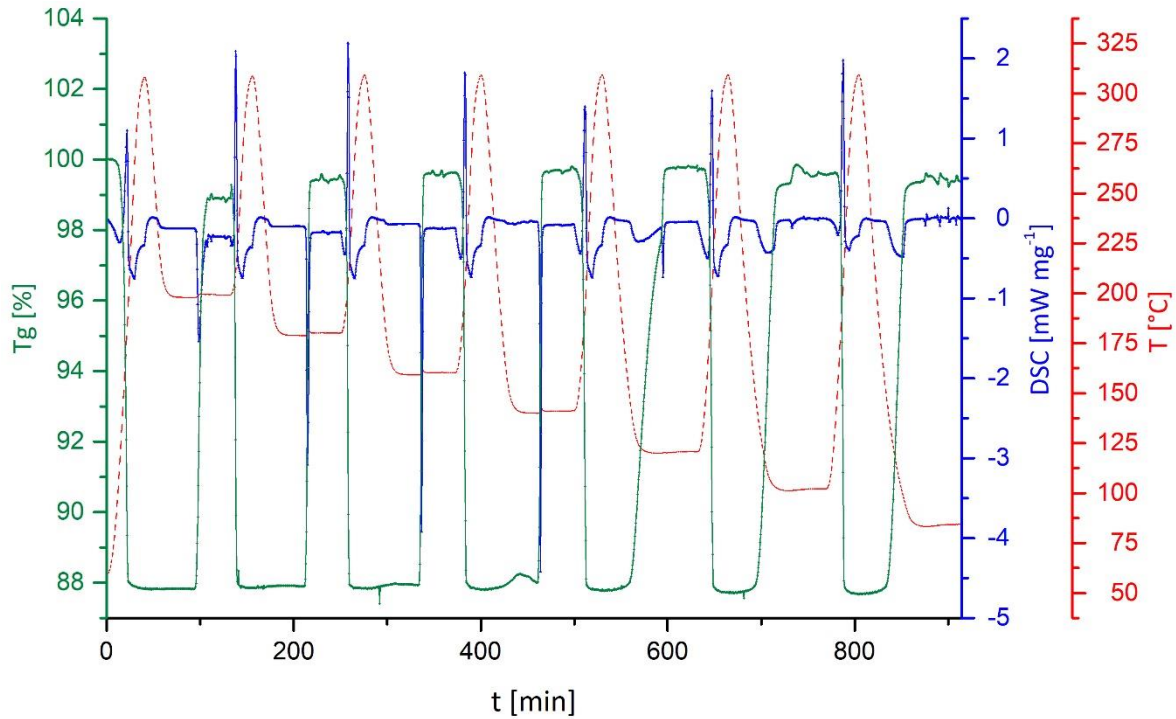


Figure 2: STA analysis of isothermal cycles of  $\text{CaC}_2\text{O}_4 \cdot \text{H}_2\text{O} / \text{CaC}_2\text{O}_4$  at different temperature levels

Also the economic benefit of implementing TCES-cycles in the energy management was demonstrated by several economic feasibility studies, illustrating that *e.g.* with the waste heat from Lenzing AG,<sup>23</sup> the complete district heating for the Austrian city of Salzburg could be supplied.<sup>24</sup>

### 5.3. Kinetics of chemical reactions

In chemical kinetics there are different possibilities to gain information about the reaction rate and the kinetic models describing different influences on the behavior of a chemical reaction. The reaction rate can be described with the following general equation.

$$\dot{\alpha} = g(\alpha) \cdot f(T)$$

In this general expression for the reaction rate  $\dot{\alpha}$  of a simple reaction  $g(\alpha)$  is the degree-of-conversion-dependent function and  $f(T)$  the temperature-dependent function.

The Arrhenius equation is a formula in the form of this simple general expression for the temperature dependence of reaction rates. It gives the dependence of the rate constant of a chemical reaction on the absolute temperature, a pre-exponential factor and other constants of the reaction.

$$\dot{\alpha} = A e^{-\frac{E_a}{RT}}$$



In this equation  $A$  is the pre-exponential factor, which is for a given chemical reaction a constant. According to collision theory  $A$  is the frequency of collisions in the correct orientation with respect to a possible subsequent reaction,  $E_a$  is the activation energy for the reaction,  $T$  is the absolute temperature and  $R$  is the universal gas constant.<sup>25</sup>

There are several solid-state kinetic models, which are a theoretical, mathematical descriptions of experimental observations. A model can describe a certain reaction type and translates it into a rate equation. Some of the models have been developed based on different mechanistic assumptions. Other models are more empirically based and, therefore, give sometimes good numeric results, but with little mechanistic meaning. Therefore, different rate expressions are produced from these models. In solid-state kinetics, mechanistic interpretations usually involve identifying a reasonable reaction model because a detailed information about each individual reaction steps is often difficult to obtain.<sup>26, 27</sup>

A different approach is the non-parametric kinetics method (NPK), where the two functions of the equation can be decoupled, without the need of any assumptions about the functionality of  $g(\alpha)$  and  $f(T)$ . The method provides two independent vectors directly from experimental measurements, the first one containing information about  $g(\alpha)$  and the second about  $f(T)$ .<sup>28</sup>

## 5.4. Used analytical methods and measurement techniques

### 5.4.1. In-situ powder X-Ray diffraction (p-XRD) for hydration reactions

A PANalytical B.V. MPD Pro diffractometer was used to perform the P-XRD in Bragg Brentano geometry within a scattering angle  $5^\circ < 2\theta < 90^\circ$  for Cu  $K_{\alpha 1,2}$ -radiation. The instrumental resolution was defined on the primary side by a  $\frac{1}{2}^\circ$  fixed divergent entrance slit followed by a 0.04 rad Soller slit. A 0.04 rad Soller slit was placed before the X'celerator detector operated in the 1D continuous line mode. The detector to sample distance for this instrument is 240 mm. The hydration reaction of the samples was performed in an Anton Paar XRK 900 sample chamber, connected to an evaporation coil kept at 300 °C. Using a HPLC-pump, 3 g min<sup>-1</sup> water were evaporated and the resulting steam were passed through the sample (4 mm thickness) with 0.2 L min<sup>-1</sup> nitrogen as carrier gas. During rehydration the sample temperature was constantly kept at 50 °C, as governed by the thermocouple in the ceramic sample holder. Nevertheless, the atmospheric temperature in the reaction chamber is uncontrolled and due to the introduction of high-temperature steam, most likely higher than that of the sample holder. During the experiment, any condensation within the sample chamber

cannot be observed, as the reaction chamber does not allow for optical inspection whilst operation. On opening the chamber, no condensed water was found either inside of the housing or on the sample. Therefore, we assume condensation inside the reaction chamber not being a problem spoiling our results.

#### 5.4.2. *In-situ* p-XRD of ammonization reactions

The same diffractometer equipped with an Anton Paar XRK 900 sample chamber was connected to two software controlled Natec Sensor MFCs one suitable for NH<sub>3</sub> and the other one operating the N<sub>2</sub> flow for purging the sample chamber with inert atmosphere.

#### 5.4.3. *In-situ* p-XRD O<sub>2</sub>/air of redox reactions

The same diffractometer equipped with an Anton Paar HTK 1200 sample chamber was used. In contrast to the XRK 900 setup in his case the sample was placed in a flat ceramic crucible and the reactive atmosphere was not passed through the sample but had to diffuse through a 0.7 mm thick layer of sample.

The diffractograms were evaluated using the PANalytical program suite HighScorePlus v4.6a.<sup>29</sup> A background correction and a K<sub>α2</sub> strip were performed. Phase assignment is based on the ICDD-PDF4+ database,<sup>30</sup> the exact phase composition, shown in the conversion plots, was obtained via Rietveld-refinement incorporated in the program suite HighScorePlus v4.6a.<sup>29</sup>

#### 5.4.4. TG / DSC of rehydration reactions

All STA data including rehydration steps were performed on a Netzsch STA 449 C Jupiter® equipped with a combined TGA-DSC sample holder using open aluminum oxide crucibles containing sample masses between 20 and 30 mg. The system was equipped with a water vapor furnace, including an air-cooled double jacket and a heated vapor inlet. The oven is operable between 25 °C and 1250 °C, regulated by an S-type thermocouple. The steam was produced in an Adrop water vapor generator, which was set to 105 °C. The water vapor was transferred into the furnace via a heated transfer line and a heated collar, the transfer line was set to 105 °C. To prevent condensation of the water, a carrier gas stream of 100 ml N<sub>2</sub> min<sup>-1</sup> was used. The protective gas stream was set to 5 ml N<sub>2</sub> min<sup>-1</sup>. The gas flow was controlled using red-y smart series mass-flow controller by Voegtlin with an operable range between 2-100 ml min<sup>-1</sup>.

#### 5.4.5. TG / DSC of ammonization and redox reactions

All STA data including reaction steps and oxidizing or reducing atmospheres, as well as ammonia atmospheres were performed on a Netzsch STA 449 C Jupiter® equipped with a combined TGA-DSC sample holder using open aluminum oxide crucibles containing sample masses between 20 and 30 mg. The system was equipped with a water vapor furnace, including an air-cooled double jacket and a heated vapor inlet. The oven is operable between 25 °C and 1250 °C, regulated by an S-type thermocouple. In this case the Adrop water vapor generator and the heated transfer line were detached and the red-y smart series mass-flow controller by Voegtlin were connected to the instrument directly. The gas mixing was performed via gas mixture in T-connectors.

#### 5.4.6. TG / DSC of decomposition reactions

Thermal decomposition data were obtained using a Netzsch STA 449 F1 Jupiter® system equipped with an automatic sample changer and heating rates of 2, 5 and 10 °C min<sup>-1</sup> under N<sub>2</sub> atmosphere between 50 °C and 450 °C using either open or closed aluminum crucibles.

#### 5.4.7. Brunauer, Emmett and Teller (BET) Specific surface area calculation

The specific surface of the samples was determined by nitrogen sorption measurements, which were performed on an ASAP 2020 (Micromeritics) instrument. The samples (amounts between 100-200 mg) were degassed under vacuum at 80 °C overnight prior to measurement. The surface area was calculated according to Brunauer, Emmett and Teller (BET).<sup>31</sup>

#### 5.4.8. Scanning Electron Microscope (SEM)

A JEOL JSM-5410 analogue scanning electron microscope equipped with a Bruker AXS digitalizing signal processing unit was used to obtain 2D images of the particles of the powder samples. The samples were mounted on carbon pellets on top of the sample holder and plasma vacuum deposition was used to coat the samples with a thin layer of gold to ensure conductivity. The gold coating was performed using a Baltec Med020 sputtering system. The sample was evacuated for 10 minutes at 7·10<sup>-4</sup> mbar, followed by adjustment of an Ar pressure of 10<sup>-2</sup> mbar. For the evaporation of the gold target a current of 150 mA for 150 seconds was used.

#### 5.4.9. Data Evaluation and Plotting

All measurement curves and diagrams were exported from the measurement software and plotted for publication using the software package Origin Lab Corporation OriginPro 2016.

SEM images were adjusted for brightness and contrast using Adobe Photoshop CSS Version 12.4.

#### 5.5. Remark on the thesis

This PhD-thesis is presented in the cumulative form following the guidelines “Richtlinie des Vizerektors für Lehre über die Verfassung von kumulativen Dissertationen an der Technischen Universität Wien” from 1<sup>st</sup> October 2014, consisting of an introductory chapter followed by four accepted publications and seven submitted papers.

[https://www.tuwien.ac.at/fileadmin/t/ukanzlei/Richtlinie\\_fuer\\_kumulative\\_Dissertationen.pdf](https://www.tuwien.ac.at/fileadmin/t/ukanzlei/Richtlinie_fuer_kumulative_Dissertationen.pdf)

[http://www.tuwien.ac.at/fileadmin/t/ukanzlei/t-ukanzlei-english/Theses\\_-\\_Writing\\_of\\_Theses\\_by\\_publication.pdf](http://www.tuwien.ac.at/fileadmin/t/ukanzlei/t-ukanzlei-english/Theses_-_Writing_of_Theses_by_publication.pdf)

## 6. PUBLISHED JOURNAL ARTICLES

### 6.1. Probing cycle stability and reversibility in thermochemical energy storage – $\text{CaC}_2\text{O}_4 \cdot \text{H}_2\text{O}$ as perfect match?

Christian Knoll, Danny Müller, Werner Artner, Jan M. Welch, Andreas Werner, Michael Harasek, Peter Weinberger; *Applied Energy*, **2017**, *187*, 1-9;

#### **Abstract:**

The dehydration and subsequent rehydration of calcium oxalate monohydrate has yet to find application in thermochemical energy storage. Unlike for many other salt hydrates, complete reversibility of the dehydration-rehydration reaction was observed. Additionally, it was found that the rehydration temperature is strongly affected by the water vapor concentration: Full reversibility is not only achieved at room-temperature, but, depending on the water vapor concentration, at up to 200 °C. This allows isothermal switching of the material between charging and discharging by a change of the  $\text{H}_2\text{O}$ -partial pressure. Cycle stability of the material was tested by a long-term stress experiment involving 100 charging and discharging cycles. No signs of material fatigue or reactivity loss were found. In-situ powder X-ray diffraction showed complete rehydration of the material within 300 s. The experimental findings indicate that the  $\text{CaC}_2\text{O}_4 \cdot \text{H}_2\text{O}/\text{CaC}_2\text{O}_4$  system is perfectly suited for technical application as a thermochemical energy storage medium.

#### **Contribution:**

Conception of the study, STA measurements, evaluation and interpretation, *in situ* nonambient p-XRD reaction chamber setup, measurements, evaluation and interpretation, data treatment and partial writing of the manuscript.

### 6.2. Combining *in-situ* X-ray diffraction with thermogravimetry and differential scanning calorimetry – An investigation of $\text{Co}_3\text{O}_4$ , $\text{MnO}_2$ and $\text{PbO}_2$ for thermochemical energy storage

Danny Müller, Christian Knoll, Werner Artner, Michael Harasek, Christian Gierl-Mayer, Jan M. Welch, Andreas Werner, Peter Weinberger; *Solar Energy*, **2017**, *153*, 11–24;

#### **Abstract:**

Metal oxides with multiple accessible oxidation states are considered as promising candidates for high-temperature thermochemical energy storage materials. To shed light on the chemical

processes involved in redox thermochemical energy storage materials, *in-situ* powder diffraction was used in combination with atmospheric control to investigate the redox-reactions of  $\text{Co}_3\text{O}_4$ ,  $\text{MnO}_2$  and  $\text{PbO}_2$  under various conditions. Thermogravimetry and differential scanning calorimetry under the same conditions provided information on heat-flows and mass-changes. In contrast to theoretical thermodynamic considerations, only  $\text{Co}_3\text{O}_4$  and  $\text{Mn}_2\text{O}_3/\text{Mn}_3\text{O}_4$  (originating from  $\text{MnO}_2$ ) were found fully reversible. In the case of  $\text{PbO}_2$  for none of the numerous intermediate phases any kind of reversibility was observed. The effect of the  $\text{O}_2$ -concentration in the reactive atmosphere was most distinct for the  $\text{Mn}_2\text{O}_3$  system, notably affecting the reduction/oxidation temperatures, whereas for the  $\text{Co}_3\text{O}_4$  system only a moderate influence of the  $\text{O}_2$  concentration was found. Based on the stability of the intermediate phases under various atmospheres, an isothermal TCES-cycle for  $\text{Co}_3\text{O}_4$  and  $\text{Mn}_2\text{O}_3$  was investigated, triggering the redox-process by an abrupt change of reactive-gas atmosphere. The fast reaction rate combined with a significant down-shift of the reaction temperatures compared to an isokinetic redox reaction suggests application as a chemical heat pump, as well towards a broadened operational profile not only in combination with concentrating solar power plants, but also with *e.g.* recycling of industrial flue gas heat.

**Contribution:**

Partial conception of the study, STA measurements, evaluation and interpretation, *in situ* nonambient p-XRD measurements, evaluation and interpretation, data treatment and partial writing of the manuscript.

### 6.3. High-Temperature Energy Storage: Kinetic Investigations of the $\text{CuO}/\text{Cu}_2\text{O}$ Reaction Cycle

Markus Deutsch, Florian Horvath, Christian Knoll, Daniel Lager, Christian Gierl-Mayer, Peter Weinberger, and Franz Winter; *Energy & Fuels*, **2017**, 31 (3), 2324-2334;

**Abstract:**

Thermochemical energy storage (TCES) is considered a possibility to enhance the energy utilization efficiency of various processes. One promising field is the application of thermochemical redox systems in combination with concentrated solar power (CSP). There, reactions of metal oxides are in the focus of research, because they allow for an increase in the process temperature. The reaction system  $\text{CuO}/\text{Cu}_2\text{O}$  has been reported as a suitable candidate for TCES. For proper development and modeling of combined CSP–TCES processes, reliable kinetic data are necessary. This work studies the reduction of  $\text{CuO}$  and the oxidation of  $\text{Cu}_2\text{O}$

under isothermal and isokinetic conditions. The reactions are analyzed using a simultaneous thermal analysis (STA) and a lab-scale fixed-bed reactor. The reaction behavior shows significant differences between both analyses. To develop kinetic models, the non-parametric kinetic (NPK) approach is used. This model-free approach is expanded by the Arrhenius correlation to increase the applicable temperature range of the models. The resulting models are evaluated and compared. Furthermore, the cycle stability of the system over 20 cycles is assessed for a small sample mass in the STA and a large sample mass in the fixed-bed reactor.

**Contribution:**

p-XRD measurements, evaluation and interpretation, discussion of experimental findings, data treatment and assistance in writing of the manuscript.

## 6.4. An extension of the NPK method to include the pressure dependency of solid state reactions

Markus Deutsch, Felix Birkelbach, Christian Knoll, Michael Harasek, Andreas Werner, Franz Winter; *Thermochimica Acta*, **2017**, *654*, 168-178;

**Abstract:**

A novel method to identify the pressure dependency for reactions of the type  $A(s) \rightleftharpoons B(s) + C(g)$  is proposed. It is an extension of the non-parametric kinetic analysis (NPK) method as it identifies the pressure dependency in addition to the temperature and conversion dependency of the reaction. This is done by analyzing kinetic data in a three-dimensional data space (conversion, temperature, pressure) and attributing the variation of the conversion rate to these independent variables. Thus a reduction from a three-dimensional problem to three one-dimensional problems is achieved. The derivation of a kinetic model can then be performed for each dependency independently, which is easier than deriving a model directly from the data. This work presents the basic approach of the identification and combination of the three dependencies to build a full kinetic model. Also, the interpretation of the model to achieve a physically motivated model is illustrated. Then the method is applied to identify the complex reaction kinetics of the decomposition of  $CdCO_3$  based on a set of thermogravimetric measurements. It is shown that it is possible to identify interaction terms between the dependency terms.

**Contribution:**

STA measurements, evaluation and interpretation, *in situ* nonambient p-XRD measurements, evaluation and interpretation, data treatment and assistance in writing of the manuscript.

## 7. SUBMITTED JOURNAL ARTICLES

### 7.1. Calcium Doping Facilitates Water Dissociation in Magnesium Oxide

Danny Müller, Christian Knoll, Thomas Ruh, Werner Artner, Jan M. Welch, Herwig Peterlik, Elisabeth Eitenberger, Gernot Friedbacher, Michael Harasek, Peter Blaha, Klaudia Hradil, Andreas Werner, Peter Weinberger; *Advanced Sustainable Systems*, submitted 28.09.2017

#### **Abstract:**

Calcium doping of magnesium oxide results in significantly increased water dissociation rates, thus enhancing both hydration rate and reaction completeness of hydration compared to pure MgO. For a series of mixed magnesium-calcium oxides ( $\text{Mg}_x\text{Ca}_{1-x}\text{O}$ ) with varying Ca-contents between 0 and 40 % the material of a composition  $\text{Mg}_{0.9}\text{Ca}_{0.1}\text{O}$  shows the fastest rehydration, transforming completely within 80 minutes to the mixed hydroxide. In consecutive dehydration / rehydration cycles reasonable cycle stability is found. A “regeneration” of the aged material (reactivity reduced by excessive cycling) in liquid water re-establishes the initial rehydration reactivity. Density Functional Theory (DFT) calculations support the experimental findings, confirming that calcium doping can reduce the energy of the rate limiting water dissociation reaction exploiting both electronic and steric (size) effects.

#### **Contribution:**

Partial conception of the study, preparation and characterization of samples, STA measurements, evaluation and interpretation, *in situ* nonambient p-XRD reaction chamber setup, measurements, evaluation and interpretation, data treatment and partial writing of the manuscript.

### 7.2. An *in-situ* powder X-Ray diffraction study on the rehydration-reactivity of low temperature calcined $\text{Mg}(\text{OH})_2$

Danny Müller, Christian Knoll, Werner Artner, Jan M. Welch, Norbert Freiberger, Roland Nilica, Manfred Schreiner, Michael Harasek, Klaudia Hradil, Andreas Werner, Peter Weinberger; *Applied Energy*, submitted 06.10.2017

#### **Abstract**

Highly active MgO was investigated as a thermochemical energy storage (TCES) material. Special focus was given to the effects of thermal dehydration of  $\text{Mg}(\text{OH})_2$  to MgO: High



calcination temperatures and long dwell times notably affect the reactivity of MgO towards rehydration due to sintering processes. A detailed comparative study of the factors governing the rehydration reactivity, including calcination temperature and duration, resulting particle size, morphology and specific surface area and rehydration conditions, is presented. To obtain a correlation between calcination temperature, time and reactivity, sample rehydration was combined with an *in-situ* powder X-ray diffraction (P-XRD) setup. The best results and conversion rates were obtained by calcination of Mg(OH)<sub>2</sub> for 4 hours at 375 °C and subsequent rehydration in the P-XRD using 1 g min<sup>-1</sup> steam. *In-situ* calcined and rehydrated samples in the P-XRD setup showed remarkably higher rehydration reactivity, revealing ageing effects on prolonged storage of the calcined material. Experiments applying the optimized calcination and rehydration conditions in a laboratory-scale fluidized bed reactor were promising for a targeted TCES-cycle: After an initial peak-temperature of 71.5 °C, for more than 50 minutes a reaction temperature between 50-60 °C was achieved.

#### **Contribution:**

Partial conception of the study, preparation and characterization of samples, *in situ* nonambient p-XRD reaction chamber setup, measurements, evaluation and interpretation, SEM-images, BET measurements, setup of fluidized bed reactor, data treatment and partial writing of the manuscript.

### **7.3. Influence of the Particle Morphology on Cycle Stability and Hydration Behavior of Magnesium Oxide**

Danny Müller, Christian Knoll, Werner Artner, Jan M. Welch, Norbert Freiberger, Roland Nilica, Elisabeth Eitenberger, Gernot Friedbacher, Michael Harasek, Klaudia Hradil, Andreas Werner, Herwig Peterlik, Peter Weinberger; *Applied Energy*, submitted 17.10.2017

#### **Abstract**

Magnesium oxide (MgO) is a promising material for thermochemical energy storage of medium temperature waste heat. The modest calcination temperature of Mg(OH)<sub>2</sub> (350 °C – 450 °C) complements a broad variety of waste heat sources in various industrial production processes perfectly. So far, the main obstacle to application of the material in energy storage systems is its limited cycle stability. To overcome this issue, Mg(OH)<sub>2</sub>, MgCO<sub>3</sub> and MgC<sub>2</sub>O<sub>4</sub>·2H<sub>2</sub>O were compared as precursor materials for MgO-production. Depending on the precursor, the particle morphology of the resulting MgO changes, resulting in different hydration behavior and cycle stability. A regeneration step developed during the study, leading to decomposition of

agglomerates after repeated calcination / hydration cycles, restores the initial reactivity of the material. The herein presented variation of particle morphology and regeneration of spent material overcome the major obstacles of the  $\text{Mg}(\text{OH})_2$  /  $\text{MgO}$  energy storage process.

**Contribution:**

Conception of the study, STA measurements, evaluation and interpretation, *in situ* nonambient p-XRD reaction chamber setup, measurements, evaluation and interpretation, BET measurements, data treatment and partial writing of the manuscript.

## 7.4. Magnesium oxide from natural magnesite samples as thermochemical energy storage material

Christian Knoll, Danny Müller, Werner Artner, Jan M. Welch, Norbert Freiberger, Roland Nilica, Elisabeth Eitenberger, Gernot Friedbacher, Andreas Werner, Peter Weinberger, Michael Harasek; *Journal of Energy Chemistry*, submission delayed due to patent issues

**Abstract**

Thermochemical energy storage based on the  $\text{Mg}(\text{OH})_2$  /  $\text{MgO}$  cycle is considered as attractive process for recycling of industrial waste heat between 350-400 °C. Based on a recent study, revealing  $\text{MgCO}_3$ -derived  $\text{MgO}$  as highly attractive starting material for such a storage cycle, three different natural magnesites were investigated to analyze the process-performance using industrially available raw-materials. Whereas, the varying amounts of  $\text{Ca}^{2+}$  and  $\text{Fe}^{2+}$  as major impurities did not notably affect the reactivity / cycle stability within the series, compared to the analytically pure reference material a notable decrease of performance was evidenced.

**Contribution:**

Conception of the study, *in situ* nonambient p-XRD reaction chamber setup, measurements, evaluation and interpretation, BET measurements, data treatment and partial writing of the manuscript.

## 7.5. Metal oxides for thermochemical energy storage – From gas-triggered isothermal cycling to low-temperature applications with increased $\text{O}_2$ pressure

Christian Knoll, Georg Gravogl, Werner Artner, Elisabeth Eitenberger, Gernot Friedbacher, Andreas Werner, Ronald Miletich, Peter Weinberger, Danny Müller, Michael Harasek; *Conference Proceedings Solar World Congress Abu Dhabi 2017*, submitted 15.10.2017

## Abstract

Metal oxides providing various, reversibly accessible oxidation states are in the focus as auspicious materials for high-temperature thermochemical energy storage (TCES) materials. Among all principally suitable metal oxides due to equilibrium temperature and, in particular, reaction rate and reversibility, only the couple  $\text{Co}_3\text{O}_4 / \text{CoO}$  and to a smaller extend  $\text{Mn}_2\text{O}_3 / \text{Mn}_3\text{O}_4$  are considered as suitable candidates. Based on recent studies on isothermal TCES-cycles, the impact of temperature and increased  $\text{O}_2$ -pressure on the reaction rate was investigated by varying the  $\text{O}_2$ -partial pressure in the low-temperature oxidation of the reduced oxide. Whereas  $\text{Mn}_3\text{O}_4$  was found to react too slow for a process at lower temperatures,  $\text{CoO}$  was found suitable. For an increase of the  $\text{O}_2$  pressure to 6 bar between 500 – 550 °C an attractive oxidation behavior was observed. At 900 °C  $\text{Co}_3\text{O}_4 / \text{CoO}$  could be cycled within 4.5 minutes between both oxidation states by changing the atmosphere from  $\text{N}_2$  to  $\text{O}_2$  and vice versa.

## Contribution:

Conception of the study, STA measurements, evaluation and interpretation, *in situ* nonambient p-XRD reaction, measurements, evaluation and interpretation, data treatment and partial writing of the manuscript.

## 7.6. Transition metal ammoniates for thermochemical energy storage

Danny Müller, Christian Knoll, Christian Jordan, Jan M. Welch, Andreas Werner, Michael Harasek, Peter Weinberger; *Journal of Materials Chemistry A*, submitted 14.11.2017

## Abstract

On the quest for novel materials applicable as thermochemical energy storage (TCES) materials at medium-temperature levels between 25 °C - 400 °C, the class of transition metal ammoniates was so far widely neglected. In the present study a series of metal chlorides and sulphates were investigated for their performance as TCES-materials, reversibly forming in the presence of ammonia the corresponding ammine-complexes. Among the investigated materials high storage densities and high cycle stabilities were found. In the case of the chlorides decomposition in the presence of ammonia caused slow degradation. In contrast, sulphates are perfectly stable and reversible under the investigated conditions. Aiming for a combination of high storage densities and complete reversibility, for  $\text{CuSO}_4$  the best performance was obtained. According to the presented results, selected transition metal ammoniates are

suggested as attractive new materials for high-performance TCES-applications, allowing due to their high storage densities for efficient combination with e.g. solar heating to overcome non-operational times.

### **Contribution**

Assistance in the conception of the study, preparation of samples, STA adjustment for NH<sub>3</sub> and measurements, evaluation and interpretation, *in situ* nonambient p-XRD setup, reactions, measurements, evaluation and interpretation, data treatment and partial writing of the manuscript.

## **7.7. Lab-scale demonstration of thermochemical energy storage with NH<sub>3</sub> and impregnated-loaded zeolites**

Danny Müller, Christian Knoll, Georg Gravogl, Andreas Werner, Michael Harasek, Ronald Miletich, Peter Weinberger; *Conference Proceedings Solar World Congress Abu Dhabi 2017*, submitted 15.10.2017

### **Abstract**

High energy densities are one key-feature of thermochemical energy storage materials. Among the substance classes featuring the highest energy densities are oxides and carbonates, having both operational temperature profiles between 800 °C - 1200 °C. Comparable high energy contents are provided by the reaction between ammonia and (transition) metal salts, operable in a medium-temperature range between 150 °C - 450 °C. Due to the toxicity of ammonia a closed cycle preventing the release of ammonia to the surrounding environment would be necessary. Herein, CuSO<sub>4</sub> and CuCl<sub>2</sub> are investigated in a laboratory scale reactor for their application in thermochemical energy storage with ammonia as reactive gas. In the current setup after 80 seconds peak temperatures of 312 °C and 238 °C respectively were measured. To circumvent the notable volume expansion during the reaction with ammonia, both copper salts were loaded on zeolite 13X, yielding matrix-supported composite materials. Operation of those materials in the laboratory scale reactor under ammonia revealed, that the rapid temperature increase and the high peak temperatures could be retained, simultaneously simplifying the handling of the materials.

### **Contribution:**

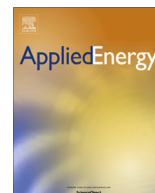
Assistance in the conception of the study, designing and setup of the final reactor design, preparation of parts of the samples, operation of some of the reactor runs, evaluation and interpretation of the results, data treatment and assistance in the writing of the manuscript.

## 8. REFERENCES

1. M. Deutsch, D. Müller, C. Aumeyr, C. Jordan, C. Gierl-Mayer, P. Weinberger, F. Winter, A. Werner, *Systematic search algorithm for potential thermochemical energy storage systems*. Applied Energy, 2016. **183**(Supplement C): p. 113-120.
2. J. Cot-Gores, A. Castell, L. F. Cabeza, *Thermochemical energy storage and conversion: A-state-of-the-art review of the experimental research under practical conditions*. Renewable and Sustainable Energy Reviews, 2012. **16**(7): p. 5207-5224.
3. U. Nations, Kyoto protocol, 1997.
4. U. N. Treatie, Paris agreement, No. 54113, , 2015.
5. IEA, *Heating without global warming: Market developments and policy considerations for renewable heat*. 2014.
6. P. Arce, M. Medrano, A. Gil, E. Oró, L. F. Cabeza, *Overview of thermal energy storage (TES) potential energy savings and climate change mitigation in Spain and Europe*. Applied Energy, 2011. **88**(8): p. 2764-2774.
7. IEA, *Co-generation and Renewables. Solutions for a low-carbon energy future*. <https://www.iea.org/publications/freepublications/publication/co-generation-and-renewables-solutions-for-a-low-carbon-energy-future.html>, 2011.
8. S. M. Hasnain, *Review on sustainable thermal energy storage technologies, Part I: heat storage materials and techniques*. Energy Conversion and Management, 1998. **39**(11): p. 1127-1138.
9. K. Shine, J. Fuglestedt, K. Hailemariam, N. Stuber, *Alternatives to the Global Warming Potential for Comparing Climate Impacts of Emissions of Greenhouse Gases*. climatic change, 2005. **68**(3): p. 281-302.
10. D. Rahm, *Sustainable Energy and the States, Essay on Politics Markets and Leadership*. McFarland, North Carolina, 2002. **1st ed.**
11. C. Wyman, J. Castle, F. Kreith, *A review of collector and energy storage technology for intermediate temperature applications*. Solar Energy, 1980. **24**(6): p. 517-540.
12. S. Hasnain, M. Smiai, Y. Al-Saedi, M. Al-Khaldi, *Energy Research Institute-Internal Report*. KACST, Riyadh, Saudi Arabia, 1996.
13. K. E. N'Tsoukpoe, H. Liu, N. Le Pierrès, L. Luo, *A review on long-term sorption solar energy storage*. Renewable and Sustainable Energy Reviews, 2009. **13**(9): p. 2385-2396.
14. D. Lefebvre, F. H. Tezel, *A review of energy storage technologies with a focus on adsorption thermal energy storage processes for heating applications*. Renewable and Sustainable Energy Reviews, 2017. **67**(Supplement C): p. 116-125.
15. A. Abedin, M. Rosen, *A Critical Review of Thermochemical Energy Storage Systems*. The Open Renewable Energy Journal, 2011. **4**: p. 42-46.
16. W. M. Haynes, *CRC handbook of chemistry and physics*. 2016, Taylor & Francis.
17. T. Bauer, W.-D. Steinmann, D. Laing, R. Tamme, *Thermal Energy Storage Materials and Systems*. Annual Review of Heat Transfer, 2012. **15**(15): p. 131-177.
18. H. Zhang, J. Baeyens, G. Cáceres, J. Degreè, Y. Lv, *Thermal energy storage: Recent developments and practical aspects*. Progress in Energy and Combustion Science, 2016. **53**: p. 1-40.
19. P. Neveu, J. Castaing, *Solid-gas chemical heat pumps: field of application and performance of the internal heat of reaction recovery process*. Heat Recovery Systems and CHP, 1993. **13**(3): p. 233-251.

20. V. Goetz, F. Elie, B. Spinner, *The structure and performance of single effect solid-gas chemical heat pumps*. Heat Recovery Systems and CHP, 1993. **13**(1): p. 79-96.
21. T. Li, R. Wang, R. Oliveira, L. Wang, *Performance analysis of an innovative multimode, multisalt and multieffect chemisorption refrigeration system*. AIChE Journal, 2007. **53**(12): p. 3222-3230.
22. T. X. Li, R. Z. Wang, J. K. Kiplagat, H. Chen, L. W. Wang, *A new target-oriented methodology of decreasing the regeneration temperature of solid-gas thermochemical sorption refrigeration system driven by low-grade thermal energy*. International Journal of Heat and Mass Transfer, 2011. **54**(21): p. 4719-4729.
23. <https://www.lenzing.com/home.html>.
24. J. Widhalm, *Thermochemische Energiespeicherung bezogen auf realitätsnahe Anwendungsfälle*. Ph.D.-thesis, TU Wien, 2016.
25. S. Arrhenius, *Über die Dissociationswärme und den Einfluss der Temperatur auf den Dissociationsgrad der Elektrolyte*. Zeitschrift für physikalische Chemie, 1889. **4**(1): p. 96-116.
26. M. E. Brown, *Stocktaking in the kinetics cupboard*. Journal of Thermal Analysis and Calorimetry, 2005. **82**(3): p. 665-669.
27. A. Khawam, D. R. Flanagan, *Solid-State Kinetic Models: Basics and Mathematical Fundamentals*. The Journal of Physical Chemistry B, 2006. **110**(35): p. 17315-17328.
28. R. Serra, J. Sempere, R. Nomen, *A new method for the kinetic study of thermoanalytical data:: The non-parametric kinetics method*. Thermochimica Acta, 1998. **316**(1): p. 37-45.
29. T. Degen, M. Sadki, E. Bron, U. König, G. Nénert, *The HighScore suite*. Powder Diffraction, 2014. **29**(2): p. 13-18.
30. <http://www.icdd.com>.
31. S. Brunauer, P. H. Emmett, E. Teller, *Adsorption of Gases in Multimolecular Layers*. Journal of the American Chemical Society, 1938. **60**(2): p. 309-319.





## Probing cycle stability and reversibility in thermochemical energy storage – $\text{CaC}_2\text{O}_4 \cdot \text{H}_2\text{O}$ as perfect match?



Christian Knoll<sup>a,b</sup>, Danny Müller<sup>a,\*</sup>, Werner Artner<sup>c</sup>, Jan M. Welch<sup>d</sup>, Andreas Werner<sup>e</sup>, Michael Harasek<sup>b</sup>, Peter Weinberger<sup>a</sup>

<sup>a</sup> Institute of Applied Synthetic Chemistry, TU Wien, Getreidemarkt 9/163-AC, A-1060 Vienna, Austria

<sup>b</sup> Institute of Chemical Engineering, TU Wien, Getreidemarkt 9/163-AC, A-1060 Vienna, Austria

<sup>c</sup> X-Ray Center, TU Wien, Getreidemarkt 9/163-AC, A-1060 Vienna, Austria

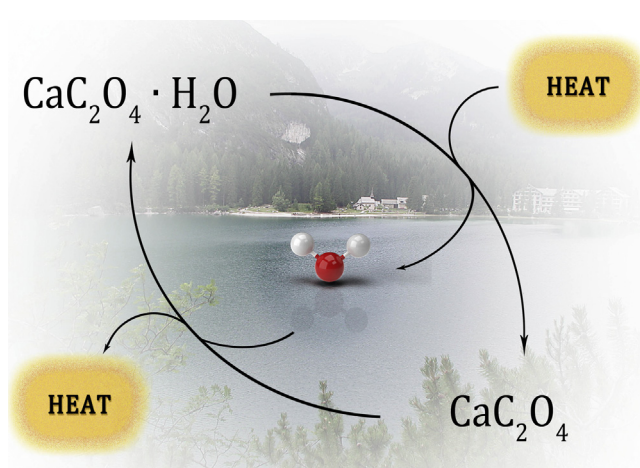
<sup>d</sup> Atominstytut, TU Wien, Stadionallee 2, 1020 Vienna, Austria

<sup>e</sup> Institute for Energy Systems and Thermodynamics, TU Wien, Getreidemarkt 9/163-AC, A-1060 Vienna, Austria

### HIGHLIGHTS

- $\text{CaC}_2\text{O}_4 \cdot \text{H}_2\text{O}$  dehydration is fully reversible between 25 °C and 200 °C.
- Isothermal cycling between hydrate and anhydrate phase can be triggered by the water vapour concentration.
- High reaction rates and full reversibility demonstrated over 100 cycles.
- Material shows no ageing effects or reactivity decrease.

### GRAPHICAL ABSTRACT



### ARTICLE INFO

#### Article history:

Received 23 September 2016

Received in revised form 10 November 2016

Accepted 13 November 2016

#### Keywords:

Calcium oxalate monohydrate

Full reversibility

Cycle stability

Water vapour concentration

Chemical heat pump

Thermochemical energy storage

### ABSTRACT

The dehydration and subsequent rehydration of calcium oxalate monohydrate has yet to find application in thermochemical energy storage. Unlike for many other salt hydrates, complete reversibility of the dehydration–rehydration reaction was observed. Additionally, it was found that the rehydration temperature is strongly affected by the water vapour concentration: Full reversibility is not only achieved at room-temperature, but, depending on the water vapour concentration, at up to 200 °C. This allows isothermal switching of the material between charging and discharging by a change of the  $\text{H}_2\text{O}$ -partial pressure. Cycle stability of the material was tested by a long-term stress experiment involving 100 charging and discharging cycles. No signs of material fatigue or reactivity loss were found. *In-situ* powder X-ray diffraction showed complete rehydration of the material within 300 s. The experimental findings indicate that the  $\text{CaC}_2\text{O}_4 \cdot \text{H}_2\text{O}/\text{CaC}_2\text{O}_4$  system is perfectly suited for technical application as a thermochemical energy storage medium.

© 2016 Elsevier Ltd. All rights reserved.

### 1. Introduction

According to the international energy agency two-thirds of all energy produced energy is wasted due to inefficiency in production

\* Corresponding author.

E-mail address: [danny.mueller@tuwien.ac.at](mailto:danny.mueller@tuwien.ac.at) (D. Müller).

and conversion processes [1,2]. Increased attention to this issue by the scientific community and governmental organizations has led to different improvements such as increased focus on renewable energy sources and international agreements such as the Kyoto-protocol to limit greenhouse-gas emissions [3]. Nevertheless, the weak point in the overall energy balance the energy loss predominantly in form of unused waste heat is still widely ignored [4].

Utilization of waste heat is an attractive and effective approach to a more efficient energy balance. One method of achieving this objective could be storage and re-use of waste heat. Thermal energy storage transfers thermal energy to a storage medium, decoupling energy availability and demand [5,6]. The stored heat could be used for heating, cooling, or drying purposes, as well as for power generation. Generally, three types of thermal energy storage systems are employed: Sensible heat storage (using liquid or solid storage media) [7–9], latent heat storage (using phase-change materials) [10,11] and thermochemical heat storage (using reversible chemical reactions) [5,6].

Compared to latent or sensible heat storage, the major advantages of thermochemical energy storage systems (TCES) are the high storage density, long-term storage ability and finally the cost efficiency. According to the principle of a TCES-system given in Eq. (1) after separation of the products B and C no back-reaction can occur, decreasing the storage efficiency.



In current literature many different potential materials for TCES-systems are discussed [6]. For a technically promising TCES-system high energy density, complete reversibility of the reaction, reasonably fast reaction kinetics and high cycle stability are required. Many systems may have these characteristics, nevertheless, only a limited number of materials have been systematically investigated.

To increase the scope of suitable materials for a TCES-application a search algorithm capable of a systematic database evaluation with subsequent extraction of potentially suitable reversible reactions was developed [12]. One possible hereto investigated candidate for energy storage applications,  $\text{CaC}_2\text{O}_4 \cdot \text{H}_2\text{O}$ , was suggested by this search. Although dehydration of  $\text{CaC}_2\text{O}_4 \cdot \text{H}_2\text{O}$  should be reversible, to the best of our knowledge, the only report on this system in the context of energy storage relates to phase change materials, in which the application of  $\text{CaC}_2\text{O}_4 \cdot \text{H}_2\text{O}$  as nucleation inhibitor is investigated [13]. Several studies focus on the kinetics of the dehydration of  $\text{CaC}_2\text{O}_4 \cdot \text{H}_2\text{O}$  [13–22], whereas only a single study of rehydration kinetics appears in literature [23,24]. The scarcity of literature data and the results of our database search suggest the utility of a detailed study of the dehydration/rehydration behaviour of  $\text{CaC}_2\text{O}_4 \cdot \text{H}_2\text{O}$ . The results achieved are very indicate that  $\text{CaC}_2\text{O}_4 \cdot \text{H}_2\text{O}$  is a promising material for TCES-application.

## 2. Experimental methodology

### 2.1. Material

Calcium oxalate monohydrate (CAS 5794-28-5) was obtained from Sigma-Aldrich and used as supplied. The anhydrous form was obtained by *in-situ* dehydration during the experiment unless otherwise stated.

### 2.2. Thermal analysis

Decomposition data were obtained using a Netzsch STA 449 F1 Jupiter® system equipped with an automatic sample changer and a combined TGA-DSC sample holder using open aluminium crucibles

containing sample masses between 12 and 14 mg. Heating rates of 2, 5 and 10 K min<sup>-1</sup> under N<sub>2</sub> atmosphere between 25 °C and 500 °C have been applied.

All data thermoanalytical data, including those from rehydration experiments, were collected on a Netzsch STA 449 C Jupiter® instrument equipped with a combined TGA-DSC sample holder using open aluminium oxide crucibles containing sample masses between 19 and 21 mg. The system was equipped with a water vapour furnace, including an air-cooled double jacket and a heated vapour inlet. The oven is operable between 25 °C and 1250 °C, regulated by an S-type thermocouple. The steam was produced in an Adrop water vapour generator, which was set to 105 °C. The water vapour was transferred into the furnace via a heated transfer line and a heated collar, both of which were set to 100 °C. To prevent condensation of the water, a carrier gas stream of 100 ml N<sub>2</sub> min<sup>-1</sup> was used. The protective gas stream was set to 5 ml N<sub>2</sub> min<sup>-1</sup>. The gas flow was controlled using red-y smart series mass-flow controller by Voegtlin with an operable range between 2 and 100 ml min<sup>-1</sup>.

All experiments reported were run at ambient pressure.

### 2.3. X-ray powder diffraction

The powder X-ray diffraction measurements were carried out on a PANalytical X'Pert Pro diffractometer in Bragg-Brentano geometry using Cu K<sub>α1,2</sub> radiation and an X'Celerator linear detector with a Ni-filter. For the *in-situ* experiments an Anton Paar XRK 900 sample chamber was used. The sample is mounted on a hollow ceramic powder sample holder, allowing for complete perfusion of the sample with the reactive gas. The reaction chamber is operated between 25 and 900 °C and a pressure between 1 mbar and 10 bar. The sample temperature is controlled via a NiCr-NiAl thermocouple and direct environmental heating. The gas flow was set to 0.2 L min<sup>-1</sup>, unless otherwise stated. For the moisture-setup a flow of 0.2 L min<sup>-1</sup> helium was bubbled through a 20 cm high water tank and a subsequent droplet separator, before passing through the sample. At the entry of the reaction chamber the gas had a dew-point temperature of 23.2 °C. The diffractograms were evaluated using the PANalytical program suite HighScorePlus v3.0d. A background correction and a K<sub>α2</sub> strip were performed.

### 2.4. Scanning electron microscopy

A JEOL JSM-5410 analogue scanning electron microscope equipped with a Bruker AXS digitalizing signal processing unit was used to obtain 2D images of the crystals shape of the powder samples. The samples were mounted on carbon pellets on top of the sample holder and plasma vacuum deposition was used to coat the samples with a thin layer of gold to ensure conductivity. The gold coating was performed using a Baltec Med020 sputtering system. The sample was held at 7·10<sup>-4</sup> mbar for 10 min, followed by adjustment of the pressure of 2·10<sup>-2</sup> mbar of argon. For the evaporation of the gold target a current of 150 mA for 150 s was used.

## 3. Results and discussion

### 3.1. Thermal dehydration of $\text{CaC}_2\text{O}_4 \cdot \text{H}_2\text{O}$

Before focussing on rehydration behaviour, the thermal dehydration of  $\text{CaC}_2\text{O}_4 \cdot \text{H}_2\text{O}$  at variable heating rates was investigated. The dehydration process is well-known in literature [17] and often used as standard example of a TG-analysis [25].

The results of a typical TG-DSC experiment for the release of the hydrate water molecule are shown in Figs. 1 and 2. The quantitative TG-DSC data correspond to literature [17] and are given in



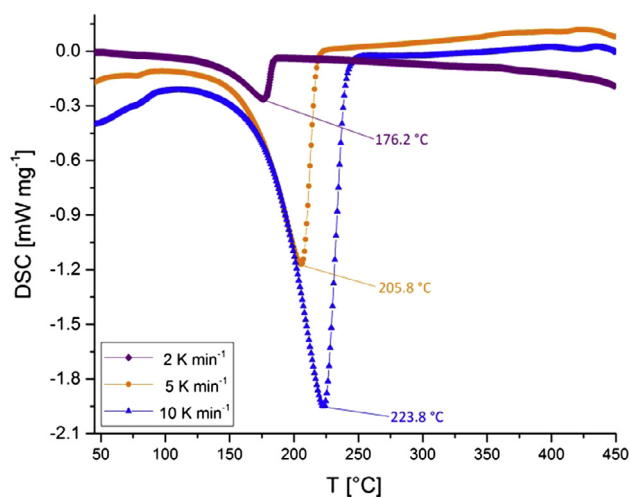


**Fig. 1.** Heat flow during the dehydration of  $\text{CaC}_2\text{O}_4\cdot\text{H}_2\text{O}$  with respect to the sample heating rate.

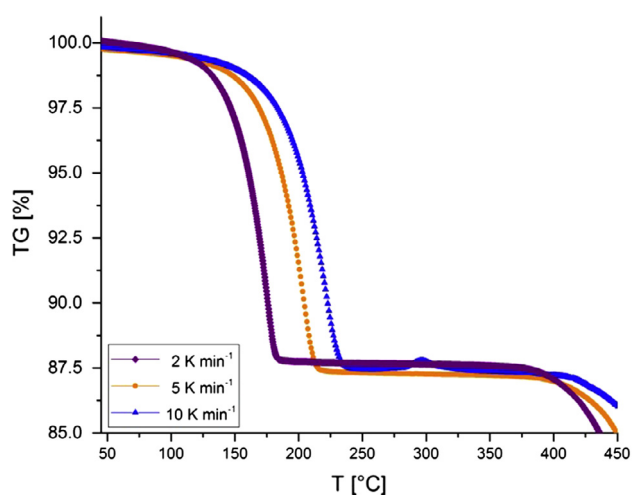


**Fig. 2.** Mass loss as a function of temperature, depicted for various heating rates for the dehydration of  $\text{CaC}_2\text{O}_4\cdot\text{H}_2\text{O}$ .

Table A.1 in the appendix. The measured enthalpy of reaction of  $467.2 \text{ J g}^{-1}$  is in good agreement to literature data [26].

For the removal of the hydrate water, the expected dependency on the sample heating rate is observed. Due to this kinetic effect changing the heating rate from  $2 \text{ K min}^{-1}$  to  $10 \text{ K min}^{-1}$ , the  $\text{peak}_{\text{max}}$ -point for the thermal dehydration is shifted  $47.6 \text{ }^\circ\text{C}$  from  $176.2 \text{ }^\circ\text{C}$  to  $223.8 \text{ }^\circ\text{C}$ . Although, this effect is well known for STA-kinetics, an unusually large shift is found here.

In the TG-signal (Fig. 2) a comparable effect is observed. The hydrate water loss occurs with a weight change of  $-12.06 \pm 0.12\%$ , corresponding to one molecule of hydrate water.

### 3.2. Effect of the heating rate and water vapour concentration on the rehydration reaction

The results obtained previously were extended to the complete dehydration/rehydration cycle using a combination of STA with a water vapour furnace. The reaction was studied applying heating rates of  $0.5 \text{ K min}^{-1}$  and  $2 \text{ K min}^{-1}$  and atmospheres having a water vapour partial pressure of  $0.084 \text{ bar}$  ( $0.4 \text{ g H}_2\text{O h}^{-1}$ ) and  $0.14 \text{ bar}$  ( $0.7 \text{ g H}_2\text{O h}^{-1}$ ). The STA-curves for these experiments are given in Fig. 3a ( $0.5 \text{ K min}^{-1}$ ) and b ( $2 \text{ K min}^{-1}$ ).

More detailed DSC and TG data for Fig. 3a and b are given in the appendix, Tables A.2 and A.3.

To better illustrate the tendencies observed in these measurements, in Fig. 4 the onset temperatures and  $\text{peak}_{\text{max}}$  temperatures of the dehydration and rehydration temperatures are plotted versus heating rate and water vapour concentration.

Apart from the kinetic shift of the  $\text{peak}_{\text{max}}$  temperature due to a varying heating rate, a similar effect is also observed for the water vapour concentration. An increase of the water vapour concentration affects the equilibrium between the hydrated and dehydrated phase of  $\text{CaC}_2\text{O}_4$  by shifting the phase stability boundary to a higher temperature. At a heating rate of  $0.5 \text{ K min}^{-1}$ , increasing the water vapour concentration from  $0.4 \text{ g h}^{-1}$  to  $0.7 \text{ g h}^{-1}$  increases the dehydration temperature by about  $11.5 \text{ }^\circ\text{C}$ . The low heating rate of  $0.5 \text{ K min}^{-1}$  was chosen to ensure an optimal heat transfer to the sample. The dehydration temperature is increased even more dramatically (by  $14.1 \text{ }^\circ\text{C}$ ) when the sample was heated at  $2 \text{ K min}^{-1}$ . For the dehydration reaction, the decomposition temperature of the hydrate phase increases with increasing heating rate and/or water vapour concentration.

For the rehydration reaction, the heating rate exhibits the reverse effect. Whereas a higher water vapour concentration increases the temperature of the initial reaction, the increased heating rate decreases the rehydration temperature. This seemingly counterintuitive observation is explained by a kinetic effect, becoming more apparent with the faster heating rate. Additionally, for the faster heating rate of  $2 \text{ K min}^{-1}$  a faster crossing of the equilibrium condition is achieved. Due to faster cooling a notable acceleration of the reaction rate (for reaction times see Tables A2 and A3) is also observed.

The synergistic effect of heating rate and water vapour concentration are highlighted in Figs. 5 and 6, showing the DSC and TG curves for the rehydration. This plot depicts the role of heating rate and water vapour concentration as independent parameters, affecting the onset of the reaction and thereby the stability bounds of the hydrate and anhydrate phase. A comparison between the green<sup>1</sup> and magenta curves ( $0.4 \text{ g H}_2\text{O h}^{-1}/0.5 \text{ K min}^{-1}$  [green] and  $0.7 \text{ g H}_2\text{O h}^{-1}/2 \text{ K min}^{-1}$  [magenta]) shows that the same increase caused in one case by a higher water vapour concentration (magenta) may also be achieved by combining a lower water vapour concentration with a reduced heating rate (green). The comparable heat flows ( $-383.9 \text{ J g}^{-1}$  [green] and  $-397.8 \text{ J g}^{-1}$  [magenta]), as well as nearly the identical rates of mass increase further confirm this correlation.

### 3.3. Correlation between rehydration temperature and water vapour concentration

To elaborate on the impact of the water vapour concentration and determine process feasibility, further investigations were undertaken. Four different vapour concentrations between  $0.4 \text{ g H}_2\text{O h}^{-1}$  ( $0.084 \text{ bar}$  partial pressure) and  $5 \text{ g H}_2\text{O h}^{-1}$  ( $0.53 \text{ bar}$  partial pressure) were selected for the rehydration reaction. For this purpose a sample of  $\text{CaC}_2\text{O}_4\cdot\text{H}_2\text{O}$  was heated to  $280 \text{ }^\circ\text{C}$  in the STA in a stream of dry nitrogen. Subsequently, the sample gas was changed to the predefined nitrogen-water vapour mixture. After a stabilization period of  $10 \text{ min}$  the sample was cooled with a rate of  $2 \text{ K min}^{-1}$ . In Figs. 7 and 8 the DSC and TG data are given.

The observed temperature shift is notably enhanced by the use of higher water vapour concentrations. The  $\text{peak}_{\text{max}}$  temperature of the reaction could be shifted between  $157.1 \text{ }^\circ\text{C}$  ( $0.4 \text{ g H}_2\text{O h}^{-1}$ ) and  $199.8 \text{ }^\circ\text{C}$  ( $5 \text{ g H}_2\text{O h}^{-1}$ ).

<sup>1</sup> For interpretation of colour in Figs. 5 and 6, the reader is referred to the web version of this article.

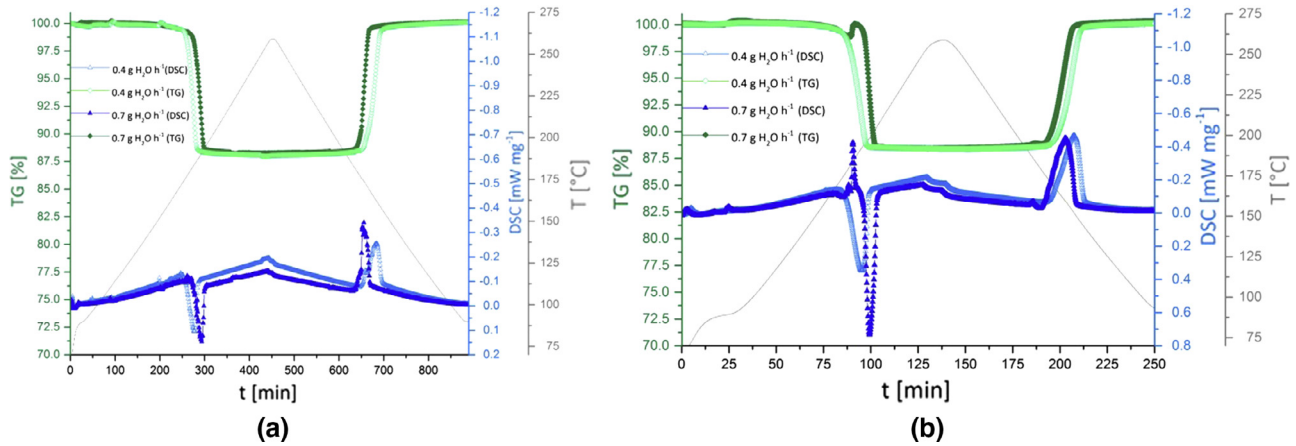


**Fig. 3.** (a) Dehydration and rehydration experiments with water vapour concentrations of 0.4 and 0.7  $\text{H}_2\text{O h}^{-1}$ , heating rate  $0.5 \text{ K min}^{-1}$ . (b) Dehydration and rehydration experiments with water vapour concentrations of 0.4 and 0.7  $\text{H}_2\text{O h}^{-1}$ , heating rate  $2 \text{ K min}^{-1}$ . The slight increase in the  $0.7 \text{ g h}^{-1}$  TG signal at 80 min is an artefact, corresponding to formation of a small water droplet on the sample holder.

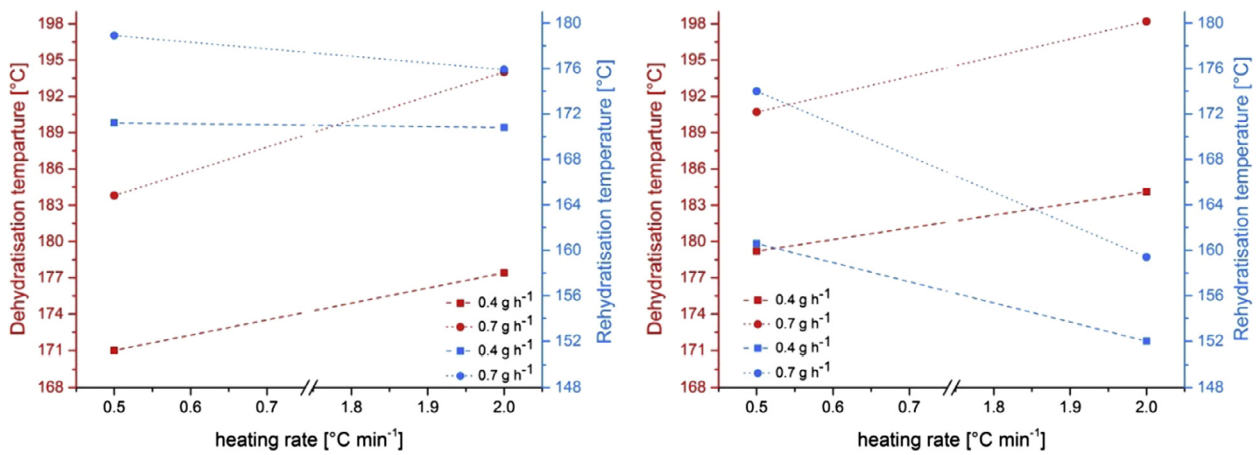


**Fig. 4.** Shift of the onset temperatures (left) and peak<sub>max</sub> temperatures (right) of the dehydration (red) and rehydration (blue) reaction with respect to heating rate and water vapour concentration. (For interpretation of the references to colour in this figure legend, the reader is referred to the web version of this article.)

Regarding a potential application in TCES, this strong dependency of the reaction temperature on the applied water vapour

concentration opens interesting new perspectives. So far, the material revealed such promising properties as fully reversible dehydra-

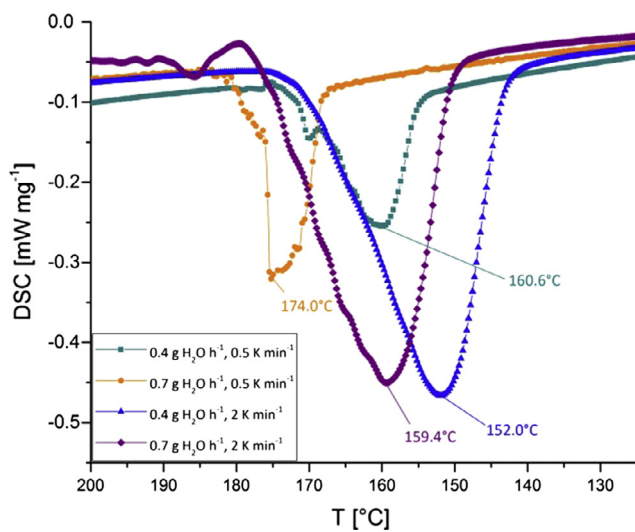


**Fig. 5.** Comparison of the DSC-curves for the rehydration reaction at different water vapour concentrations and heating rates.

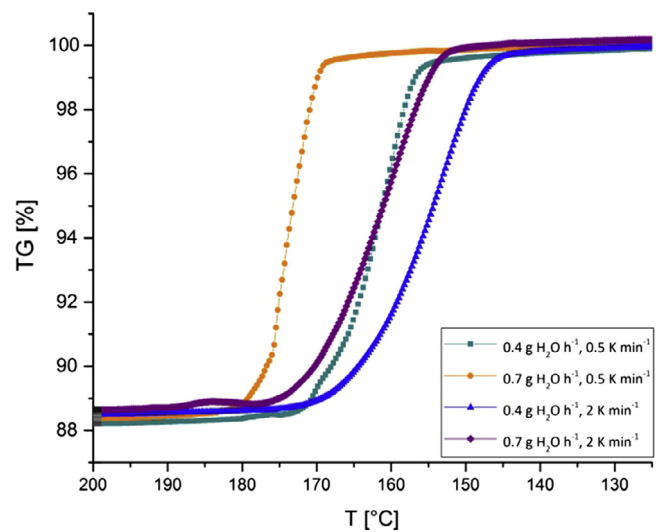


**Fig. 6.** Comparison of the mass-increase during the rehydration reaction at different water vapour concentrations and heating rates.

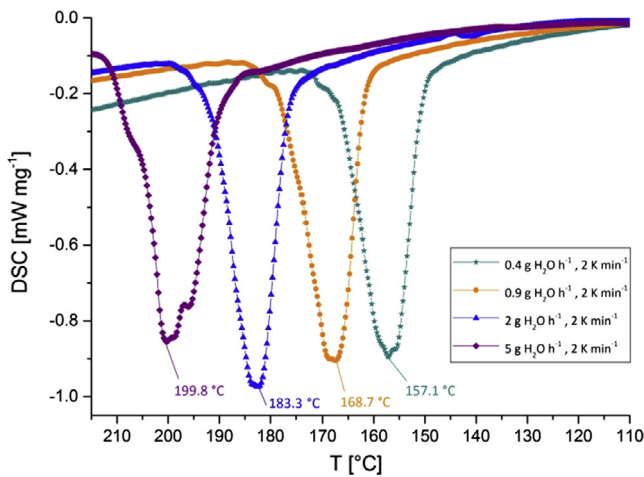


Fig. 7. Heat-flow of the rehydration reaction with respect to the water vapour concentration.

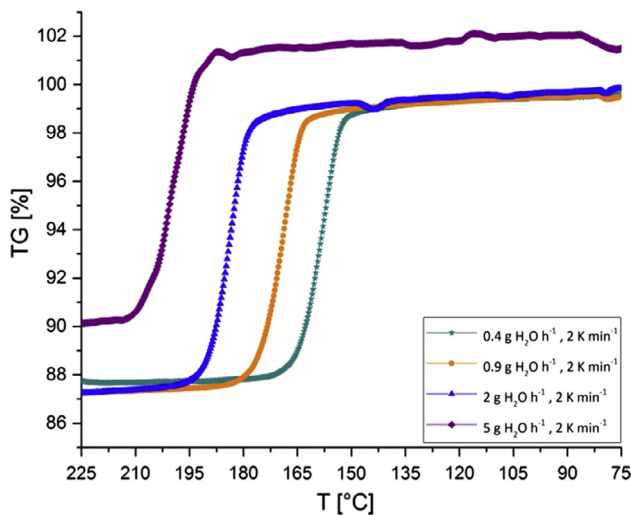


Fig. 8. Mass-change during the rehydration reaction with respect to the water vapour concentration. For all 4 curves full conversion was achieved. The shift of the 5 g H<sub>2</sub>O h<sup>-1</sup> curve about 2% is caused by condensation issues.

tion and rehydration at temperatures beyond 100 °C. This is worth mentioning, since many hydrated salts recover their complete hydrate water only at or around ambient temperature. The strong dependency on the moisture concentration allows for an isothermal cycling of the material by a change in the water vapour concentration. The process window for this approach is suggested to be between 157.1 °C, 0.4 g H<sub>2</sub>O h<sup>-1</sup> ( $p_{\text{H}_2\text{O}} = 0.084$  bar) and 199.8 °C, 5 g H<sub>2</sub>O h<sup>-1</sup> ( $p_{\text{H}_2\text{O}} = 0.53$  bar) as indicated by STA-results. The CaC<sub>2</sub>O<sub>4</sub>·H<sub>2</sub>O ↔ CaC<sub>2</sub>O<sub>4</sub> + H<sub>2</sub>O couple with its broad operational range of 42.7 °C represents a very rare example of a salt hydrate that may operate as a chemical heat pump beyond 150 °C.

### 3.4. Cycle stability of the reaction

In addition to a fast and fully reversible reaction, cycle stability is one of the most important criteria for TCES materials. The completeness of the reaction has already been verified under various conditions. To investigate the cycle stability of the material, a sample of 25 mg CaC<sub>2</sub>O<sub>4</sub>·H<sub>2</sub>O was submitted to the dehydration - rehydration cycle 100 times. The series was performed with a water vapour concentration of 0.5 g H<sub>2</sub>O h<sup>-1</sup> ( $p_{\text{H}_2\text{O}} = 0.1$  bar) and a heat-

ing rate of 5 K min<sup>-1</sup>. In Fig. 9 30 exemplarily cycles from the cycle stability experiment are shown.

Comparison of the 1st and 100th cycle demonstrates that the demand for high cycle stability is more than satisfied by the material investigated. For all 100 cycles no significant deviation in terms of reaction rate, mass change and heat flow is observed. This is an extraordinary result and clearly indicates the urgency of further experiments to develop the process on a larger scale for technical application.

### 3.5. Particle morphology and cycle stability

So far, neither the STA measurements, nor the diffraction patterns indicate ageing effects on the material studied. To further confirm this observation, different samples from the STA-cycles were analysed by scanning electron microscopy (Fig. 10).

Both the monohydrate (Fig. 10a,c,d) and the dehydrated material (Fig. 10b) appear as platelets with a notable particle fraction smaller than 3 μm. Although, for the original material a slightly larger fraction is observed, during the first dehydration cycle particle fragmentation occurs. As can be deduced by comparison of the pictures obtained after 10 cycles (Fig. 10c) and 100 cycles (Fig. 10d), the resulting distribution is more or less completely retained. Even after 100 cycles (Fig. 10d) no further fragmentation or particle sintering are observed. The particle surfaces remain smooth with clear edges and no shrinkage or cracking, typically witnessed for ageing processes is observed. This confirms visually the absence of any kind of material fatigue. These samples were only subjected to a thermal treatment in the STA, and therefore not subject to mechanical stress that occurs in a larger scale e.g. a fluidized bed reactor. Further experiments on larger scales will clarify if material fatigue or abrasion occurs under such conditions.

### 3.6. In-situ rehydration of CaC<sub>2</sub>O<sub>4</sub> in the P-XRD

Due to condensation of water in the balance of the STA setup with the water vapour furnace, a minimum temperature of 75 °C is necessary during rehydration. Based on the excellent performance of the material observed so far, the rehydration behaviour at room-temperature was investigated. This was realized by *in-situ* powder X-ray diffraction, using a gas-moistener and helium as carrier gas. A flow of 0.2 L min<sup>-1</sup> helium was bubbled through a 20 cm high water reservoir before passing through the sample. At the entrance to the reaction chamber, the gas had a dew-point temperature of 23.2 °C.

Fig. 11 shows the diffractogram of the CaC<sub>2</sub>O<sub>4</sub>·H<sub>2</sub>O phase (red) and the CaC<sub>2</sub>O<sub>4</sub> phase (blue).

To ensure *in-situ* observation of the reaction, the 2θ range between 23° and 25° was selected. In this area an unambiguous phase-assignment is possible, based on the peak-positions of the (0 2 0) reflections of the CaC<sub>2</sub>O<sub>4</sub> phase at 24.157° 2θ and the CaC<sub>2</sub>O<sub>4</sub>·H<sub>2</sub>O phase at 24.367° 2θ. The hydration reaction initiated by a flow of the moist helium through the dehydrated sample was monitored by collecting a diffractogram of the predefined area every 15 s. Fig. 12 shows a contour plot of the diffractograms obtained during the first 450 s.

From the contour-plot and the stacked representation in the insert it is apparent that after an initial period of a few diffractograms, a significant shift of the peak maximum towards the position of the (0 2 0) reflection of the hydrate-phase occurs. By evaluation of the maximum peak-positions in Fig. 13 a time dependent conversion was obtained.

The conversion rate based on the (0 2 0) reflection shows an induction period of 165 s, followed by a continuous shift of the peak maximum. After 300 s the maximum shift of the (0 2 0) reflection of the CaC<sub>2</sub>O<sub>4</sub>·H<sub>2</sub>O phase is reached. Based on these



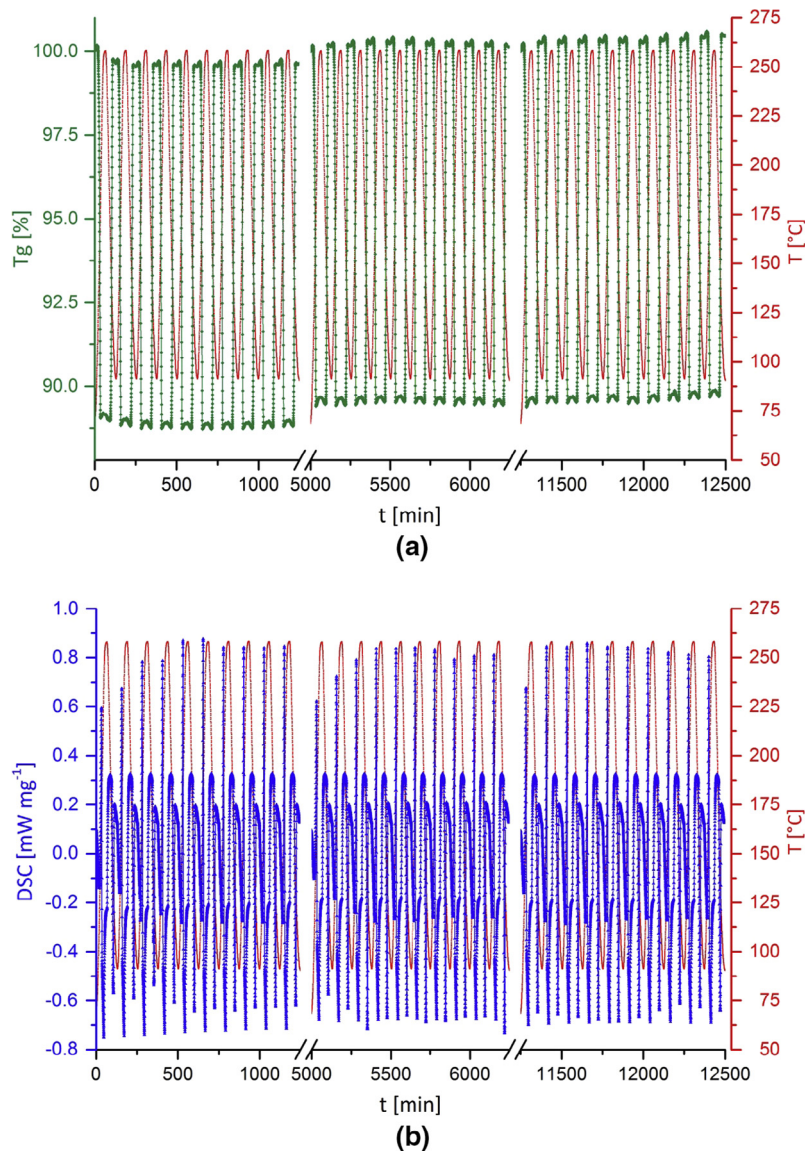


**Fig. 9.** (a) TG-curve of cycles 1–10, 51–60 and 91–100 of the  $\text{CaC}_2\text{O}_4 \cdot \text{H}_2\text{O}$  dehydration/rehydration reaction with  $0.5 \text{ g H}_2\text{O h}^{-1}$ ,  $5 \text{ K min}^{-1}$ . (b) DSC-curve of cycles 1–10, 51–60 and 91–100 of the  $\text{CaC}_2\text{O}_4 \cdot \text{H}_2\text{O}$  dehydration/rehydration reaction with  $0.5 \text{ g H}_2\text{O h}^{-1}$ ,  $5 \text{ K min}^{-1}$ .

results, the reaction is complete within 135 s. The reason for the 165 s delay at the beginning may be attributed to a kinetic inhibition effect and the transport of the water molecules to the reaction site. A similar retention was found for the rehydration in the STA in combination with the  $2 \text{ K min}^{-1}$  heating rates. The dependency of this effect on the water vapour concentration is currently subject of further investigations.

#### 4. Conclusion

The  $\text{CaC}_2\text{O}_4 \cdot \text{H}_2\text{O}/\text{CaC}_2\text{O}_4$  system was investigated using various independent methods directed at technical application as thermochemical energy storage material. STA measurements in a mixed nitrogen-water vapour atmosphere yielded a strong dependency of the reaction temperature on the heating rate applied and water vapour concentration. An increased water vapour concentration shifts the phase stability boundary towards higher temperatures, thus extending the stability regime of the hydrate phase. For the rehydration reaction this effect is opposite the heating rate, as a

higher heating rate equalizes the temperature increase of the increased vapour concentration.

In absolute values, the peak<sub>max</sub> temperature for the rehydration reaction is shifted from  $157.1 \text{ }^\circ\text{C}$  for a vapour concentration of  $0.4 \text{ g H}_2\text{O h}^{-1}$  ( $p_{(\text{H}_2\text{O})} = 0.084 \text{ bar}$ ) to  $199.8 \text{ }^\circ\text{C}$  for  $5 \text{ g H}_2\text{O h}^{-1}$  ( $p_{(\text{H}_2\text{O})} = 0.53 \text{ bar}$ ). These large shifts of the peak temperature related to the vapour concentration allow for a potential application as a chemical heat pump, thus having a broad operational possibility at high temperatures. Our results state an operational range between room-temperature and  $200 \text{ }^\circ\text{C}$ . This region may be further extended by higher water vapour concentrations. In general, the charging and discharging reaction can be independently tuned by variation of the temperature or the water vapour concentration. This allows switching the material isothermally between charging and discharging only by a change of the  $\text{H}_2\text{O}$  partial pressure.

To assess the materials' performance on repeated charging/discharging cycles – a crucial requirement for all TCES-materials – a long-term stress experiment over 100 cycles was performed. Heat flow and mass change were perfectly constant and unchanged without any indication of ageing effects. This result was also con-

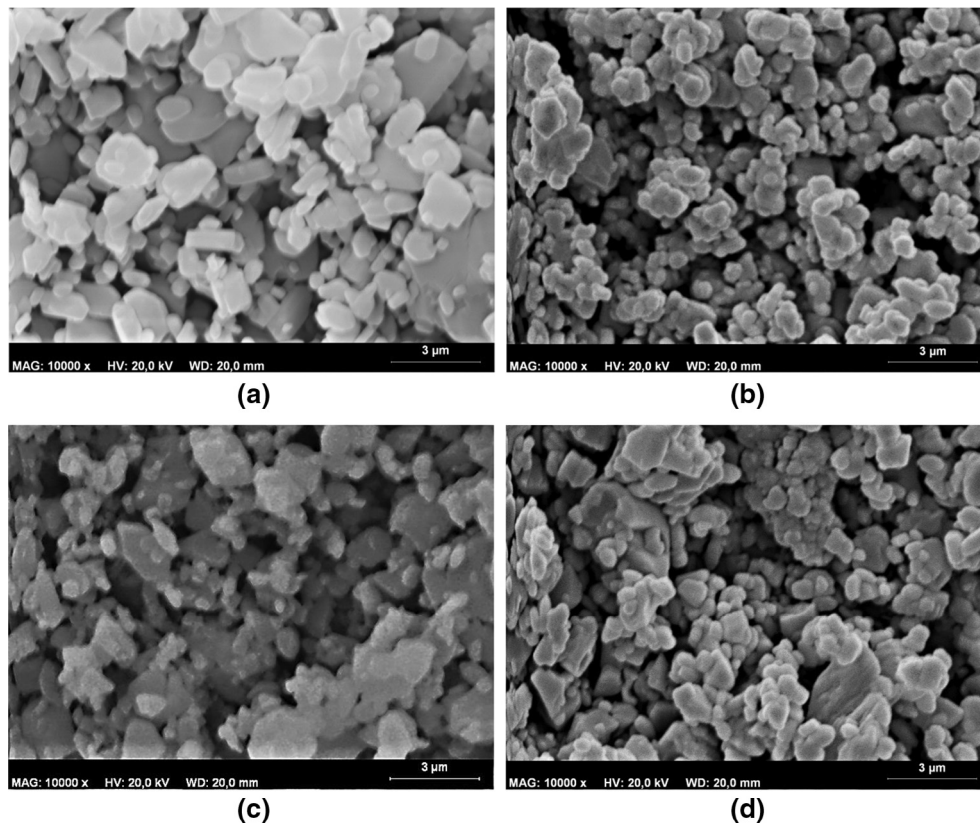


**Fig. 10.** (a)  $\text{CaC}_2\text{O}_4 \cdot \text{H}_2\text{O}$ , starting material. (b)  $\text{CaC}_2\text{O}_4$ , anhydrate phase before 1st cycle. (c)  $\text{CaC}_2\text{O}_4 \cdot \text{H}_2\text{O}$  after 10 cycles. (d)  $\text{CaC}_2\text{O}_4 \cdot \text{H}_2\text{O}$  after 100 cycles.

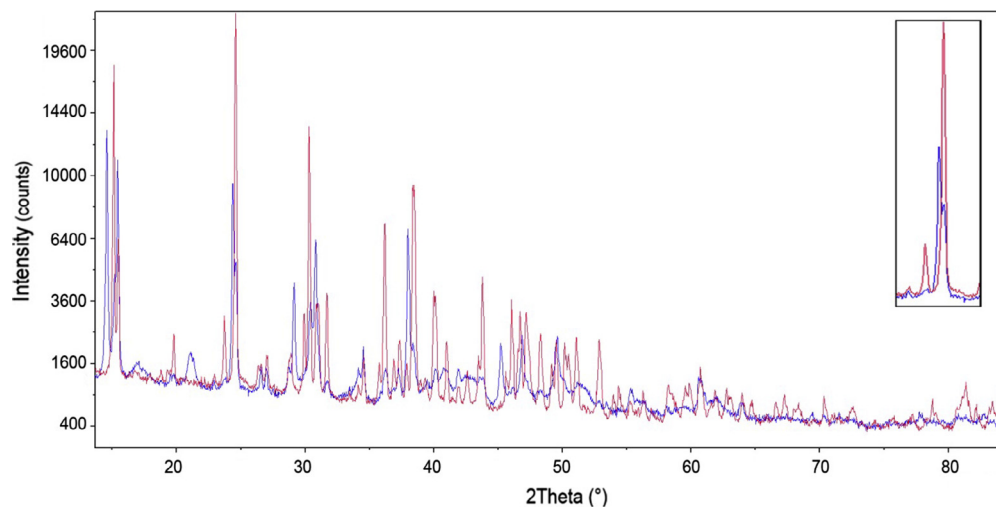


**Fig. 11.** P-XRD of the  $\text{CaC}_2\text{O}_4 \cdot \text{H}_2\text{O}$  (red) and the  $\text{CaC}_2\text{O}_4$  (blue). (For interpretation of the references to colour in this figure legend, the reader is referred to the web version of this article.)

firmed by SEM analysis, as no sign of fragmentation, sintering or any form of material fatigue was observed.

*In-situ* powder X-ray diffraction was used to follow the reaction under ambient conditions. This resulted in a complete conversion of the material within 300 s after an initial delay of 165 s.

In combination, the results are highly promising and suggest a technical application, as the material features high cycle stability, complete reversibility, rapid reaction rates and reproducible overall performance. Further investigations regarding the materials'

performance in a larger scale, e.g. in a fluidized bed reactor are ongoing in our group.

In summary, the properties rendering calcium oxalate an attractive material for technical TCES application, in addition to cycle stability and the rapid conversion evidenced in the P-XRD, the most interesting property of this system is its broad operational range. Most salt hydrates considered for TCES purposes form their hydrate at temperatures below 100 °C.  $\text{CaC}_2\text{O}_4 \cdot \text{H}_2\text{O}$  is unusual in this regard, since, depending on water vapour concentration the release of the stored energy can occur well above 100 °C. This

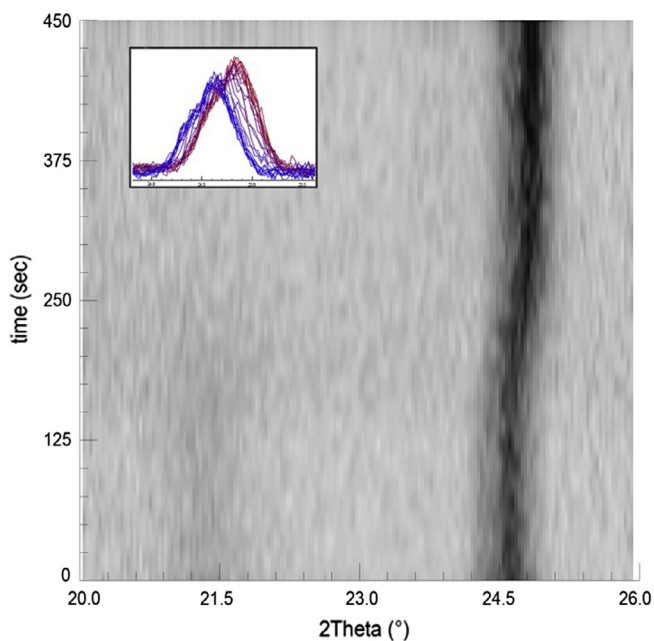


**Fig. 12.** Contour plot of the individual diffractograms taken between  $t = 0$  and 450 s. Insert: Stacked diffractograms, showing the change in the peak-position during the rehydration. Diffractograms were collected between 20 and  $26^\circ 2\theta$ , with a duration of 15 s.

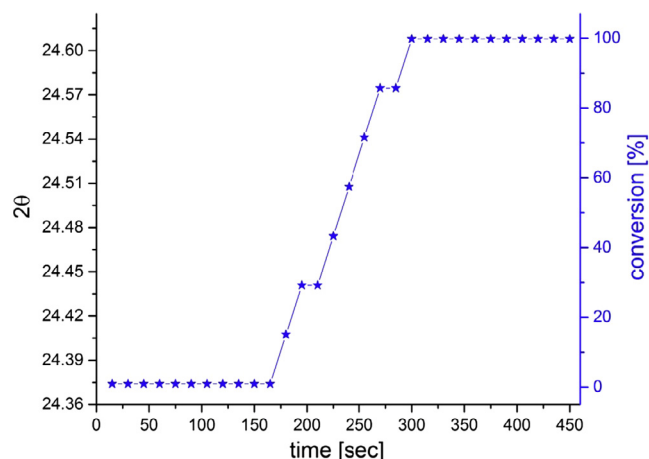


**Fig. 13.** Time-dependent conversion of the rehydration reaction, based on the evaluation of the peak positions of the (0 2 0) reflection. The shifted peak-positions compared to the database values are attributed to an off-set of the sample stage.

would allow for release of the stored heat at temperatures only slightly below the charging temperature. For industrial purposes it is preferable that the temperature difference between charging and discharging reactions be small, leading to a high exergy. Such a behaviour is usually only found for redox-reactions of metal oxides, which are investigated for high-temperature TCES in combination with concentrating solar power plants.

This loading/unloading behaviour by a change in the  $H_2O$ -partial pressure enables a cost-efficient application for low-temperature heating purposes. Such concepts can range from civil use in form of district heating up to industrial processes. A possible industrial design could include the recycling of flue-gas heat via the oxalate-system for drying purposes, preheating of process materials (as gasses or liquids) or hot water supply. It is hoped that this will stimulate other groups working in this area to investigate unestablished materials. As seen in the case of  $CaC_2O_4 \cdot H_2O$ , there is

a good possibility to identify new materials with promising properties, which than may also be capable of increasing the general visibility and thus technical interest in this field.

### Conflict of interest

The authors declare no conflict of interest.

### Acknowledgement

This work was financially supported by the Austrian Research Promotion Agency (FFGForschungsförderungsgesellschaft), project 841150 and project 848876.

The X-ray centre (XRC) of the TU Wien is acknowledged for providing access to the powder X-ray diffractometer. Moreover, we want to acknowledge Prof. Hermann Kronberger from the Institute of Chemical Technologies and Analytics, TU Wien for providing access to the scanning electron microscope and Udo Starzacher for technical support and Jan Welch from the Atominstutit TU Wien for proofreading.

### Appendix A. Supplementary material

Supplementary data associated with this article can be found, in the online version, at <http://dx.doi.org/10.1016/j.apenergy.2016.11.053>.

### References

- [1] IEA. Co-generation and renewables: solutions for a low-carbon energy future; 2011.
- [2] IEA. Heating without global warming: market developments and policy considerations for renewable heat; 2014.
- [3] Shine Keith P, Fuglestedt JS, Hailemariam Kinfe, Stuber Nicola. Alternatives to the global warming potential for comparing climate impacts of emissions of greenhouse gases. *Climatic Change* 2005;68:281–302.
- [4] Ali H, Abedin MAR. A critical review of thermochemical energy storage systems. *Open Renew Energy J* 2011;4:42–6.
- [5] Xu J, Wang RZ, Li Y. A review of available technologies for seasonal thermal energy storage. *Sol Energy* 2014;610–38.
- [6] Yan T, Wang RZ, Li TX, Wang LW, Fred Ishugah T. A review of promising candidate reactions for chemical heat storage. *Renew Sustain Energy Rev* 2015;43:13–31.
- [7] Dinker A, Agarwal M, Agarwal GD. Heat storage materials, geometry and applications: a review. *J Energy Inst* 2015. doi: <http://dx.doi.org/10.1016/j.joei.2015.10.002>.
- [8] Hasnain SM. Review on sustainable thermal energy storage technologies, Part I: Heat storage materials and techniques. *Energy Convers Manage* 1998;39:1127–38.
- [9] Zalba B, Marín JM, Cabeza LF, Mehling H. Review on thermal energy storage with phase change: materials, heat transfer analysis and applications. *Appl Therm Eng* 2003;23:251–83.
- [10] Cabeza LF, Castell A, Barreneche C, de Gracia A, Fernández AI. Materials used as PCM in thermal energy storage in buildings: a review. *Renew Sustain Energy Rev* 2011;15:1675–95.
- [11] Tian Y, Zhao CY. A numerical investigation of heat transfer in phase change materials (PCMs) embedded in porous metals. *Energy* 2011;36:5539–46.
- [12] Deutsch M, Müller D, Aumeyr C, Jordan C, Gierl-Mayer C, Weinberger P, et al. Systematic search algorithm for potential thermochemical energy storage systems. *Appl Energy* 2016;183:113–20.
- [13] Lane GA. Phase change materials for energy storage nucleation to prevent supercooling. *Sol Energy Mater Sol Cells* 1992;27:135–60.
- [14] Vlaev L, Nedelchev N, Gyurova K, Zagorcheva M. A comparative study of non-isothermal kinetics of decomposition of calcium oxalate monohydrate. *J Anal Appl Pyrol* 2008;81:253–62.
- [15] Tanaka H, Ohshima S, Ichiba S, Negita H. Kinetics and mechanism of the thermal dehydration of calcium oxalate monohydrate. *Thermochim Acta* 1981;48:137–46.
- [16] Rak J, Skurski P, Gutowski M, Błażejowski J. Thermodynamics of the thermal decomposition of calcium oxalate monohydrate examined theoretically. *J Therm Anal* 1995;43:239–46.
- [17] M'Bark ben Chanaa ML, Bertrand Gilles. Exploration systematique de la cinetique de rehydratation d'un sel renversable. Example de la Reaction  $CaC_2O_4 + H_2O \rightarrow CaC_2O_4 \cdot H_2O$ . *Thermochim Acta* 1986;97:369–85.
- [18] M'Bark ben Chanaa ML, Bertrand Gilles. Exploration systematique de la cinetique de rehydratation d'un sel renversable. II. Essai de generalisation des lois cinetiques. *Thermochim Acta* 1986;108:289–303.

- [19] Masuda Y, Ito Y, Ito R, Iwata K. Kinetic study of the thermal dehydration of calcium oxalate monohydrate. *Thermochim Acta* 1986;99:205–15.
- [20] Honcová P, Svoboda R, Pilný P, Sádovská G, Barták J, Beneš L, et al. Kinetic study of dehydration of calcium oxalate trihydrate. *J Therm Anal Calorim* 2015;124:151–8.
- [21] Duval D, Condrate RA. A raman spectral study of the dehydration of calcium oxalate monohydrate. *Appl Spectrosc* 1988;42:701–3.
- [22] Christy AA, Nodland E, Burnham AK, Kvalheim OM, Dahl B. Determination of kinetic parameters for the dehydration of calcium oxalate monohydrate by diffuse reflectance FT-IR spectroscopy. *Appl Spectrosc* 1994;48:561–8.
- [23] Chanaa MBB. Exploration systematique de la cinetique de rehydratation d'un sel renversible. III. Role de la masse initiale de l'enchantillon. *Thermochim Acta* 1988;126:265–78.
- [24] Chanaa MBB, Lallemand M, Bertrand G. Exploration systematique de la cinetique de rehydratation d'un sel renversible. *Thermochim Acta* 1986;97:369–85.
- [25] (Ed.) PJJH. Principles of thermal analysis and calorimetry. Royal Society of Chemistry; 2002.
- [26] Sádovská G, Wolf G. Enthalpy of dissolution and thermal dehydration of calcium oxalate hydrates. *J Therm Anal Calorim* 2014;119:2063–8.

## Appendix A: Supplementary Tables

**Table A.1:** DSC and TG data for fig.1 and fig.2

	2 K min <sup>-1</sup>	5 K min <sup>-1</sup>	10 K min <sup>-1</sup>
DSC-onset [°C]	143.8	165.8	183.4
DSC-peak <sub>max</sub> [°C]	176.2	205.8	223.8
heat flow [J g <sup>-1</sup> ]	187.5	488.4	446
TG-onset [°C]	152.1	177.9	195.0
mass-loss [%]	12.02	12.23	11.94

**Table A.2:** DSC and TG data for fig.3a and fig.3b, dehydration

	0.5 K min <sup>-1</sup>		2 K min <sup>-1</sup>	
	0.4 g H <sub>2</sub> O h <sup>-1</sup>	0.7 g H <sub>2</sub> O h <sup>-1</sup>	0.4 g H <sub>2</sub> O h <sup>-1</sup>	0.7 g H <sub>2</sub> O h <sup>-1</sup>
DSC-onset [°C]	179.2	183.8	170.6	194.0
DSC-peak <sub>max</sub> [°C]	179.2	190.7	184.1	198.2
heat flow [J g <sup>-1</sup> ]	341.9	351.5	332.1	389.2
TG-onset [°C]	172.9	184.2	173.3	194.7
mass-loss [%]	-11.47	-11.22	-11.27	-11.55

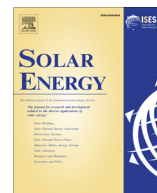
**Table A.3:** DSC and TG data for fig.3a and fig.3b, rehydration

	0.5 K min <sup>-1</sup>		2 K min <sup>-1</sup>	
	0.4 g H <sub>2</sub> O h <sup>-1</sup>	0.7 g H <sub>2</sub> O h <sup>-1</sup>	0.4 g H <sub>2</sub> O h <sup>-1</sup>	0.7 g H <sub>2</sub> O h <sup>-1</sup>
DSC-onset [°C]	154.3	167.3	143.4	150.5
DSC-peak <sub>max</sub> [°C]	160.6	174.0	152.0	159.4
heat flow [J g <sup>-1</sup> ]	-383.9	-413.6	-368.7	-397.8
TG-onset [°C]	156.7	170.5	147.3	154.2
mass-loss [%]	11.18	11.21	11.26	11.25



**Table A.4:** DSC and TG data for fig.7 and fig.8, rehydration

	0.4 g H <sub>2</sub> O h <sup>-1</sup>	0.9 g H <sub>2</sub> O h <sup>-1</sup>	2 g H <sub>2</sub> O h <sup>-1</sup>	5 g H <sub>2</sub> O h <sup>-1</sup>
DSC-onset [°C]	179.2	183.8	170.6	194.0
DSC-peak <sub>max</sub> [°C]	157.1	168.7	183.3	199.8
heat flow [J g <sup>-1</sup> ]	-319.7	-312.4	-303.5	-303.1
TG-onset [°C]	152.9	164.7	180.0	195.2
mass-loss [%]	11.31	11.32	11.66	11.09



# Combining *in-situ* X-ray diffraction with thermogravimetry and differential scanning calorimetry – An investigation of $\text{Co}_3\text{O}_4$ , $\text{MnO}_2$ and $\text{PbO}_2$ for thermochemical energy storage



Danny Müller<sup>a,\*</sup>, Christian Knoll<sup>a,b</sup>, Werner Artner<sup>c</sup>, Michael Harasek<sup>b</sup>, Christian Gierl-Mayer<sup>e</sup>, Jan M. Welch<sup>f</sup>, Andreas Werner<sup>d</sup>, Peter Weinberger<sup>a</sup>

<sup>a</sup> Institute of Applied Synthetic Chemistry, TU Wien, Getreidemarkt 9/163-AC, A-1060 Vienna, Austria

<sup>b</sup> Institute of Chemical, Environmental & Biological Engineering, TU Wien, Getreidemarkt 9, A-1060 Vienna, Austria

<sup>c</sup> X-ray Center, TU Wien, Getreidemarkt 9, A-1060 Vienna, Austria

<sup>d</sup> Institute for Energy Systems and Thermodynamics, TU Wien, Getreidemarkt 9, A-1060 Vienna, Austria

<sup>e</sup> Institute of Chemical Technologies and Analytics, TU Wien, Getreidemarkt 9, A-1060 Vienna, Austria

<sup>f</sup> Atominstytut, TU Wien, Stadionallee 2, 1020 Vienna, Austria

## ARTICLE INFO

### Article history:

Received 17 November 2016

Received in revised form 9 May 2017

Accepted 11 May 2017

### Keywords:

Metal oxide

Redox system

Non-ambient P-XRD

Isothermal redox cycle

Thermochemical energy storage

## ABSTRACT

Metal oxides with multiple accessible oxidation states are considered as promising candidates for high-temperature thermochemical energy storage materials. To shed light on the chemical processes involved in redox thermochemical energy storage materials, *in-situ* powder diffraction was used in combination with atmospheric control to investigate the redox-reactions of  $\text{Co}_3\text{O}_4$ ,  $\text{MnO}_2$  and  $\text{PbO}_2$  under various conditions. Thermogravimetry and differential scanning calorimetry under the same conditions provided information on heat-flows and mass-changes.

In contrast to theoretical thermodynamic considerations, only  $\text{Co}_3\text{O}_4$  and  $\text{Mn}_2\text{O}_3/\text{Mn}_3\text{O}_4$  (originating from  $\text{MnO}_2$ ) were found fully reversible. In the case of  $\text{PbO}_2$  for none of the numerous intermediate phases any kind of reversibility was observed. The effect of the  $\text{O}_2$ -concentration in the reactive atmosphere was most distinct for the  $\text{Mn}_2\text{O}_3$  system, notably affecting the reduction/oxidation temperatures, whereas for the  $\text{Co}_3\text{O}_4$  system only a moderate influence of the  $\text{O}_2$  concentration was found.

Based on the stability of the intermediate phases under various atmospheres, an isothermal TCES-cycle for  $\text{Co}_3\text{O}_4$  and  $\text{Mn}_2\text{O}_3$  was investigated, triggering the redox-process by an abrupt change of reactive-gas atmosphere. The fast reaction rate combined with a significant down-shift of the reaction temperatures compared to an isokinetic redox reaction suggests application as a chemical heat pump, as well towards a broadened operational profile not only in combination with concentrating solar power plants, but also with e.g. recycling of industrial flue gas heat.

© 2017 Elsevier Ltd. All rights reserved.

## 1. Introduction

Heat-storage systems are considered a promising method for minimization of heat loss in industry and other environments (Abedin and Rosen, 2011; Dinker et al., 2017). Concepts based on latent heat storage or phase change materials have already been commercialized (Cabeza et al., 2011; Xu et al., 2014; Tian and Zhao, 2011), whereas thermochemical energy storage (TCES) is still a rather academic approach. In fact, TCES could prove superior to established systems, as it provides higher storage capacity, broader

operational temperature range and negligible loss on storage (Bauer et al., 2012; Yan et al., 2015; Zhang et al., 2016).

Depending on the target application, proper selection of the TCES-material allows temperature range tuning from low-temperature “household-applications” up to the high-temperature regime in e.g. concentrating solar power plants. Salt hydrates as  $\text{CaC}_2\text{O}_4 \cdot \text{H}_2\text{O}$  have been investigated for temperature regimes between 100 and 200 °C (Knoll et al., 2017; van Essen et al., 2009), whereas e.g. decomposition of hydroxides as  $\text{Mg}(\text{OH})_2$  or  $\text{Ca}(\text{OH})_2$  (Kato et al., 2009) and ammoniates (Yan et al., 2015) are applicable up to 400–600 °C. Finally, oxide carbonation or oxide redox-couples allow for heat-storage at temperatures above 1000 °C (Kuravi et al., 2012; Prieto et al., 2016).

\* Corresponding author.

E-mail address: [danny.mueller@tuwien.ac.at](mailto:danny.mueller@tuwien.ac.at) (D. Müller).

In the case of oxides, energy storage is realized by reversible redox-reactions of metal oxides with different stable oxides in variable oxidation states. The charging reaction causes a reduction of the metal center, whereas during the liberation of the stored heat a higher oxidation state is reformed:



The interest in such high-temperature storage materials is related mainly to solar power plants and high temperature batch processes, for which heat storage is crucial to bridging non-operational times (Prieto et al., 2016). Carbonates could also be operated in high-temperature cycles, but the necessary carbon dioxide for the energy liberation needs to be stored. This drawback is overcome in the case of oxides, as the reoxidation reaction is not necessarily operated under pure oxygen, thus instead using air. Apart of the economic benefit the technological implementation is simplified.

Metal oxides as TCES-materials have been under investigation since the 1980s (Ervin, 1977), and many efforts in this direction exist (Block and Schmäcker, 2016). A review article of André et al. summarizes the most recent achievements (André et al., 2016). The most prominent example is the high-temperature redox-chemistry of  $Co_3O_4$ . Apart from its cost and toxicity, its performance is promising (Agrafiotis et al., 2014; Hutchings et al., 2006; Pagkoura et al., 2014). Cycle stability and high energy output – crucial points for a TCES-material – have been established (Agrafiotis et al., 2014), and a multitude of recent studies focus on material improvement and processing: Agrafiotis et al. reported the redox-cycling of  $Co_3O_4$  on several solid supports for implementation in a reactor-setup (Agrafiotis et al., 2016b; Agrafiotis et al., 2015a, 2015b), as well as the combination with  $Mn_2O_3$  in a cascade-energy storage concept (Agrafiotis et al., 2016a). Other approaches, focussing on faster reoxidation of  $CoO$ , concentrate on the spinel-chemistry of  $Co_3O_4$ , leading to the formation of binary metal oxides (Babiniec et al., 2015; Block et al., 2014; Pagkoura et al., 2016). Material fatigue and mechanical stress were investigated through studies of cycle stability (Karagiannakis et al., 2016; Pagkoura et al., 2014) and concepts for implementation in technological processes have already been developed (Neises et al., 2012). In addition to the  $Co_3O_4/CoO$  couple, several groups have investigated the high-temperature redox-chemistry of  $Mn_2O_3/Mn_3O_4$  as a thermochemical storage material (Alonso et al., 2013; Carrillo et al., 2014, 2015; Chen et al., 2013). So far, only minor information on the phases involved in the redox-cycle, correlations between temperature and oxygen-concentration, as well as the boundary conditions for oxidation and reduction in dependency to the reactive-gas atmosphere are available for the pure oxides. Due to the inferior redox-reversibility and oxidation kinetics of  $Mn_3O_4$  compared to  $CoO$ , mixed manganese-oxides were investigated. The main efforts in this area have focussed on perovskite-chemistry (Babiniec et al., 2015, 2016) and doping  $Mn_2O_3$  with Fe (Carrillo et al., 2015), both approaches significantly improved the redox reversibility.

To identify new oxide candidates for high-temperature thermochemical energy storage (André et al., 2016), three thermodynamically potentially reversible oxide redox-reactions (Deutsch et al., 2016) were assessed for application in heat storage. In general, selection criteria for potentially suitable oxide-reactions were an equilibrium temperature below 1200 °C and a high storage density. Finally, only redox-reactions switching between different oxides were accepted to avoid issues with elementary metals during the storage-cycle. According to theoretical data, not only  $Co_3O_4$ , but also  $MnO_2$  and  $PbO_2$  should be suitable for reversible heat-storage at high temperatures. To shed light on the chemical processes during the redox-cycle, temperature dependent *in-situ*

powder X-ray diffraction (P-XRD) was selected as method of choice.  $Co_3O_4$  was selected mainly to validate the P-XRD and thermogravimetry/differential scanning calorimetry (TGA/DSC) data. Nevertheless, *in-situ* phase-determination for the redox-processes in oxidation and reduction of cobalt oxides – especially dependency to the  $O_2$  partial pressure – are lacking.

The aims of the current study are twofold. For the pure oxides  $Co_3O_4$ ,  $MnO_2$  and  $PbO_2$  a detailed investigation of the involved phases during the redox-process under various atmospheres was performed. For this purpose a combination of non-ambient *in-situ* P-XRD and TGA/DSC was selected, allowing for correlation of phase changes and phase percentages with gravimetric data. Secondly, a special focus was on the investigation of boundary conditions of the stability regime of the different (intermediate) phases as dependent on the reactive-gas atmosphere. This information was gathered with the aim of developing an isothermal TCES-cycle.

## 2. Experimental methods

### 2.1. Material

Cobalt(II,III) oxide (99.995%, CAS 1308-06-1), manganese(IV) oxide (99.99%, CAS 1313-13-9) and lead(IV) oxide (99.998%, CAS 1309-60-0) were obtained from Sigma-Aldrich and used as supplied.

### 2.2. Thermal analysis

For thermal analysis of the redox-reactions a Netzsch TGA/DSC 449 C Jupiter® equipped with a water vapour furnace including an air-cooled double jacket was used. The oven operates between 25 °C and 1250 °C, regulated by an S-type thermocouple. Cobalt and manganese samples were measured between ambient temperature and 1100 °C, whereas for lead a temperature profile between ambient temperature and 750 °C was used. Oxygen and nitrogen gases were 99.999% and obtained from Messer. For all measurements under air a mixture of 21%  $O_2$  and 79%  $N_2$  was applied. The gas flow was set to 25 ml  $min^{-1}$ , controlled and mixed with Vögtlin Instruments “red-y” mass flow controllers. A sample mass of 20 mg in an open  $Al_2O_3$  crucible was used for all experiments with heating and cooling rates of 10 °C  $min^{-1}$ . The DSC was calibrated according to the procedure suggested by Netzsch, using the In, Sn, Bi, Zn, Al and Ag standards provided by the manufacturer.

### 2.3. X-Ray powder diffraction

The powder X-ray diffraction measurements were carried out on a PANalytical X'Pert Pro diffractometer in Bragg-Brentano geometry using  $Cu K_{\alpha 1,2}$  radiation and an X'Celerator linear detector with a Ni-filter. For the *in-situ* experiments an Anton Paar HTK 1200 N sample chamber was used. The sample is mounted on a ceramic powder sample holder. The reaction chamber is operated between 25 and 1200 °C and ambient pressure. The sample temperature is controlled via a Pt 10% RhPt thermocouple and direct environmental heating. The gas flow was set to 0.2 L  $min^{-1}$ , unless otherwise stated. The diffractograms were evaluated using the PANalytical program suite HighScorePlus v3.0d with a background correction and a  $K_{\alpha 2}$  strip.

The diffractograms were collected within 180 s each 10 °C after a thermal stabilization period of 180 s. The 2D-plots of the diffractograms between 50 and 1100 °C (50–750 °C for  $PbO_2$ ) qualitatively show the phase-transformations, whereas in the accompanying plots show quantitative temperature-dependent conversion in percentages.

Asymmetry in the 2D-plots at lower 2 $\theta$ -values in higher temperature measurements is caused by the thermal expansion of the unit cell.

### 3. Results and discussion

In this comparative combined P-XRD and thermoanalytical study, the temperature dependent redox-behaviour of the Co<sub>3</sub>O<sub>4</sub>/CoO, MnO<sub>2</sub>/Mn<sub>2</sub>O<sub>3</sub>/Mn<sub>3</sub>O<sub>4</sub> and PbO<sub>2</sub>/PbO were investigated under atmospheres of air, nitrogen and pure oxygen. Additionally, after reduction under nitrogen atmosphere, the materials were thermally re-oxidized under oxygen to examine the behaviour of the system in a low-temperature regime. A low temperature process may be applicable to acyclic temperature-dependent use or isothermal energy storage processes driven by changing oxygen concentration rather than temperature.

#### 3.1. The Co<sub>3</sub>O<sub>4</sub>/CoO system

Thermochemical reduction of Co<sub>3</sub>O<sub>4</sub> is one of the most promising redox reaction based high-temperature chemical energy storage methods under current investigation, combining high reaction rates with a large reaction enthalpy ( $\sim 830 \text{ J g}^{-1}$ ) (Chase, 1998). Although detailed application-oriented studies of many composite systems have appeared (Agrafiotis et al., 2016a, 2016b; Agrafiotis et al., 2014, 2015a, 2015b), the structural and chemical processes involved in the redox-cycle have yet to be investigated in detail. Therefore, guided by initial thermoanalytical studies (see Fig. 1), the behaviour of the Co<sub>3</sub>O<sub>4</sub>/CoO system through heating and cooling cycles under several different atmospheres was investigated using temperature dependent *in-situ* P-XRD (see Fig. 2).

In general, the P-XRD results agree very well with the thermoanalytical results and those previously reported in literature (Agrafiotis et al., 2014; Hutchings et al., 2006; Pagkoura et al., 2014). On heating, microcrystalline Co<sub>3</sub>O<sub>4</sub> shows a single phase up to an atmosphere dependent limit (630 °C under a nitrogen atmosphere; Fig. 2A, 840 °C under air; Fig. 2B, and 855 °C under oxygen; Fig. 2C) at which point rapid reduction to CoO is observed under an oxygen atmosphere or in air. Under a nitrogen atmosphere reduction begins at a lower temperature (630 °C), but conversion to CoO proceeds more slowly than in the other cases. Upon cooling under air or oxygen CoO is rapidly and quantitatively

re-oxidized to Co<sub>3</sub>O<sub>4</sub>, whereas under nitrogen, no re-oxidation is observed. No crystalline phases other than Co<sub>3</sub>O<sub>4</sub> and CoO are observed over the course of the heating and cooling cycles described under any atmosphere. In Fig. 2A and B the 2D-plot of the diffractograms show around 780 °C a shift of the peak-positions to lower 2 $\theta$ -values, which is not explained thoroughly by the mentioned thermal expansion of the unit cell. In this regime additionally to the normal (linear) thermal expansion also a partial spin-crossover in the Co<sub>3</sub>O<sub>4</sub> spinel-structure of the Co<sup>3+</sup> from a low-spin to a high-spin occurs, thus causing a larger expansion of the unit cell (Liu and Prewitt, 1990).

Since, as is expected chemically, the temperature at which reduction from Co<sub>3</sub>O<sub>4</sub> to CoO is initiated is dependent on the oxygen content of the atmosphere, the temperature dependence of the re-oxidation of CoO to Co<sub>3</sub>O<sub>4</sub> under oxygen was also investigated both by temperature dependent *in-situ* P-XRD (see Fig. 2D) and thermal analysis (Fig. 1). Re-oxidation of CoO is found to begin at 460 °C under oxygen and proceed, at a more or less constant rate, to completion just below 700 °C. Once again, no crystalline phases other than Co<sub>3</sub>O<sub>4</sub> and CoO are observed. Additionally, this result suggests the possibility of a medium-temperature (480–630 °C) redox energy storage cycle operated not by changing process temperature, but rather by changing the oxygen content of the gas atmosphere under which the process is occurring.

Similarly, to the potential for a medium-temperature energy storage cycle described above, reactive gas atmosphere dependent composition should also be observed around 850 °C. Therefore, the feasibility of a so far widely ignored isothermal redox energy storage cycle driven by reactive gas atmosphere was investigated. For TCES applications, minimization of the temperature spread between charging and discharging of the storage system is essential for a successful technical application (Abedin and Rosen, 2011; Solé et al., 2012). Thus, from a thermal efficiency or exergy point of view, isothermal cycle operation is superior to classical latent heat or phase change TES systems. The focus of the ongoing research activities has been to identify TCES systems with high storage capacities and fast kinetics for which isothermal or near-isothermal operation can be achieved by changing the fugacities of the reactive gases to achieve charging/discharging rather than by switching stability ranges through temperature change.

Thermoanalysis was the method of choice investigating an isothermal redox-cycle (Fig. 3), as the data point density for TGA-DSC analysis is much higher than for P-XRD. Instantaneous change

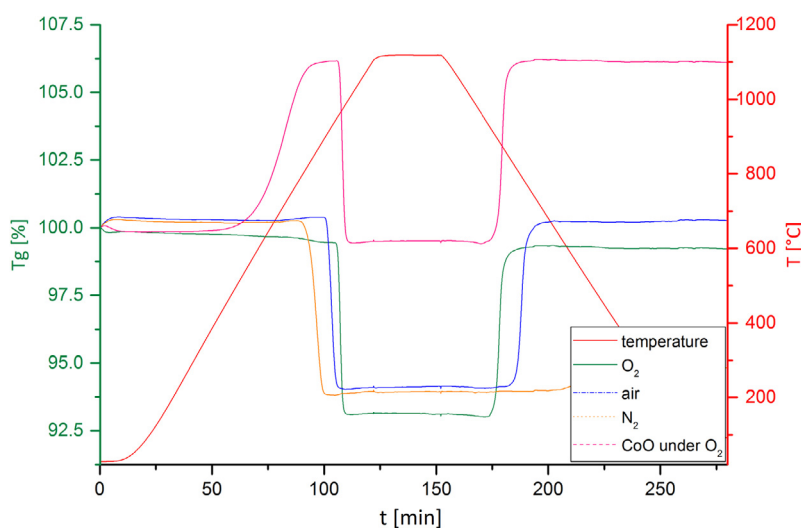
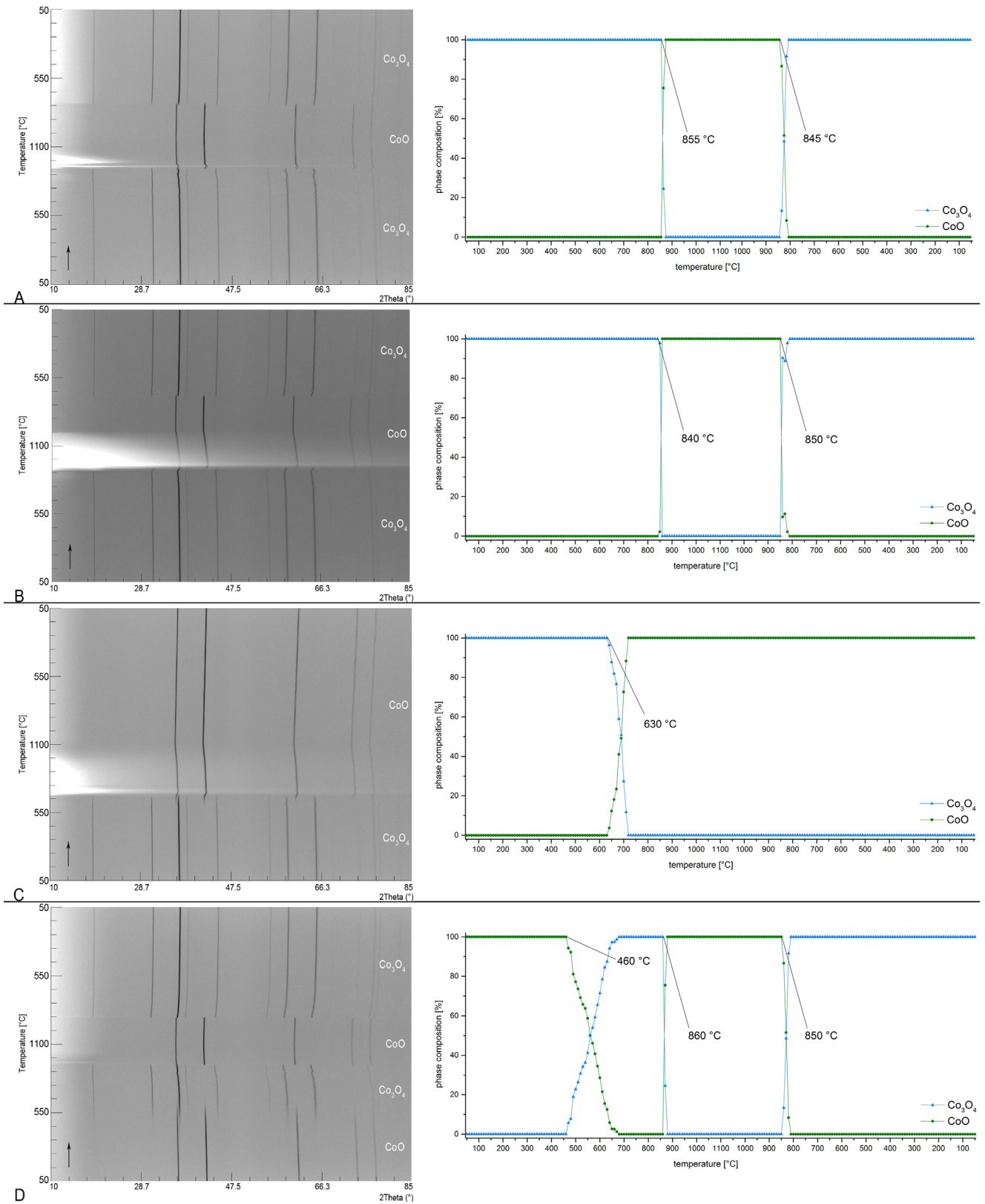


Fig. 1. Mass-changes during redox-cycles under various atmospheres for Co<sub>3</sub>O<sub>4</sub>. Detailed values for single experiments are given in the Appendix A in Tables A.1 and A.2 and agree to literature data. (Agrafiotis et al., 2014; Hutchings et al., 2006; Pagkoura et al., 2014).



**Fig. 2.** Changes in sample composition during a  $\text{Co}_3\text{O}_4$  redox-cycle under  $\text{O}_2$  (A), under air (B),  $\text{N}_2$  (C) and  $\text{O}_2$  after reduction under  $\text{N}_2$  (D).

of atmosphere from  $\text{N}_2$  to  $\text{O}_2$  (left) at 848 °C or from  $\text{N}_2$  to air (right) results in the oxidation of  $\text{CoO}$  to  $\text{Co}_3\text{O}_4$ . For both  $\text{O}_2$  and air the redox-process is fully reversible with a mass-change of  $7 \pm 0.04\%$ , also the energy liberated under either atmosphere

( $-538.9 \pm 75.06 \text{ J g}^{-1}$ ; see Table A.3) is comparable. The only atmosphere dependent difference in the processes is found in the reaction rate, since under  $\text{O}_2$  the reaction is complete after 10.4 min, whereas in air the complete oxidation is somewhat slower taking



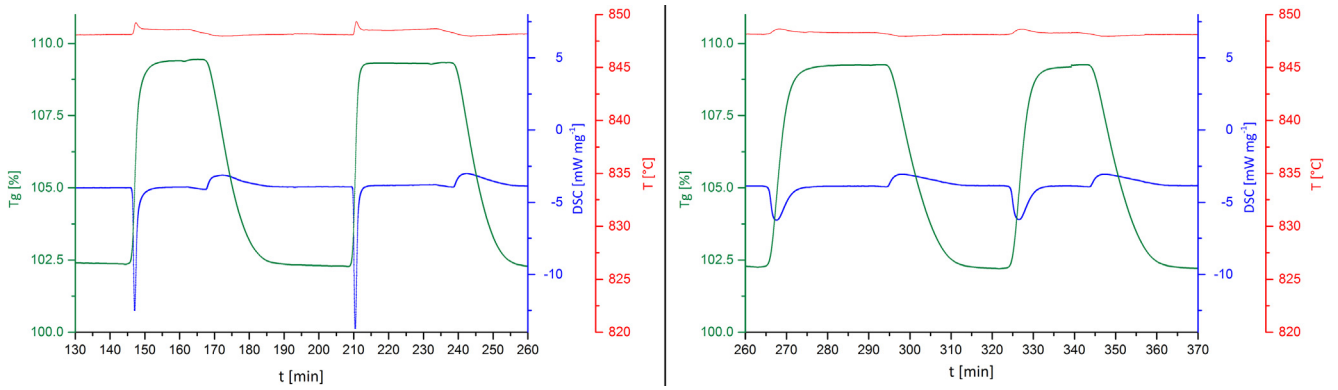


**Fig. 3.** Mass-changes and calorimetric behaviour under isothermal conditions at 848 °C, changing the atmosphere. Left: Change from N<sub>2</sub> to O<sub>2</sub>; Right: Change from N<sub>2</sub> to air.

15.4 min. Although, the reaction using pure O<sub>2</sub> is faster, as the oxidation under air takes only one and a half times as long and is technologically more interesting. Complete reduction back to CoO under N<sub>2</sub> takes 23 min.

Finally, the *in-situ* P-XRD system was also used to investigate the effect of repeated thermal cycling on the Co<sub>3</sub>O<sub>4</sub>/CoO redox energy storage system (Fig. 4). Material was subjected to five heating and cooling cycles from 800 °C to 1000 °C. As for the experi-

ments described above, the P-XRD data agree very well with the thermoanalytical data and do not indicate the formation of any species other than the cobalt oxides expected.

Having demonstrated the good agreement between thermoanalytical data and P-XRD results on the well-known system of Co<sub>3</sub>O<sub>4</sub>/CoO, the same approach was used to investigate the phase composition during the redox-cycles in the systems of MnO<sub>2</sub> and PbO<sub>2</sub>.

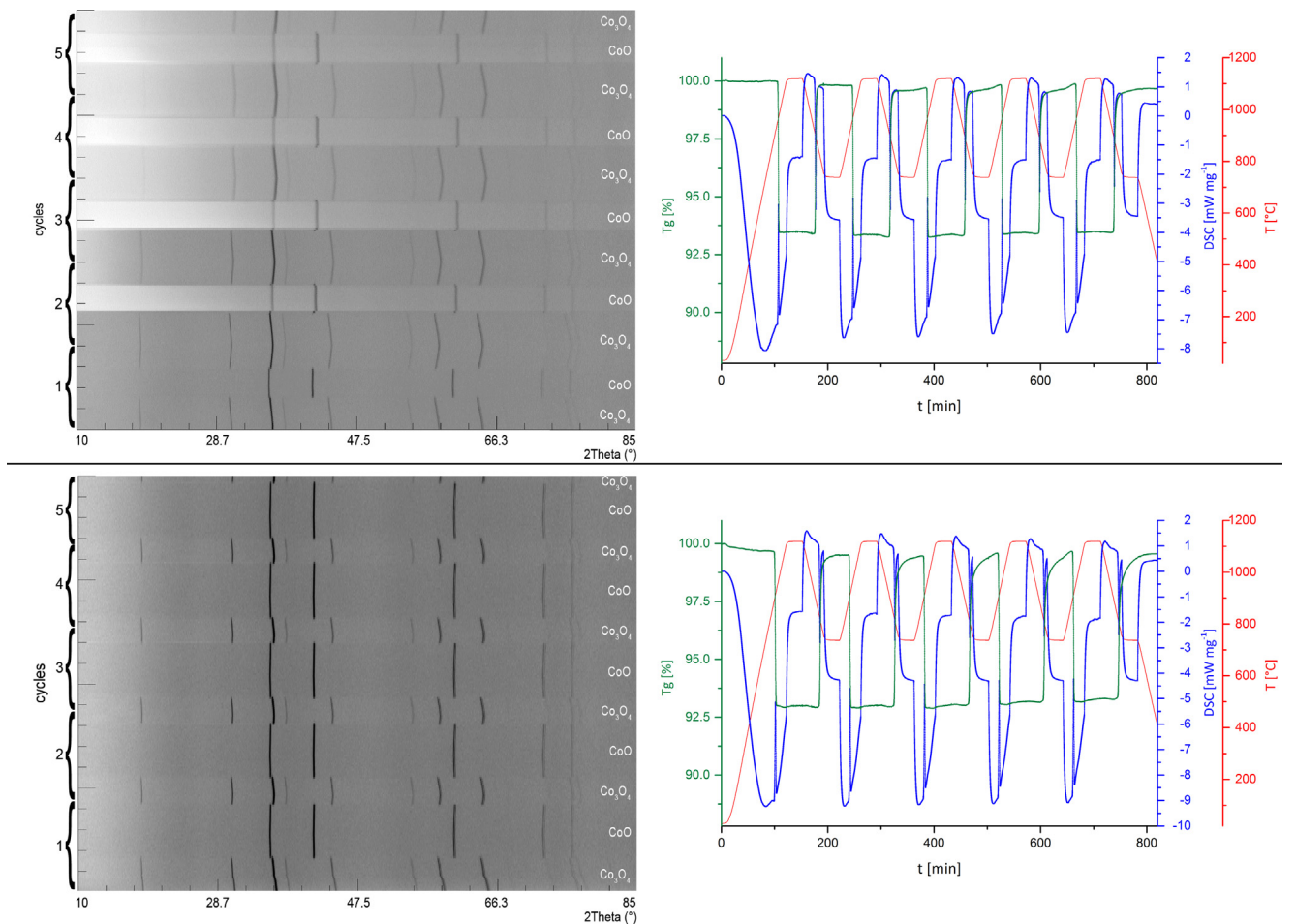


**Fig. 4.** Correlation of P-XRD and TGA/DSC data for 5 Co<sub>3</sub>O<sub>4</sub> redox-cycles under O<sub>2</sub> (top) and air (bottom) [In the DSC-curves of the cyclic redox-experiments notable artefacts of the oven-heating are witnessed. The calorimetric values from Tables A.1 and A.2 are consistent to literature (Agrafiotis et al., 2014; Block and Schmäcker, 2016), where similar issues with artefacts are observed during the DSC-runs. (Block et al., 2014)].



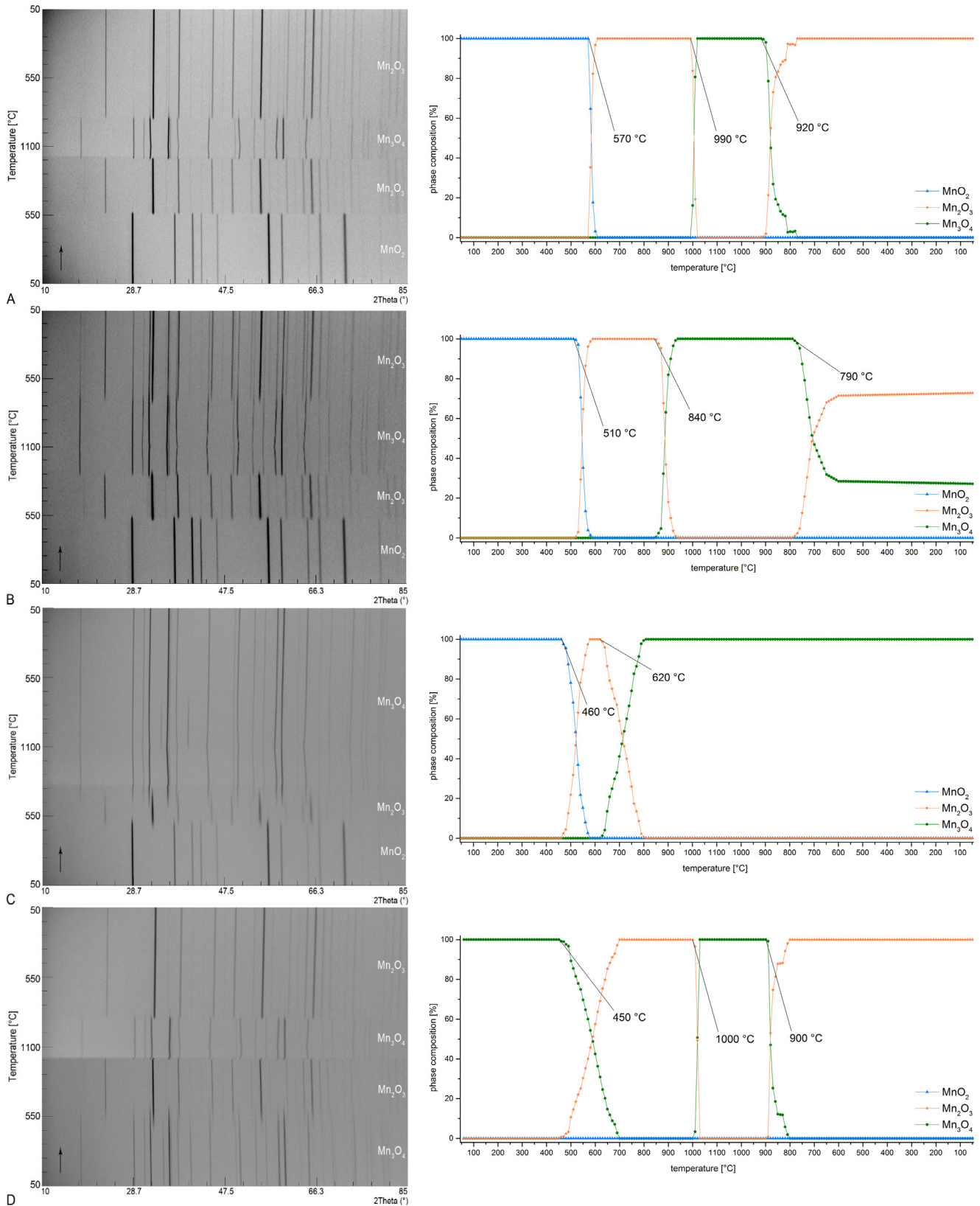


**Fig. 5.** Changes in sample composition during a  $\text{MnO}_2$  redox-cycle under  $\text{O}_2$  (A), under air (B),  $\text{N}_2$  (C) and  $\text{O}_2$  after reduction under  $\text{N}_2$  (D).

### 3.2. The $\text{Mn}_2\text{O}_3/\text{Mn}_3\text{O}_4$ system

In contrast to thermodynamic data showing that  $\text{MnO}_2$  should undergo reversible redox-chemistry (Deutsch et al., 2016), only

reversibility between  $\text{Mn}_2\text{O}_3$  and  $\text{Mn}_3\text{O}_4$ , as known from literature, was observed. Whereas the reduction of the  $\text{Mn}^{(\text{IV})}$ -state is irreversible under the conditions investigated, the redox-behaviour of the  $\text{Mn}^{(\text{III})}$  and  $\text{Mn}^{(\text{II,III})}$ -phases is notably affected



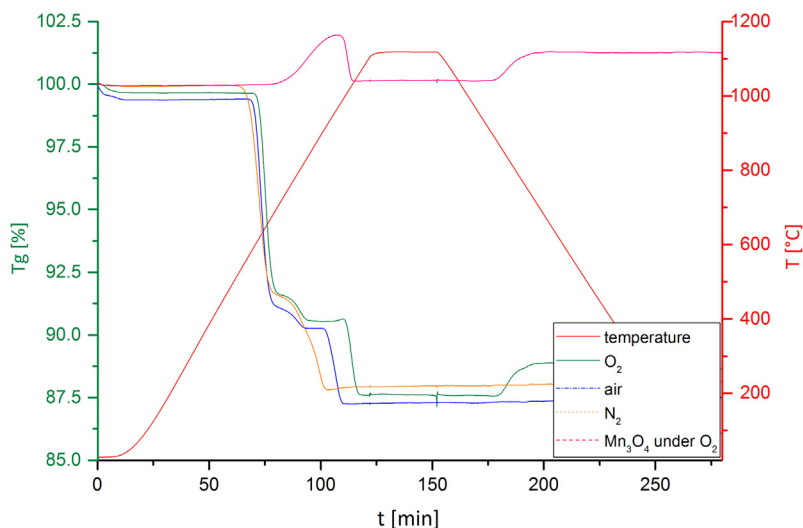


Fig. 8. Mass-changes during redox-cycles under various atmospheres for  $\text{MnO}_2$ .

slower than in the case of the Co-system. The same reaction in air is limited to a final conversion of 73%  $\text{Mn}_2\text{O}_3$  (Fig. 5B). Heating an  $\text{Mn}_3\text{O}_4$ -sample under an  $\text{O}_2$  atmosphere (Fig. 5D) shows, that in the Mn-system a similar medium-temperature cycle including a gas-change between 620 °C (reduction) and 450 °C (oxidation) should also be possible.

For the isothermal redox-reaction, the same conditions as those successfully applied in the Co-system, were used.

In contrast to the non-isothermal experiments, on instantaneous gas-change a fast and complete redox reaction is observed (see Fig. 6). After reduction to  $\text{Mn}_3\text{O}_4$  under  $\text{N}_2$  switching the atmosphere to  $\text{O}_2$  yields a mass-increase of 3.1% with a concomitant heat-flow of  $-137.0 \pm 6.17 \text{ J g}^{-1}$  (see Table A.7). This corresponds to the complete oxidation of the  $\text{Mn}_3\text{O}_4$  to  $\text{Mn}_2\text{O}_3$ . The oxidation is accomplished within 16.9 min, whereas the subsequent reduction under  $\text{N}_2$  takes 17 min. The reaction-rate in this case is comparable to the CoO-oxidation under air, although only approximately  $\frac{1}{4}$  of the energy is obtained.

Attempts to perform the same isothermal cycle under air failed, as no significant reaction occurred within 120 min at this temperature.

Samples of  $\text{MnO}_2$  were cycled 5 times under  $\text{O}_2$  and air and monitored in parallel by both P-XRD and TGA/DSC. After initial reduction of  $\text{MnO}_2$  to  $\text{Mn}_2\text{O}_3$ , satisfactory reversibility is observed under  $\text{O}_2$  both by P-XRD and TGA/DSC. The mass-increase and heat-flow is identical to the values obtained for the single TGA/DSC runs, represented in Fig. 7. For air as reactive gas the sluggish reoxidation behaviour found in the P-XRD (Fig. 5B) prevents cycling under the conditions applied in the TGA/DSC (Fig. 7, right). In the P-XRD the results of the thermal analysis were confirmed, cycling the material under the same conditions as before under  $\text{O}_2$ .

To correlate the P-XRD data with thermal analysis, TGA/DSC measurements of the  $\text{MnO}_2$  system were performed under various atmospheres. Due to the slower kinetics of the redox-reaction and the lack of equilibration time (heating/cooling rate of  $10 \text{ °C min}^{-1}$ ) compared to the P-XRD, complete reoxidation of  $\text{Mn}_3\text{O}_4$ , even under  $\text{O}_2$  is not achieved. In the TGA run, a mass-increase during cooling of only 1.31% was observed (Fig. 8). This corresponds to reoxidation of 44.1% of the  $\text{Mn}_2\text{O}_3$ . An even more apparent change in reactivity is observed for the experiment under air (Fig. 8), were

no observable reoxidation could be achieved. Heating a sample of  $\text{Mn}_3\text{O}_4$  under  $\text{O}_2$  (Fig. 8) leads first to a mass-increase of 1.98%, corresponding to a complete oxidation to  $\text{Mn}_2\text{O}_3$ . After subsequent decomposition due to the slower reoxidation whilst cooling only 92.4% of the initially formed  $\text{Mn}_2\text{O}_3$  are recovered. Interestingly for this second cycle of  $\text{Mn}_3\text{O}_4$  oxidation a notably higher conversion to  $\text{Mn}_2\text{O}_3$  is found. The single TGA/DSC-curves are shown in Fig. A2 (detailed values for the single experiments are given in the Appendix A in Tables A.4–A.6).

### 3.3. The $\text{PbO}_2/\text{PbO}$ system

Although, the desirable reversibility of the reduction of  $\text{PbO}_2$  could not be observed under the conditions investigated, this system was the most challenging with respect to its chemical behaviour. The reduction of  $\text{PbO}_2$  was investigated between 50 °C and 750 °C. At temperatures above 750 °C  $\text{PbO}$  tends to diffuse into the used alumina crucibles. With increasing temperature the  $\text{Pb}^{(\text{IV})}$ -oxide is reduced stepwise to  $\text{Pb}^{(\text{II,IV})}$ -oxide in form of the lead sesquioxide  $\text{Pb}_2\text{O}_3$ , which then converts to the  $\text{Pb}^{(\text{II,IV})}$ -oxide  $\text{Pb}_3\text{O}_4$ . At temperatures above 590 °C  $\text{Pb}^{(\text{II})}$ -oxide is formed, in both its tetragonal (litharge) and orthorhombic (massicot) modifications. With increasing temperature, the metastable tetragonal phase is converted into the orthorhombic one, which is the only present species above 730 °C and completely stable whilst cooling under an  $\text{O}_2$  atmosphere. To elucidate whether, like the Mn-system, a partial reversibility, e.g. between the  $\text{Pb}_3\text{O}_4$  and  $\text{Pb}_2\text{O}_3$  systems is possible, cycles with an adjusted temperature profile were performed (Fig. A4). In none of the experiments could any reoxidation be observed.

In Fig. 9 the stepwise decomposition of  $\text{PbO}_2$  under the various atmospheres is shown.

Similarly to the previously investigated systems, a decrease in atmospheric  $\text{O}_2$  content causes a narrowing of the stability-regime of the different mixed oxides of lead (Fig. 9B and C). For the attempted reoxidation of  $\text{PbO}$  under  $\text{O}_2$ -atmosphere, only the thermal expansion of the unit cell was observed.

TGA/DSC analysis also shows the stabilizing effect of an  $\text{O}_2$  atmosphere as observed by P-XRD with a small plateau following the decomposition to  $\text{Pb}_2\text{O}_3$  and  $\text{Pb}_3\text{O}_4$  which decreases in size with reduced  $\text{O}_2$  partial pressure. Under an atmosphere of  $\text{N}_2$  the

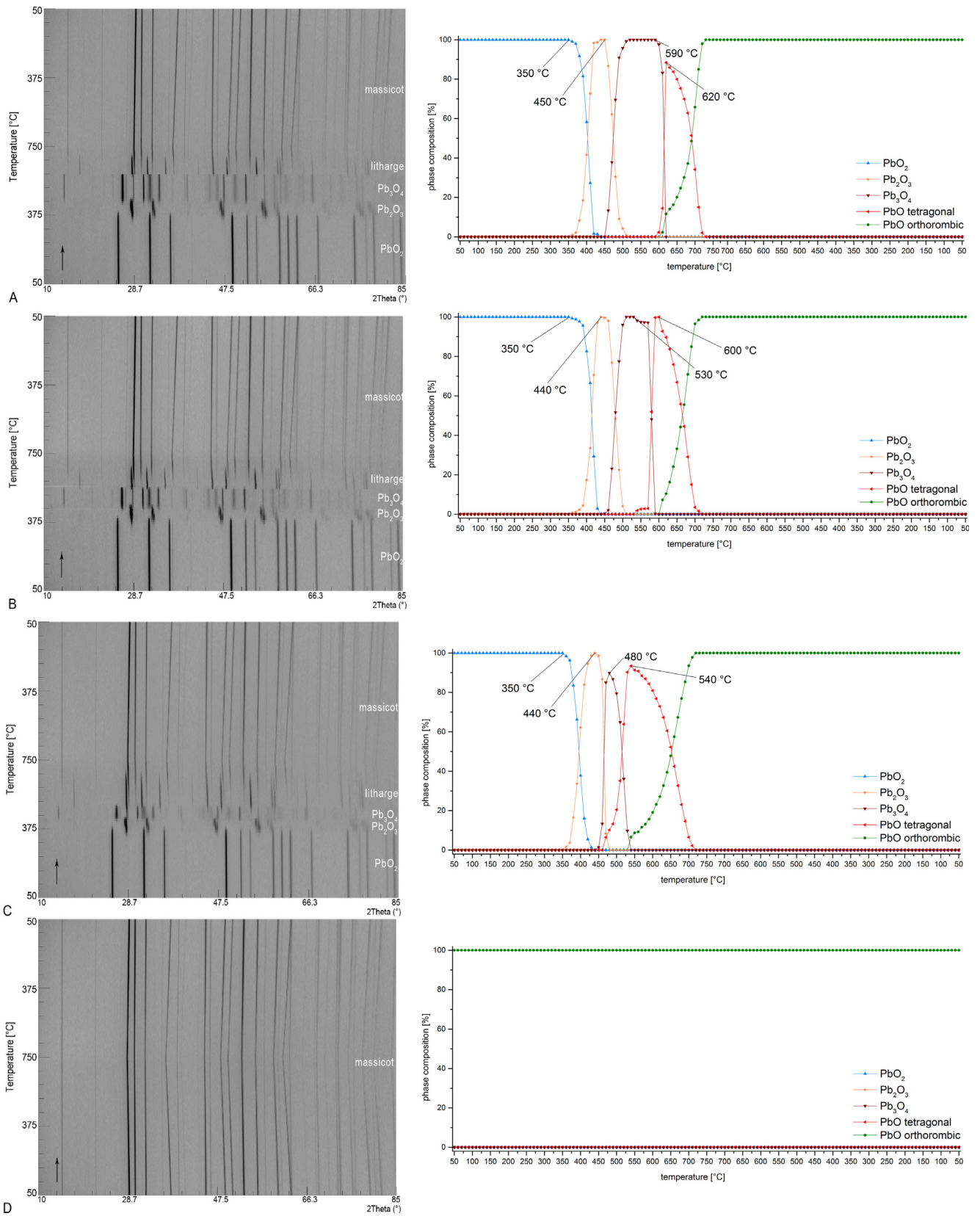


Fig. 9. Changes in sample composition during a PbO<sub>2</sub> redox-cycle under O<sub>2</sub> (A), under air (B), N<sub>2</sub> (C) and O<sub>2</sub> after reduction under N<sub>2</sub> (D).



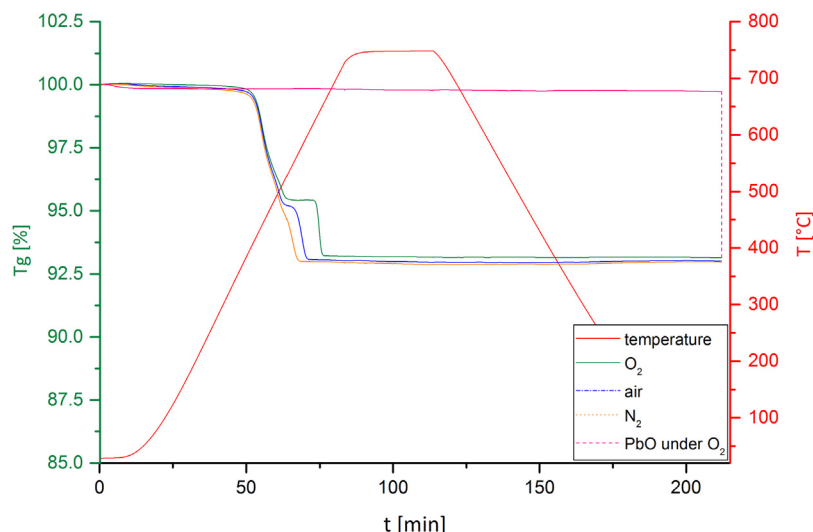


Fig. 10. Mass-changes during redox-cycles under various atmospheres for  $\text{PbO}_2$ .

stepwise decomposition from  $\text{PbO}_2$  to  $\text{PbO}$  is no longer distinguishable as only a gradual mass-loss is observed. The single TGA/DSC-curves are shown in Fig. A3. As observed from the P-XRD experiments,  $\text{PbO}$  is completely unaffected by a heating and cooling cycle under  $\text{O}_2$  (Fig. 10).

The numerical values for mass loss and calorimetric data are found in the Appendix A, Tables A.8–A.10, as far as they could be derived from the measurements.

To this point, the main reason for ignoring lead oxides as potential thermochemical energy storage materials has been their inherent toxicity rendering them inappropriate for an environmentally benign process. However, in addition to these concerns, we have found that lead-based systems also lack ready reversibility.

#### 4. Conclusion

Three different oxides,  $\text{Co}_3\text{O}_4$ ,  $\text{MnO}_2$  and  $\text{PbO}_2$  were investigated by combined P-XRD-TGA/DSC studies with regard to their reversible redox properties, reactivity under various atmospheres and thus suitability for thermochemical energy storage at elevated temperatures.

Studies of  $\text{Co}_3\text{O}_4$  agree well with previous work and clearly demonstrate the applicability and usefulness of P-XRD as tool to glean additional information concerning the crystalline phases present. In addition, it was found that an isothermal energy storage cycle involving change of reactive gas atmosphere rather temperature is also feasible for the cobalt oxide system. In the case of  $\text{MnO}_2$  only the  $\text{Mn}_2\text{O}_3/\text{Mn}_3\text{O}_4$  reaction was found to be reversible. The importance of  $\text{O}_2$  concentration and slower rates of reaction were also apparent. Operation of the redox cycle under an  $\text{O}_2$  atmosphere led to complete reoxidation of the  $\text{Mn}_3\text{O}_4$ , whereas under air only 72.8%  $\text{Mn}_3\text{O}_4$  could be reoxidized. Finally, it was found that the oxidation of *in-situ* reduced  $\text{Mn}_3\text{O}_4$  under  $\text{O}_2$  allows for operation of an energy storage cycle at lower temperatures. For  $\text{PbO}_2$  under none of the conditions applied could a reversible cycle be established. This applies also to all intermediates, as several attempts failed to cycle at least one of the intermediate oxidation states. The reduction of  $\text{PbO}_2$  includes 3 different stages, ending finally with the  $\beta$ - $\text{PbO}$ . From  $\text{PbO}_2$  in a first step the  $\text{Pb}^{(\text{II,IV})}$  sesquioxide  $\text{Pb}_2\text{O}_3$  is obtained, which decomposes further to the

mixed  $\text{Pb}^{(\text{II,IV})}$  oxide  $\text{Pb}_3\text{O}_4$ . Depending on the type of atmosphere the final decomposition to  $\text{PbO}$  occurs stepwise to the tetragonal  $\alpha$ - $\text{PbO}$ , which converts on continued heating to the  $\beta$ -phase, or parallel, were both  $\alpha$ - and  $\beta$ - $\text{PbO}$  coexist in the sample. In the TGA/DSC-measurements the single steps of the decomposition, well resolved under  $\text{O}_2$ -atmosphere smudge with decreased  $\text{O}_2$  content, finally leading to a gradual mass-loss up to 540 °C under  $\text{N}_2$ -atmosphere.

In contrast to theoretical predictions suggesting that all three oxides investigated should react reversibly and thus be highly suitable for TCES, only the known  $\text{Co}_3\text{O}_4$  and  $\text{Mn}_2\text{O}_3$  were found to show any degree of reversible reaction. Once reduced, the  $\text{Mn}^{(\text{IV})}$  oxidation state in the  $\text{MnO}_2$  system and none of the intermediate phases between  $\text{Pb}^{(\text{IV})}$  in  $\text{PbO}_2$  and  $\text{Pb}^{(\text{II})}$  in  $\text{PbO}$  were accessible. This clearly demonstrates the limit of algorithm-based material selection established by theoretical thermodynamic values: Although, by a nonbiased approach new reaction couples for thermochemical energy storage may be found, only a detailed experimental investigation can confirm their practical suitability.

Nonetheless, several technologically attractive possibilities are apparent from these studies including the possibility of medium-temperature cycling enabled by reactive gases other than air. Use of reactive gases other than air might also allow acyclic or isothermal operation of redox energy storage systems. Therefore we suggest that studies focused on oxidic TCES-materials under gas-change conditions might serve to further expand the applicability of TECS materials in concentrating solar energy power plants and recycling of industrial flue gas heat.

#### Acknowledgement

This work was financially supported by the Austrian Research Promotion Agency (FFG–Forschungsförderungsgesellschaft), project 841150 and project 848876.

The X-ray center (XRC) of the TU Wien is acknowledged for providing access to the powder X-ray diffractometer.

#### Appendix A

See Figs. A1–A4 and Tables A.1–A.10.

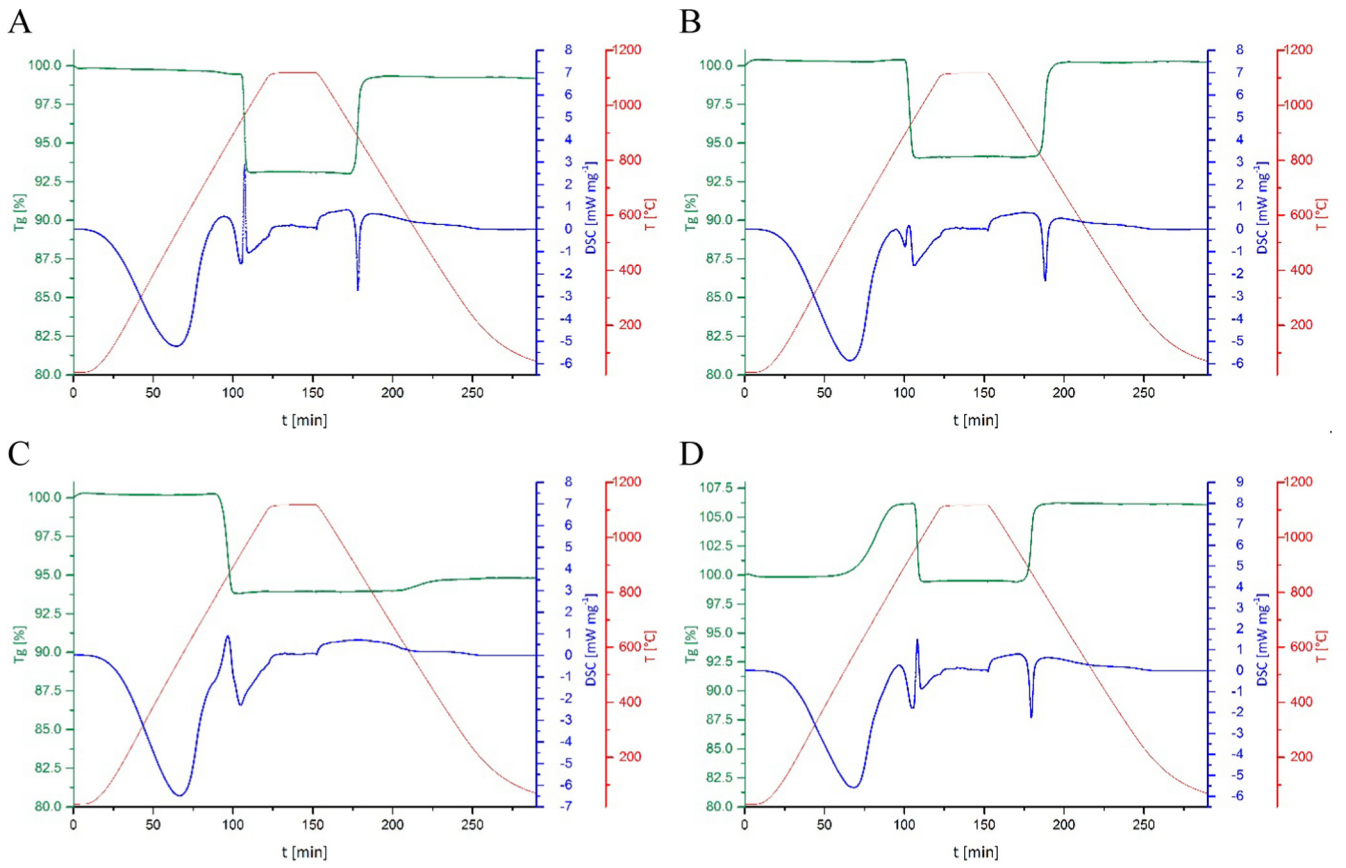


**Fig. A.1.** Mass-changes and calorimetric behaviour of a  $\text{Co}_3\text{O}_4$  during redox-cycles for: (A)  $\text{Co}_3\text{O}_4$  under  $\text{O}_2$ , (B)  $\text{Co}_3\text{O}_4$  under air, (C)  $\text{Co}_3\text{O}_4$  under  $\text{N}_2$  and (D)  $\text{CoO}$  under  $\text{O}_2$ .

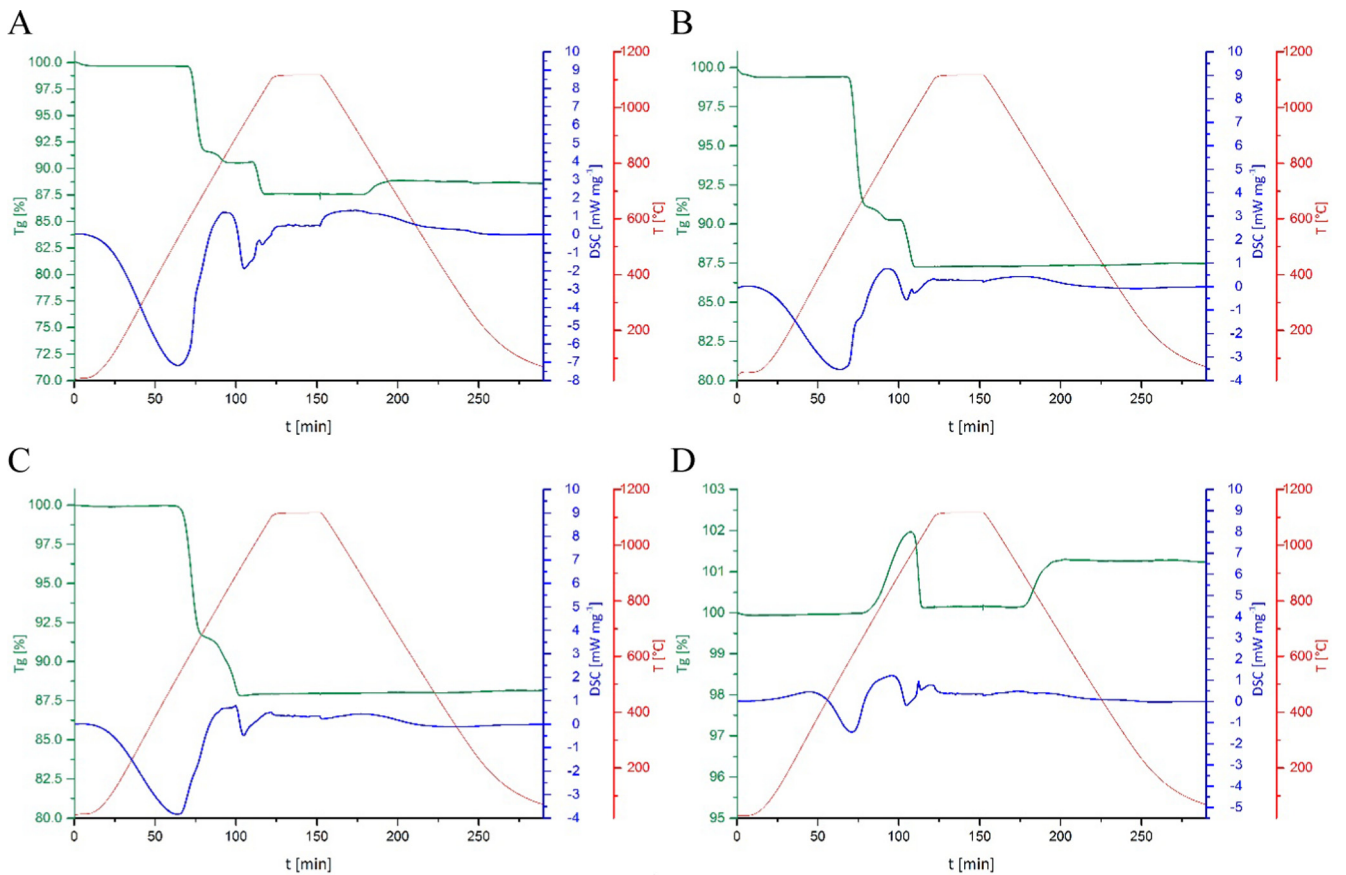


**Fig. A.2.** Mass-changes and calorimetric behaviour of a  $\text{MnO}_2$  during redox-cycles for: (A)  $\text{MnO}_2$  under  $\text{O}_2$ , (B)  $\text{MnO}_2$  under air, (C)  $\text{MnO}_2$  under  $\text{N}_2$  and (D)  $\text{Mn}_3\text{O}_4$  under  $\text{O}_2$ .



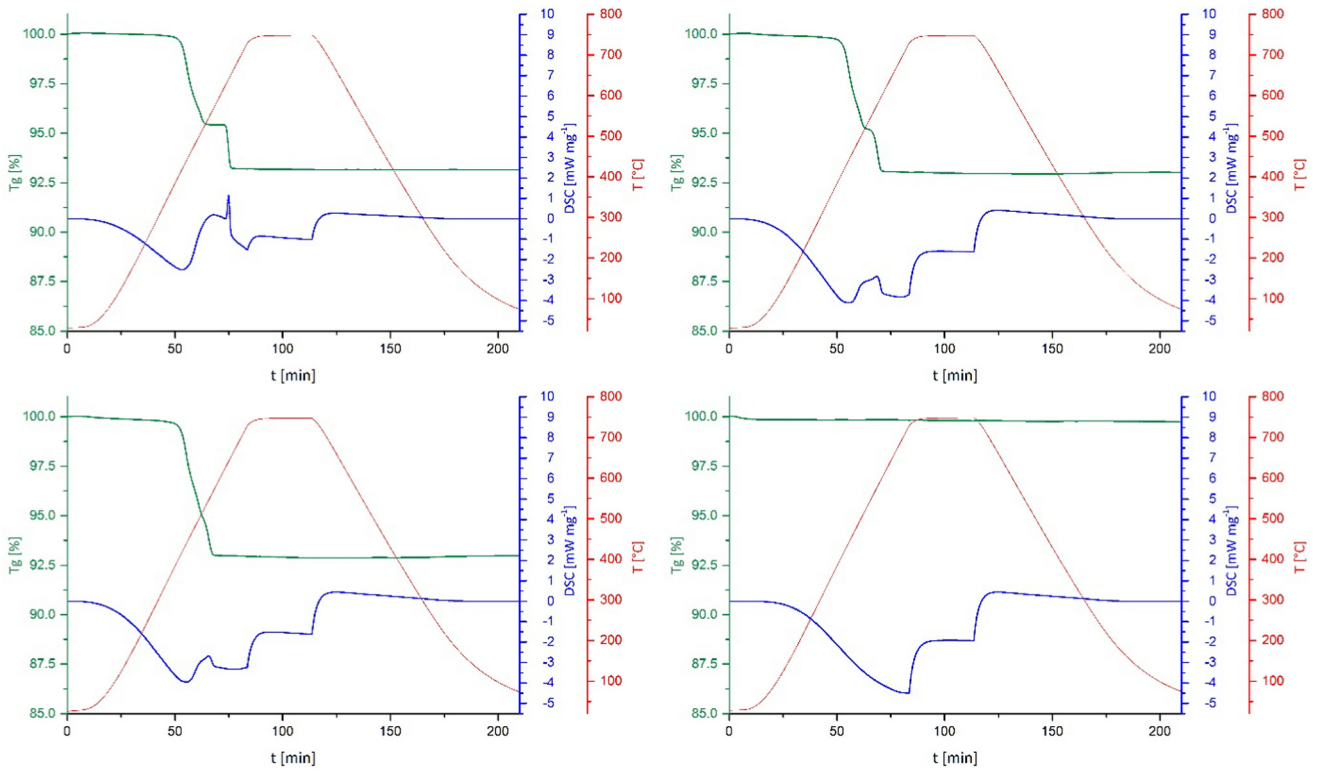


Fig. A.3. Mass-changes and calorimetric behaviour of a  $\text{PbO}_2$  during redox-cycles for: (A)  $\text{PbO}_2$  under  $\text{O}_2$ , (B)  $\text{PbO}_2$  under air, (C)  $\text{PbO}_2$  under  $\text{N}_2$  and (D)  $\text{PbO}$  under  $\text{O}_2$ .

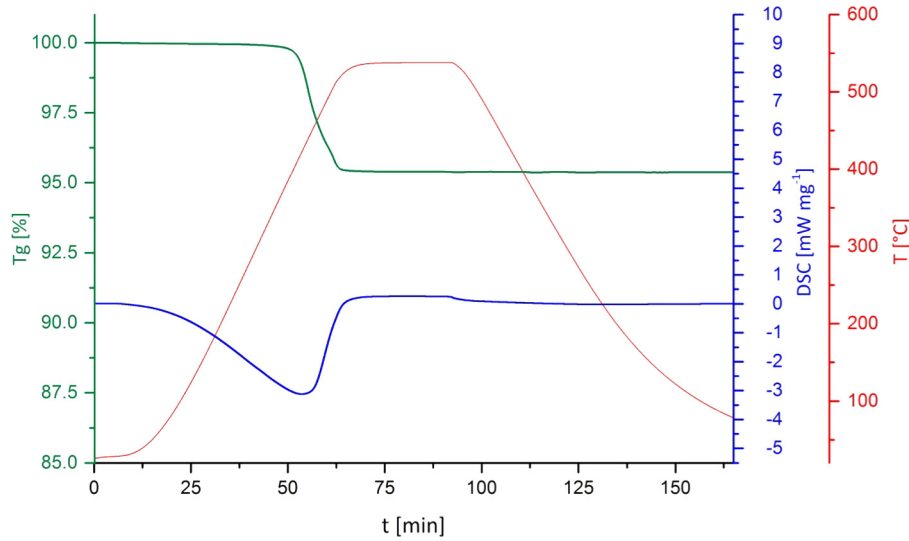


Fig. A.4. Mass-changes and calorimetric behaviour of a  $\text{PbO}_2$  sample under an atmosphere of  $\text{O}_2$ , heated to  $550^\circ\text{C}$  corresponding to a  $\text{Pb}_3\text{O}_4$ -phase.

Table A.1

DSC and TG data for  $\text{Co}_3\text{O}_4 \rightarrow \text{CoO}$  in Fig. 2.

	$\text{O}_2$	air	$\text{N}_2$	$\text{O}_2$ after $\text{N}_2$
DSC-onset [ $^\circ\text{C}$ ]	955.7	893.2	734.8	–
DSC-Peak [ $^\circ\text{C}$ ]	966.7	910.3	850.1	578.5
heat flow [ $\text{J g}^{-1}$ ]	418.7	483.3	596.7	–
TG-onset [ $^\circ\text{C}$ ]	958.0	897.6	813.6	542.8
mass-change [%]	–6.29	–6.34	–6.80	+6.59

Table A.2

DSC and TG data for  $\text{CoO} \rightarrow \text{Co}_3\text{O}_4$  in Fig. 2.

	$\text{O}_2$	air	$\text{N}_2$	$\text{O}_2$ after $\text{N}_2$	$\text{O}_2$ after $\text{N}_2$ (b)
DSC-onset [ $^\circ\text{C}$ ]	882.5	804.7	–	902.6	959.1
DSC-Peak [ $^\circ\text{C}$ ]	870.3	790.6	–	882.6	967.1
heat flow [ $\text{J g}^{-1}$ ]	273.0	242.8	–	271.3	397.6
TG-onset [ $^\circ\text{C}$ ]	894.5	804.5	–	901.2	959.9
mass-change [%]	+4.91	+3.46	–	+6.08	–6.86

**Table A.3**DSC and TG data for the isothermal redox-reaction of  $\text{Co}_3\text{O}_4$ .

	1 <sup>st</sup> oxidation O <sub>2</sub>	2 <sup>nd</sup> oxidation O <sub>2</sub>	1 <sup>st</sup> oxidation air	2 <sup>nd</sup> oxidation air
heat flow [ $\text{J g}^{-1}$ ]	−593.8	−574.9	−558.4	−428.4
mass-change [%]	+7.05	+7.04	+6.97	+6.97
	1 <sup>st</sup> reduction N <sub>2</sub>	2 <sup>nd</sup> reduction N <sub>2</sub>	3 <sup>rd</sup> reduction N <sub>2</sub>	
heat flow [ $\text{J g}^{-1}$ ]	546.6	477.8	482.4	
mass-change [%]	−7.12	−7.05	−7.02	

**Table A.4**DSC and TG data for  $\text{MnO}_2 \rightarrow \text{Mn}_2\text{O}_3$  in Fig. 6.

	O <sub>2</sub>	air	N <sub>2</sub>	O <sub>2</sub> after N <sub>2</sub>
DSC-onset [°C]	−	593.4	−	−
DSC-Peak [°C]	644.0	628.0	−	−
heat flow [ $\text{J g}^{-1}$ ]	182.8	166.2	−	−
TG-onset [°C]	622.3	597.2	572.2	−
mass-change [%]	−8.03	−8.26	−8.26	−

**Table A.5**DSC and TG data for  $\text{Mn}_2\text{O}_3 \rightarrow \text{Mn}_3\text{O}_4$  in Fig. 6.

	O <sub>2</sub>	air	N <sub>2</sub>	O <sub>2</sub> after N <sub>2</sub>
DSC-onset [°C]	1004.1	942.6	−	−
DSC-Peak [°C]	1032.7	970.0	−	−
heat flow [ $\text{J g}^{-1}$ ]	118.9	41.72	−	−
TG-onset [°C]	1010.7	921.9	834.0	878.9
mass-change [%]	−2.97	−3.00	−3.59	−1.15

**Table A.6**DSC and TG data for  $\text{Mn}_3\text{O}_4 \rightarrow \text{Mn}_2\text{O}_3$  in Fig. 6.

	O <sub>2</sub>	air	N <sub>2</sub>	O <sub>2</sub> after N <sub>2</sub>	O <sub>2</sub> after N <sub>2</sub> (b)
DSC-onset [°C]	−	−	−	−	999.6
DSC-Peak [°C]	−	−	−	−	1011.1
heat flow [ $\text{J g}^{-1}$ ]	−	−	−	−	50.29
TG-onset [°C]	852.1	−	−	739.5	996.3
mass-change [%]	1.31	−	−	+1.98	1.83

**Table A.7**DSC and TG data for the isothermal redox-reaction of  $\text{Mn}_2\text{O}_3$ .

	1 <sup>st</sup> oxidation O <sub>2</sub>	2 <sup>nd</sup> oxidation O <sub>2</sub>	3 <sup>rd</sup> oxidation O <sub>2</sub>
heat flow [ $\text{J g}^{-1}$ ]	−130.3	−142.4	−138.4
mass-change [%]	+3.03	+3.06	+3.06
	1 <sup>st</sup> reduction N <sub>2</sub>	2 <sup>nd</sup> reduction N <sub>2</sub>	
heat flow [ $\text{J g}^{-1}$ ]	97.16	118.6	
mass-change [%]	−3.13	−3.11	

**Table A.8**DSC and TG data for  $\text{PbO}_2 \rightarrow \text{Pb}_2\text{O}_3$  in Fig. 8.

	O <sub>2</sub>	air	N <sub>2</sub>	O <sub>2</sub> after N <sub>2</sub>
DSC-onset [°C]	−	−	−	−
DSC-Peak [°C]	−	−	−	−
heat flow [ $\text{J g}^{-1}$ ]	−	−	−	−
TG-onset [°C]	414.3	414.0	415.2	−
mass-change [%]	−4.47	−4.61	−3.44	−

**Table A.9**DSC and TG data for  $\text{Pb}_2\text{O}_3 \rightarrow \text{Pb}_3\text{O}_4$  in Fig. 8.

	O <sub>2</sub>	air	N <sub>2</sub>	O <sub>2</sub> after N <sub>2</sub>
DSC-onset [°C]	631.2	−	−	−
DSC-Peak [°C]	640.6	−	−	−
heat flow [ $\text{J g}^{-1}$ ]	122.8	−	−	−
TG-onset [°C]	633.4	563.3	454.5	−
mass-change [%]	−2.23	−2.19	−1.38	−

**Table A.10**DSC and TG data for  $\text{Pb}_3\text{O}_4 \rightarrow \text{PbO}$  in Fig. 8.

	O <sub>2</sub>	air	N <sub>2</sub>	O <sub>2</sub> after N <sub>2</sub>
DSC-onset [°C]	−	−	−	−
DSC-Peak [°C]	−	−	−	−
heat flow [ $\text{J g}^{-1}$ ]	−	−	−	−
TG-onset [°C]	−	−	539.2	−
mass-change [%]	−	−	−1.89	−

## References

- Abedin, Ali H., Rosen, Marc A., 2011. A critical review of thermochemical energy storage systems. *Open Renew. Energy J.* 4, 42–46.
- Agrafiotis, C., Roeb, M., Schmücker, M., Sattler, C., 2014. Exploitation of thermochemical cycles based on solid oxide redox systems for thermochemical storage of solar heat. Part 1: testing of cobalt oxide-based powders. *Sol. Energy* 102, 189–211.
- Agrafiotis, C., Roeb, M., Schmücker, M., Sattler, C., 2015a. Exploitation of thermochemical cycles based on solid oxide redox systems for thermochemical storage of solar heat. Part 2: redox oxide-coated porous ceramic structures as integrated thermochemical reactors/heat exchangers. *Sol. Energy* 114, 440–458.
- Agrafiotis, C., Tesari, S., Roeb, M., Schmücker, M., Sattler, C., 2015b. Exploitation of thermochemical cycles based on solid oxide redox systems for thermochemical storage of solar heat. Part 3: cobalt oxide monolithic porous structures as integrated thermochemical reactors/heat exchangers. *Sol. Energy* 114, 459–475.
- Agrafiotis, C., Becker, A., Roeb, M., Sattler, C., 2016a. Exploitation of thermochemical cycles based on solid oxide redox systems for thermochemical storage of solar heat. Part 5: testing of porous ceramic honeycomb and foam cascades based on cobalt and manganese oxides for hybrid sensible/thermochemical heat storage. *Sol. Energy* 139, 676–694.
- Agrafiotis, C., Roeb, M., Sattler, C., 2016b. Exploitation of thermochemical cycles based on solid oxide redox systems for thermochemical storage of solar heat. Part 4: screening of oxides for use in cascaded thermochemical storage concepts. *Sol. Energy* 139, 695–710.
- Alonso, E., Hutter, C., Romero, M., Steinfeld, A., Gonzalez-Aguilar, J., 2013. Kinetics of  $\text{Mn}_2\text{O}_3$ – $\text{Mn}_3\text{O}_4$  and  $\text{Mn}_3\text{O}_4$ – $\text{MnO}$  redox reactions performed under concentrated thermal radiative flux. *Energy Fuels* 27 (8), 4884–4890.
- André, L., Abanades, S., Flamant, G., 2016. Screening of thermochemical systems based on solid-gas reversible reactions for high temperature solar thermal energy storage. *Renew. Sustain. Energy Rev.* 64, 703–715.
- Babiniec, S.M., Coker, E.N., Miller, J.E., Ambrosini, A., 2015. Investigation of  $\text{La}_x\text{Sr}_{1-x}\text{Co}_y\text{M}_{1-y}\text{O}_{3-\delta}$  ( $M = \text{Mn, Fe}$ ) perovskite materials as thermochemical energy storage media. *Sol. Energy* 118, 451–459.
- Babiniec, S.M., Coker, E.N., Miller, J.E., Ambrosini, A., 2016. Doped calcium manganites for advanced high-temperature thermochemical energy storage. *Int. J. Energy Res.* 40 (2), 280–284.
- Bauer, T., Steinmann, W.-D., Laing, D., Tamme, R., 2012. Thermal energy storage materials and systems. *Ann. Rev. Heat Transf.* 15 (15), 131–177.
- Block, T., Schmücker, M., 2016. Metal oxides for thermochemical energy storage: a comparison of several metal oxide systems. *Sol. Energy* 126, 195–207.

- Block, T., Knoblauch, N., Schmücker, M., 2014. The cobalt-oxide/iron-oxide binary system for use as high temperature thermochemical energy storage material. *Thermochim. Acta* 577, 25–32.
- Cabeza, L.F., Castell, A., Barreneche, C., de Gracia, A., Fernández, A.I., 2011. Materials used as PCM in thermal energy storage in buildings: a review. *Renew. Sustain. Energy Rev.* 15 (3), 1675–1695.
- Carrillo, A.J., Serrano, D.P., Pizarro, P., Coronado, J.M., 2014. Thermochemical heat storage based on the  $Mn_2O_3/Mn_3O_4$  redox couple: influence of the initial particle size on the morphological evolution and cyclability. *J. Mater. Chem. A* 2 (45), 19435–19443.
- Carrillo, A.J., Serrano, D.P., Pizarro, P., Coronado, J.M., 2015. Improving the thermochemical energy storage performance of the  $Mn_2O_3/Mn_3O_4$  redox couple by the incorporation of iron. *ChemSusChem* 8 (11), 1947–1954.
- Chase, M.W., 1998. NIST-JANAF Thermochemical Tables, 4th ed. *J. Phys. Chem. Ref. Data Monogr.* 9.
- Chen, S., Liu, F., Xiang, Q., Feng, X., Qiu, G., 2013. Synthesis of  $Mn_2O_3$  microstructures and their energy storage ability studies. *Electrochim. Acta* 106, 360–371.
- Deutsch, M., Müller, D., Aumeyr, C., Jordan, C., Gierl-Mayer, C., Weinberger, P., Winter, F., Werner, A., 2016. Systematic search algorithm for potential thermochemical energy storage systems. *Appl. Energy* 183, 113–120.
- Dinker, A., Agarwal, M., Agarwal, G.D., 2015. Heat storage materials, geometry and applications: a review. *J. Energy Inst.* 90 (1), 1–11. <http://dx.doi.org/10.1016/j.joei.2015.10.002>.
- Ervin, G., 1977. Solar heat storage using chemical reactions. *J. Solid State Chem.* 22 (1), 51–61.
- Hutchings, K., Wilson, M., Larsen, P., Cutler, R., 2006. Kinetic and thermodynamic considerations for oxygen absorption/desorption using cobalt oxide. *Solid State Ionics* 177 (1–2), 45–51.
- Karagiannakis, G., Pagkoura, C., Halevas, E., Baltzopoulou, P., Konstandopoulos, A.G., 2016. Cobalt/cobaltous oxide based honeycombs for thermochemical heat storage in future concentrated solar power installations: multi-cyclic assessment and semi-quantitative heat effects estimations. *Sol. Energy* 133, 394–407.
- Kato, Y., Takahashi, R., Sekiguchi, T., Ryu, J., 2009. Study on medium-temperature chemical heat storage using mixed hydroxides. *Int. J. Refrig.* 32 (4), 661–666.
- Knoll, C., Müller, D., Artner, W., Welch, J.M., Werner, A., Harasek, M., Weinberger, P., 2017. Probing cycle stability and reversibility in thermochemical energy storage –  $CaC_2O_4 \cdot H_2O$  as perfect match? *Appl. Energy* 187, 1–9.
- Kuravi, S., Goswami, Y., Stefanakos, E.K., Ram, M., Jotshi, C., Pendyala, S., Trahan, J., Sridharan, P., Rahman, M., Krakow, B., 2012. Thermal energy storage for concentrating solar power plants. *Technol. Innovation* 14 (2), 81–91.
- Liu, X., Prewitt, C., 1990. High-temperature X-ray diffraction study of  $Co_3O_4$ : transition from normal to disordered spinel. *Phys. Chem. Miner.* 17 (2).
- Neises, M., Tescari, S., de Oliveira, L., Roeb, M., Sattler, C., Wong, B., 2012. Solar-heated rotary kiln for thermochemical energy storage. *Sol. Energy* 86 (10), 3040–3048.
- Pagkoura, C., Karagiannakis, G., Zygogianni, A., Lorentzou, S., Kostoglou, M., Konstandopoulos, A.G., Rattenbury, M., Woodhead, J.W., 2014. Cobalt oxide based structured bodies as redox thermochemical heat storage medium for future CSP plants. *Sol. Energy* 108, 146–163.
- Pagkoura, C., Karagiannakis, G., Halevas, E., Konstandopoulos, A.G., 2016.  $Co_3O_4$ -based honeycombs as compact redox reactors/heat exchangers for thermochemical storage in the next generation CSP plants. 1734, 050037.
- Prieto, C., Cooper, P., Fernández, A.I., Cabeza, L.F., 2016. Review of technology: thermochemical energy storage for concentrated solar power plants. *Renew. Sustain. Energy Rev.* 60, 909–929.
- Solé, A., Fontanet, X., Barreneche, C., Martorell, I., Fernández, A.I., Cabeza, L.F., 2012. Parameters to take into account when developing a new thermochemical energy storage system. *Energy Proc.* 30, 380–387.
- Tian, Y., Zhao, C.Y., 2011. A numerical investigation of heat transfer in phase change materials (PCMs) embedded in porous metals. *Energy* 36 (9), 5539–5546.
- van Essen, V.M., Cot Gores, J., Bleijendaal, L.P.J., Zondag, H.A., Schuitema, R., Bakker, M., van Helden, W.G.J., 2009. Characterization of salt hydrates for compact seasonal thermochemical storage, pp. 825–830.
- Xu, J., Wang, R.Z., Li, Y., 2014. A review of available technologies for seasonal thermal energy storage. *Sol. Energy*, 610–638.
- Yan, T., Wang, R.Z., Li, T.X., Wang, L.W., Fred, Ishugah T., 2015. A review of promising candidate reactions for chemical heat storage. *Renew. Sustain. Energy Rev.* 43, 13–31.
- Zhang, H., Baeyens, J., Cáceres, G., Degrève, J., Lv, Y., 2016. Thermal energy storage: recent developments and practical aspects. *Prog. Energy Combust. Sci.* 53, 1–40.

# High-Temperature Energy Storage: Kinetic Investigations of the CuO/Cu<sub>2</sub>O Reaction Cycle

Markus Deusch,<sup>\*,†</sup> Florian Horvath,<sup>†</sup> Christian Knoll,<sup>†,‡</sup> Daniel Lager,<sup>§</sup> Christian Gierl-Mayer,<sup>||</sup> Peter Weinberger,<sup>‡</sup> and Franz Winter<sup>†</sup>

<sup>†</sup>Institute of Chemical Engineering, <sup>‡</sup>Institute of Applied Synthetic Chemistry, and <sup>||</sup>Institute of Chemical Technologies and Analytics, Technische Universität (TU) Wien, 1060 Vienna, Austria

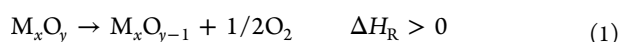
<sup>§</sup>AIT Austrian Institute of Technology GmbH, Center for Energy, 1210 Vienna, Austria

**ABSTRACT:** Thermochemical energy storage (TCES) is considered a possibility to enhance the energy utilization efficiency of various processes. One promising field is the application of thermochemical redox systems in combination with concentrated solar power (CSP). There, reactions of metal oxides are in the focus of research, because they allow for an increase in the process temperature. The reaction system CuO/Cu<sub>2</sub>O has been reported as a suitable candidate for TCES. For proper development and modeling of combined CSP–TCES processes, reliable kinetic data are necessary. This work studies the reduction of CuO and the oxidation of Cu<sub>2</sub>O under isothermal and isokinetic conditions. The reactions are analyzed using a simultaneous thermal analysis (STA) and a lab-scale fixed-bed reactor. The reaction behavior shows significant differences between both analyses. To develop kinetic models, the non-parametric kinetic (NPK) approach is used. This model-free approach is expanded by the Arrhenius correlation to increase the applicable temperature range of the models. The resulting models are evaluated and compared. Furthermore, the cycle stability of the system over 20 cycles is assessed for a small sample mass in the STA and a large sample mass in the fixed-bed reactor.

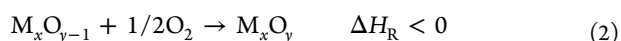
## INTRODUCTION

Thermochemical energy storage (TCES) has been in the focus of researchers for the last couple of years as a result of its advantages and potential compared to other thermal storage technologies.<sup>1</sup> The achieved energy storage densities of TCES systems are up to 5 times higher than comparable latent heat storage systems and up to 15 times higher than sensible heat storage systems.<sup>2</sup> Additionally, the heat is stored in the form of chemical energy, which makes energy storage possible without the need for sophisticated and expensive insulation.<sup>3–5</sup> This makes TCES especially suitable for high-temperature applications, such as the combination with concentrated solar power (CSP). In this cases, TCES can be used to increase their production during times with low sunlight (e.g., when the sun is blocked by clouds or after sunset).<sup>6,7</sup> Especially, redox systems of metal oxides are deemed to be suitable as a result of their operating temperature.<sup>8,9</sup> Wong et al. analyzed 16 potential metal oxide systems following the oxidation reaction (eq 2).<sup>10</sup> From these systems, only BaO, Co<sub>3</sub>O<sub>4</sub>, CuO, Fe<sub>2</sub>O<sub>3</sub>, and Mn<sub>2</sub>O<sub>3</sub> displayed the necessary behavior for a suitable TCES material. Co<sub>3</sub>O<sub>4</sub> showed the most promising results, according to Wong,<sup>11</sup> and was further analyzed in terms of reversibility and energy storage capacity.<sup>12–14</sup> The cycle ability of Mn<sub>2</sub>O<sub>3</sub> has already been proven by Carrillo et al.<sup>15</sup> and compared to Co<sub>3</sub>O<sub>4</sub>.<sup>16</sup>

reduction



oxidation



As pointed out by Alonso et al., copper oxide is highly available in emerging CSP markets, such as Mexico and Chile, therefore, reducing the material price compared to other metal oxides.<sup>17</sup> In terms of energy storage capacity, CuO is as capable as Co<sub>3</sub>O<sub>4</sub> (811 kJ/kg for CuO and 844 kJ/kg for Co<sub>3</sub>O<sub>4</sub> at their theoretical transition temperature in air) and better than Mn<sub>2</sub>O<sub>3</sub> (202 kJ/kg).<sup>11</sup> Both facts consolidate the potential of CuO as a TCES candidate.

For the proper design of the reactor, in which the solid-state reaction should take place, the knowledge of the reaction kinetics for the applied system is crucial.<sup>18</sup> Additionally, faster reaction kinetics mean that the process has a shorter response time. The kinetics of the system CuO/Cu<sub>2</sub>O has been investigated as a possible oxygen carrier for chemical looping combustion (CLC). Several groups reported a reduction of the oxidation rate in air at higher temperatures.<sup>19,20</sup> Clayton et al. studied the oxidation and reduction kinetics of Cu-based carrier materials with a CuO loading of up to 50%.<sup>21,22</sup> Their work focused on the development of kinetic expressions aimed at better describing the observed oxidation profiles of cuprous-oxide-based oxygen carriers. Zhu et al. investigated the oxidation of Cu<sub>2</sub>O in a temperature range of 600–1050 °C during the copper oxidation with and without an initial thin CuO layer.<sup>23</sup>

The goal of this work is the development of reliable kinetic models for the reaction system CuO/Cu<sub>2</sub>O as it occurs in a TCES application. Previous works investigated the system only for CLC application, in which copper-based carriers with CuO

**Special Issue:** In Honor of Professor Brian Haynes on the Occasion of His 65th Birthday

**Received:** September 14, 2016

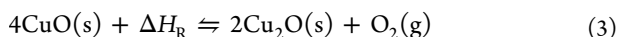
**Revised:** December 27, 2016

**Published:** January 4, 2017

loading up to 64% are used.<sup>21,22</sup> For TCES, applications would result in an reduced energy density of at least 37%. Therefore, it is important to measure kinetics without possible effects of carrier material. The kinetic analysis was performed in a simultaneous thermal analysis (STA) and in a lab-scale fixed-bed reactor. The cycle stability of the system is analyzed on a chemical reaction level in a STA and on a macroscopic level in a lab-scale fixed-bed reactor to further investigate the applicability for TCES.

## FUNDAMENTALS

**CuO/Cu<sub>2</sub>O System.** Used as a TCES material, the copper in CuO cycles between the Cu(II) cupric state and the Cu(I) cuprous state.



For this reaction, the equilibrium relation can be derived as

$$K = \frac{a_{\text{Cu}_2\text{O}}^2 a_{\text{O}_2}}{a_{\text{CuO}}^4} \quad (4)$$

where  $a_i$  represents the activity of the corresponding species. The activity of pure solids (CuO and Cu<sub>2</sub>O) can be assumed to be 1, and the activity of O<sub>2</sub> can be expressed as its fugacity, with  $p^\ominus$  being the standard pressure of 1 bar.

$$a_{\text{O}_2} = \frac{f_{\text{O}_2}}{p^\ominus} \quad (5)$$

With the simplification that O<sub>2</sub> behaves like an ideal gas, then the fugacity is equal to the partial pressure of oxygen  $p_{\text{O}_2}$  in the reaction atmosphere, resulting in

$$K = \frac{p_{\text{O}_2}}{p^\ominus} \quad (6)$$

With the Gibbs equation for free energy

$$\Delta G_{\text{R}}^T = \Delta H_{\text{R}}^T - T\Delta S_{\text{R}}^T = -RT \ln(K) \quad (7)$$

where  $\Delta G_{\text{R}}^T$ ,  $\Delta H_{\text{R}}^T$  and  $\Delta S_{\text{R}}^T$  are the free Gibbs energy, the reaction enthalpy, and the reaction entropy at temperature  $T$ , respectively. Equation 6 leads to the stability equation of the system

$$\ln\left(\frac{p_{\text{O}_2}}{p^\ominus}\right) = \frac{-\Delta H_{\text{R}}^T}{RT} + \frac{\Delta S_{\text{R}}^T}{R} \quad (8)$$

This equation is represented graphically in the stability diagram in Figure 1. As shown there, CuO reacts to Cu<sub>2</sub>O in air ( $p_{\text{O}_2} = 0.21$  bar) at temperatures over 1028 °C.<sup>24</sup>

**Kinetic Identification.** In this work, the non-parametric kinetic (NPK) analysis method was chosen for the kinetic analysis of the CuO/Cu<sub>2</sub>O cycle. The NPK method was developed by Serra et al. and Sempere et al.<sup>25–28</sup> for isokinetic measurements and generalized by Heal.<sup>29,30</sup> The method is free of *a priori* established models and avoids explicit kinetic models as well as the Arrhenius law. In principle, the method separates the effect of conversion  $\alpha$  and temperature  $T$  on the conversion rate  $d\alpha/dt$ . In the following, the method is described in more detail. On the basis of the general kinetic equation

$$\frac{d\alpha}{dt} = f(\alpha)k(T) \quad (9)$$

the conversion rate  $d\alpha/dt$  can be seen as a continuous three-dimensional surface based on the conversion dependency  $f(\alpha)$

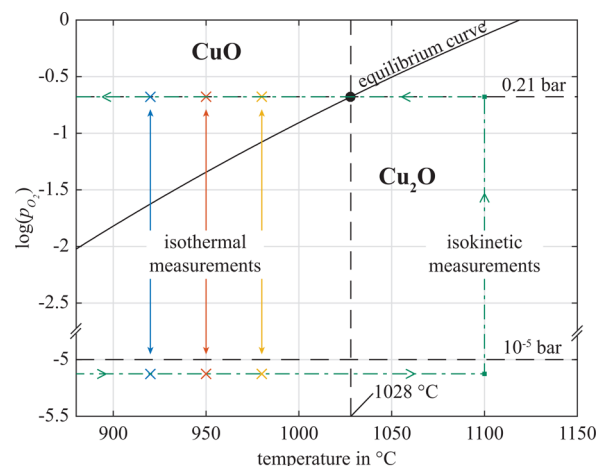


**Figure 1.** Stability diagram for CuO/Cu<sub>2</sub>O based on data from the HSC Database<sup>24</sup> shown with the investigated experimental conditions.

and the temperature dependency  $k(T)$ . This surface can be discretized and written in a  $(n \times m)$  matrix  $A$  (bold uppercase letters symbolize matrices, and bold lowercase letters symbolize vectors), so that the matrix element  $A_{ij}$  gives the conversion rate for  $\alpha_i$  and  $T_j$ , as shown in eq 10.

$$A = \begin{bmatrix} f(\alpha_1)k(T_1) & f(\alpha_1)k(T_2) & \cdots & f(\alpha_1)k(T_m) \\ f(\alpha_2)k(T_1) & f(\alpha_2)k(T_2) & \cdots & f(\alpha_2)k(T_m) \\ \vdots & \vdots & \ddots & \vdots \\ f(\alpha_n)k(T_1) & f(\alpha_n)k(T_2) & \cdots & f(\alpha_n)k(T_m) \end{bmatrix} \quad (10)$$

The analysis applied on isothermal experiments results in a matrix  $A$ , where each column represents one measurement. The incorporation of isokinetic measurements results in a widely empty matrix; therefore, it requires the implementation of submatrices in  $A$ . Further details can be found in the literature.<sup>25–27</sup>

As a result of the discretization,  $A$  can be written as a matrix product

$$A = \mathbf{f}\mathbf{k}^T \quad (11)$$

with the vectors  $\mathbf{f}$  and  $\mathbf{k}$  defined as

$$\mathbf{f} = [f(\alpha_1)f(\alpha_2)\dots f(\alpha_n)]^T \quad (12)$$

$$\mathbf{k} = [k(T_1)k(T_2)\dots k(T_m)]^T \quad (13)$$

Using the singular value decomposition (SVD),<sup>31</sup> the matrix  $A$  is decomposed into three matrices

$$A = \mathbf{U}\mathbf{S}\mathbf{V}^T \quad (14)$$

with  $\mathbf{U}$  and  $\mathbf{V}$  being orthonormal matrices and  $\mathbf{S}$  being a diagonal matrix, whose entries are the singular values of  $A$ . If the investigated reaction can be described by eq 9, then only the first entry of  $\mathbf{S}$  is significantly different from zero. From this follows that only the first columns of  $\mathbf{U}$  and  $\mathbf{V}^T$  are significant. Therefore, eq 14 can be reduced to

$$A = \mathbf{u}\mathbf{s}\mathbf{v}^T \quad (15)$$

with  $s = S(1)$  and  $\mathbf{u}$  and  $\mathbf{v}^T$  being the first columns of  $\mathbf{U}$  and  $\mathbf{V}^T$ , respectively. In comparison of eq 15 to eq 11, the following correlations can be found:

$$\mathbf{u} = c_1 \mathbf{f} \quad (16)$$



$$\mathbf{v} = c_2 \mathbf{k} \quad (17)$$

$$s = \frac{1}{c_1 c_2} \quad (18)$$

with  $c_1$  and  $c_2$  being scaling constants.

Hence, by application of a SVD analysis on  $A$ , two independent vectors  $\mathbf{u}$  and  $\mathbf{v}$  are found, which are proportional to the conversion dependency  $f$  and the temperature dependency  $k$  of the reaction.

When the temperature dependency of the reaction  $k(T)$  is assumed to follow the Arrhenius law

$$k(T) = A e^{-E_a/RT} \quad (19)$$

then the activation energy  $E_a$  and the pre-exponential factor  $A$  can be calculated from the linearization with eq 19

$$\ln(k(T)) = \ln(v_T) = \ln(c_2 A) - \frac{E_a}{RT} \quad (20)$$

where  $v_T$  represents the value of  $\mathbf{v}$  for temperature  $T$ .

The pre-exponential factor  $A$  cannot be calculated directly from the axis section of eq 20 because the scales of the quantities are lost in the matrix decomposition process.<sup>29</sup> This can be seen in eq 18. When  $c_1$  is multiplied by an arbitrary factor and  $c_2$  is divided by the same factor, the result of eq 15 would not change but the vectors  $\mathbf{u}$  and  $\mathbf{v}$  would be shifted. Therefore,  $A$  can only be calculated if the conversion dependency  $f(\alpha)$  is found (this gives  $c_1$ ). This can be performed by fitting different conversion models into  $\mathbf{u}$ . At this point, 29 different conversion models for  $f(\alpha)$  are known in the literature.<sup>32</sup> In this work, the identification of  $E_a$  has been performed, where possible, because it grants the possibility to increase the temperature range of the kinetic model to a certain extent. The identification of the conversion model does not grant any additional information for the simulation and was, therefore, omitted.

## EXPERIMENTAL SETUP

**Material.** The material used for all experiments was a granular CuO from Merck Emsure. The particle size distribution of the granulate material can be seen in Figure 2. For further analysis, the granulate was

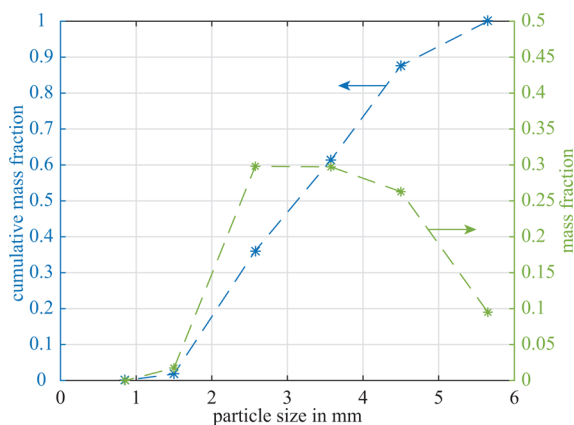


**Figure 2.** Mass-based particle size distribution of the CuO granulate. Drawn points represent the mean value of the mesh size.

ground with a Retsch planetary ball mill PM 100 and sieved afterward. For the analysis, the fraction with a particle size between 32 and 45  $\mu\text{m}$  was used. A Brunauer–Emmett–Teller (BET) surface analysis resulted in a specific surface of the milled material of 3.1  $\text{m}^2/\text{g}$ . The phase composition yielding >99.9% pure CuO phase was determined by X-ray powder diffraction.

**STA.** The STA measurements were performed in a Netzsch STA 449 F1 Jupiter with a differential thermal analysis (TGA-DTA) measurement setup. The sample mass in all STA measurements was  $151.2 \pm 0.6$  mg of CuO. The measurements were performed according to Figure 3.

For isokinetic STA measurements, the sample was heated with a constant heating rate  $\beta$  up to 1100  $^\circ\text{C}$  in  $\text{N}_2$  atmosphere ( $p_{\text{O}_2} < 10^{-5}$  bar). Then, the atmosphere was switched to synthetic air ( $p_{\text{O}_2} = 0.21$  bar), and the sample was cooled with a cooling rate equal to the heating rate. In this work, heating rates of 2, 5, and 10 K/min were applied.

For isothermal STA measurements, the sample was heated under a synthetic air atmosphere with 10 K/min up to the measurement temperature. When a constant sample temperature was achieved, the atmosphere was switched to  $\text{N}_2$ , inducing the reduction. After the reduction was completed, the atmosphere was switched back to synthetic air to start the oxidation. At the end of the oxidation, the sample was cooled with 10 K/min. In this work, isothermal STA measurements were performed at 920, 950, and 980  $^\circ\text{C}$ .

The use of  $\text{N}_2$  during the reduction was motivated by the fact that the system CuO/Cu<sub>2</sub>O has an eutectic point at 1091  $^\circ\text{C}$  and 35% Cu<sub>2</sub>O.<sup>33</sup> A reduction under air ( $p_{\text{O}_2} = 0.21$  bar) would require temperatures above 1028  $^\circ\text{C}$  (see Figure 1). Operating the system this close to its melting point could pose problems, such as sintering or partial melting, in the operation of the TCES system.

The cycle test was performed at 950  $^\circ\text{C}$ . The sample was heated with 10 K/min in a synthetic air atmosphere. When isothermal conditions were reached, the cycle was started. The cycle consisted of two segments: (1) reduction under a  $\text{N}_2$  atmosphere for 60 min and (2) oxidation under a synthetic air atmosphere for 75 min.

The cycle was repeated 20 times. Then, the sample was cooled with 10 K/min to room temperature.

From the mass signal  $m(t)$  of each measurement, the mass content of CuO  $w(t)$  can be calculated on the basis of

$$w(t) = \frac{m(t) - m_0 \nu}{m_0 - m_0 \nu} \quad \text{with} \quad \nu = \frac{M_{\text{Cu}_2\text{O}}}{2M_{\text{CuO}}} \quad (21)$$

with  $M_{\text{CuO}}$  and  $M_{\text{Cu}_2\text{O}}$  being the molar masses of CuO and Cu<sub>2</sub>O, respectively, and  $m_0$  being the sample mass of CuO at the beginning. The term  $m_0 \nu$  is equal to the theoretical mass of Cu<sub>2</sub>O after full conversion. The conversion  $\alpha$  in the case of the oxidation is equal to  $w(t)$ , and in case of the reduction,  $\alpha = 1 - w(t)$  is valid.

**Fixed-Bed Reactor.** A reactor was used to investigate the reaction under macroscopic conditions. Its schematic setup is shown in Figure 4. It consists of two tubes on top of each other with an inner diameter of 40 mm. The lower tube is the preheating zone and is filled with sand for better heat transfer onto the reaction gas. In the reaction chamber, the material was placed on a glass frit. The quartz glass frit with a pore size between 160 and 250  $\mu\text{m}$  is used to evenly distribute the reaction gas over the cross section of the reactor. The reactor is heated with resistance heating shells up to 1100  $^\circ\text{C}$ . The temperature control is performed on the basis of the temperature inside the reactor, which is measured with a thermocouple type K within the CuO bulk. To achieve different gas atmospheres,  $\text{N}_2$  and  $\text{O}_2$  can be mixed via two mass flow controllers. After passing the reactor, the reactive gas passes a gas cooling system into a gas analyzer, which measures the  $\text{O}_2$  concentration  $c_{\text{O}_2}$ . Compressed air is used for outer cooling of the reactor and better temperature control. In the reactor, isothermal tests at 930, 950, and 980  $^\circ\text{C}$  with 50 g of CuO granulate material were performed. The material was heated with a gas flow of 2.5 L/min  $\text{N}_2/\text{O}_2$  mixture with  $p_{\text{O}_2} = 0.21$  bar to simulate air. When isothermal conditions were reached in the reactor, the reaction atmosphere was switched to 2.5 L/min  $\text{N}_2$  ( $p_{\text{O}_2} \leq 10^{-5}$  bar) to induce the reduction (see Figure 1). When the  $\text{O}_2$  concentration reached zero in the off-gas, the reduction was assumed to be completed and the oxidation was started. This was performed by switching back to the starting reaction atmosphere of 2.5 L/min  $\text{N}_2/\text{O}_2$  mixture ( $p_{\text{O}_2} = 0.21$  bar).

The cycle test was similar to the test in the STA. The test used 50.8267 g of CuO. The sample was heated in a mixed gas flow



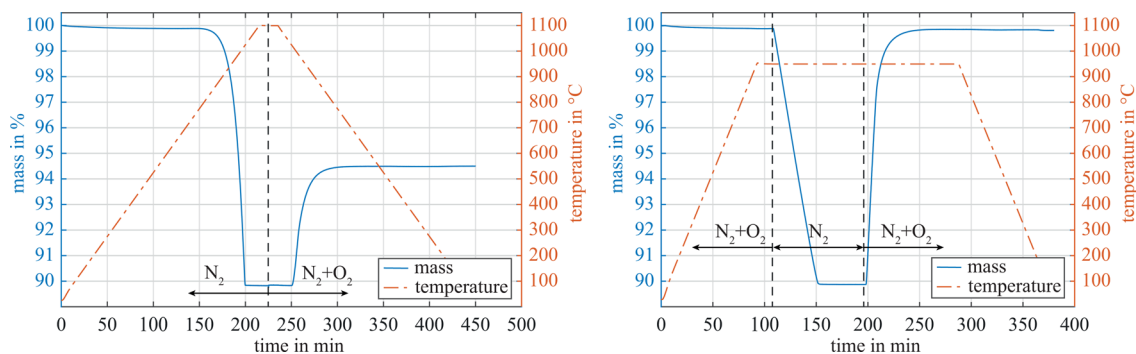


**Figure 3.** Representative measurement procedure in the STA for kinetic analysis: (left) isokinetic measurement with  $\beta = 5$  K/min and (right) isothermal measurement with  $T = 950$  °C.

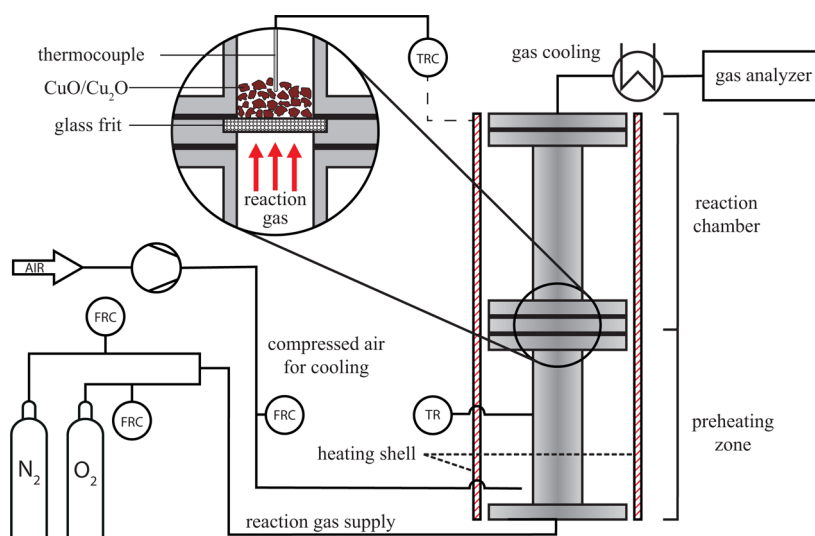


**Figure 4.** Schematic setup of the reactor used for kinetic measurements under fixed-bed conditions.

of 2 L/min  $N_2$  and 0.5 L/min  $O_2$ . When isothermal conditions at 950 °C were reached, the cycle was started. The cycle consisted of two segments: (1) reduction under 2.5 L/min  $N_2$  for 200 min and (2) oxidation under 2 L/min  $N_2$  and 0.5 L/min  $O_2$  for 130 min.

The cycle was repeated 23 times.

The conversion  $\alpha$  in this case is calculated on the  $O_2$  concentration  $c_{O_2}$  following

$$\alpha(t) = \frac{\int_0^t \dot{V} \Delta c_{O_2}(t) dt}{\int_0^{t_{\text{end}}} \dot{V} \Delta c_{O_2}(t) dt} \quad (22)$$

where  $\dot{V}$  is the volumetric gas flow through the reactor,  $t_{\text{end}}$  is the duration of the reaction, and  $\Delta c_{O_2}(t)$  is the difference in  $c_{O_2}$  between an empty reactor and a reactor filled with reactive material. The change of  $\dot{V}$  as a result of released or consumed  $O_2$  is negligible.

**X-ray Powder Diffraction.** The powder X-ray diffraction measurements were carried out using a PANalytical X'Pert diffractometer in Bragg–Brentano geometry using  $Cu K\alpha_{1,2}$  radiation, an X'Celerator linear detector with a Ni filter, sample spinning with back loading zero background sample holders, and  $2\theta = 4\text{--}90^\circ$  ( $T = 25$  °C). The diffractograms were evaluated using the PANalytical program suite HighScorePlus, version 3.0d. A background correction and a  $K\alpha_2$  strip were performed.

**BET Analyzer.** The analysis of the specific surface of the samples was determined with nitrogen sorption measurements on an ASAP 2020 (Micromeritics) instrument. The samples (amounts between 100 and 200 mg) were degassed under vacuum at 80 °C overnight prior to the measurement. The surface area was calculated according to the BET method.<sup>34</sup>

## RESULTS

**STA Measurements.** The results of the isokinetic STA measurements are shown in Figure 5. In the left diagram, the reduction of CuO in a  $N_2$  atmosphere during heating can be seen for different heating rates. It reveals that the system reacts completely, regardless of the heating rate, with the typical shift of the conversion curve to higher temperatures for higher heating rates. The right diagram shows the oxidation of  $Cu_2O$  during cooling in a synthetic air atmosphere. There, the reached content of CuO strongly depends upon the cooling rate, with the slowest rate reaching the highest CuO content. The reaction stops as the temperature falls below 800 °C. This behavior is similar for all investigated cooling rates; therefore, it can be concluded that the available energy at temperature levels below 800 °C is not enough to promote the reaction. Hence, the reaction is kinetically limited by the temperature. This also explains the difference in final conversions, because the sample in a measurement with a slower cooling rate remains longer in a temperature range above 800 °C, where the reaction occurs. As a result of this, the temperatures 920, 950, and 980 °C were chosen for the isothermal measurements, because the reaction has a relevant reaction rate in this temperature range.

The isothermal measurements are shown in Figure 6. The left diagram shows the reduction of CuO in a  $N_2$  atmosphere, and the right diagram shows the oxidation of  $Cu_2O$  in a synthetic air atmosphere. In both cases, the conversion is complete. On one hand, it can be seen that a higher temperature results in faster

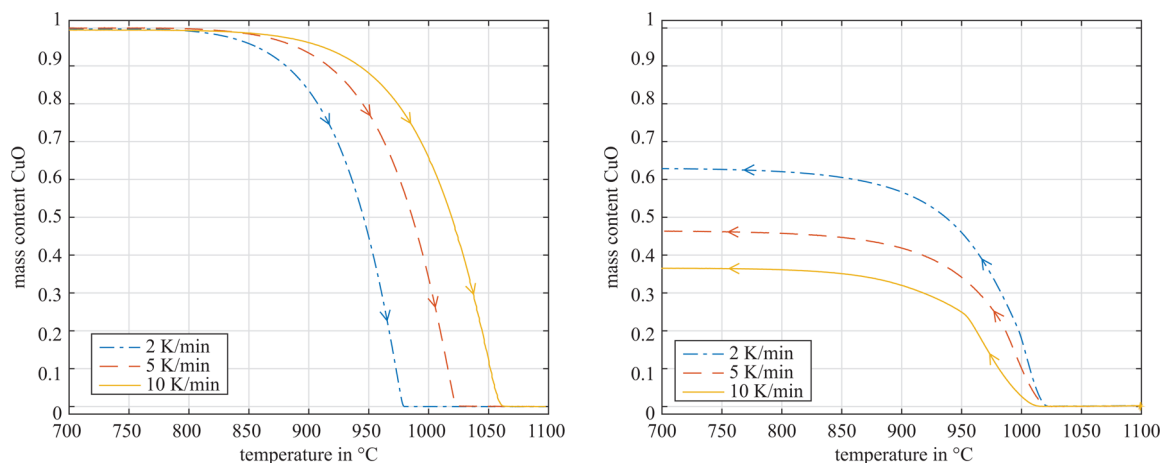


**Figure 5.** Isokinetic STA measurements at different heating/cooling rates: (left) reduction in  $N_2$  during heating and (right) oxidation in synthetic air during cooling.

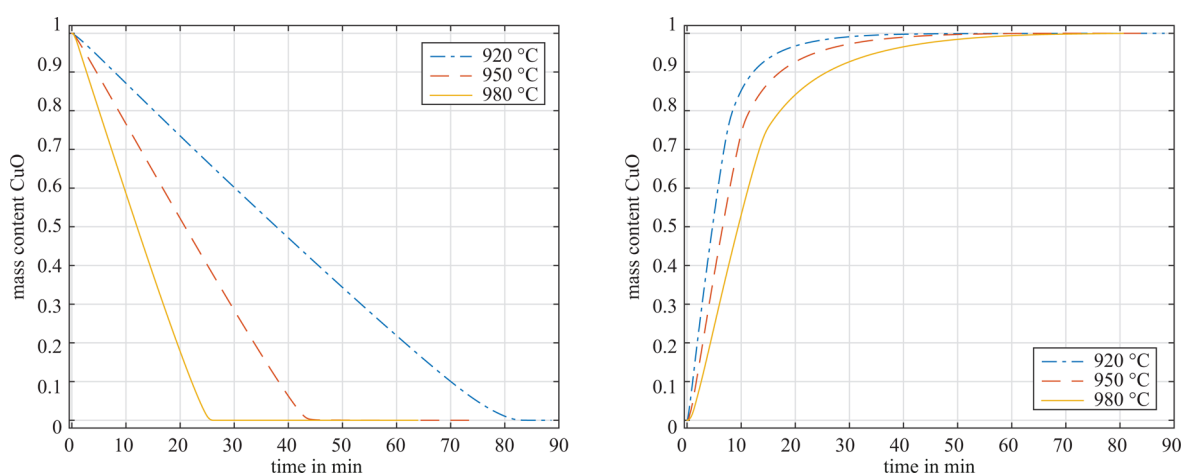


**Figure 6.** Isothermal STA measurements at different temperatures: (left) reduction in  $N_2$  and (right) oxidation in synthetic air.

reduction. On the other hand, the oxidation is slowed with an increased temperature as reported in the literature.<sup>21</sup> Additionally, the isothermal experiments are used to measure the energy turnover during the reaction. Figure 7 shows the differential scanning calorimetry (DSC) signal during a measurement at 950 °C. The baseline was constructed according to Höhne et al.<sup>35</sup>

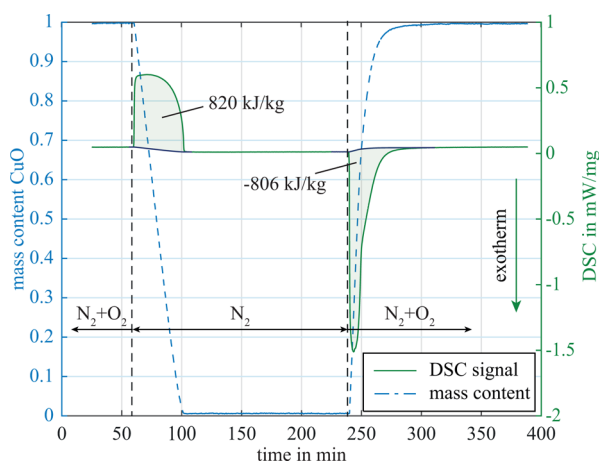


**Figure 7.** Energy uptake/release during the conversion in an isothermal measurement at 950 °C.

The absorbed energy during the reduction (820 kJ/kg of CuO) is slightly higher than the released energy during the oxidation (806 kJ/kg of CuO). This is most likely due to produced oxygen, which exits the crucible during the reduction, thus, taking away some energy, which is measured as additional cooling of the sample. Still, both values are within 1% error to the value reported in the literature (811 kJ/kg of CuO<sup>11</sup>).

**Reactor Measurements.** The results of the measurements in the test reactor are presented in Figure 8. All measurements reached full conversion, which was verified by X-ray powder diffraction analysis. The major difference between the STA measurements and the reactor measurements is that the oxidation does not slow with the increasing temperature. This is most likely connected to a better mass transport inside the bulk as a result of the flow through of the reactive gas compared to the laminar transport in the STA crucible.

Additionally, it has to be noted that the temperature inside the reactor for the oxidation is not constant. As a result of the big sample mass in the reactor (50 g), the released energy influences the local sample temperature inside the reactor. As a result of the thermal inertia of the system, the released energy results in non-isothermal measurement conditions, which are recorded by the thermocouple within the bulk material. Figure 9 shows representatively the deviation of the isothermal temperature of 950 °C during the oxidation. The released energy can hardly

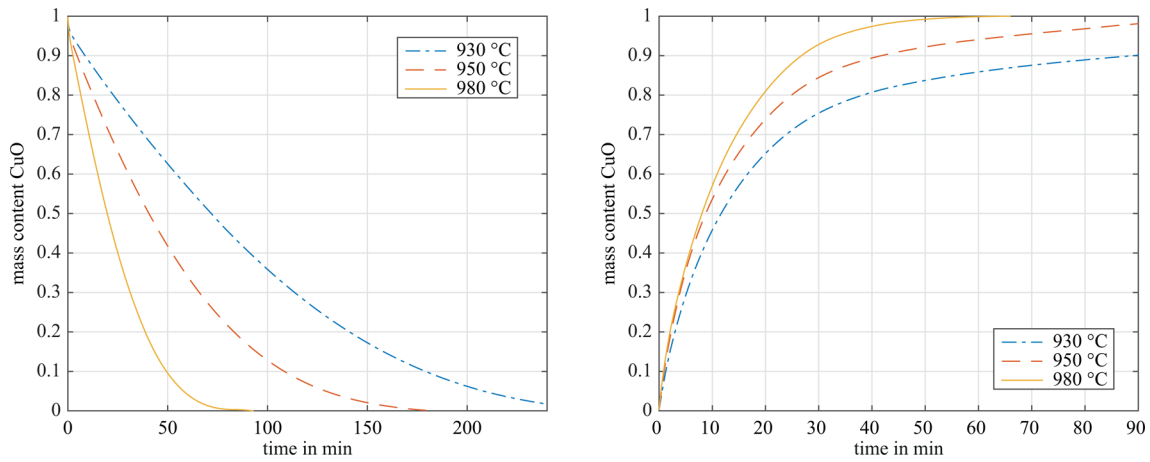


Figure 8. Measurements in the fixed-bed reactor at different starting temperatures: (left) reduction in  $N_2$  and (right) oxidation in synthetic air.

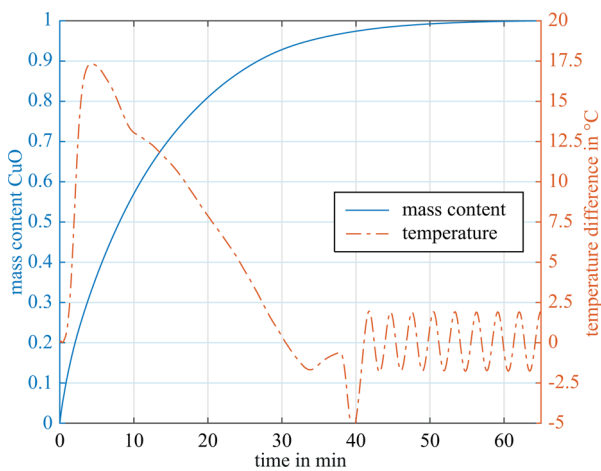


Figure 9. Temperature change in the reaction zone as a result of the released energy during oxidation at 950 °C starting temperature.

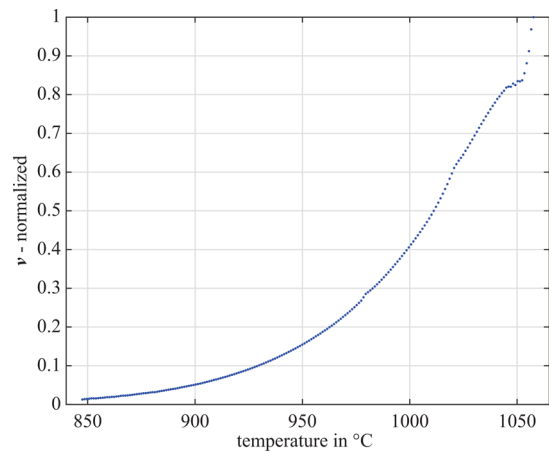


Figure 11. Temperature dependency vector  $\nu$  derived from isokinetic measurements of the reduction of  $CuO$  in  $N_2$ .

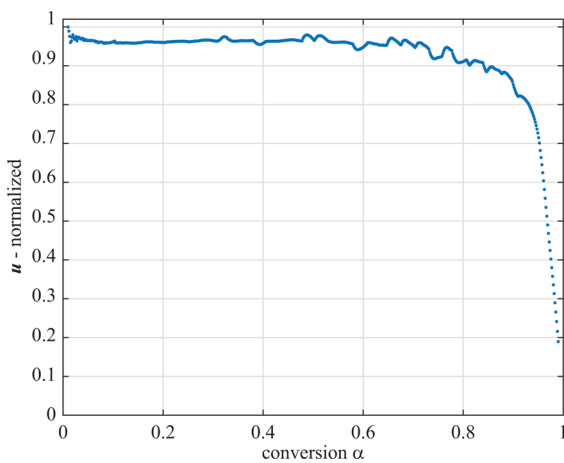


Figure 10. Conversion dependency vector  $u$  derived from isokinetic measurements of the reduction of  $CuO$  in  $N_2$ .

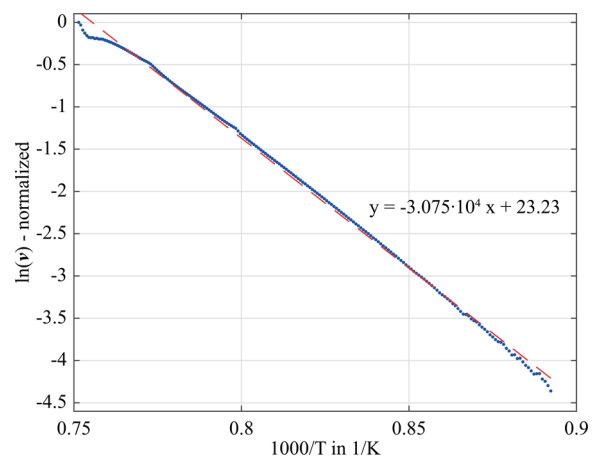


Figure 12. Arrhenius plot of  $\nu$  derived from isokinetic measurements of the reduction of  $CuO$  in  $N_2$ .

be compensated by the cooling of the reactor. This further consolidates the system  $CuO/Cu_2O$  as a promising CSP–TCES system.

**Kinetic Identification.** All models presented in this work can be downloaded at the projects homepage [solidheat.project.tuwien.ac.at](http://solidheat.project.tuwien.ac.at).

**Reduction.** The kinetic identification of the reduction was performed on the isokinetic STA measurements (Figure 5). Using the NPK method, this resulted in a model based on eq 15, with  $s = 2.949 \times 10^{-3} s^{-1}$  and the vectors  $u$  and  $\nu$  as shown in Figures 10 and 11. Linearization of  $\nu$  based on eq 20 results in the Arrhenius plot in Figure 12. From the slope of the fitted linear

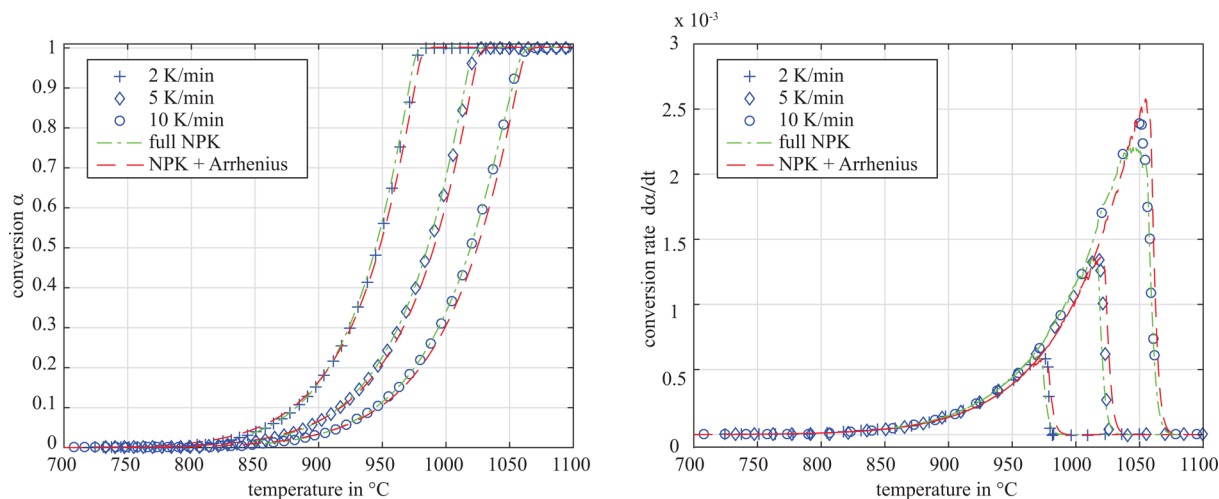


Figure 13. Simulation of the isokinetic measurements of the reduction of CuO with the identified model.

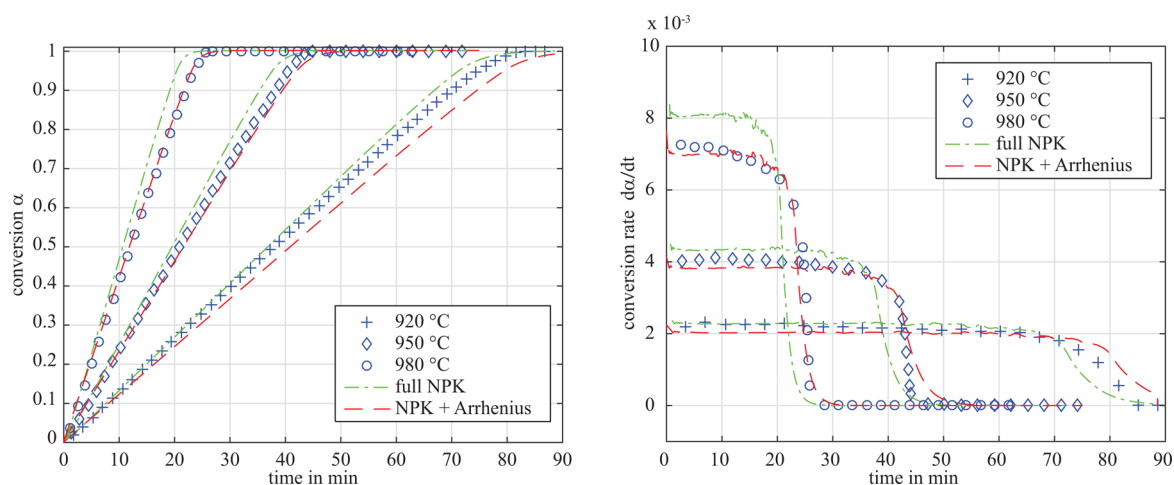


Figure 14. Simulation of the isothermal measurements of the reduction of CuO with the model identified from isokinetic measurements.

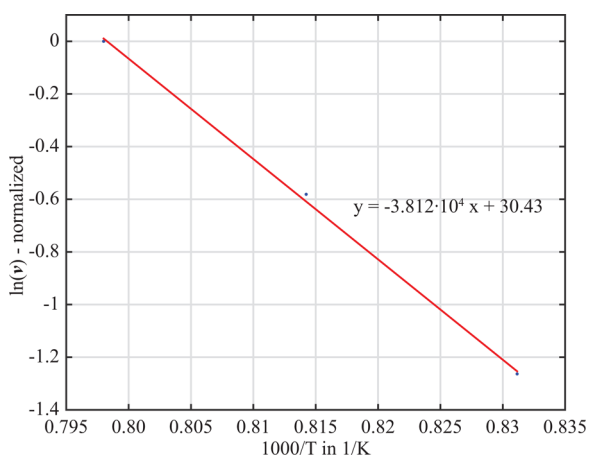


Figure 15. Arrhenius plot of  $\nu$  derived from isothermal measurements of the reduction of CuO in the reactor.

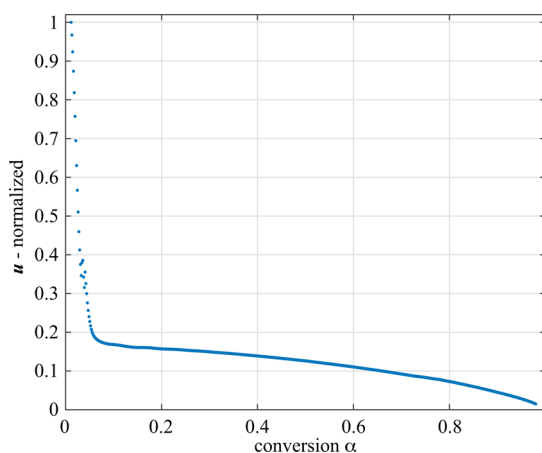


Figure 16. Conversion dependency vector  $u$  derived from isothermal measurements of the reduction of CuO in the reactor.

equation, the apparent activation energy  $E_a$  for the reduction can be calculated as 255.68 kJ/mol.

Therefore, both the isokinetic measurements and the isothermal measurements were simulated on the basis of the model derived from the isokinetic data. Additionally, the simulation was performed in two different ways.

With the kinetic information calculated with the NPK method, the reduction was simulated in two ways. Once, with the result of the NPK method used directly to simulate the conversion (“full NPK”) and once with the temperature dependency described by the identified Arrhenius equation (“NPK + Arrhenius”). Often the conversion dependency found by the NPK method is valid in

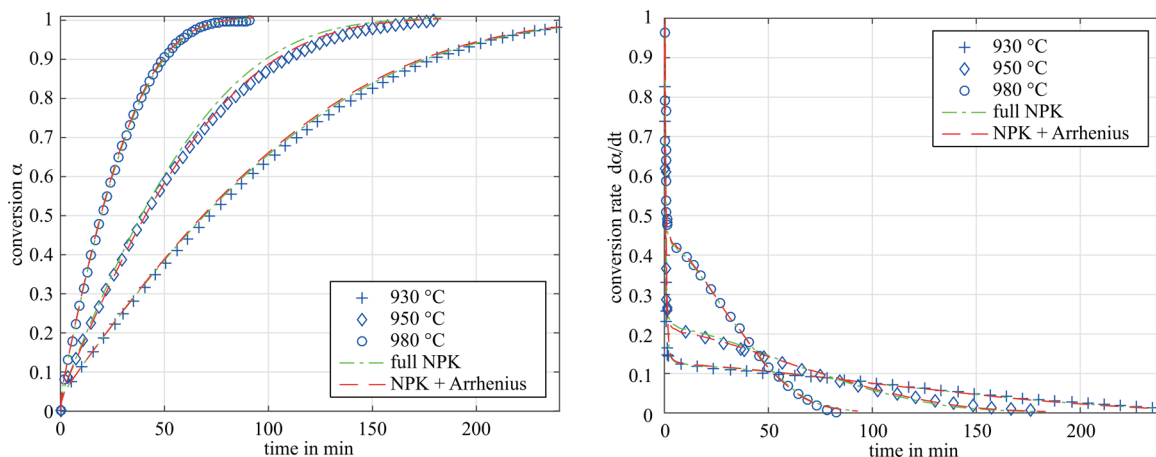


Figure 17. Simulation of the isothermal measurements of the reduction of CuO in the test rig.

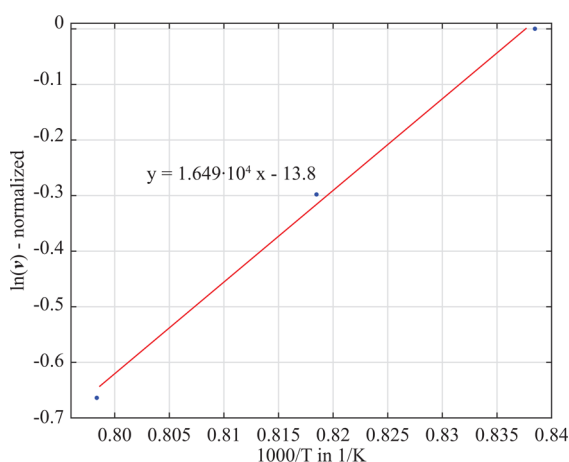


Figure 18. Arrhenius plot of  $v$  derived from isothermal STA measurements of the oxidation of  $\text{Cu}_2\text{O}$ .

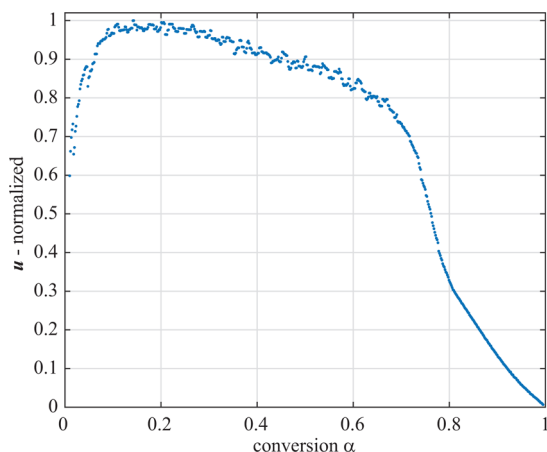


Figure 19. Conversion dependency vector  $u$  derived from isothermal STA measurements of the oxidation of  $\text{Cu}_2\text{O}$ .

a sufficient range, but the temperature dependency is limited. By fitting the Arrhenius equation, an extrapolation is possible and, therefore, the temperature range in which the model is applicable is increased. Note that the apparent pre-exponential factor is only correct in combination with the vector  $u$ , identified by the NPK method (see the Kinetic Identification section). Figure 13 shows the fit of the simulated isokinetic measurements

to the actual measurements for conversion and conversion rate. Both methods reproduce the measurements well, and while the full NPK method is limited to temperatures above 850 °C as a result of  $u$  (Figure 11), the combination of NPK and Arrhenius equation is capable of giving the behavior of the reaction below 850 °C.

The results of the simulation of the isothermal experiments are shown in Figure 14. There, it can be seen that the models fit the measurements reasonably well, especially because the model was identified from isokinetic data.

Additionally, the reduction in the reactor is analyzed. Because only three temperature levels are available, vector  $v$  consists of only 3 points. The activation energy  $E_a$  based on the corresponding Arrhenius plot (Figure 15) was calculated as 316.9 kJ/mol. The difference between  $E_a$  in the STA and the fixed-bed reactor leads to the conclusion that the reaction in the STA is not only governed by the intrinsic reaction kinetic but also by mass transfer.<sup>36</sup> One can also see that the conversion dependency  $u$  (Figure 16) differs from the dependency found in the STA measurements. Note, that the dead volume in the reactor smears the change of the  $\text{O}_2$  concentration in the off-gas. This is especially significant at the beginning of the reduction, when the atmosphere in the reactor is changed from synthetic air to  $\text{N}_2$ . This causes the steep drop at the beginning of  $u$ . Thus, it is assumed that the conversion dependency is only valid for  $\alpha > 0.1$ . With the identified model for the reactor, it was also possible to reproduce the measurement results satisfactorily (Figure 17).

**Oxidation.** Because the isokinetic STA measurements of the oxidation reaction (see Figure 5) do not reach full conversion, it is not possible to calculate the conversion dependency for a satisfying conversion range. Therefore, the NPK method was performed on the isothermal STA experiments. The identified vectors  $u$  and  $v$  are shown in Figures 18 and 19. The shape of  $u$  in the oxidation differs from the reduction; thus, it can be concluded that the conversion mechanism differs between reduction and oxidation. Again, vector  $v$  consists of only three points. Also, as expected from the isothermal measurement data, the fitted linear equation in the Arrhenius plot of  $v$  has a positive slope, resulting in a apparent activation energy  $E_a$  of  $-137.10$  kJ/mol. Nevertheless, the simulation can reproduce the measurement with good accuracy (Figure 20).

The result of the kinetic identification of the oxidation in the reactor is shown in Figures 21 and 22. In contrast to the other isothermal measurements, vector  $v$  consists of more than 3 points. This is due to the non-isothermal condition described



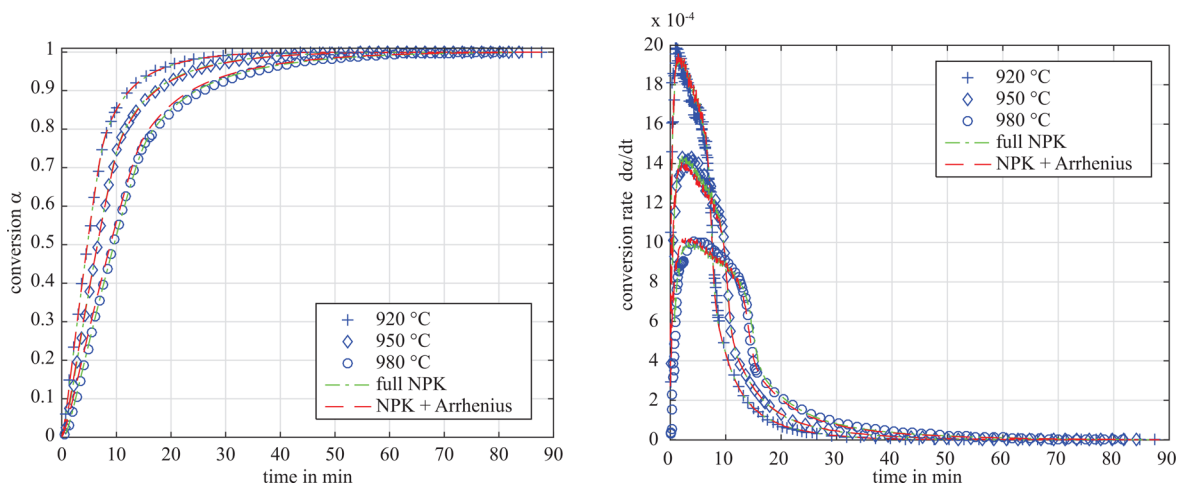


Figure 20. Simulation of the isothermal STA measurements of the oxidation of  $\text{Cu}_2\text{O}$ .

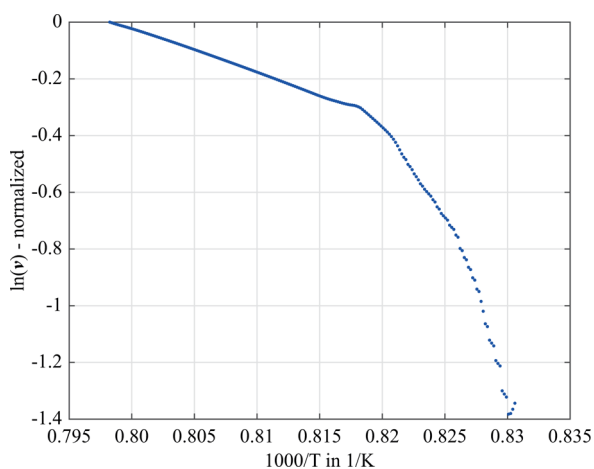


Figure 21. Arrhenius plot of  $\nu$  derived from isothermal measurements of the oxidation of  $\text{Cu}_2\text{O}$  in the reactor.

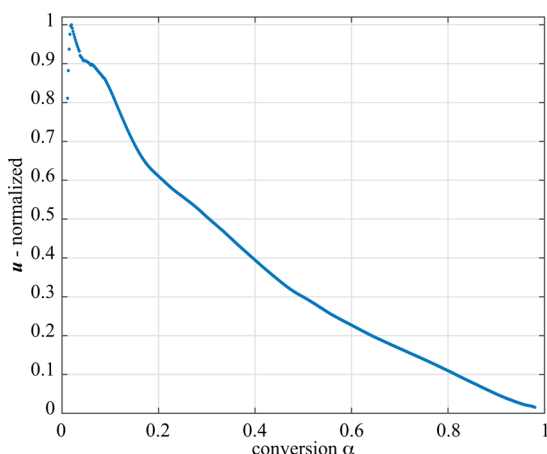


Figure 22. Conversion dependency vector  $u$  derived from isothermal measurements of the oxidation of  $\text{Cu}_2\text{O}$  in the reactor.

in the **Reactor Measurements** section. This can be considered in the kinetic identification by the NPK method, and therefore, additional temperature information is extracted from the data. As a downside, a non-isotropic temperature field occurs, reducing the quality of the identified model and leading to a higher deviation of the simulation from the measurement (Figure 23).

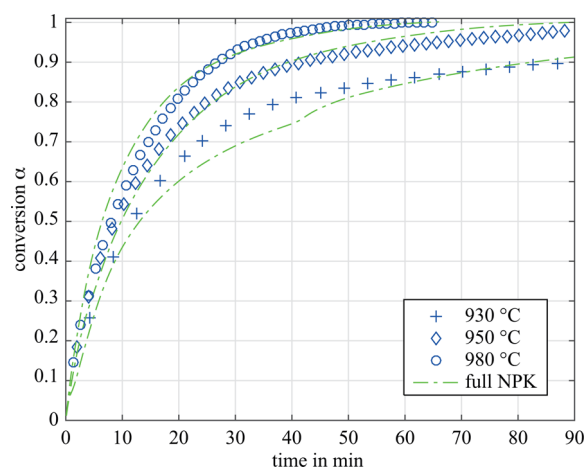


Figure 23. Simulation of the isothermal measurements of the oxidation of  $\text{Cu}_2\text{O}$  in the reactor.

**Cycle Test.** The cycle stability test in the STA is shown in Figure 24. The diagram shows the change of the conversion in the sample and the energy flow over 20 cycles. One can see that the form of the conversion curve changes only minorly over the cycles. There is no sign of chemical degradation; in fact, after 10 cycles, the system reaches nearly theoretical conversion.

An equivalent cycle test was performed in the reactor, with the result that the granular material sintered together, blocking the reaction after a few cycles. Figure 25 shows the sintering of the material after the first and last cycles. Additionally, the sintered material was cut in half (Figure 25D). It can be seen that the surface of the material sintered completely together, while the granular structure is still present in the inner core of the sample, thus, blocking most of the reactive surface. Additionally, cavities of  $\text{Cu}_2\text{O}$  were formed in the edge regions, which was confirmed by a XRD analysis. On the basis of this behavior, it can be concluded that a fixed-bed process is not practical for energy storage. An alternative option would be to use a rotary reactor, because it prevents the sintering as a result of relative movement of the particles, as suggested by Alonso et al.<sup>17</sup>

## CONCLUSION

In this work, the kinetic behavior and the cycle stability of the TCES system  $\text{CuO}/\text{Cu}_2\text{O}$  were analyzed in a STA and a fixed-bed reactor. On the basis of isokinetic and isothermal measurements,



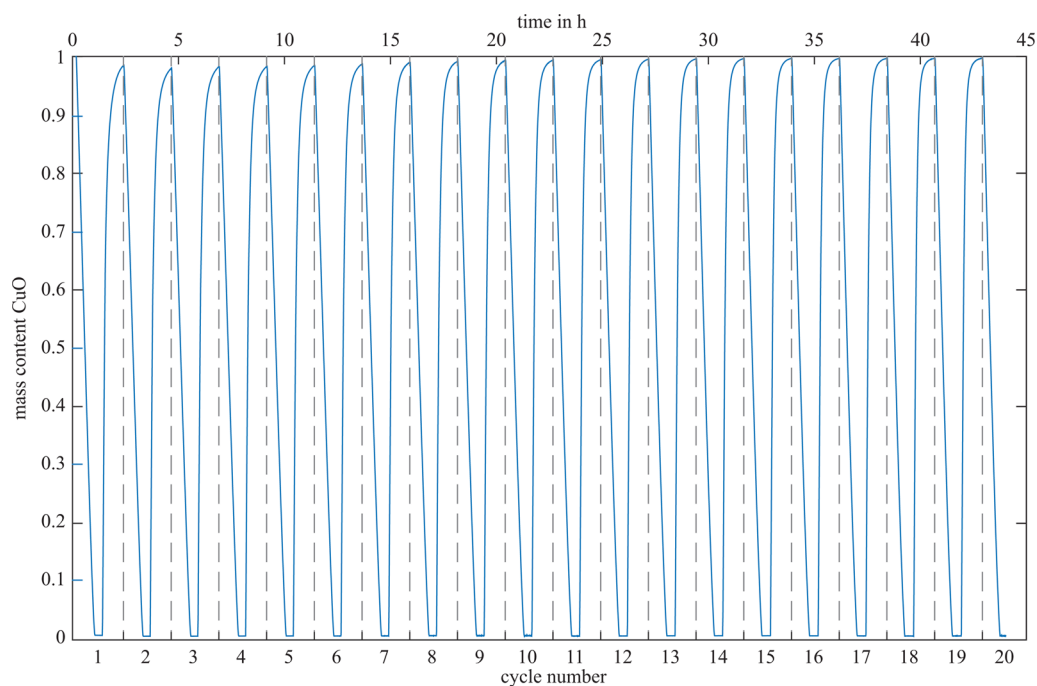


Figure 24. CuO reaction behavior over 20 cycles in the STA at 950 °C and changing N<sub>2</sub>/synthetic air atmospheres.



Figure 25. Sintering of the granulate material in the fixed-bed reactor: (A and B) top and side views after 1 cycle, (C) top view after 20 cycles, and (D) inside view of the material after 20 cycles.

kinetic models were derived for oxidation and reduction. To identify these models, the NPK method was applied, which is an *a priori* model-free approach. Then, the Arrhenius correlation was introduced to the models to expand the applicable temperature range. The measurements revealed a distinctively different behavior between the oxidation in the STA and the fixed-bed reactor. In the STA, the oxidation slowed with an increased temperature as described in the literature. This results in a negative apparent activation energy  $E_a$  of  $-137.10$  kJ/mol. Such behavior was not observed in the fixed-bed reactor, where a mechanistic change was detected, through a change of  $E_a$ , but no negative  $E_a$  has been found. A comparison between the available literature<sup>21,22,37,38</sup> and this work shows significant differences in the kinetics of the reaction system. Clayton et al. presented conversion times around 1–2 min for the reduction, and Hu et al.

reported that the reaction occurs within 10 min, while the reaction in this work took around 40 min for full conversion. All three publications conducted their measurements in thermogravimetric analysis (TGA) or STA. The main difference between all publications is the sample material.

While Clayton et al. used copper-based oxygen carriers with TiO<sub>2</sub> and ZrO<sub>2</sub> as support material, Hu et al. used an oxygen-carrier-based Al<sub>2</sub>O<sub>3</sub>. The support material reduces the CuO content to around 40%, which directly reduced the energy density. Thus, this work used granular CuO. Johansson et al. reported that different support materials have different effects on the reactivity of system Mn<sub>3</sub>O<sub>4</sub>/MnO. A similar effect could explain the different kinetic behaviors. Further examinations are needed to identify the decisive factor behind this different behavior. In the fixed-bed reactor, the system showed a high-energy output during oxidation, proving the capability of CuO as a TCES material. In the STA, the reaction system shows an excellent cycle stability over the course of 20 cycles. In the fixed-bed reactor, heavy sintering occurred, which reduced the reaction to a minimum by blocking most of the reactive surface. This allowed only the outermost layer of the material to react. Further investigations show that the sample in the STA also sintered, but as a result of the small thickness of the sample in the crucible, no reaction hindering effect was measured. Thus, a fixed-bed process is not suitable for application; instead, a system with movement of the material to prevent sintering should be considered. Overall, the study shows that the system CuO/Cu<sub>2</sub>O is a valid candidate for TCES in combination with CSP, but further investigations are necessary.

## ■ AUTHOR INFORMATION

### Corresponding Author

\*E-mail: [markus.deutsch@tuwien.ac.at](mailto:markus.deutsch@tuwien.ac.at)

### ORCID

Markus Deutsch: 0000-0001-5384-9479

Peter Weinberger: 0000-0003-4172-6193

## Notes

The authors declare no competing financial interest.

## ACKNOWLEDGMENTS

The authors thank the Austrian Research Promotion Agency (FFG) for the financial support of the project SolidHeat Kinetics (848876). The X-ray center (XRC) of TU Wien is acknowledged for providing access to the powder X-ray diffractometers.

## REFERENCES

- (1) Aydin, D.; Casey, S. P.; Riffat, S. The latest advancements on thermochemical heat storage systems. *Renewable Sustainable Energy Rev.* **2015**, *41*, 356–367.
- (2) Abedin, A. H.; Rosen, M. A. A critical review of thermochemical energy storage systems. *Open Renewable Energy J.* **2011**, *4*, 42–46.
- (3) Nagel, T.; Shao, H.; Singh, A. K.; Watanabe, N.; Roßkopf, C.; Linder, M.; Wörner, A.; Kolditz, O. Non-equilibrium thermochemical heat storage in porous media: Part 1—Conceptual model. *Energy* **2013**, *60*, 254–270.
- (4) Li, T.; Wang, R.; Kiplagat, J. K.; Kang, Y. Performance analysis of an integrated energy storage and energy upgrade thermochemical solid-gas sorption system for seasonal storage of solar thermal energy. *Energy* **2013**, *50*, 454–467.
- (5) Michel, B.; Mazet, N.; Mauran, S.; Stitou, D.; Xu, J. Thermochemical process for seasonal storage of solar energy: Characterization and modeling of a high density reactive bed. *Energy* **2012**, *47*, 553–563.
- (6) Romero, M.; Steinfeld, A. Concentrating solar thermal power and thermochemical fuels. *Energy Environ. Sci.* **2012**, *5*, 9234–9245.
- (7) Zaversky, F.; García-Barberena, J.; Sánchez, M.; Astrain, D. Transient molten salt two-tank thermal storage modeling for CSP performance simulations. *Sol. Energy* **2013**, *93*, 294–311.
- (8) Deutsch, M.; Müller, D.; Aumeyr, C.; Jordan, C.; Gierl-Mayer, C.; Weinberger, P.; Winter, F.; Werner, A. Systematic search algorithm for potential thermochemical energy storage systems. *Appl. Energy* **2016**, *183*, 113–120.
- (9) Pardo, P.; Anxionnaz-Minvielle, Z.; Rougé, S.; Cognet, P.; Cabassud, M. Ca(OH)<sub>2</sub>/CaO reversible reaction in a fluidized bed reactor for thermochemical heat storage. *Sol. Energy* **2014**, *107*, 605–616.
- (10) Wong, B.; Brown, L.; Schaube, F.; Tamme, R.; Sattler, C. Oxide based thermochemical heat storage. *Proceedings of the 16th SolarPACES Conference*; Perpignan, France, Sept 21–24, 2010.
- (11) Wong, B. *Thermochemical Heat Storage for Concentrated Solar Power: Thermochemical System Reactor Design for Thermal Energy Storage: Phase II Final Report for the Period September 30, 2008 through April 30, 2011*; U.S. Department of Energy: Washington, D.C., 2011; GA-C27137.
- (12) Neises, M.; Tescari, S.; de Oliveira, L.; Roeb, M.; Sattler, C.; Wong, B. Solar-heated rotary kiln for thermochemical energy storage. *Sol. Energy* **2012**, *86*, 3040–3048.
- (13) Block, T.; Knoblauch, N.; Schmücker, M. The cobalt-oxide/iron-oxide binary system for use as high temperature thermochemical energy storage material. *Thermochim. Acta* **2014**, *577*, 25–32.
- (14) Agrafiotis, C.; Roeb, M.; Schmücker, M.; Sattler, C. Exploitation of thermochemical cycles based on solid oxide redox systems for thermochemical storage of solar heat. Part 1: Testing of cobalt oxide-based powders. *Sol. Energy* **2014**, *102*, 189–211.
- (15) Carrillo, A. J.; Serrano, D. P.; Pizarro, P.; Coronado, J. M. Thermochemical heat storage based on the Mn<sub>2</sub>O<sub>3</sub>/Mn<sub>3</sub>O<sub>4</sub> redox couple: Influence of the initial particle size on the morphological evolution and cyclability. *J. Mater. Chem. A* **2014**, *2*, 19435–19443.
- (16) Carrillo, A. J.; Moya, J.; Bayón, A.; Jana, P.; de la Peña O'Shea, V. A.; Romero, M.; Gonzalez-Aguilar, J.; Serrano, D. P.; Pizarro, P.; Coronado, J. M. Thermochemical energy storage at high temperature via redox cycles of Mn and Co oxides: Pure oxides versus mixed ones. *Sol. Energy Mater. Sol. Cells* **2014**, *123*, 47–57.
- (17) Alonso, E.; Pérez-Rábago, C.; Licurgo, J.; Fuentealba, E.; Estrada, C. A. First experimental studies of solar redox reactions of copper oxides for thermochemical energy storage. *Sol. Energy* **2015**, *115*, 297–305.
- (18) Solé, A.; Fontanet, X.; Barreneche, C.; Martorell, I.; Fernández, A. I.; Cabeza, L. F. Parameters to take into account when developing a new thermochemical energy storage system. *Energy Procedia* **2012**, *30*, 380–387.
- (19) Abad, A.; Mattisson, T.; Lyngfelt, A.; Rydén, M. Chemical-looping combustion in a 300 W continuously operating reactor system using a manganese-based oxygen carrier. *Fuel* **2006**, *85*, 1174–1185.
- (20) Eyring, E. M.; Konya, G.; Lighty, J. S.; Sahir, A. H.; Sarofim, A. F.; Whitty, K. Chemical Looping with Copper Oxide as Carrier and Coal as Fuel. *Oil Gas Sci. Technol.* **2011**, *66*, 209–221.
- (21) Clayton, C. K.; Sohn, H. Y.; Whitty, K. J. Oxidation Kinetics of Cu<sub>2</sub>O in Oxygen Carriers for Chemical Looping with Oxygen Uncoupling. *Ind. Eng. Chem. Res.* **2014**, *53*, 2976–2986.
- (22) Clayton, C. K.; Whitty, K. J. Measurement and modeling of decomposition kinetics for copper oxide-based chemical looping with oxygen uncoupling. *Appl. Energy* **2014**, *116*, 416–423.
- (23) Zhu, Y.; Mimura, K.; Isshiki, M. Oxidation Mechanism of Cu<sub>2</sub>O to CuO at 600–1050°C. *Oxid. Met.* **2004**, *62*, 207–222.
- (24) Roine, A. *HSC Chemistry 6.12*; Outotec Research Oy: Pori, Finland, 2007.
- (25) Serra, R.; Sempere, J.; Nomen, R. A new method for the kinetic study of thermoanalytical data: The non-parametric kinetics method. *Thermochim. Acta* **1998**, *316*, 37–45.
- (26) Sempere, J.; Nomen, R.; Serra, R. Progress in Non-parametric Kinetics. *J. Therm. Anal. Calorim.* **1999**, *56*, 843–849.
- (27) Serra, R.; Nomen, R.; Sempere, J. The Non-Parametric Kinetics A New Method for the Kinetic Study of Thermoanalytical Data. *J. Therm. Anal. Calorim.* **1998**, *52*, 933–943.
- (28) Sempere, J.; Nomen, R.; Serra, R.; Soravilla, J. The NPK method: An innovative approach for kinetic analysis of data from thermal analysis and calorimetry. *Thermochim. Acta* **2002**, *388*, 407–414.
- (29) Heal, G. R. A generalisation of the non-parametric, NPK (SVD) kinetic analysis method: Part 1. Isothermal experiments. *Thermochim. Acta* **2005**, *426*, 15–21.
- (30) Heal, G. R. A generalisation of the non-parametric, NPK (SVD) kinetic analysis method: Part 2. Non-isothermal experiments. *Thermochim. Acta* **2005**, *426*, 23–31.
- (31) Golub, G. H.; Reinsch, C. Singular value decomposition and least squares solutions. *Numerische Mathematik* **1970**, *14*, 403–420.
- (32) Dickinson, C. F.; Heal, G. R. Solid-liquid diffusion controlled rate equations. *Thermochim. Acta* **1999**, *340–341*, 89–103.
- (33) Neumann, J. P.; Zhong, T.; Chang, Y. A. The Cu–O (Copper–Oxygen) System. *Bull. Alloy Phase Diagrams* **1984**, *5*, 136–140.
- (34) Brunauer, S.; Emmett, P. H.; Teller, E. Adsorption of Gases in Multimolecular Layers. *J. Am. Chem. Soc.* **1938**, *60*, 309–319.
- (35) Höhne, G.; Hemminger, W. F.; Flammersheim, H. J. *Differential Scanning Calorimetry*; Springer: Berlin, Germany, 2013.
- (36) Szekely, J. *Gas–Solid Reactions*; Elsevier: Amsterdam, Netherlands, 2012.
- (37) Hu, W.; Donat, F.; Scott, S. A.; Dennis, J. S. Kinetics of oxygen uncoupling of a copper based oxygen carrier. *Appl. Energy* **2016**, *161*, 92–100.
- (38) Johansson, M.; Mattisson, T.; Lyngfelt, A. Investigation of Mn<sub>3</sub>O<sub>4</sub> with Stabilized ZrO<sub>2</sub> for Chemical-Looping Combustion. *Carbon Capture Storage* **2006**, *84*, 807–818.



## An extension of the NPK method to include the pressure dependency of solid state reactions



Markus Deutsch<sup>a</sup>, Felix Birkelbach<sup>b,\*</sup>, Christian Knoll<sup>c</sup>, Michael Harasek<sup>a</sup>, Andreas Werner<sup>b</sup>, Franz Winter<sup>a</sup>

<sup>a</sup> TU Wien, Institute of Chemical Engineering, 1060 Vienna, Austria

<sup>b</sup> TU Wien, Institute for Energy Systems and Thermodynamics, 1060 Vienna, Austria

<sup>c</sup> TU Wien, Institute of Applied Synthetic Chemistry, 1060 Vienna, Austria

### ARTICLE INFO

#### Keywords:

Heterogeneous kinetics  
Pressure dependency  
NPK  
CdCO<sub>3</sub>

### ABSTRACT

An novel method to identify the pressure dependency for reactions of the type  $A(s) \rightleftharpoons B(s) + C(g)$  is proposed. It is an extension of the non-parametric kinetic analysis (NPK) method as it identifies the pressure dependency in addition to the temperature and conversion dependency of the reaction. This is done by analyzing kinetic data in a three-dimensional data space (conversion, temperature, pressure) and attributing the variation of the conversion rate to these independent variables. Thus a reduction from a three-dimensional problem to three one-dimensional problems is achieved. The derivation of a kinetic model can then be performed for each dependency independently, which is easier than deriving a model directly from the data. This work presents the basic approach of the identification and combination of the three dependencies to build a full kinetic model. Also, the interpretation of the model to achieve a physically motivated model is illustrated. Then the method is applied to identify the complex reaction kinetics of the decomposition of CdCO<sub>3</sub> based on a set of thermogravimetric measurements. It is shown that it is possible to identify interaction terms between the dependency terms.

### 1. Introduction

The kinetics of a reaction often determines its technological applicability and directly influences how economically feasibly a process based on that reaction is. Knowledge of the reaction kinetics is fundamental to choose optimal reaction conditions and to achieve satisfying conversion.

Many solid-state decompositions follow the simple reaction



The kinetics of such reactions is often modelled based on the reaction rate  $da/dt$ . It is generally described as a product of the contributions of three independent variables, the conversion  $\alpha$ , the temperature  $T$  and the pressure  $p$  by the differential equation

$$\frac{d\alpha}{dt} = f(\alpha)k(T)h(p) \quad (2)$$

In case of reactions that follow Eq.(1) the pressure relevant is the partial pressure of the gaseous component C. The literature on solid state kinetic identification focuses mainly on the determination of conversion dependency  $f(\alpha)$  and temperature dependency  $k(T)$ , while

the identification of the pressure dependency  $h(p)$  is often neglected [1]. Yet the pressure dependency is of great interest for reactor design since some reactor types, e.g., fluidized bed reactors, feature high concentration gradients of the reactant gas across the bed height. To take this effect into account, knowledge about the pressure dependency of the reaction is absolutely necessary [2].

To describe the conversion dependency  $f(\alpha)$  different conversion models are used. These conversion models are mathematical descriptions of the measured process during the reactions. For solid state reactions, various different models have been proposed. Some of them represent physical processes (e.g. nucleation, diffusion) as their mathematical description has been derived on certain mechanistic assumptions. Others are purely mathematical. Khawam et al. and Dickinson et al. describe 28 different models and give an overview over the different models and their underlying assumptions [3,4]. Table 1 shows the models, relevant for this work.

The temperature dependency is usually described by the Arrhenius equation

$$k(T) = A \exp\left(\frac{-E_a}{RT}\right) \quad (3)$$

\* Corresponding author.

E-mail address: [felix.birkelbach@tuwien.ac.at](mailto:felix.birkelbach@tuwien.ac.at) (F. Birkelbach).

<http://dx.doi.org/10.1016/j.tca.2017.05.019>

Received 17 March 2017; Received in revised form 3 May 2017; Accepted 25 May 2017

Available online 30 May 2017

0040-6031/ © 2017 Elsevier B.V. All rights reserved.



Nomenclature			
$A$	pre-exponential factor (1/s)	$\mathbf{k}$	vector of temperature dependency values (1/s)
$\mathbf{A}$	reaction rate tensor (1/s)	$m$	sample mass (mg)
$\mathbf{A}_p$	matrix for pressure dependency identification (1/s)	$p_{\text{CO}_2}$	partial pressure of CO <sub>2</sub> (bar)
$\mathbf{A}_T$	matrix for temperature dependency identification (1/s)	$\mathbf{p}$	vector of pressure values (bar)
$E_a$	activation energy (J/mol)	$p$	pressure (bar)
$R$	gas constant (J/mol K)	$s_p$	singular value of the pressure identification (1/s)
$R^2$	goodness of fit value (1)	$s_T$	singular value of the temperature identification (1)
$T$	temperature (K)	$s$	singular value from SVD (1)
$\mathbf{T}$	vector of temperature values (K)	$t$	time (s)
$c, c_1, c_2, c_3$	scaling factors (1)	$\mathbf{u}$	result vector from SVD corresponding to $\mathbf{f}$ (1)
$f(\alpha)$	conversion dependency (1)	$\mathbf{v}$	result vector from SVD corresponding to $\mathbf{k}$ (1/s)
$\mathbf{f}$	vector of conversion dependency values (1)	$\mathbf{w}$	result vector from SVD corresponding to $\mathbf{h}$ (1)
$h(p)$	pressure dependency (1)	$\alpha$	conversion (1)
$\mathbf{h}$	vector of pressure dependency values (1)	$\boldsymbol{\alpha}$	vector of conversion values (1)
$k(T)$	temperature dependency (1/s)	$\beta$	heating rate (K/s)
		$\chi, \omega, \psi$	pressure model parameters (–)

with the activation energy  $E_a$  and the pre-exponential factor  $A$ .

The pressure dependency models  $h(p)$  that have been considered in this work are given in Table 2. They were commonly found in the literature. Most of these models are empirical and allow only limited physical interpretation. The only exception is the model ‘p2’, which is a generalization of the  $(1 - p/p_{\text{eq}})$ -model that has been derived on theoretical grounds in [5–7].

In this work a novel method to determine the pressure dependency and to build a combined kinetic model is presented. It is an extension of the NPK method. The NPK method is a numeric method that was developed by Serra et al. and Sempere et al. [11–14] to identify the temperature and conversion dependency from constant heating rate measurements. It was then generalized by Heal [15,16] for isothermal measurements.

It does not rely on a priori established models and avoids explicit kinetic models as well as the Arrhenius law. From a mathematical point of view, the only assumptions are the choice of the independent variables and the multiplicativity of the contributions of each factor. In principle, the method separates the effect of conversion  $\alpha$ , temperature  $T$  and partial pressure  $p$  of the gaseous component C on the conversion rate  $d\alpha/dt$ . This is done according to the general kinetic equation Eq. (2).

Typically, measurements are performed at constant pressure to determine the temperature dependency  $k(T)$  and the conversion dependency  $f(\alpha)$ . This simplifies Eq. (2) to the well known expression

$$\left. \frac{d\alpha}{dt} \right|_{p_1} = f(\alpha)k(T)h(p_1) = f(\alpha)k'(T) \quad (4)$$

It can be seen that the effect of  $h(p_1)$  results in a factor which would usually be incorporated in the temperature dependency when no pressure dependency is considered. This attribution is a result of the common assumption that the temperature dependency follows the Arrhenius equation Eq. (3).

**Table 1**  
Selection of relevant conversion dependency models [3,4].

Model ID	Type	$f(\alpha)$
A1	Avrami–Erofeyev	$4(1 - \alpha)[-\ln(1 - \alpha)]^{3/4}$
A2	Avrami–Erofeyev	$2(1 - \alpha)[-\ln(1 - \alpha)]^{1/2}$
A3	Avrami–Erofeyev	$3(1 - \alpha)[-\ln(1 - \alpha)]^{2/3}$
A4	Avrami–Erofeyev	$4/3(1 - \alpha)[-\ln(1 - \alpha)]^{1/4}$
A5	Avrami–Erofeyev	$3/2(1 - \alpha)[-\ln(1 - \alpha)]^{1/3}$
B1	Prout–Tompkins	$\alpha(1 - \alpha)$
R2	Contracting area	$2(1 - \alpha)^{1/2}$
R3	Contracting volume	$3(1 - \alpha)^{2/3}$
R4	Interface	$3/2(1 - \alpha)^{1/3}$

Thus, the value of  $h(p_1)$  is incorporated in the pre-exponential factor during the identification as  $A = A_{\text{Arr}}h(p_1)$ . Note, that this is always the case for other identification methods (e.g. Ozawa, Flynn and Wall (OFW) method [17–19], Kissinger method [20,21]), when the pressure dependency is neglected.

To identify the pressure dependency it is necessary to vary the pressure affecting the reaction. In this work this is the partial pressure of the gaseous component. If the temperature is kept constant during the measurements then Eq. (2) can be reduced to

$$\left. \frac{d\alpha}{dt} \right|_{T_1} = f(\alpha)k(T_1)h(p) = f(\alpha)h'(p) \quad (5)$$

In this case the contribution of  $k(T_1)$  is incorporated into  $h'(p)$ .

In the following section the identification of  $f(\alpha)$ ,  $k'(T)$  and  $h'(p)$  from measurement data is described and a novel method is introduced to combine these results to find the full model with  $k(T)$  and  $h(p)$ . Then the method is applied to real data to analyze the decomposition of CdCO<sub>3</sub>.

## 2. The extended NPK method

For better understanding and as a proof of concept of the presented method, a single step decomposition reaction based on Eq. (1) is assumed. The example reaction follows conversion model ‘A1’ (see Table 1), the Arrhenius temperature dependency with  $A = 10^9 \text{ s}^{-1}$  and  $E_a = 60 \text{ kJ/mol}$  and the pressure dependency ‘p2’ (see Table 2) with  $\omega = 1$  and  $\psi = 4$ . This results in the following dependencies:

$$f(\alpha) = 4(1 - \alpha)[-\ln(1 - \alpha)]^{3/4} \quad (6)$$

$$k(T) = 10^9 \exp\left(\frac{-6 \cdot 10^4}{8.314T}\right) \quad (7)$$

$$h(p) = (1 - p)^4 \quad (8)$$

The input for the method is generated by simulating measurements based on the example reaction. For the identification of the temperature dependency, constant heating rate measurements with a heating rate  $\beta$

**Table 2**  
Pressure dependency models, Greek symbols are model parameters.

Model ID	$h(p)$	Literature
p1	$p^\chi$	[8]
p2	$(\omega - p)^\omega$	[5–7,9]
p3	$p^\chi(\omega - p)^\omega$	
p4	$\exp(\chi p)$	[10]

of 2, 5, 7, 10 and 15 K/min at  $p = 0.3$  bar are simulated. To identify the pressure dependency isothermal measurements at 310 K and different pressure levels (0.1, 0.2, 0.3, 0.4 and 0.5 bar) are simulated.

### 2.1. Identification of $k'(T)$ and $f(\alpha)$

To identify the temperature dependency  $k'(T)$  and the conversion dependency  $f(\alpha)$  the NPK Method introduced by Serra, Sempre and Nomen [11–13] is applied.

For isobaric conditions, the conversion rate  $da/dt$  in Eq.(4) can be thought of as a continuous three dimensional surface in the  $\alpha$ - $T$ -space. This surface can be discretized for fixed values of  $\alpha = [\alpha_1 \dots \alpha_l]^T$  and  $T = [T_1 \dots T_m]^T$  and written in a  $(l \times m)$  matrix  $\mathbf{A}_T$ <sup>1</sup> so that the matrix element  $(i, j)$  gives the conversion rate at  $\alpha_i$  and  $T_j$ . It can be shown that the matrix  $\mathbf{A}_T$  can be written as matrix product  $\mathbf{A}_T = \mathbf{f}\mathbf{k}'^T = \mathbf{f} \otimes \mathbf{k}'$  with the dependency vectors  $\mathbf{f} = [f(\alpha_1) \dots f(\alpha_l)]^T$  and  $\mathbf{k}' = [k'(T_1) \dots k'(T_m)]^T$ . Thus, matrix  $\mathbf{A}_T$  is by definition a rank-1 matrix.

When measured conversion rate values are arranged in  $\mathbf{A}_T$  the singular value decomposition (SVD) [22] can be utilized to decompose the matrix according to

$$\mathbf{A}_T = \sum_{i=1}^n s_i \mathbf{u}_i \otimes \mathbf{v}_i = s_1 \mathbf{u}_1 \otimes \mathbf{v}_1 + \sum_{i=2}^n s_i \mathbf{u}_i \otimes \mathbf{v}_i \quad (9)$$

where  $s_i$  is the norm of the submatrix, the singular value, and  $\mathbf{u}_i$  and  $\mathbf{v}_i$  are normalized row and column vectors, respectively.

The SVD returns a successive best first order approximation of the matrix  $\mathbf{A}_T$ . Thus, if the assumption of multiplicativity in Eq.(4) holds, all but the first singular value will be zero. Since real data contain measurement errors, all singular values will differ from zero. If the reaction follows Eq.(4), the first singular value will be significantly bigger than the others. Then the SVD can be truncated after the first term, since it is safe to assume that the remaining terms only contain noise.

This simplifies Eq.(9) to

$$\mathbf{A}_T = s_1 \mathbf{u}_1 \otimes \mathbf{v}_1 = s_T \mathbf{u} \otimes \mathbf{v} \stackrel{\dagger}{=} \mathbf{f} \otimes \mathbf{k}' \quad (10)$$

The SVD attributes the variation of the conversion rate to the independent variables  $\alpha$  and  $T$ , but the scales of the quantities are lost during the matrix decomposition process and combined into the singular value  $s_T$  [15]. To determine the sought-after dependency vectors  $\mathbf{f}$  and  $\mathbf{k}'$  the scaling of  $s_T$  must be attributed to  $\mathbf{u}$  and  $\mathbf{v}$  accordingly.

Fig. 4 shows the identified conversion dependency vector  $\mathbf{u}$  (left) and the identified temperature dependency vector  $\mathbf{v}$  (middle) for the example reaction.

### 2.2. Identification of $h'(p)$

To identify the pressure dependency of a reaction  $h'(p)$  information about the reaction rate at different pressure levels is needed. Due to limitations of the analytical equipment, measurements with continuously changing pressure are usually not possible. This is especially true for TGA (thermogravimetric analysis) measurements where each pressure change results in oscillations and errors in the weight signal due to pressure surges. Thus the most promising approach is to measure under isobaric conditions at different pressure levels. Nevertheless the proposed method can handle measurements with continuously changing pressure in the same way as constant heating rate measurements during the temperature dependency identification.

The identification of the pressure dependency  $h'(p)$  is accomplished in the same way as the identification of the temperature dependency  $k'(T)$  described in the previous section.

Eq.(5) can be visualized as a surface, in the  $\alpha$ - $p$ -space. Fig. 1 shows this surface for the example reaction at  $T = 310$  K. The dashed lines on the surface represent the trajectory of isobaric measurements. The

dotted lines visualize the change of the surface for isobaric measurements with increasing temperature.

The discretization of the surface at fixed values of  $\alpha = [\alpha_1 \dots \alpha_l]^T$  and  $p = [p_1 \dots p_n]^T$  results in the  $(l \times n)$  matrix  $\mathbf{A}_p$ , which can be expressed as the matrix product of the dependency vectors  $\mathbf{f} = [f(\alpha_1) \dots f(\alpha_l)]^T$  and  $\mathbf{h}' = [h'(p_1) \dots h'(p_n)]^T$ .

Arranging measured conversion rate values in the matrix  $\mathbf{A}_p$  and performing a rank-1 approximation with the SVD analysis leads to

$$\mathbf{A}_p = s_p \hat{\mathbf{u}} \otimes \mathbf{w} \stackrel{\dagger}{=} \mathbf{f} \otimes \mathbf{h}' \quad (11)$$

with the singular value  $s_p$  of this decomposition and the normalized row and column vectors  $\hat{\mathbf{u}}$  and  $\mathbf{w}$  respectively. The right curve in Fig. 4 shows the calculated pressure dependency vector  $\mathbf{w}$  for the given example.

As the conversion dependency  $\mathbf{f}$  is identical for both identifications, the identified conversion dependency vectors  $\mathbf{u}$  and  $\hat{\mathbf{u}}$  must be equal, apart from a constant factor.

$$\mathbf{u} = c \hat{\mathbf{u}} \quad (12)$$

Fig. 2 shows the comparison between the identified conversion dependencies  $\mathbf{u}$  and  $\hat{\mathbf{u}}$ , both normalized to 1. The deviation between both identifications originates from numerical errors in the decomposition algorithm. The difference is negligible though. When applying the extended NPK method it should always be confirmed that the conversion vectors of each identification step coincide.

### 2.3. Combining the dependency vectors

To create a numerical representation of the full model according to Eq. (2) the identified dependency vectors  $\mathbf{u}$ ,  $\mathbf{v}$  and  $\mathbf{w}$  have to be combined correctly. Similarly to the matrices  $\mathbf{A}_T$  and  $\mathbf{A}_p$ , a three dimensional  $(l \times m \times n)$  tensor  $\mathbf{A}$  can be built, which represents a discretization of Eq.(2) in the  $\alpha$ - $T$ - $p$ -space.

$$\mathbf{A} = \mathbf{f} \otimes \mathbf{k} \otimes \mathbf{g} \stackrel{\dagger}{=} s \mathbf{u} \otimes \mathbf{v} \otimes \mathbf{w} \quad (13)$$

The difficulty of combining the identified dependency vectors  $\mathbf{u}$ ,  $\mathbf{v}$  and  $\mathbf{w}$  lies in finding the residual scaling factor  $s$ .

The matrix  $\mathbf{A}_T$  for the identification of the temperature dependency represents a slices of  $\mathbf{A}$  at a specific pressure. Similarly,  $\mathbf{A}_p$  for the identification of the pressure dependency represents a slices of  $\mathbf{A}$  at a specific temperature. This is visualized in Fig. 3. The axes span the tensor  $\mathbf{A}$ , while the red and the blue panes symbolize the matrices  $\mathbf{A}_T$  and  $\mathbf{A}_p$ . The contour lines represent the conversion rate  $da/dt$  the solid black lines represent various measurements used for the identification and the black dashed line is the intersection line of the two panes.

In mathematical terms this can be written as

$$\mathbf{A}|_{p_1} = \mathbf{A}_T = s_T \mathbf{u} \otimes \mathbf{v} \quad (14)$$

Here, the notation  $\mathbf{A}|_{T_1}$  means that the tensor  $\mathbf{A}$  is evaluated at  $T_1$  reducing its dimensions to a matrix. If  $T_1$  lies between the discretization points, then the values are interpolated. Similarly,  $\mathbf{v}|_{T_1}$  denotes an evaluation of  $\mathbf{v}$  at  $T_1$  which results in a scalar value.

To find the value of  $s$ , the intersection vector of the slices  $\mathbf{A}_T$  and  $\mathbf{A}_p$  at  $T = T_1$  and  $p = p_1$  has to be considered (dashed line in Fig. 3). At this intersection the following equation holds

$$\mathbf{A}|_{T_1, p_1} = \mathbf{A}_T|_{T_1} \quad (15)$$

Substituting Eqs. (13) and (14) into (15) results in

$$s \mathbf{u} \mathbf{v}|_{T_1} \mathbf{w}|_{p_1} = s_T \mathbf{u} \mathbf{v}|_{T_1} \quad (16)$$

which yields

$$s = \frac{s_T}{\mathbf{w}|_{p_1}} \quad (17)$$

It is also possible to calculate the scaling factor  $s$  by considering the

<sup>1</sup> Bold upper-case letters symbolize matrices or tensors, bold lower-case letter vectors.



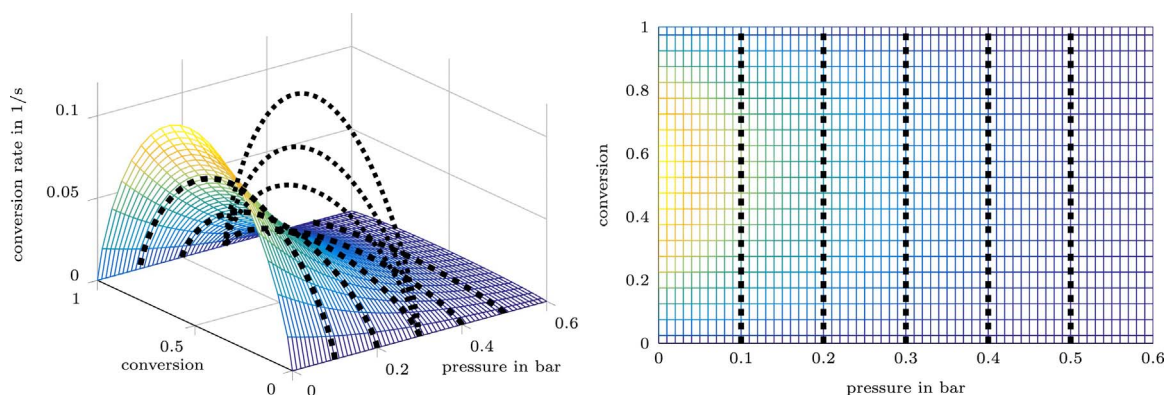


Fig. 1. Reaction rate surface for the example at constant temperature  $T = 310$  K. Dashed lines (--) represent isobaric experiments, dotted lines (..) the change of the surface with increasing temperature.

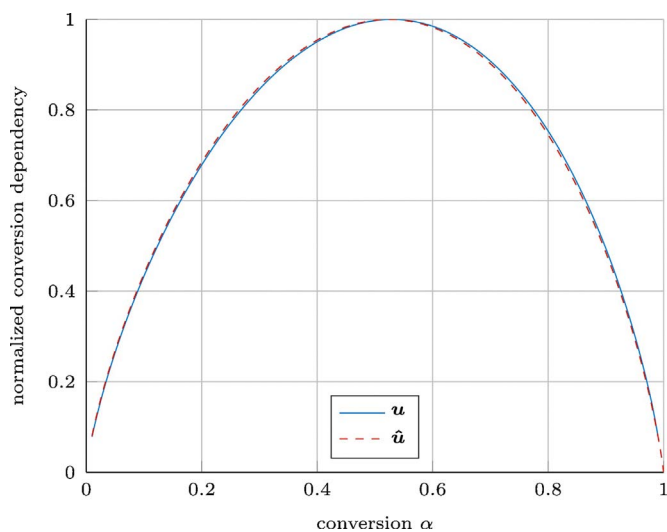


Fig. 2. Comparison of the conversion dependency vector  $u$  and  $\hat{u}$  from the identification of  $v$  and  $w$ , respectively.

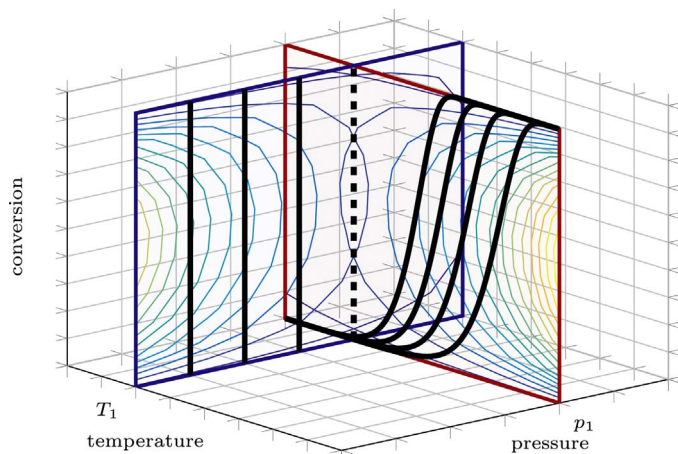


Fig. 3. Visualization of two slices of the tensor  $A$  at  $T_1$  and  $p_1$ , respectively. The contour lines represent the change of the conversion rate  $da/dt$ , the solid black line represent various measurements used for the identification and the black dashed line is the intersection line between the two panes. (For interpretation of the references to color in text near the reference citation, the reader is referred to the web version of this article.)

pressure identification matrix  $A|_{T_1, p_1} = A_p|_{p_1}$ . Then  $\hat{s} = s_p/v|_{T_1}$ .

Incorporating this into (13) yields

$$A = s_T u \otimes v \otimes \frac{w}{w|_{p_1}} = s_p \hat{u} \otimes \frac{v}{v|_{T_1}} \otimes w \quad (18)$$

Provided that (12) holds the two scaling factors  $s$  and  $\hat{s}$  should have the same value. The deviation can be used to assess the quality of the decomposition procedure. In case of the example reaction the relative difference between the values is 0.53%.

Fig. 4 shows all identified dependency vectors. With the scaling factor  $s = 0.1008$  they represent the full numeric model.

#### 2.4. Interpretation of the dependency vectors

Now that the effect of each dependency vector has been identified, the next step is to arrive at a physical interpretation of the identified dependency vectors. To do that model functions are fitted to each vector.

To describe the conversion dependency vector  $u$ , different conversion models  $f(\alpha)$  are considered. In total, 28 different conversion models described by [3] and [4] have been fitted, the most relevant for this work are listed in Table 1. Since none of the models has extra parameters the only fitting parameter is a constant scaling factor  $c_1$ .

First all models are fitted to the conversion dependency vector  $u$  with the least-squares-method. Based on the  $R^2$ -value (see Table 3) the five best fitting models are selected and plotted (Fig. 5).

Since the resulting  $R^2$  values are often very similar a pairwise  $F$ -test is performed to discriminate between the models. The best fitting model is compared to each of the other models. Then the result of the  $F$ -test is a  $p$ -value that reflects the statistical probability of the first model being an improvement over the other model. The result is deemed to be statistically significant if the  $p$ -value is greater than 0.95. The results in Table 3 show that model A1 is a significantly better fit than all the other considered models. Hence the proposed method successfully identified the conversion model that was used to simulate the example data.

To identify the best fitting model for the pressure dependency the same procedure as above is used. In addition to the model parameters the scaling factor  $c_2$  is fitted with each model. The fitted models are plotted in Fig. 6 and the statistical results are provided in Table 4. The two highest scoring models, p2 and p3, result in almost identical  $R^2$ -values. This comes as no surprise since p3 is an extension of p2. Here, the  $F$ -test allows us to discriminate between the two models: Only with a probability of 7% is the model p3 an improvement over the second best model p2. Since this value is far below the significance threshold of 0.95 the simpler model with less parameters, p2, is chosen.

Again the presented method identified the correct model and with  $\omega = 1.014$  and  $\chi = 4.102$  also the recovered values of the model parameters are very accurate.

With the two fitted scaling factors  $c_1$  and  $c_2$  the last scaling factor  $c_3 = s/(c_1 c_2)$  can be calculated. Assuming that the temperature dependency follows the Arrhenius equation in Eq.(3) the following holds:

$$c_3 v|_T = A \exp\left(\frac{-E_a}{RT}\right) \quad (19)$$

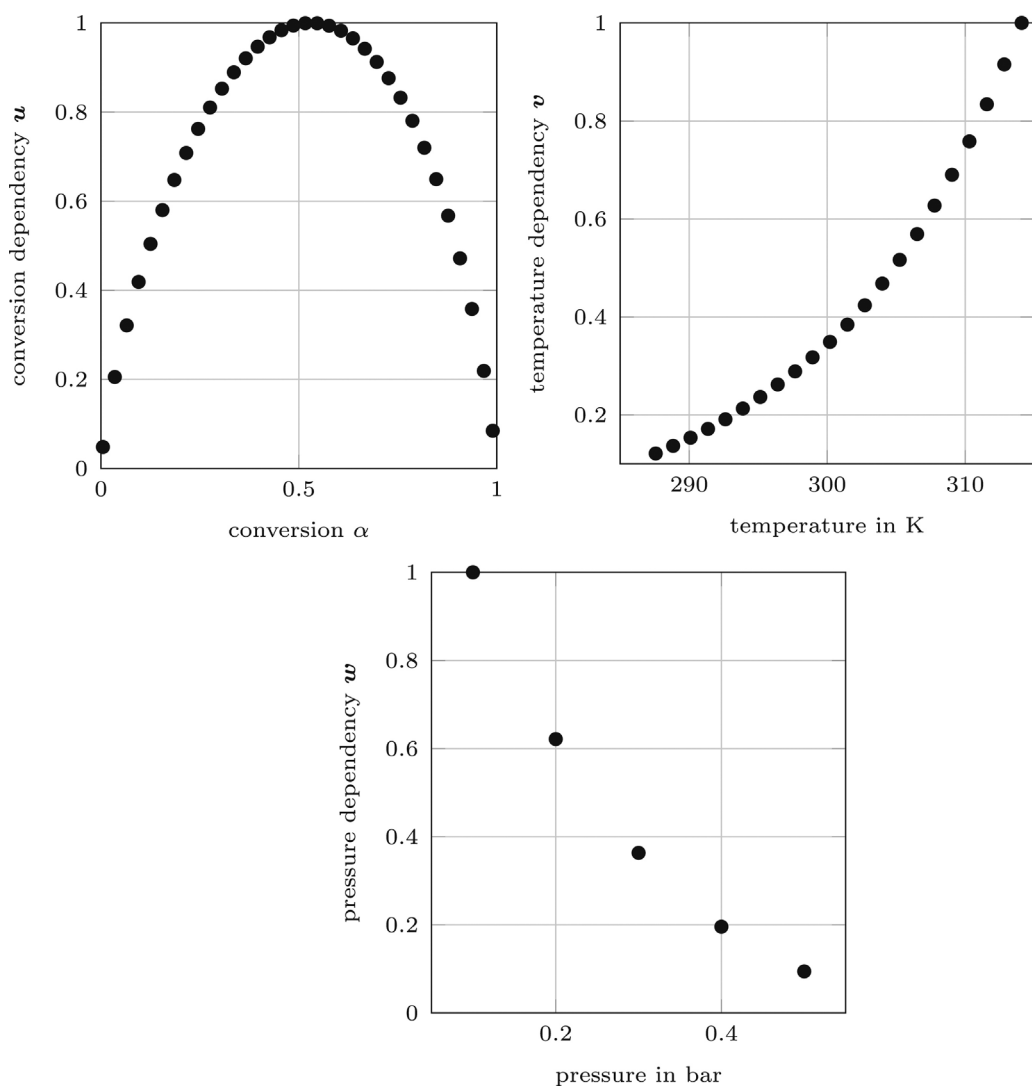


Fig. 4. Normalized dependency vectors  $u$  (left),  $v$  (middle) and  $w$  (right) for the example reaction ( $s = 0.1008$ ).

**Table 3**  
Goodness of fit values of the five best fitting conversion models for the example reaction.

Model ID	$R^2$	$p$
A1	0.9998	
A3	0.9648	1.000
B1	0.9468	1.000
A2	0.6914	1.000
A5	0.1042	1.000

By fitting the function to the data (see Fig. 7) the Arrhenius parameters can be calculated as  $A = 7.44 \cdot 10^8$  1/s and  $E_a = 59.2$  kJ/mol. As with the results of the two prior identification steps these values are very accurate. Even though the difference between the identified and the original Arrhenius parameter might seem quite big, it has to be kept in mind that this type of logarithmic fit is very insensitive to a change of the pre-exponential factor.

As a final verification step the simulated measurements that have been used as input for the method will be reproduced. First, to demonstrate the efficacy of combined pressure-temperature NPK decomposition only the identified dependency vectors given in Fig. 4 are used. Second, the derived model equations from this section are used to show that the method is a useful tool for kinetic model identification. Figs. 8 and 9 show the simulated measurements with the initial model (blue), the dependency vectors (green) and the identified model (red). Both,

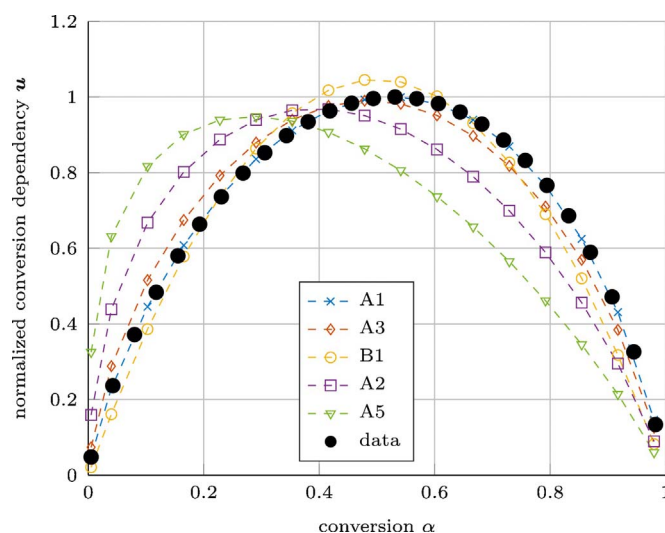


Fig. 5. Identified conversion dependency vector  $u$  for the example reaction with fitted conversion models according to Table 1.

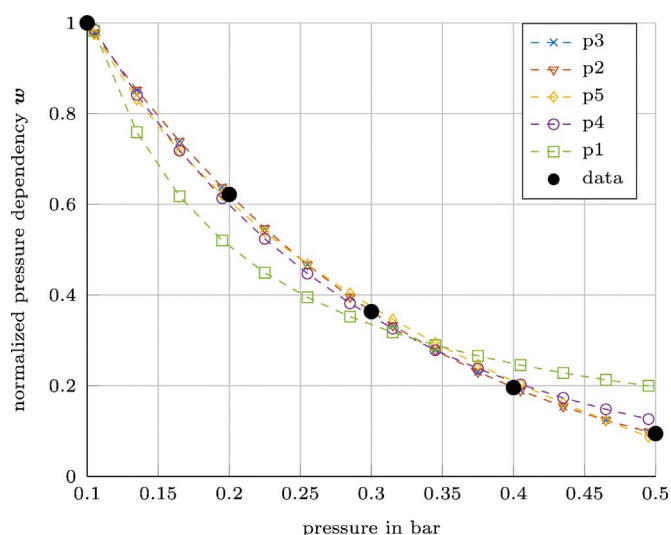


Fig. 6. Identified pressure dependency vector  $w$  for the example with fitted pressure models according to Table 2. The difference of models p2 and p3 is within the range of numerical error, therefore they cannot be distinguished in this plot.

Table 4  
Goodness of fit values of the pressure dependency models for the example reaction.

Model ID	$R^2$	$P$
p3	1.0000	
p2	1.0000	0.066
p5	0.9987	0.999
p4	0.9966	0.999
p1	0.9460	1.000

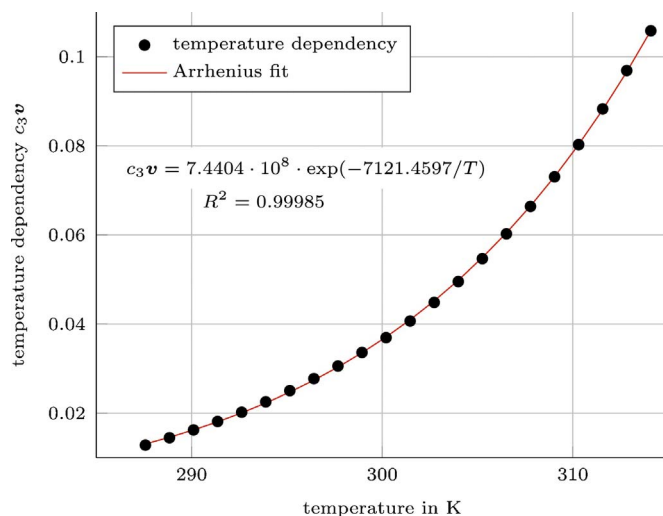


Fig. 7. Temperature dependency vector  $c_3v$  of the example reaction with Arrhenius fit.

the vector based and the model based simulations fit the initial data very well.

### 3. Decomposition of $\text{CdCO}_3$

#### 3.1. Measurements

To test the proposed method on real data the decomposition of  $\text{CdCO}_3$  was analyzed. This reaction follows the equation



The material used for all decomposition experiments was  $\text{CdCO}_3$

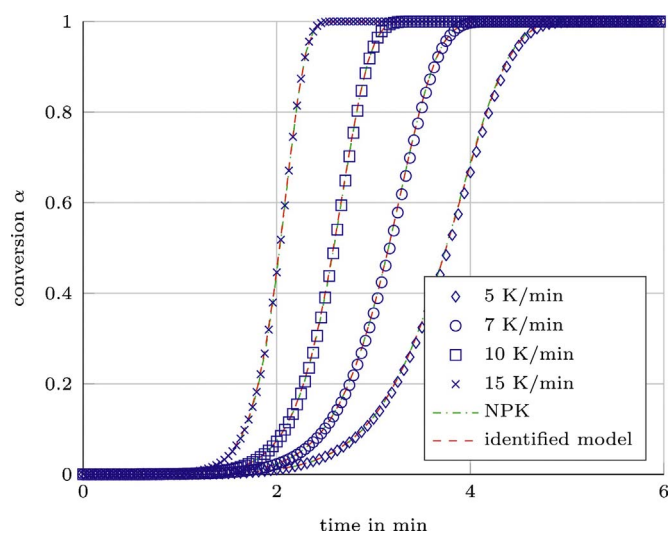


Fig. 8. Simulation result for constant heating rate measurements of the example reaction with different heating rates  $\beta$  at  $p = 0.3$  bar. (For interpretation of the references to color in text near the reference citation, the reader is referred to the web version of this article.)

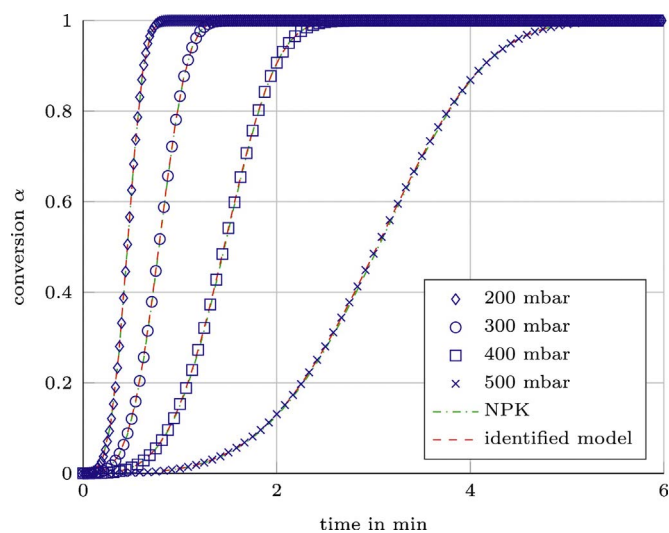


Fig. 9. Simulation result for isothermal measurements of the example reaction at different pressures at  $T = 310$  K. (For interpretation of the references to color in text near the reference citation, the reader is referred to the web version of this article.)

Purissimum from Merck. For the STA measurements a fraction with a particle size between  $180 \mu\text{m}$  and  $250 \mu\text{m}$  was used.

The STA measurements were done in a Netzsch STA 449 F1 Jupiter with a differential thermal analysis (TGA-DTA) measurement setup in open Al-crucibles. The sample mass in all STA measurements was  $5 \pm 0.05$  mg  $\text{CdCO}_3$ .

To identify the temperature dependency  $k(T)$  constant heating rate measurements with different heating rates ( $\beta = 2, 5, 7, 10$  and  $15$  K/min) at a constant  $\text{CO}_2$  partial pressure  $p_{\text{CO}_2} = 100$  mbar were performed. To identify the pressure dependency  $h(p)$  isothermal experiments were performed: The sample was heated under  $\text{CO}_2$  atmosphere ( $p_{\text{CO}_2} = 1$  bar) at a rate of  $10$  K/min up to the measurement temperature. When a constant sample temperature was reached, the atmosphere was switched to a  $\text{CO}_2/\text{N}_2$  mixture to induce the decomposition. The measurements were performed at  $633$  K with  $\text{CO}_2$  partial pressures of  $25, 50, 100, 150$  and  $200$  mbar. The partial pressure of  $\text{N}_2$  was chosen in a way that the total pressure was always  $1$  bar. Fig. 10 shows typical measurement curves for constant heating rate and isothermal measurements.

The conversion  $\alpha$  can be calculated from the mass signal  $m(t)$  as

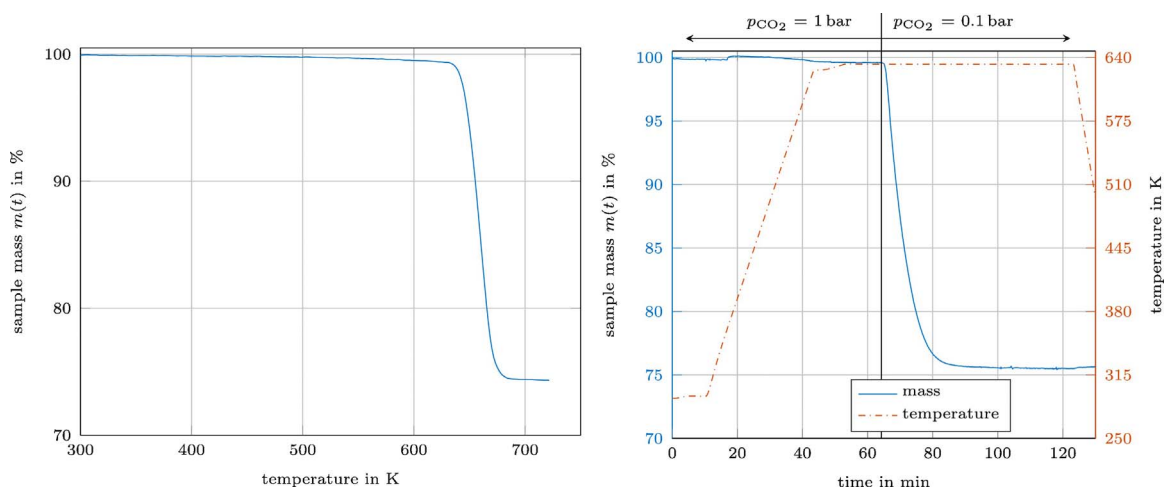


Fig. 10. Representative measurement curves in the STA for kinetic analysis. left: constant heating rate measurement with  $\beta = 10$  K/min and  $p_{\text{CO}_2} = 100$  mbar, right: isothermal measurement with  $T = 633$  K and atmosphere change from  $p_{\text{CO}_2} = 1$  bar to  $p_{\text{CO}_2} = 100$  mbar.

$$\alpha(t) = \frac{m_0 - m(t)}{m_0 - m_\infty} \tag{21}$$

where  $m_0$  is the initial sample mass,  $m(t)$  is the sample mass at time  $t$  and  $m_\infty$  is the sample mass at the end of the decomposition. XRD analyses of the material after STA measurements were performed to confirm full conversion.

### 3.2. Model identification

The procedure to decompose the measurement data into dependency vectors is the same as described in the previous section. The data lie in the  $T$ - $p_{\text{CO}_2}$ - $\alpha$ -space. Within this space, the measurements to identify the temperature dependency lie on an isobaric pane and the measurements to identify the pressure dependency lie on an isothermal

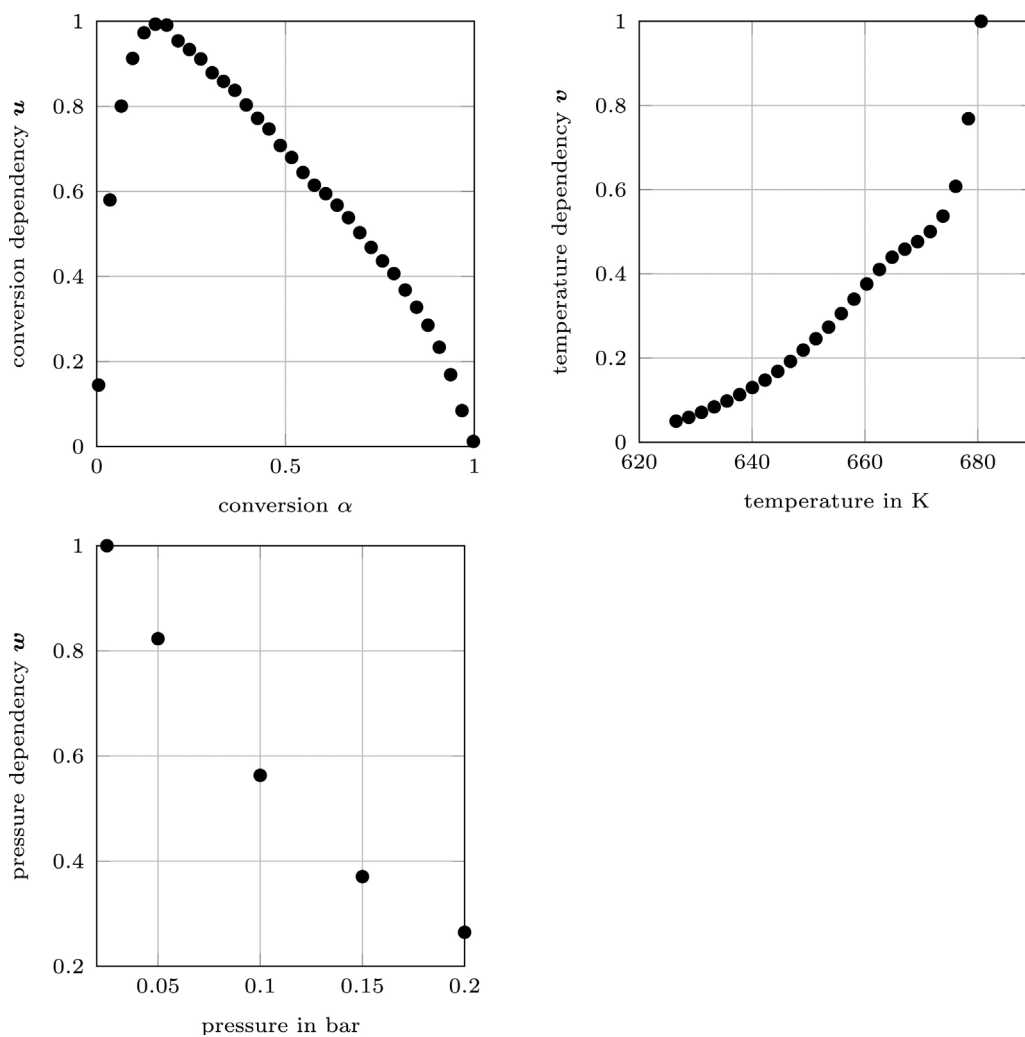


Fig. 11. Normalized dependency vectors  $u$  (left),  $v$  (middle) and  $w$  (right) for the decomposition of  $\text{CdCO}_3$  ( $s = 0.455$ ).



pane. The measurements were performed in such a way that the panes intersect at  $T = 633$  K and  $p_{\text{CO}_2} = 100$  mbar (see Fig. 3).

The identified dependency vectors are shown in Fig. 11. Their combination resulted in a scaling factor  $s = 0.455$ . The applicability of the rank-1 approximation was checked at each identification step.

The conversion dependency vector  $\mathbf{u}$  was taken from the pressure dependency identification step. This was done, because the measurements for the pressure dependency are performed under isothermal conditions. Thus, reducing possible error sources, due to heat transfer effects within the sample during constant heating rate measurements.

To derive model equations, the fitting procedure described in Section 2.4 has been applied to the identified dependency vectors.

The conversion dependency vector  $\mathbf{u}$  and the five best fitting models from Table 1 are plotted in Fig. 12. Table 5 shows the corresponding statistical results. Based on the  $p$ -values it can be seen that the  $F$ -test unambiguously identifies the model A4 as the best fitting one. The Avrami–Erofeev nucleation models are often found to describe various decomposition reactions [23,24]. Criado et al. found that the reaction follows most likely a first order decomposition, but based on provided data the fit of the model R3 is not significantly worse [25]. Authors of both works used isothermal experiments without atmosphere change. Thus it is likely that the beginning of the reaction is not properly considered in the identification. If the fitting of the conversion models is only done for a range of  $\alpha$  between 0.2 and 1, then the R-models would result in a good fit. Mu et al. also stated that the reaction follows model R3 but did not include A-models in the identification [26].

Fig. 13 shows the identified pressure dependency vector  $\mathbf{w}$  alongside the fitted pressure models from Table 2. The statistic results are listed in Table 6. The fitting results show that all models fit the data well. Yet, from a mathematical point of view, the model p4 is to be preferred, not only because it produces the smallest error, but also because it only has one parameter. The models p3 and p2 fit the data almost equally well, but this might just be due to the higher number of degrees of freedom. This fact is taken into account by the  $F$ -test resulting in a probability of almost 100% of p4 being better than p2 and p3. It has to be noted, that model p4 has no direct physically motivated derivation, despite being used in the literature [10]. Thus we strive to present a mathematical representation of the data rather than a physically bullet proof model.

The temperature dependency vector was identified based on constant heating rate measurements at  $p_{\text{CO}_2} = 100$  mbar. The result is shown in Fig. 14. It can be seen that there is a clear deviation from the typical Arrhenius form of the temperature dependency. Thus, an interaction effect between the temperature and another factor is expected.

### 3.3. Investigation of the interaction effect

To further investigate, the constant heating rate experiments for the determination of the temperature dependency were repeated in inert  $\text{N}_2$  atmosphere ( $p_{\text{CO}_2} \leq 10^{-5}$  bar). By comparing the resulting plot (Fig. 15) with the one at  $p_{\text{CO}_2} \leq 100$  mbar two observations can be made. First, the absence of  $\text{CO}_2$  changed the temperature dependency vector  $\mathbf{w}$ . As a result the quality of the fit increased significantly. Second, a change in the slope of the fitted linear equation is detectable. Thus, the activation energy changes as a result of the pressure change. This was also observed by Criado et al. [25]. Both observations led to the conclusion that an interaction effect between pressure and temperature exists.

The existence of an interaction effect does not violate the assumptions of the NPK method since each SVD is performed on either on an isothermal or an isobaric pane, where the interaction effect is “constant”. Only the combination of the results on multiple panes can reveal the interaction effect.

To investigate the interaction effect the pressure dependency vector  $\mathbf{w}$  was identified at different temperatures. At each temperature level the data was decomposed into a conversion dependency vector and a pressure dependency vector as described in Section 2.2. The identified

conversion dependency vectors agree extremely well as can be seen in Fig. 16. Thus an interaction effect with the conversion  $\alpha$  can be ruled out. Fig. 17 shows the identified pressure dependency vectors. It can be seen that the pressure dependency vector gets steeper at lower temperature. This can be taken into account by making the  $\chi$  parameter temperature dependent. In this work a linear temperature dependency of  $\chi$  is assumed, which is mathematically justifiable as it can be seen in Fig. 18. With this temperature dependency of  $\chi$  the pressure dependency  $h(p_{\text{CO}_2}, T)$  is given by

$$h(p_{\text{CO}_2}, T) = \exp((0.3216T + 211.7)p_{\text{CO}_2}) \quad (22)$$

with  $T$  in K and  $p_{\text{CO}_2}$  in bar.

To determine the Arrhenius parameters  $E_a$  and  $A$ , the temperature dependency vector identified in inert atmosphere is used. From this vector  $E_a$  and  $A$  can be directly determined by Eq. (3), since the pressure dependency does not contribute. This is a result of  $h(p_{\text{CO}_2} \leq 10^{-5} \text{ bar}, T) \approx 1$  regardless of the temperature  $T$ . This results in an activation energy  $E_a = 162.9$  kJ/mol and a pre exponential factor  $A = 1.11 \cdot 10^{11}$  1/s for the decomposition of  $\text{CdCO}_3$ . L'vov et al. calculated for  $E_a$  a value of 151 kJ/mol for the decomposition of  $\text{CdCO}_3$  [27], while Mu et al. measured a value of 150.5 kJ/mol [26]. For the pre exponential factor  $A$  they determined a value of  $6.67 \cdot 10^9$  1/s, but they identified a different conversion model, which is why the values are hardly comparable.

### 3.4. Validation of the identified models

In this work two models have been derived. The first model was the combination of the dependency vectors of the extended NPK method (Fig. 11). The derivation of this model was purely data driven with the only modelling assumption being the multiplicativity of the contribution of the factors. The second model is a further development of the first by identifying underlying functions in the dependency vectors. This resulted in the following function based model:

$$\frac{d\alpha}{dt} = f(\alpha)k(T)h(p_{\text{CO}_2}, T) \quad (23)$$

$$f(\alpha) = 4/3(1 - \alpha)[- \ln(1 - \alpha)]^{1/4} \quad (24)$$

$$k(T) = 1.11 \cdot 10^{11} \exp\left(\frac{-1.629 \cdot 10^5}{8.314T}\right) \quad (25)$$

$$h(p_{\text{CO}_2}, T) = \exp((-0.3216T + 211.7)p_{\text{CO}_2}) \quad (26)$$

The temperature  $T$  is in K, the pressure  $p_{\text{CO}_2}$  in bar.

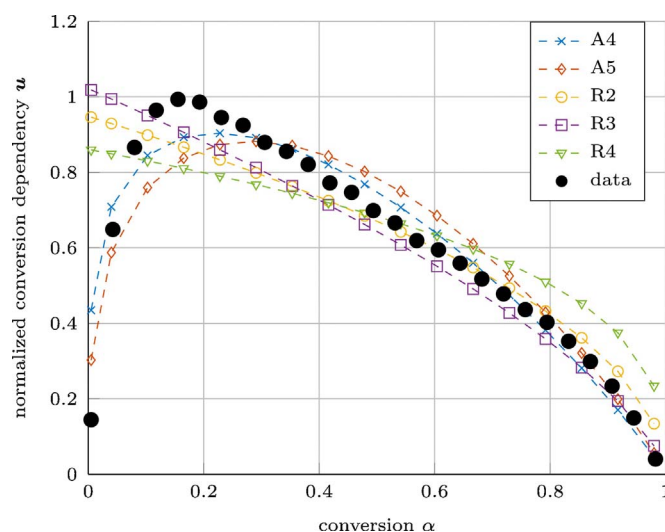
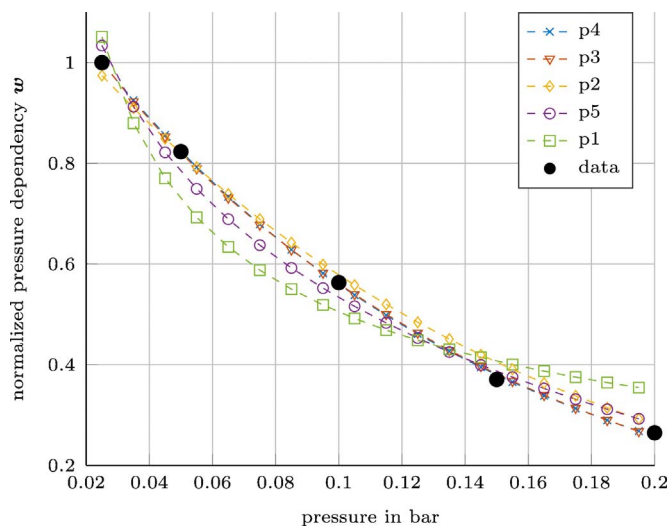


Fig. 12. Conversion dependency vector  $\mathbf{u}$  of the decomposition of  $\text{CdCO}_3$  with fitted conversion models according to Table 1.



**Table 5**  
Goodness of fit values of the five best fitting conversion models for the decomposition of CdCO<sub>3</sub>.

Model ID	R <sup>2</sup>	p
A4	0.9484	
A5	0.9045	1.000
R2	0.7722	1.000
R3	0.7320	1.000
R4	0.7101	1.000



**Fig. 13.** Pressure dependency vector *w* of the decomposition of CdCO<sub>3</sub> with fitted conversion models according to Table 2.

**Table 6**  
Statistic results of the pressure dependency fitting.

Model ID	R <sup>2</sup>	p
p4	0.9996	
p3	0.9995	1.000
p2	0.9937	1.000
p1	0.9373	0.999

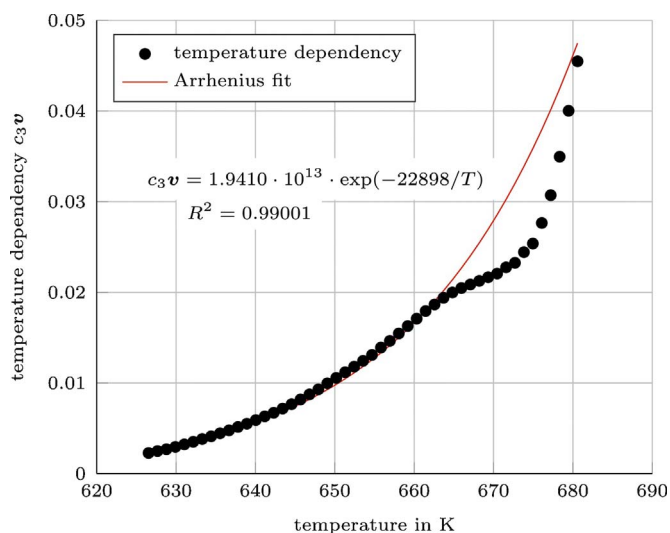


**Fig. 14.** Temperature dependency vector *c<sub>3v</sub>* from constant heating rate measurements of the CdCO<sub>3</sub> decomposition at *p*<sub>CO<sub>2</sub></sub> = 100 mbar with Arrhenius fit.

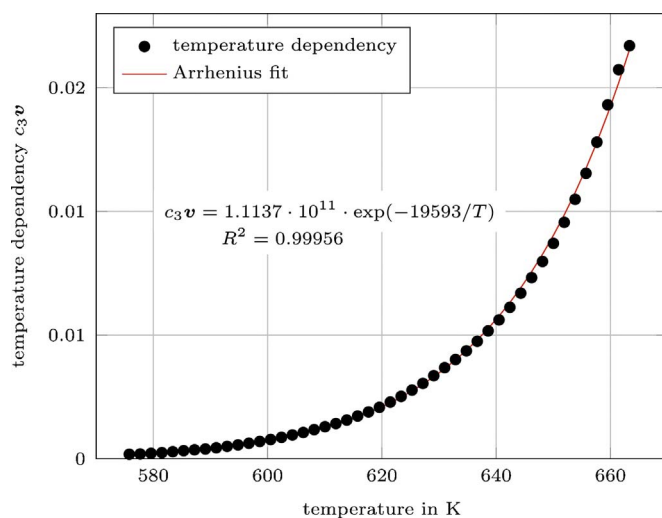


**Fig. 15.** Temperature dependency vector *c<sub>3v</sub>* from constant heating rate measurements of the CdCO<sub>3</sub> decomposition at *p*<sub>CO<sub>2</sub></sub> ≤ 10<sup>-5</sup> bar with Arrhenius fit.

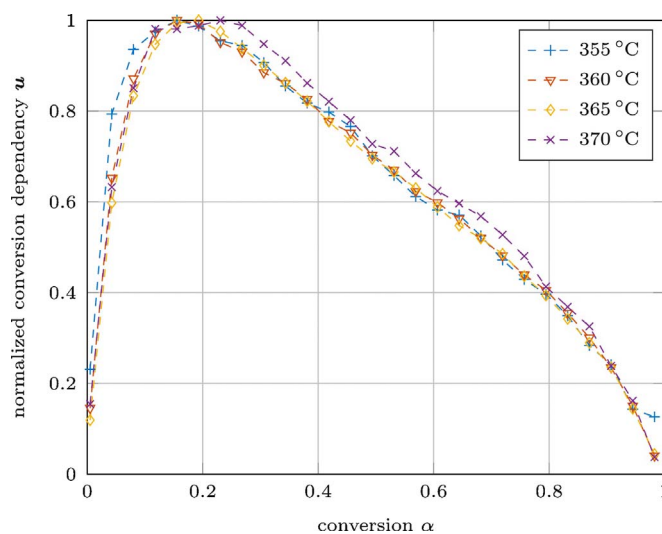


**Fig. 16.** Identified conversion dependencies at different temperature levels and *p*<sub>CO<sub>2</sub></sub> = 100 mbar.

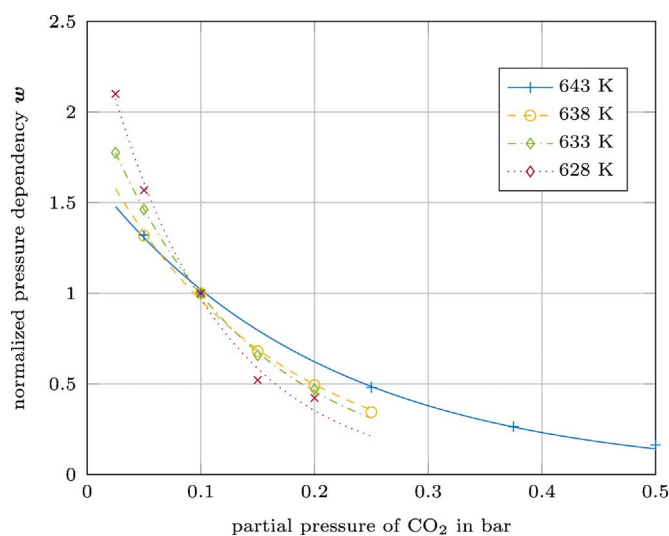


**Fig. 17.** Effect of the temperature on the pressure dependency vector *w*. All vectors were normalized at *p*<sub>CO<sub>2</sub></sub> = 100 mbar for comparison. The lines are the best fit using pressure model p4.

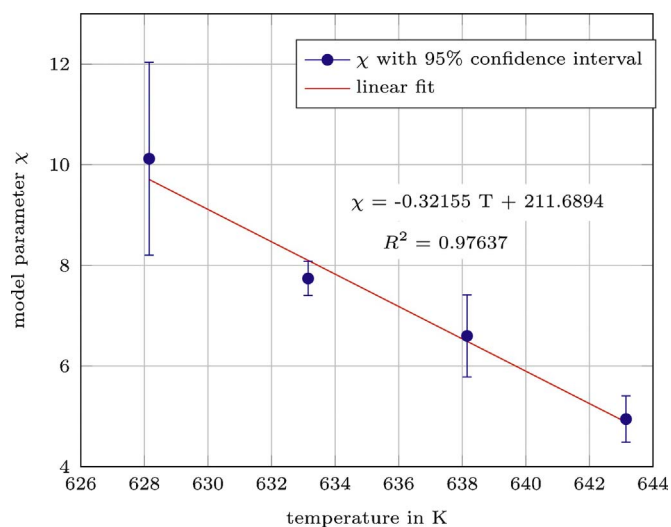


Fig. 18. Temperature dependency of the model parameter  $\chi$ . The error bars shows the 95% confidence interval of  $\chi$  as a result of the optimization.

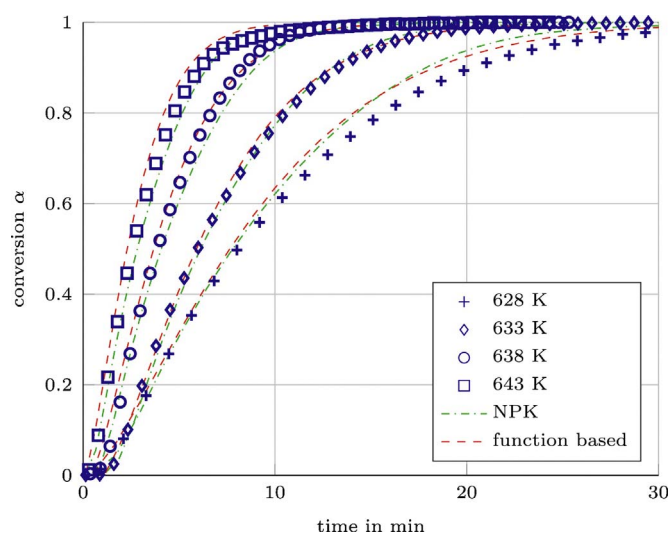


Fig. 19. Simulation result for isothermal measurements of the  $\text{CdCO}_3$  decomposition at different temperatures with  $p_{\text{CO}_2} = 100$  mbar.

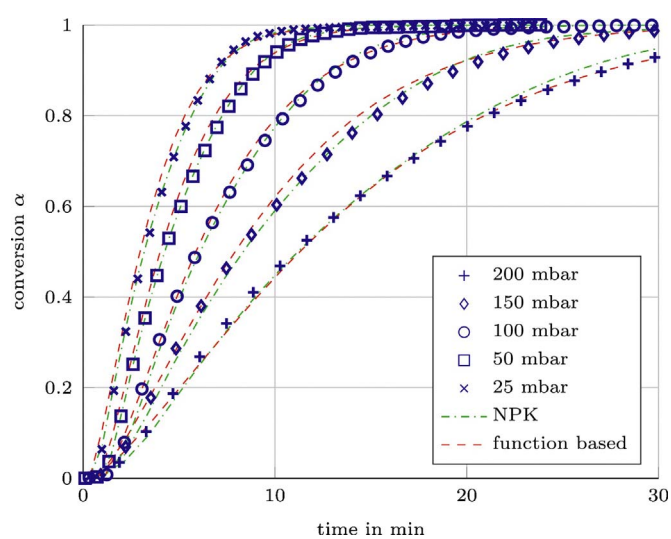


Fig. 20. Simulation result for isobaric measurements of the  $\text{CdCO}_3$  decomposition at different  $p_{\text{CO}_2}$  with  $T = 633$  K.

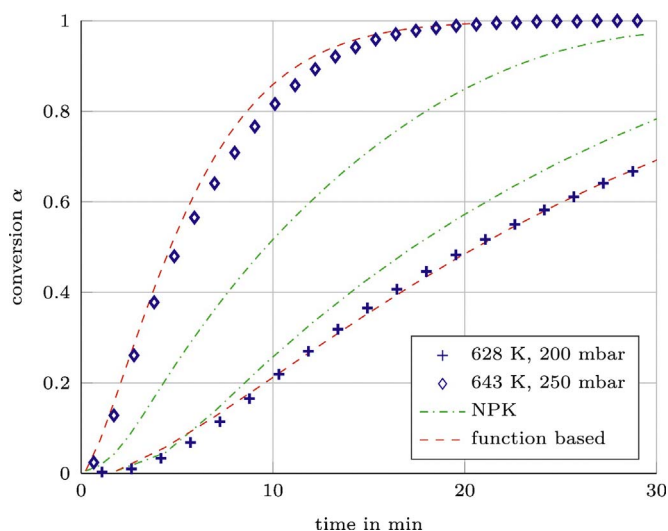


Fig. 21. Simulation result for measurements of the  $\text{CdCO}_3$  decomposition outside the identified region.

For validation of both identified models isothermal measurements at  $p_{\text{CO}_2} = 100$  mbar and isobaric measurements at  $T = 633$  K were simulated and compared to measured data. Figs. 19 and 20 show that both the vector based model (NPK) and the function based model (function based) fit the measured data for measurements that lie on the panes of the  $T$ - $p_{\text{CO}_2}$ - $\alpha$ -space, used for the identification. The simulation results for measurements outside the temperature and pressure region used for the identification show a difference between the two models (Fig. 21). The vector based model is not capable to reproduce the measurement, as the found interaction between temperature and pressure is not described by the model. The function based model shows a good agreement between the measurements and the simulation. This implies that the functions chosen to describe the dependencies and the interaction are reasonable.

#### 4. Conclusion

In this work a novel method to analyze solid-state reactions is presented. The method extends the NPK method to also identify a pressure dependency in addition to the temperature and conversion dependency. It does so by splitting a three-dimensional problem ( $\alpha$ ,  $T$ ,  $p$ ) into three one-dimensional problems, thus reducing its complexity. The method is based on the assumption that the effect of  $\alpha$ ,  $T$  and  $p$  are linked multiplicatively. By arranging measurement data in special data matrices a singular value decomposition can be utilized to approximate the underlying dependencies. The resulting vectors can be combined to build a full model or they can be further analyzed to get insight into the underlying physical processes.

To test the presented method on real data, the decomposition of  $\text{CdCO}_3$  was analyzed. Simulation with the resulting empirical model showed good agreement with the measured data. The application to real measurements also showed that the method is capable of detecting interactions between the variables. The kinetics of the decomposition was found to follow the conversion model A4, an Arrhenius temperature dependency with an activation energy  $E_a = 162.9$  kJ/mol and a pre exponential factor  $A = 1.11 \cdot 10^{11}$  1/s and pressure model p4. Furthermore the identified interaction between temperature and pressure was successfully modeled into the fit parameter of the pressure model.

#### Acknowledgments

The authors would like to thank the Austrian Research Promotion Agency (FFG) for their financial support of the projects SolidHeat

Kinetics (#848876) and SolidHeat Pressure (#853593).

## References

- [1] S. Vyazovkin, A.K. Burnham, J.M. Criado, L.A. Pérez-Maqueda, C. Popescu, N. Sbirrazzuoli, Ictac kinetics committee recommendations for performing kinetic computations on thermal analysis data, *Thermochim. Acta* 520 (1–2) (2011) 1–19, <http://dx.doi.org/10.1016/j.tca.2011.03.034> <http://www.sciencedirect.com/science/article/pii/S0040603111002152>.
- [2] K. Darkwa, A. Ianakiev, P.W. O'Callaghan, Modelling and simulation of adsorption process in a fluidised bed thermochemical energy reactor, *Appl. Thermal Eng.* 26 (8–9) (2006) 838–845, <http://dx.doi.org/10.1016/j.applthermaleng.2005.10.008> <http://www.sciencedirect.com/science/article/pii/S1359431105003303>.
- [3] A. Khawam, D.R. Flanagan, Solid-state kinetic models: basics and mathematical fundamentals, *J. Phys. Chem. B* 110 (35) (2006) 17315–17328, <http://dx.doi.org/10.1021/jp06>.
- [4] C.F. Dickinson, G.R. Heal, Solid–liquid diffusion controlled rate equations, *Thermochim. Acta* 340–341 (1999) 89–103, [http://dx.doi.org/10.1016/S0040-6031\(99\)00256-7](http://dx.doi.org/10.1016/S0040-6031(99)00256-7) <http://www.sciencedirect.com/science/article/pii/S0040603199002567>.
- [5] M. Barret Pierre, Expression théorique en fonction de la pression de la loi de vitesse de croissance d'une solide, *Comptes rendus hebdomadaires des séances de l'Académie des sciences. Série C, Sci. Chim.* 266 (1968) 856–859.
- [6] A.W. Searcy, D. Beruto, Kinetics of endothermic decomposition reactions: 2. Effects of the solid and gaseous products, *J. Phys. Chem.* 82 (1978) 163–167.
- [7] M. Reading, D. Dollimore, R. Whitehead, The measurement of meaningful kinetic parameters for solid state decomposition reactions, *J. Thermal Anal.* 37 (9) (1991) 2165–2188, <http://dx.doi.org/10.1007/BF01905585>.
- [8] A.K. Burnham, R.K. Weese, A.P. Wemhoff, J.L. Maienschein, A historical and current perspective on predicting thermal cookoff behavior, *J. Thermal Anal. Calorim.* 89 (2) (2007) 407–415, <http://dx.doi.org/10.1007/s10973-006-8161-6>.
- [9] C.K. Clayton, K.J. Whitty, Measurement and modeling of decomposition kinetics for copper oxide-based chemical looping with oxygen uncoupling, *Appl. Energy* 116 (2014) 416–423, <http://dx.doi.org/10.1016/j.apenergy.2013.10.032> <http://www.sciencedirect.com/science/article/pii/S0306261913008520>.
- [10] J. Khinast, G.F. Krammer, C. Brunner, G. Staudinger, Decomposition of limestone: the influence of CO<sub>2</sub> and particle size on the reaction rate, *Chem. Eng. Sci.* 51 (4) (1996) 623–634, [http://dx.doi.org/10.1016/0009-2509\(95\)00302-9](http://dx.doi.org/10.1016/0009-2509(95)00302-9) <http://www.sciencedirect.com/science/article/pii/0009250995003029>.
- [11] R. Serra, J. Sempere, R. Nomen, A new method for the kinetic study of thermo-analytical data: the non-parametric kinetics method, *Thermochim. Acta* 316 (1) (1998) 37–45, [http://dx.doi.org/10.1016/S0040-6031\(98\)00295-0](http://dx.doi.org/10.1016/S0040-6031(98)00295-0) <http://www.sciencedirect.com/science/article/pii/S0040603198002950>.
- [12] R. Serra, R. Nomen, J. Sempere, The non-parametric kinetics a new method for the kinetic study of thermoanalytical data, *J. Thermal Anal. Calorim.* 52 (3) (1998) 933–943, <http://dx.doi.org/10.1023/A:1010120203389>.
- [13] J. Sempere, R. Nomen, R. Serra, Progress in non-parametric kinetics, *J. Thermal Anal. Calorim.* 56 (2) (1999) 843–849, <http://dx.doi.org/10.1023/A:1010178827890>.
- [14] J. Sempere, R. Nomen, R. Serra, J. Soravilla, The npk method: an innovative approach for kinetic analysis of data from thermal analysis and calorimetry, *Thermochim. Acta* 388 (1–2) (2002) 407–414, [http://dx.doi.org/10.1016/S0040-6031\(02\)00037-0](http://dx.doi.org/10.1016/S0040-6031(02)00037-0) <http://www.sciencedirect.com/science/article/pii/S0040603102000370>.
- [15] G.R. Heal, A generalisation of the non-parametric, npk (svd) kinetic analysis method: Part 1. isothermal experiments, *Thermochim. Acta* 426 (1–2) (2005) 15–21, <http://dx.doi.org/10.1016/j.tca.2004.07.004> <http://www.sciencedirect.com/science/article/pii/S004060310400293X>.
- [16] G.R. Heal, A generalisation of the non-parametric, npk (svd) kinetic analysis method: Part 2. non-isothermal experiments, *Thermochim. Acta* 426 (1–2) (2005) 23–31, <http://dx.doi.org/10.1016/j.tca.2004.07.003>.
- [17] J.H. Flynn, L.A. Wall, A quick, direct method for the determination of activation energy from thermogravimetric data, *J. Polym. Sci. B: Polym. Lett.* 4 (5) (1966) 323–328, <http://dx.doi.org/10.1002/pol.1966.110040504>.
- [18] J.H. Flynn, L.A. Wall, General treatment of the thermogravimetry of polymers, *J. Res. Nat. Bur. Stand.* 70 (6) (1966) 487–523.
- [19] T. Ozawa, A new method of analyzing thermogravimetric data, *Bull. Chem. soc. Jpn.* 38 (11) (1965) 1881–1886.
- [20] H.E. Kissinger, Variation of peak temperature with heating rate in differential thermal analysis, *J. Res. Natl. Bureau Stand.* 57 (4) (1956) 217–221.
- [21] H.E. Kissinger, Reaction kinetics in differential thermal analysis, *Anal. Chem.* 29 (11) (1957) 1702–1706 <https://www.scopus.com/inward/record.uri?eid=2-s2.0-33749213901&partnerID=40&md5=5e0322a3789a252fd913d0ec69d70a11>.
- [22] G.H. Golub, C. Reinsch, Singular value decomposition and least squares solutions, *Numer. Math.* 14 (5) (1970) 403–420, <http://dx.doi.org/10.1007/BF02163027>.
- [23] J. Graetz, J.J. Reilly, Decomposition kinetics of the alh<sub>3</sub> polymorphs, *J. Phys. Chem. B* 109 (47) (2005) 22181–22185, <http://dx.doi.org/10.1021/jp0546960>.
- [24] S. Wang, Q. Gao, J. Wang, Thermodynamic analysis of decomposition of thiourea and thiourea oxides, *J. Phys. Chem. B* 109 (36) (2005) 17281–17289, <http://dx.doi.org/10.1021/jp051620v>.
- [25] J.M. Criado, M. González, M. Macias, Influence of CO<sub>2</sub> pressure on the kinetics of thermal decomposition of cdco<sub>3</sub>, *Thermochim. Acta* 113 (1987) 31–38, [http://dx.doi.org/10.1016/0040-6031\(87\)88304-1](http://dx.doi.org/10.1016/0040-6031(87)88304-1).
- [26] J. Mu, D.D. Perlmutter, Thermal decomposition of carbonates, carboxylates, oxalates, acetates, formates, and hydroxides, *Thermochim. Acta* 49 (2) (1981) 207–218, [http://dx.doi.org/10.1016/0040-6031\(81\)80175-X](http://dx.doi.org/10.1016/0040-6031(81)80175-X).
- [27] B.V. L'vov, Mechanism and kinetics of thermal decomposition of carbonates, *Thermochim. Acta* 386 (1) (2002) 1–16, [http://dx.doi.org/10.1016/S0040-6031\(01\)00757-2](http://dx.doi.org/10.1016/S0040-6031(01)00757-2).

**Article type: Communication****Title: Calcium Doping Facilitates Water Dissociation in Magnesium Oxide**

*Danny Müller\*, Christian Knoll, Thomas Ruh, Werner Artner, Jan M. Welch, Herwig Peterlik, Elisabeth Eitenberger, Gernot Friedbacher, Michael Harasek, Peter Blaha, Klaudia Hradil, Andreas Werner, Peter Weinberger*

Dr. Danny Müller, Christian Knoll, Priv.Do. Peter Weinberger  
Institute of Applied Synthetic Chemistry, TU Wien  
Getreidemarkt 9/163-AC, A-1060 Vienna, Austria  
E-mail: danny.mueller@tuwien.ac.at  
Christian Knoll, Prof. Michael Harasek  
Institute of Chemical, Environmental & Biological Engineering, TU Wien  
Getreidemarkt 9/166, A-1060 Vienna, Austria  
Thomas Ruh, Prof. Peter Blaha  
Institute of Materials Chemistry, TU Wien  
Getreidemarkt 9/165, A-1060 Vienna, Austria  
Werner Artner, Dr. Klaudia Hradil  
X-Ray Center, TU Wien  
Getreidemarkt 9, A-1060 Vienna, Austria  
Dr. Jan M. Welch  
Atominstitut, TU Wien  
Stadionallee 2, 1020 Vienna, Austria  
Prof. Herwig Peterlik  
Faculty of Physics, University of Vienna  
Boltzmannngasse 5, 1090 Vienna, Austria  
Elisabeth Eitenberger, Prof. Gernot Friedbacher  
Institute of Chemical Technologies and Analytics, TU Wien  
Getreidemarkt 9/164, A-1060 Vienna, Austria  
Prof. Andreas Werner  
Institute for Energy Systems and Thermodynamics, TU Wien  
Getreidemarkt 9/302, A-1060 Vienna, Austria

**Keywords:** water dissociation, magnesium oxide, calcium doping, thermochemical energy storage

**Abstract:**

Calcium doping of magnesium oxide results in significantly increased water dissociation rates, thus enhancing both hydration rate and reaction completeness of hydration compared to pure MgO. For a series of mixed magnesium-calcium oxides ( $\text{Mg}_x\text{Ca}_{1-x}\text{O}$ ) with varying Ca-contents between 0 and 40 % the material of a composition  $\text{Mg}_{0.9}\text{Ca}_{0.1}\text{O}$  shows the fastest

rehydration, transforming completely within 80 minutes to the mixed hydroxide. In consecutive dehydration / rehydration cycles reasonable cycle stability is found. A “regeneration” of the aged material (reactivity reduced by excessive cycling) in liquid water re-establishes the initial rehydration reactivity. Density Functional Theory (DFT) calculations support the experimental findings, confirming that calcium doping can reduce the energy of the rate limiting water dissociation reaction exploiting both electronic and steric (size) effects.

Three major requirements for future sustainable energy management have been established including reduction of greenhouse gas emissions, promotion and increased use of renewable energy sources, and enhancing the efficiency of energy use.<sup>[1, 2]</sup> Whereas the first two issues are widely discussed and the subject of international treaties such as the Kyoto protocol<sup>[3]</sup> and the Paris-agreement,<sup>[4]</sup> awareness of the poor overall-efficiency of today’s energy economy is rather limited. Heat is the most ubiquitously used form of energy, including in electricity generation, power plants or industry.<sup>[5]</sup> In this context, in 2011, the International Energy Agency (IEA) estimated in a report entitled “Solutions for a low-carbon energy future” that global energy loss through waste heat accounts for 2/3 of the overall energy production.<sup>[6]</sup> Therefore, methods suitable for reduction of waste heat or reutilization thereof could contribute significantly to a sustainable energy management.<sup>[7-9]</sup>

Among the different approaches to this challenge, thermochemical energy storage (TCES) is a highly appealing concept, since by means of a reversible chemical reaction a suitable material energy is converted from thermal to chemical energy. The charged material may be stored for any period of time without further losses or additional infrastructure (such as insulation), until, by addition of the proper reactant, the discharging reaction, releasing the stored energy in form of heat, is initiated.<sup>[2, 10-12]</sup> The economic benefit of implementing TCES-cycles in the energy management was demonstrated by several economic feasibility studies, illustrating



that *e.g.* with the waste heat from Lenzing AG,<sup>[13]</sup> the complete district heating for the Austrian city of Salzburg could be supplied.<sup>[14]</sup>

Materials for a technological implementation of TCES processes should be cheap, highly cycle stable, show fast reaction kinetics and be completely reversible. Mg(OH)<sub>2</sub> undergoes reversible calcination and hydration and is readily available in large quantities. With calcination temperatures between 350 °C and 450 °C it is also compatible with many industrial waste heat sources.<sup>[15, 16]</sup> Although the Mg(OH)<sub>2</sub> / MgO TCES cycle is well known,<sup>[15, 17-20]</sup> low cycle stability and incomplete hydration impede application. In literature different efforts were made to improve the reactivity and thermal conductivity of the material by addition of lithium-salts<sup>[21-23]</sup> increasing the reaction rate, and the preparation of composite materials with expanded graphite.<sup>[20, 24-26]</sup> The issue of limited reactivity and low cycle stability is mainly related to the kinetic inhibition of the critical dissociation of water on the MgO surface.<sup>[27]</sup> Interestingly, for the isostructural CaO\* the water dissociation is comparably favorable,<sup>[27]</sup> leading to rapid and complete hydroxide formation on contact with water. To improve the rates of water dissociation during MgO hydration, a series of Ca<sup>2+</sup> doped MgO materials was prepared to investigate the influence of variable amounts of calcium on the kinetic barrier of water dissociation during MgO hydration.

Mixed Mg<sub>1-x</sub>Ca<sub>x</sub>(OH)<sub>2</sub> was obtained by precipitation of the hydroxide from an aqueous solution of MgCl<sub>2</sub>·6H<sub>2</sub>O and 0 - 40 mol % CaCl<sub>2</sub>·6H<sub>2</sub>O with NaOH<sup>†</sup>. After calcination at 375 °C, the Mg<sub>1-x</sub>Ca<sub>x</sub>O samples were rehydrated with steam, while monitoring for reaction progress and completeness by *in-situ* powder X-Ray diffraction (for details see SI). As reference material, a sample of commercially available Mg(OH)<sub>2</sub> calcined under the same conditions as the Mg<sub>1-x</sub>Ca<sub>x</sub>O was used (**Figure 1a**). After 2 hours of rehydration a maximum

---

\* Ca(OH)<sub>2</sub> / CaO as thermochemical storage material is well known, but due to the required calcination temperatures around 600 °C much more restricted regarding its scope of application.<sup>[28, 29]</sup>

† All experimental details are given in the supporting information. The exact Mg-Ca ratios were determined by X-Ray fluorescence analysis (**table S1**).

conversion of 42.8 % was found, which decreased within the next 5 consecutive cycles to a final yield of 4.4 % Mg(OH)<sub>2</sub>. From **Figure 1b** the advantageous effect of the Ca doping is clear, since for all experimentally investigated Ca-doped oxides a significantly higher rehydration rate is observed. The fastest reaction rate was found for Mg<sub>0.9</sub>Ca<sub>0.1</sub>O for which, after 80 minutes, the oxide was completely converted to the mixed hydroxide. For larger Ca amounts the final conversion decreased slightly to roughly 80 % hydroxide phase after 120 minutes. These experiments were readily reproducible, both on the same batch of material, as well as on newly prepared samples, as in all cases for repeated rehydration experiments highly comparable rehydration rates were found.

As observed for the MgO reference material, the conversion of Mg<sub>1-x</sub>Ca<sub>x</sub>O showed a decrease through multiple calcination-rehydration cycles (**Figure 1c**). The reason for the decreased reactivity of the pure MgO was attributed to its smaller primary crystallite size, as well as to a notable tendency toward agglomeration, resulting in a very compact assembly encumbering the transport of H<sub>2</sub>O molecules to the reactive surface. To better understand this effect on a nanometric scale, small angle X-Ray scattering (SAXS) was used. For this purpose, freshly synthesized material, its calcined oxide, as well as a sample after six cycles were compared for both pure commercial Mg(OH)<sub>2</sub> and Mg<sub>0.8</sub>Ca<sub>0.2</sub>(OH)<sub>2</sub>.

The SAXS-patterns (**Figure 2a**) were described by a model combining the unified scattering function of Beaucage<sup>[30]</sup> (resulting in a radius of gyration  $R_g$  and a fractal dimension  $d_f$ ) with a packing factor from a hard sphere model,<sup>[31, 32]</sup> describing the agglomeration of units (distance  $R_{HS}$  and hard sphere volume ratio  $\eta$ ). The most striking differences are the larger size of Mg<sub>0.8</sub>Ca<sub>0.2</sub>O ( $R_g = 3.2$  nm,  $R_{HS} = 5.0$  nm) in comparison to MgO ( $R_g = 1.8$  nm,  $R_{HS} = 2.6$  nm), as well as the larger hard sphere volume ratio ( $\eta = 0.18$ ) for MgO in comparison to Mg<sub>0.8</sub>Ca<sub>0.2</sub>O ( $\eta = 0.01$ ). This confirms the greater degree of agglomeration of the units in MgO than for Mg<sub>0.8</sub>Ca<sub>0.2</sub>O. After six consecutive calcination / rehydration cycles, the former

agglomerates were decomposed due to the notable volume work associated with the  $\text{Mg}(\text{OH})_2$  /  $\text{MgO}$  transformation, but the size of the units remains smaller for  $\text{MgO}$  ( $R_g = 3.6$  nm for  $\text{MgO}$ ,  $R_g = 4.9$  nm for  $\text{Mg}_{0.8}\text{Ca}_{0.2}\text{O}$ ). The fractal dimension of  $\text{MgO}$  is  $d_f = 3.5$ , showing a more compact structure with a rough surface, whereas  $d_f = 2.75$  for  $\text{Mg}_{0.8}\text{Ca}_{0.2}\text{O}$ , is typical for a mass fractal, i.e. a completely transformed structure of a broad size variation. To establish the effect liquid water rehydration would have on the material, the kinetics of the conversion to hydroxides was measured by immersion of the samples in an excess of water under ambient conditions with *in-situ* SAXS for a freshly calcined sample of commercial  $\text{MgO}$  and  $\text{Mg}_{0.8}\text{Ca}_{0.2}\text{O}$  (**Figure 2b**). Both materials feature complete rehydration to the corresponding hydroxide, for pure  $\text{MgO}$  within two hours and within four hours for  $\text{Mg}_{0.8}\text{Ca}_{0.2}\text{O}$ . The conversion rate was calculated from the intensity difference to the fully converted material after 24 hours in water.

Based on the finding that liquid water is highly efficient in dispersing agglomerates, a regeneration process for  $\text{Mg}_{1-x}\text{Ca}_x\text{O}$  hydrating the less reactive material for 24 hours in liquid water was established. Experiments with “spent” material after 6 consecutive calcination / rehydration cycles, calcined again and subsequently rehydrated in liquid water were highly promising, as the initial reactivity of the material could be restored. In **Figure 1d** the rehydration rate of  $\text{Mg}_{0.9}\text{Ca}_{0.1}\text{O}$  is shown during the 1<sup>st</sup> and 2<sup>nd</sup>, 7<sup>th</sup> and 8<sup>th</sup>, (after 1<sup>st</sup> regeneration) and 13<sup>th</sup> and 14<sup>th</sup> cycle (after 2<sup>nd</sup> regeneration), all of them being highly comparable and complete. A complete hydration cycle is shown in **Figure S1**. From an economic point of view such a regeneration of inactive material extending the duration of use is highly desirable, as material life time and efficiency are relevant parameters for the cost-effectiveness of a TCES-process.

Although the samples containing greater than 10 % Ca could be rapidly calcined and rehydrated, a second aspect should be considered: For all samples up to 10 % Ca content only the mixed  $\text{Mg}_{1-x}\text{Ca}_x(\text{OH})_2$  phase was identified (refined against  $\text{Mg}(\text{OH})_2$ ) in the P-XRD,

whereas for higher Ca-contents the miscibility is exceeded and  $\text{Ca(OH)}_2$  is identified as an independent secondary phase (**Figure S2**, **Table S1**). These phase compositions were reproducible, although, in one case, contamination of the  $\text{Mg}_{0.9}\text{Ca}_{0.1}(\text{OH})_2$  phase 0.8 % of  $\text{Ca(OH)}_2$  was found. Calcination at 375 °C decomposes only the  $\text{Mg}_{1-x}\text{Ca}_x(\text{OH})_2$  phase, whereas the  $\text{Ca(OH)}_2$  is left unaffected. Therefore, for materials with a secondary  $\text{Ca(OH)}_2$  phase, the calculated rehydration of the  $\text{Mg}_{1-x}\text{Ca}_x\text{O}$  needs to be corrected for inert  $\text{Ca(OH)}_2$  when calculating values for overall-conversion of the material (**Table S1**). Apart from a lower overall conversion, it is imperative, from a technological point of view, to prevent the introduction of an excessive amount of inactive material.

The formation of a Ca enriched  $\text{Mg}_{1-x}\text{Ca}_x\text{O}$  phase, seeing as MgO and CaO are immiscible up to 1900 K,<sup>[33]</sup> may be explained by the origin of the material from a coprecipitated hydroxide phase. The structures of  $\text{Mg(OH)}_2$  and  $\text{Ca(OH)}_2$ , as well of MgO and CaO are isotypic, differing only in the lattice constants due to the larger ionic radius of  $\text{Ca}^{2+}$  ( $\text{Mg}^{2+}$  0.86 Å,  $\text{Ca}^{2+}$  1.14 Å).<sup>[34]</sup> According to the Rietveld refinement of P-XRD data (**Figure S3**), in the case of the hydroxides it is possible to exchange  $\text{Ca}^{2+}$  on  $\text{Mg}^{2+}$ -positions for a doping up to 10 mol%  $\text{Ca}^{2+}$ , with an accompanying lattice parameter expansion of up to 0.06 % for all lattice parameters, as shown in **Figure 3**. These results agree perfectly with a previous report on  $\text{Mg}_{1-x}\text{Ca}_x\text{O}$  samples obtained by chemical vapor deposition (CVC).<sup>[20]</sup> Whereas in the case of the CVD-preparation samples doped with greater than 12 % Ca lead to a segregation of  $\text{Ca}^{2+}$  on the surface,<sup>[35]</sup> co-precipitation of mixtures of greater than 10 mol %  $\text{Ca}^{2+}$  results in the formation of a  $\text{Ca(OH)}_2$ -phase within the precipitated material. As the mixed  $\text{Mg}_{1-x}\text{Ca}_x\text{O}$ -phase is obtained by calcination at relatively low temperatures, any diffusion-driven exsolution by phase-separation – as expected due to the immiscibility of the oxides<sup>[33]</sup> – is prevented. The origin of the materials as precipitated mixed hydroxides is also apparent under the scanning electron microscope (SEM). For all  $\text{Mg}_{1-x}\text{Ca}_x\text{O}$  samples the hexagonal platelet

shape of brucite is retained. For the mixed oxide, increasing  $\text{Ca}^{2+}$ -content results in decreasing particle size (**Figure S4**).

All  $\text{Ca}^{2+}$ -doped magnesium oxide samples show very similar thermal decomposition behavior and are completely dehydrated at 375 °C. The decomposition temperature of the mixed hydroxides deviates by only  $\sim 15$  °C from pure  $\text{Mg}(\text{OH})_2$  (**Figure S5**).<sup>‡</sup>

The impact of the  $\text{Ca}^{2+}$  dopant on the rate of the water dissociation on calcination may be attributed both to electronic and steric (size) effects enlarging the interatomic distances of the MgO-structure. Using DFT-calculations, the stability of undissociated (adsorbed) and dissociated water (hydroxyl groups on the surface are more stable than the adsorbed water molecule) were simulated. Initially, the lattice parameters and interatomic distances of a pure MgO surface were artificially increased by about 6.8 % to 4.55 Å, thus approaching the lattice parameters of a pure CaO surface ( $a=4.84$  Å). To compare this pure size-effect with an electronic one, on a pure MgO-surface one (10 %  $\text{Ca}^{2+}$  doping) or two Mg-positions (20 %  $\text{Ca}^{2+}$  doping) were exchanged with  $\text{Ca}^{2+}$ -atoms, affecting the electronic structure of the surface. In **Figure 4** the adsorption energies for the most stable structures found for all three surface models are shown (full symbols denote intact water molecules, open symbols correspond to dissociated water being more stable) as a function of lattice parameter. Whereas for a pure MgO surface with slightly enlarged lattice parameters the adsorption of intact water molecules is favoured over water dissociation, a lattice parameter extension of greater than 5.8 % results in a preference for the dissociative pathway. This confirms the initial assumption of steric influence of the  $\text{Ca}^{2+}$ -dopant. At the other hand, once the Mg-positions were exchanged with  $\text{Ca}^{2+}$ -atoms, the dissociative water adsorption at certain positions is energetically favoured over the whole considered range. This finding seems to confirm an additional, predominantly electronic, effect of  $\text{Ca}^{2+}$  doping. The electronic impact of one or

---

<sup>‡</sup> The dehydration mechanism of  $\text{Mg}(\text{OH})_2$  and a Ca-doped  $\text{Mg}_{0.97}\text{Ca}_{0.03}(\text{OH})_2$ , was investigated in literature using transition electron microscopy.<sup>[36]</sup>



two  $\text{Ca}^{2+}$ -atoms per unit cell surface area affects the adsorption energies only for small lattice parameters. In the case of one  $\text{Ca}^{2+}$  atom on the surface, initially, intact water is more stable, whereas for a second  $\text{Ca}^{2+}$  atom  $E_{\text{ads}}$  is smaller for dissociated water over the range of investigated lattice parameters. For the larger lattice parameters the  $E_{\text{ads}}$  values differ only slightly for both surface models.

To shed light on the formation of the mixed  $\text{Mg}_{1-x}\text{Ca}_x\text{O}$ -phase from a theoretical point of view, both formation enthalpy  $\Delta_f H$  and Gibbs free energy  $\Delta_f G$  for the mixed oxides were calculated. As anticipated based on the large lattice mismatch between the two oxides ( $a_{\text{calc}} = 4.26 \text{ \AA}$  for MgO and  $4.84 \text{ \AA}$  for CaO),  $\Delta_f H$  is positive for all compositions (**Figure S6**). Modelling the entropy with a regular solution model – assuming a random mixture – leads to  $\Delta_f G$ , which is also positive over the entire range of compositions at the temperature at which the materials are formed experimentally (**Figure S6**). Both results agree well with literature,<sup>[33]</sup> confirming again, that also from a theoretical point of view formation of the mixed  $\text{Mg}_{1-x}\text{Ca}_x\text{O}$ -phases is thermodynamically unfavorable and possible only by calcination of the co-precipitated mixed hydroxide.

In conclusion, it was demonstrated that doping MgO with  $\text{Ca}^{2+}$  by calcination of the co-precipitated mixed  $\text{Mg}_{1-x}\text{Ca}_x(\text{OH})_2$  species, the kinetic barrier to the water dissociation step of MgO rehydration could be significantly reduced. The maximum rehydration rate and cycle stability were dramatically increased for MgO doped with 10 %  $\text{Ca}^{2+}$ ,  $\text{Mg}_{0.9}\text{Ca}_{0.1}\text{O}$ , enabling full conversion to the corresponding hydroxide within 80 minutes. The decrease in rehydration reactivity during the following cycles was attributed to agglomeration of material during the consecutive calcination / rehydration steps, impeding the access to the reactive surface. Rehydration of the less reactive material in liquid water regenerates the initial reactivity due to degradation of the aggregates. DFT calculations demonstrated the effect of the  $\text{Ca}^{2+}$  doping as both electronic and steric in nature. Expanding the lattice-constants of an MgO (001)-surface towards the values of a corresponding CaO surface results in a more

stable water adsorption together with an increased tendency toward water dissociation (size effect), whereas exchange of  $\text{Mg}^{2+}$  atoms with  $\text{Ca}^{2+}$  lowers this energy even further (electronic effect). The outcome of this study provides not only a new material for highly efficient and economic thermochemical energy storage, but also showcases, the power of rational design and understanding on the development of new materials tailored for a certain application.

### Experimental Section

*Reference  $\text{Mg}(\text{OH})_2$ :* The commercial  $\text{Mg}(\text{OH})_2$  (0-5  $\mu\text{m}$ , 99.9% purity) used as reference comparing the mixed-oxides water dissociation performance was obtained from RHI AG.

*Preparation of Mixed Mg-Ca Oxides:* Mixtures of the appropriate amounts of  $\text{MgCl}_2 \cdot 6\text{H}_2\text{O}$  and  $\text{CaCl}_2 \cdot 6\text{H}_2\text{O}$  to produce 0.2 mol of the mixed oxide, were dissolved in 75 ml degassed  $\text{H}_2\text{O}$ . Freshly prepared 20 % NaOH solution in degassed  $\text{H}_2\text{O}$  (0.4 mol, 50 ml) were added, resulting in immediate precipitation of a voluminous white precipitate. The  $\text{Mg}_x\text{Ca}_{1-x}(\text{OH})_2$  precipitated was centrifuged and washed three times with 100 ml degassed  $\text{H}_2\text{O}$  until chloride free (verified by silver-nitrate test). The hydroxides were calcined in an electric furnace under static atmosphere for 4 hours at 375 °C, yielding the oxides of the composition  $\text{Mg}_x\text{Ca}_{1-x}\text{O}$ , where  $x= 1-0.5$  in almost quantitative yields.

### Supporting Information

Supporting Information is available from the Wiley Online Library or from the author.

### Acknowledgements

This work was financially supported by the Austrian Research Promotion Agency (FFG Forschungsförderungsgesellschaft), projects 845020, 841150 and 848876. T. Ruh

acknowledges financial support by the VSC Research Center funded by the Austrian Federal Ministry of Science, Research and Economy (bmwfw).

The X-Ray center (XRC) of TU Wien provided access to the powder X-Ray diffractometer.

The computational results presented have been achieved using the Vienna Scientific Cluster (VSC). The RHI AG is acknowledged for provision of the Mg(OH)<sub>2</sub>-reference material.

Received: ((will be filled in by the editorial staff))

Revised: ((will be filled in by the editorial staff))

Published online: ((will be filled in by the editorial staff))

## References

- [1] IEA, 2014.
- [2] P. Arce, M. Medrano, A. Gil, E. Oró, L. F. Cabeza, *Applied Energy*, 2011, 88, 2764.
- [3] United Nations, Kyoto protocol, 1997.
- [4] United Nations Treatie, Paris agreement, No. 54113, 2015.
- [5] J. Cot-Gores, A. Castell, L. F. Cabeza, *Renewable and Sustainable Energy Reviews* 2012, 16, 5207.
- [6] IEA, <https://www.iea.org/publications/freepublications/publication/co-generation-and-renewables-solutions-for-a-low-carbon-energy-future.html>, 2011.
- [7] S. M. Hasnain, *Energy Conversion and Management*, 1998, 39, 1127.
- [8] J. F. Keith Shine, K. Hailemariam, N. Stuber, *Climatic Change*, 2005, 68, 281.
- [9] D. Rahm, *Sustainable Energy and the States, Essay on Politics Markets and Leadership*, McFarland, North Carolina, 2002, 1st ed.
- [10] M. A. Rosen, A. H. Abedin, *The Open Renewable Energy Journal*, 2011, 4, 42.
- [11] T. Bauer, W.D. Steinmann, D. Laing, R. Tamme, *Annual Review of Heat Transfer*, 2012, 15, 131.
- [12] H. Zhang, J. Baeyens, G. Cáceres, J. Degreè, Y. Lv, *Progress in Energy and Combustion Science*, 2016, 53, 1.
- [13] <https://www.lenzing.com/home.html>.
- [14] J. Widhalm, Ph.D.-thesis, TU Wien 2016.
- [15] Z. Pan, C. Y. Zhao, *Energy*, 2015, 82, 611.
- [16] D. Müller, C. Knoll, N. Freiburger, R. Nilica, W. Artner, A. Werner, J. M. Welch, M. Harasek, P. Weinberger, *Applied Energy*, 2017, submitted.
- [17] Y. Kato, K. Kobayashi, Y. Yoshizawa, *Applied Thermal Engineering*, 1998, 18, 85.
- [18] Y. Kato, Y. Sasaki, Y. Yoshizawa, *Energy*, 2005, 30, 2144.
- [19] Y. Kato, Y. Yoshizawa, *International Journal of Energy Research*, 2001, 25, 129.
- [20] E. Mastronardo, L. Bonaccorsi, Y. Kato, E. Piperopoulos, C. Milone, *Applied Energy*, 2016, 162, 31.
- [21] H. Ishitobi, N. Hirao, J. Ryu, Y. Kato, *Industrial & Engineering Chemistry Research*, 2013, 52, 5321.
- [22] O. Myagmarjav, J. Ryu, Y. Kato, *Applied Thermal Engineering*, 2014, 63, 170.
- [23] O. Myagmarjav, J. Ryu, Y. Kato, *Progress in Nuclear Energy*, 2015, 82, 153.
- [24] A. Shkatulov, J. Ryu, Y. Kato, Y. Aristov, *Energy*, 2012, 44, 1028.

- [25] M. Zamengo, J. Ryu, Y. Kato, *Applied Thermal Engineering*, 2014, 64, 339.
- [26] M. Zamengo, J. Ryu, Y. Kato, *Applied Thermal Engineering*, 2014, 69, 29.
- [27] X. L. Hu, J. Carrasco, J. Klimeš, A. Michaelides, *Physical Chemistry Chemical Physics*, 2011, 13, 12447.
- [28] Y. A. Criado, M. Alonso, J. C. Abanades, *Industrial & Engineering Chemistry Research*, 2014, 53, 12594.
- [29] M. Linder, C. Roßkopf, M. Schmidt, A. Wörner, *Energy Procedia*, 2014, 49, 888.
- [30] G. Beaucage, *Journal of Applied Crystallography*, 1995, 28, 717.
- [31] D. J. Kinning, E. L. Thomas, *Macromolecules*, 1984, 17, 1712.
- [32] S. Pabisch, B. Feichtenschlager, G. Kickelbick, H. Peterlik, *Chemical Physics Letters*, 2012, 521, 91.
- [33] R. C. Doman, J. B. Barr, R. N. McNally, A. M. Alper, *Journal of the American Ceramic Society*, 1963, 46, 313.
- [34] W. E. Holleman, 2007, 102<sup>th</sup> Edt.
- [35] S. Stankic, M. Sterrer, P. Hofmann, J. Bernardi, O. Diwald, E. Knözinger, *Nano Letters*, 2005, 5, 1889.
- [36] L. S. Gomez-Villalba, A. Sierra-Fernandez, M. E. Rabanal, R. Fort, *Ceramics International*, 2016, 42, 9455.

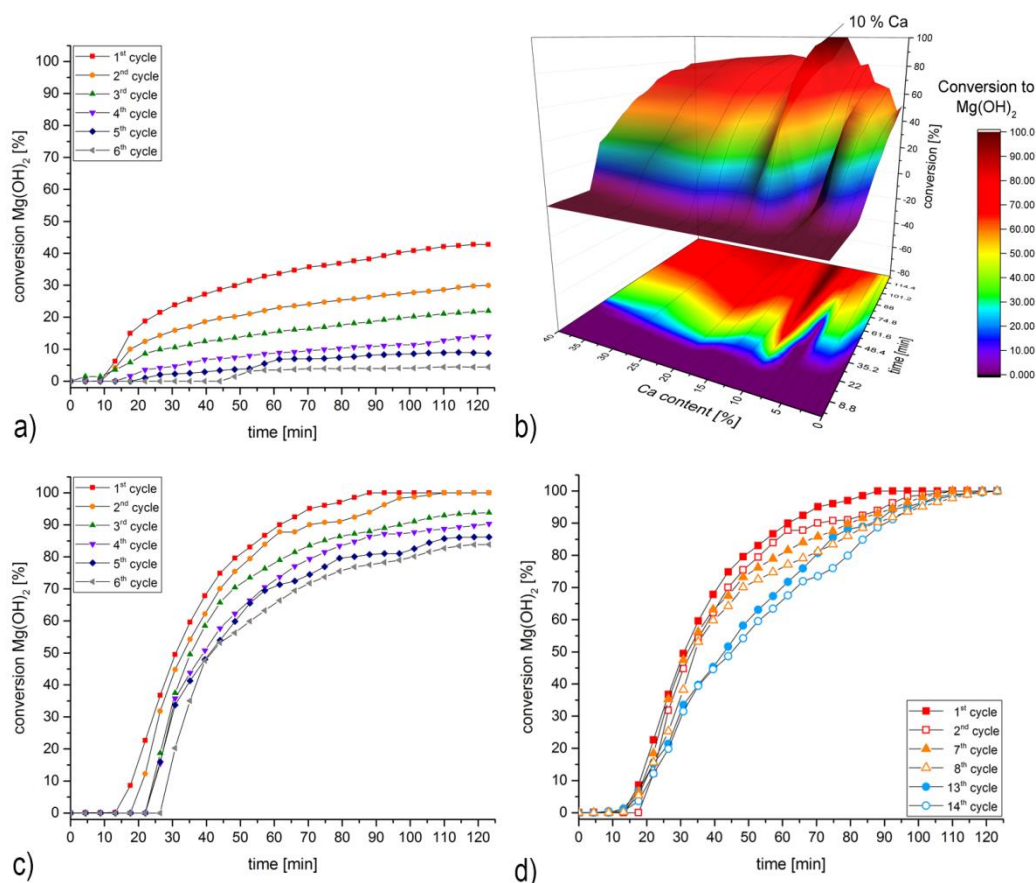


**Figure 1.** Rehydration rate and cycle stability of various  $Mg_{1-x}Ca_xO$  samples a) Commercial MgO as reference. b) Comparison of  $Mg_{1-x}Ca_xO$  with Ca content between 0 – 40% (The 3D-plot compares the final conversion of the different samples, whereas the contour-plot at the bottom directs the focus on the reaction rate / initial delay.) c)  $Mg_{0.9}Ca_{0.1}O$  d) Hydration rate of  $Mg_{0.9}Ca_{0.1}O$  to  $Mg_{0.9}Ca_{0.1}(OH)_2$  for two consecutive cycles before and after 1<sup>st</sup> and 2<sup>nd</sup> regeneration

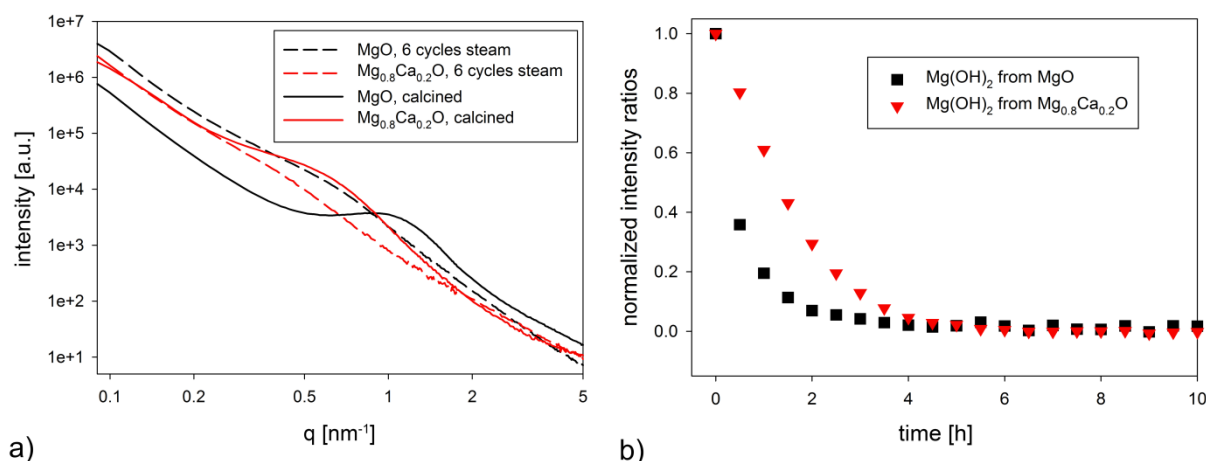


**Figure 2.** a) SAXS intensities for  $MgO$  and  $Mg_{0.8}Ca_{0.2}O$ , calcined and after 6 cycles of steam treatment. The calcined samples show small particles with a short range order (i.e. agglomeration), visible by the peak. The particles of commercial  $MgO$  are smaller and exhibit more pronounced agglomeration. b) Kinetics of conversion to the hydroxide, measured by the decrease in the intensity difference between starting (calcined) and hydroxide material. The half-life times of the hydration of  $MgO$  were determined by exponential fit to be 0.67 hours for  $MgO$  and 1.63 hours for  $Mg_{0.8}Ca_{0.2}O$ .



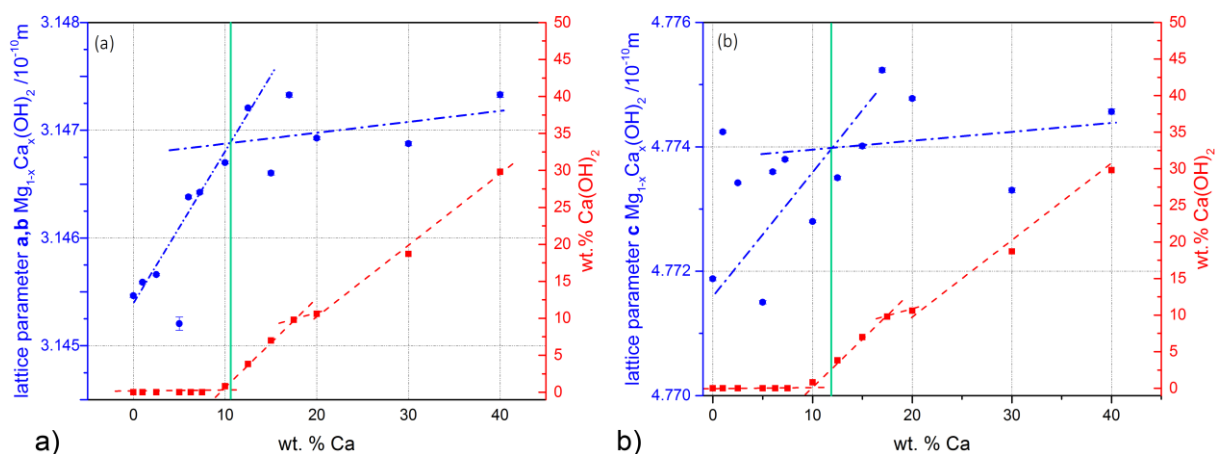


**Figure 3.** Lattice parameters of  $\text{Mg}_{1-x}\text{Ca}_x(\text{OH})_2$  versus degree of Ca-doping (left ordinate) including the amount of  $\text{Ca}(\text{OH})_2$  observed (right ordinate) for a) a-, b- and b) c-lattice parameters, respectively. The blue lines denote trends in the  $\text{Ca}^{2+}$ -content; the red lines shown for the amount of the  $\text{Ca}(\text{OH})_2$  present serve only to guide the eye. The green vertical denotes the intercept of the two different slopes for the lattice parameters observed.

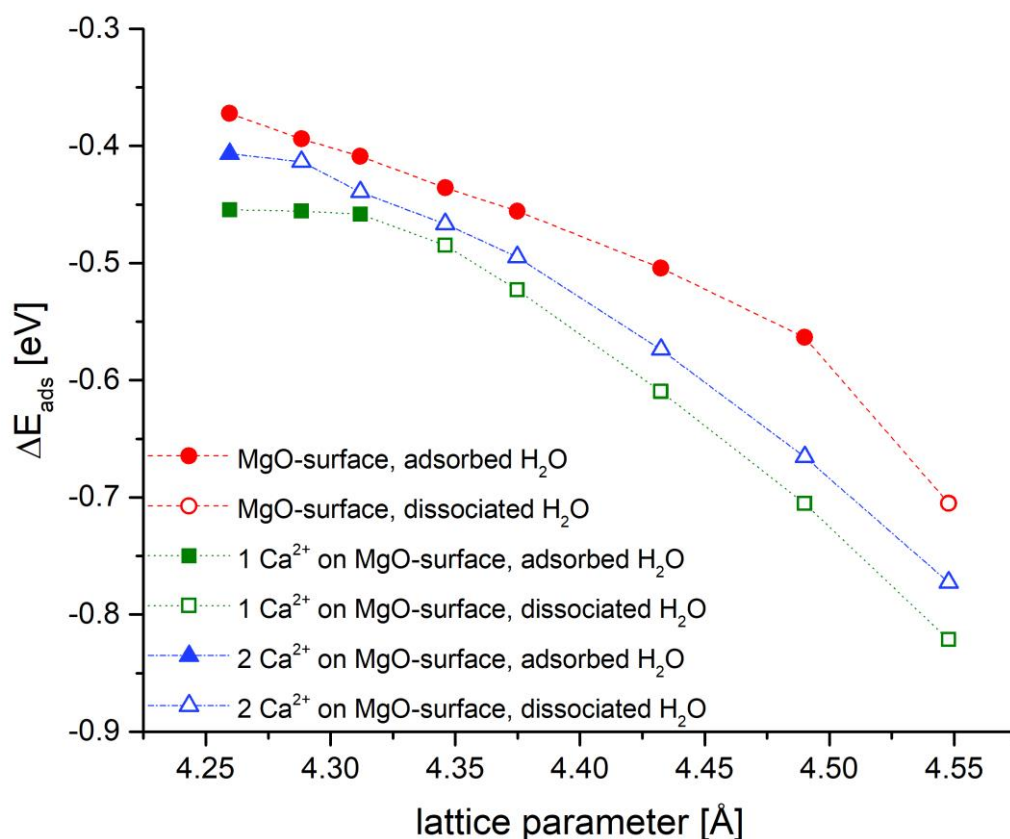


**Figure 4.** Adsorption energy  $E_{\text{ads}}$  of the most stable structure found with adsorbed (intact) and dissociated water respectively.

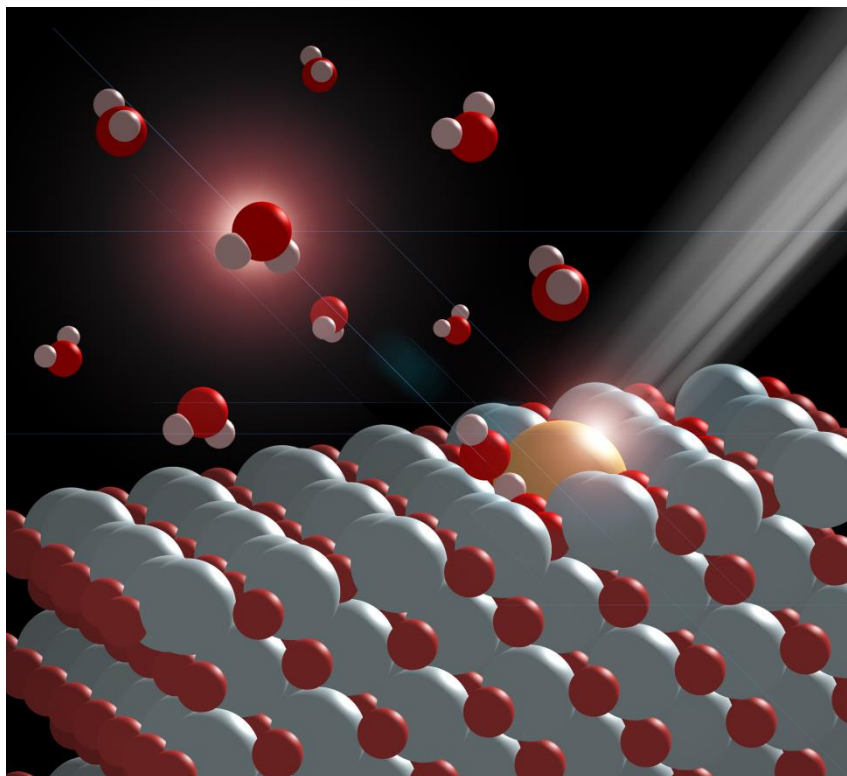
**The table of contents entry**

The water dissociation ability of Ca-doped MgO is significantly enhanced compared to pure MgO, based on a decrease in the kinetic barrier of the water dissociation step due to electronic and steric (size) effects. This allows for complete conversion of an  $\text{Mg}_{0.9}\text{Ca}_{0.1}\text{O}$  phase within 80 minutes to the corresponding mixed hydroxide.

**Keywords:** water dissociation, magnesium oxide, calcium-doping, thermochemical energy storage

**Authors:** Danny Müller\*, Christian Knoll, Thomas Ruh, Werner Artner, Jan M. Welch, Herwig Peterlik, Elisabeth Eitenberger, Gernot Friedbacher, Michael Harasek, Peter Blaha, Klaudia Hradil, Andreas Werner, Peter Weinberger

**Title:** Calcium Doping Facilitates Water Dissociation in Magnesium Oxide



## Supporting Information

### Calcium Doping Facilitates Water Dissociation in Magnesium Oxide

*Danny Müller\*, Christian Knoll, Thomas Ruh, Werner Artner, Jan M. Welch, Herwig Peterlik, Elisabeth Eitenberger, Gernot Friedbacher, Michael Harasek, Peter Blaha, Klaudia Hradil, Andreas Werner, Peter Weinberger*

*X-Ray Powder Diffraction with In-Situ Hydration:* A PANalytical B.V. MPD Pro diffractometer was used to perform the P-XRD in Bragg Brentano geometry within a scattering angle  $5^\circ < 2\theta < 90^\circ$  for Cu  $K_{\alpha 1,2}$ - radiation. The instrumental resolution was defined on the primary side by a  $\frac{1}{2}^\circ$  fixed divergent entrance slit followed by a 0.04 rad Soller slit. A 0.04 rad Soller slit was placed before the X'celerator detector operated in the 1D continuous line mode. The detector to sample distance for this instrument is 240 mm. The hydration of the  $Mg_xCa_{1-x}O$  samples was performed in an Anton Paar XRK 900 sample chamber, connected to an evaporation coil kept at 300 °C. Using a HPLC-pump, 3 g min<sup>-1</sup> water were evaporated and the resulting 3 g min<sup>-1</sup> steam were passed through the sample (4 mm thickness) with 0.2 L min<sup>-1</sup> nitrogen as carrier gas. During rehydration the sample temperature was constantly kept at 50 °C, as governed by the thermocouple in the ceramic sample holder. Nevertheless, the atmospheric temperature in the reaction chamber is uncontrolled and due to the introduction of high-temperature steam, most likely higher than that of the sample holder. During the experiment, any condensation within the sample chamber cannot be observed, as the reaction chamber does not allow for optical inspection whilst operation. On opening the chamber, no condensed water is found either inside of the housing or on the sample.

For the cycle-experiments the  $Mg_xCa_{1-x}(OH)_2$ -samples were calcined for 15 minutes at a temperature of 375 °C and subsequently cooled to 50 °C in a continuous stream of 0.2 L min<sup>-1</sup>

nitrogen (SATP-conditions). At this point the steam supply was activated and the diffractograms were collected continuously, scanning the  $5^\circ < 2\theta < 90^\circ$  within 4.4 minutes. As the sample is completely penetrated by the X-rays, the diffractograms obtained are an average of the complete sample. The experimental setup for the in-situ experiments is illustrated in **Figure S7**.

The diffractograms were evaluated using the PANalytical program suite HighScorePlus v4.6a.

<sup>[1]</sup> A background correction and a  $K_{\alpha 2}$  strip were performed. Phase assignment is based on the ICDD-PDF4+ database,<sup>[2]</sup> the exact phase composition, shown in the conversion plots, was obtained via Rietveld-refinement incorporated in the program suite HighScorePlus v4.6a.<sup>[1]</sup>

#### *Calculation of Lattice-Parameters from P-XRD:*

The calculation of the crystallographic lattice parameters for  $Mg_{1-x}Ca_xO$  with differing degrees of Ca doping were performed using the Rietveld refinement method based on the P-XRD data recorded in one dimension within a scattering angle  $5^\circ < 2\theta < 133^\circ$  with Cu  $K_{\alpha 1,2}$ -radiation. The measurements for the analysis were carried out on a MPD Pro (PANalytical B.V.) powder diffractometer in Bragg Brentano geometry. The instrumental resolution was defined on the primary side by a  $\frac{1}{2}^\circ$  fixed vertical entrance slit followed by a 0.04 rad horizontal Soller slit. A 0.04 rad horizontal Soller slit was placed before the X'celerator detector operated in the 1D continuous line mode. The detector to sample distance for this instrument is 240 mm. Approximately 10 % of a Silicon NIST Standard SR640c with a well-known lattice parameter ( $a = 5.411946 \pm 0.00005 \text{ \AA}$ ) was mixed with the  $Mg(OH)_2$  powders doped with increasing Ca content to enable a correction for the instrument parameters concerning zero shift, etc. Hence, restraining the lattice parameter for the Si phase during the Rietveld refinement, the changes in the parameters for the  $Mg(OH)_2$ - and  $Ca(OH)_2$ -phase could be evaluated within high precision, respectively. **Figure S2** shows a graphical

representation of a Rietveld refinement for the sample with 0% Ca. The residuals for the profile fit are  $R_{\text{Bragg}} = 1.9\%$  and  $R_{\text{weighted pattern}} = 6.7\%$ , respectively.

*Scanning Electron Microscopy:* SEM images were recorded on a Quanta SEM instrument from FEI under low-vacuum and in the presence of water vapor to prevent electrostatic charge.

*Small-angle X-Ray Scattering:* The samples were prepared either as powder between two tapes or in a vacuum-sealed capillary. Patterns were recorded using a microsource with X-rays from a copper target (Incoatec High Brilliance, wavelength 0.1542 nm,  $\text{CuK}\alpha$ ), a point focus (Nanostar from Bruker AXS) and a 2D detector (VÅNTEC 2000). The X-ray patterns were radially averaged and background corrected to obtain scattering intensities dependence on the scattering vector  $q = (4\pi/\lambda) \sin\theta$ , with  $2\theta$  being the scattering angle.

*Computational Details:* All DFT calculations were performed using the WIEN2k program,<sup>[3]</sup> an implementation of the full-potential linearized augmented plane wave + local orbital method. Both the calculation of the adsorption energies of water and the formation energies of the mixed oxides were done using the general gradient approximation by Perdew et al (PBE).<sup>[4]</sup>

The water adsorption was modeled with a 5-layer slab with inversion symmetry and a vacuum layer of 15 Å, starting from a  $(\sqrt{2} \times \sqrt{2})R45$  supercell of bulk MgO. Pure MgO surfaces and mixed surfaces with one and two Ca at Mg sites per unit surface area were simulated. Atomic sphere radii of 1.7, 1.1, and 0.55 bohr were used for Mg/Ca, O, and H respectively. The basis set size is determined by  $RK_{\text{max}} = 3.5$ , which is the product of the largest vector  $K_{\text{max}}$  in reciprocal space (plane wave cut-off) and the smallest atomic sphere radius, and the 2D



Brillouin zones of the surface models were sampled using a 2x2x1 Monkhorst-Pack k-mesh.<sup>[5]</sup>

The adsorption energies  $E_{\text{ads}}$  were calculated according to the following equation:

$$E_{\text{ads}} = 0.5 (E_{\text{slab+water/hydroxyls}} - E_{\text{slab}} - 2 E_{\text{water}}),$$

where  $E_{\text{slab+water/hydroxyls}}$  is the energy of the slab with water and hydroxyls respectively,  $E_{\text{slab}}$  is the energy of the clean slab, and  $E_{\text{water}}$  is the energy of a water molecule in a unit cell of the slab with all slab-atoms removed. Water was adsorbed with the oxygen above a surface cation and the hydrogens oriented toward surface oxygens (roughly along the metal-oxygen bonds of the surface) – as described by Hu et al.<sup>[6]</sup> After a relaxed structure had been found, the adsorbed water was split manually – i.e. one hydrogen was moved to neighboring oxygen. Subsequently another relaxation step was carried out to see whether the hydroxyls are stable or recombine to an adsorbed, but intact water molecule. All structures were relaxed until the residual forces were below 1 mRy/bohr.

The formation energies of the mixed oxides were calculated with primitive 2x2x2 supercells of bulk MgO (with 64 atoms per cell) – for the lowest Ca-content a 3x3x3 supercell was used – with Ca substituted for random Mg-atoms. The random substitutions were created with the program “Supercell”,<sup>[7]</sup> with the number of substituted Mg-atoms corresponding to the respective content of CaO. Atomic sphere radii of 1.7 were used for Mg, Ca, and O. The Brillouin zone was sampled with a 5x5x5 k-mesh, a  $RK_{\text{max}}$  value of 8 was used. The lattice parameters of the mixed oxides were optimized, with the starting lattice parameter chosen according to Vegard’s Law, and the atomic positions were relaxed until residual forces were smaller than 1 mRy/bohr. The formation energy  $\Delta_f H$  was derived according to:

$$\Delta_f H = E_{\text{total}} - (1-x) E_{\text{MgO}} - x E_{\text{CaO}}$$

where  $x$  is the content of CaO in the mixed oxide,  $E_{\text{MgO/CaO}}$  are the energies of bulk MgO and bulk CaO respectively and  $E_{\text{total}}$  is the energy of the mixed oxide. The calculation of the Gibbs free energy based on a regular solution model was done as described by Van de Walle et al.<sup>[8]</sup>

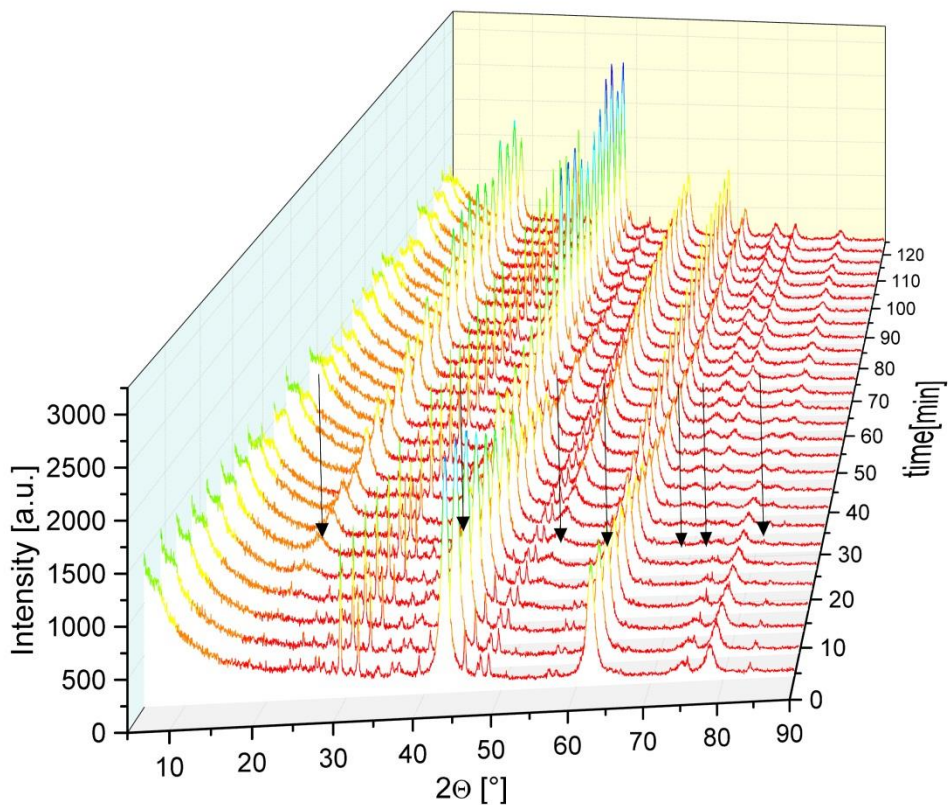


**Figure S1.** Time-dependent P-XRD pattern during the rehydration of  $Mg_{0.9}Ca_{0.1}O$ . The arrows mark the  $Mg_{0.9}Ca_{0.1}(OH)_2$ -peaks.

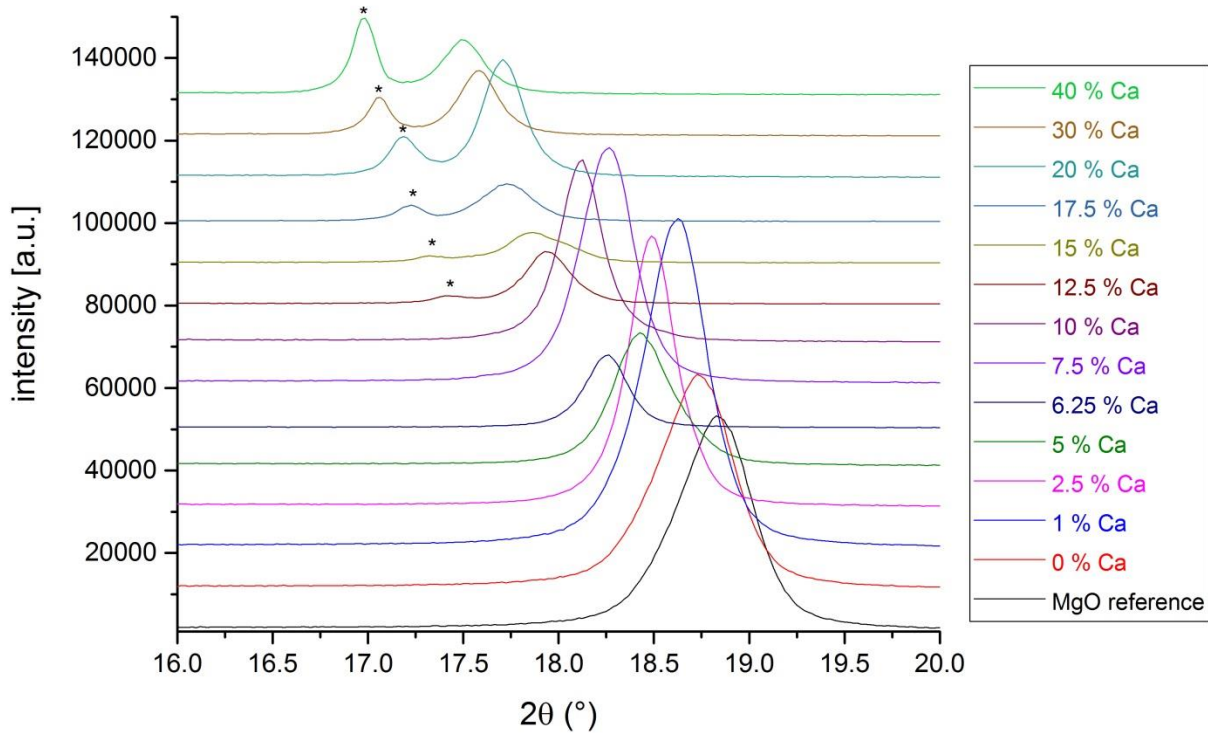


**Figure S2.** The detail of the diffractograms represents the  $\text{Mg}(\text{OH})_2$  {001}-peak at  $2\theta = 18.85$  and, for all samples with more than 10 % Ca-content forming the secondary  $\text{Ca}(\text{OH})_2$ -phase, the  $\text{Ca}(\text{OH})_2$  {001}-peak at  $2\theta = 18.29$  (marked with \*) are shown.

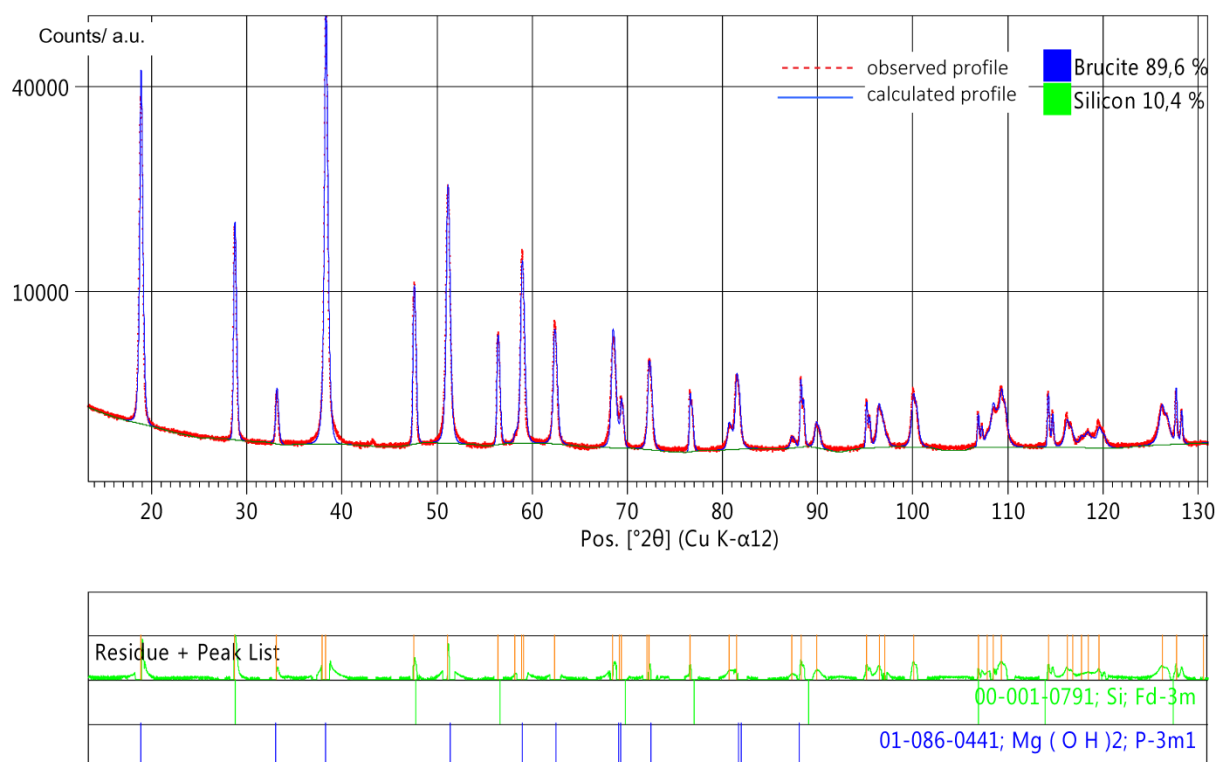


**Figure S3.** Graphical representation of the Rietveld refinement of the P-XRD measurement for 0% Ca. The dotted red lines represent the measured data whereas the solid blue line is the result of the profile fit using a Pearson VII function to describe the intensities based on the crystallographic structural model for the silicon and  $\text{Mg}(\text{OH})_2$  (Brucite) and the instrumental parameters.

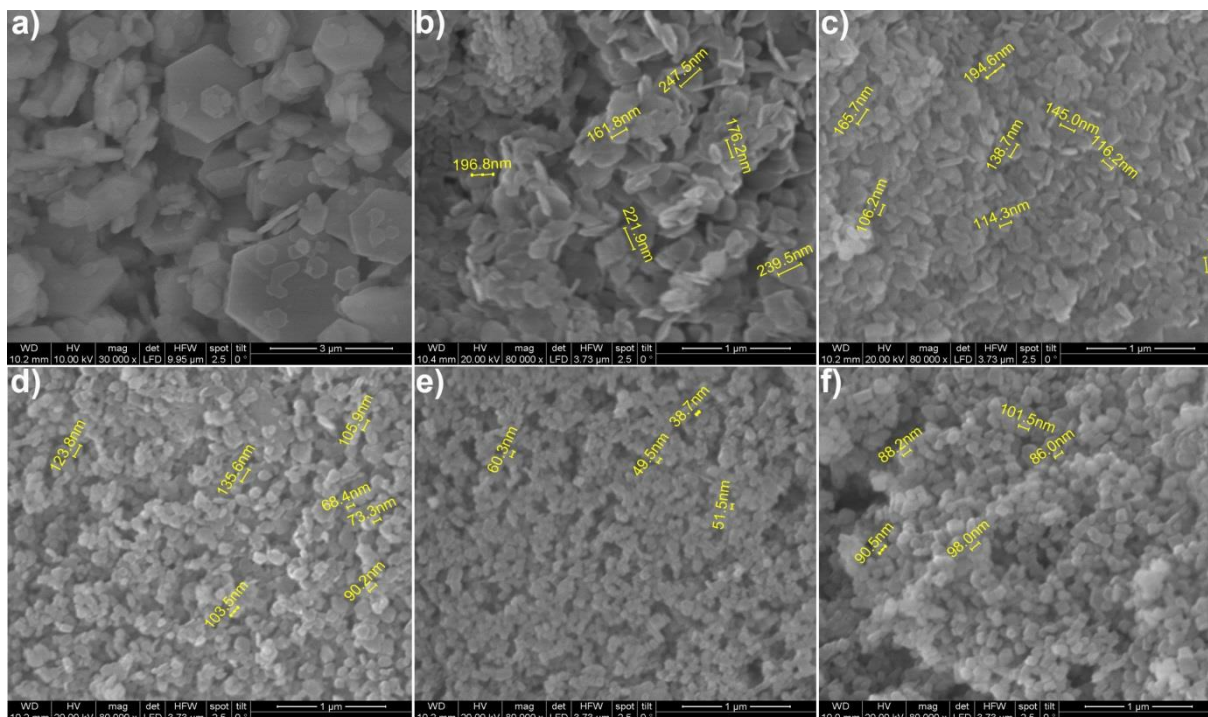


**Figure S4.** SEM-images of a) reference MgO b) MgO precipitated by NaOH (0 % Ca) c) Mg<sub>0.95</sub>Ca<sub>0.05</sub>O d) Mg<sub>0.9</sub>Ca<sub>0.1</sub>O e) Mg<sub>0.85</sub>Ca<sub>0.15</sub>O f) Mg<sub>0.8</sub>Ca<sub>0.2</sub>O

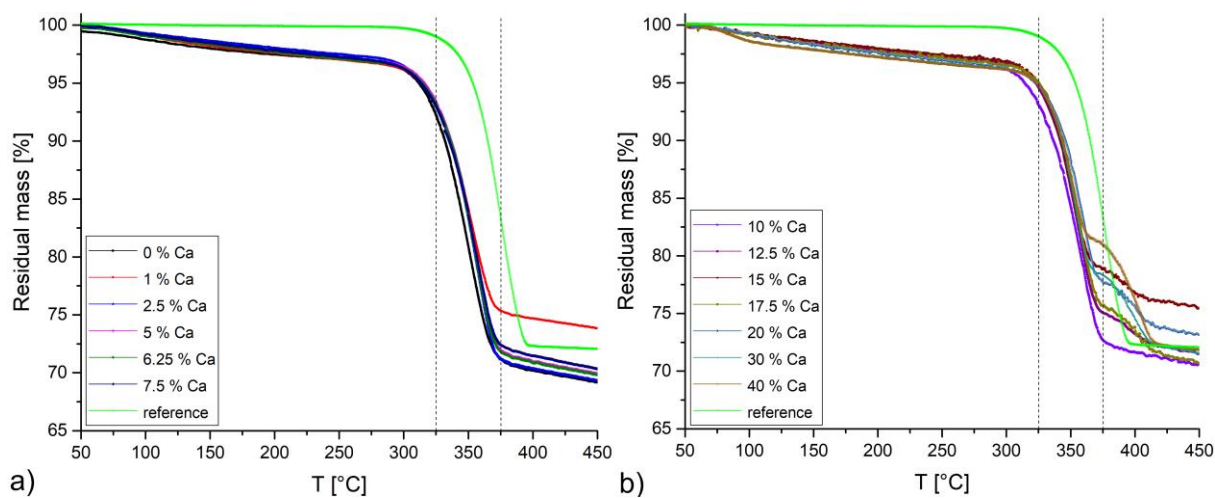


**Figure S5.** Thermogravimetric analysis of the mixed Mg-Ca hydroxides, commercial Mg(OH)<sub>2</sub> is given as reference a) Ca-contents between 0 – 7.5 % b) Ca-contents between 10 – 40 %.

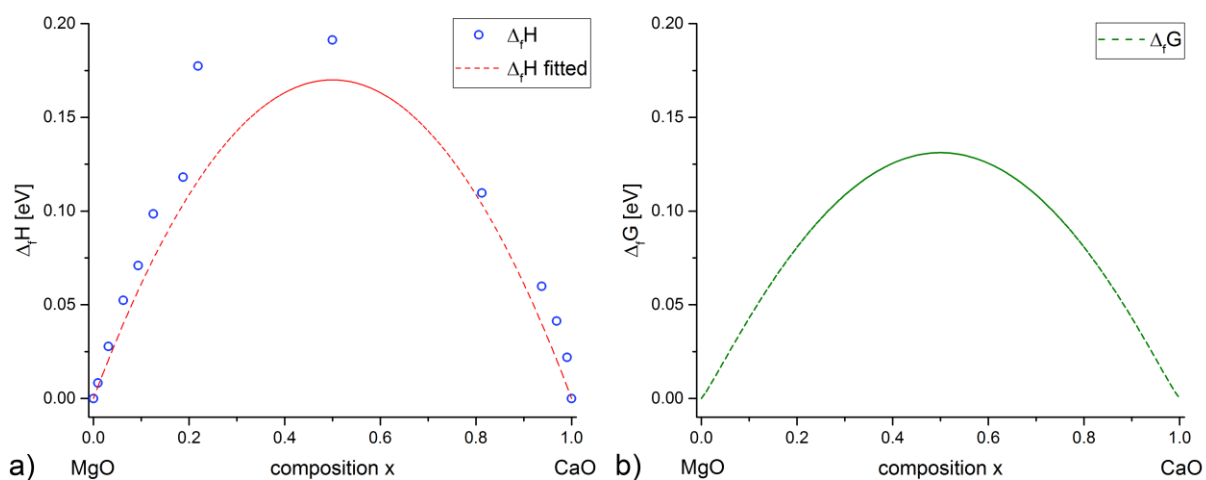


**Figure S6.** a) Enthalpy of formation ( $\Delta H_f$ ) per formula unit. The dashed line is the parabolic fit of enthalpy for the regular solution model. b) Gibbs free energy of formation per formula unit at  $T = 650$  K.

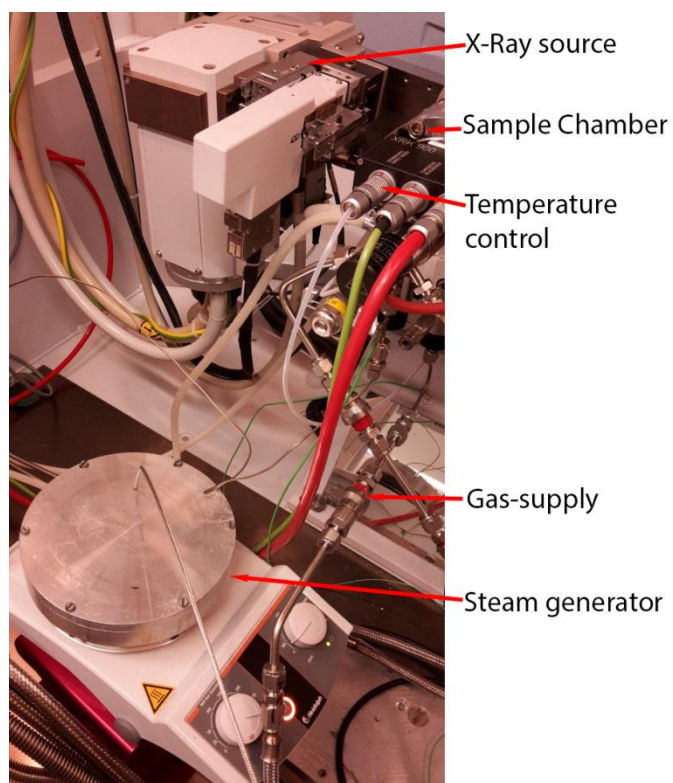


**Figure S7.** Experimental setup for rehydration in the P-XRD.



**Table S1.** Phase composition and corrected rehydration reactivity for  $\text{Mg}_{1-x}\text{Ca}_x\text{O}$  samples

Sample	Ca-content (theoretical) [%]	Ca-content (AAS) [%]	$\text{Ca}(\text{OH})_2$ content [%]	Rehydration Conversion [%] <sup>a</sup>	Corrected Conversion [%] <sup>b</sup>
Reference	0	$0 \pm 0.4$	0	42.8	42.8
1	0	$0 \pm 0.3$	0	51.8	51.8
2	1	$1.18 \pm 0.2$	0	47.3	47.3
3	2.5	$2.89 \pm 0.3$	0	63.4	63.4
4	5	$5.36 \pm 0.2$	0	67.7	67.7
5	6.25	$6.41 \pm 0.9$	0	80.8	80.8
6	7.5	$7.54 \pm 0.6$	0	79.5	79.5
7	10	$10.13 \pm 0.4$	0	100	100
8	12.5	$12.40 \pm 0.9$	5.5	82.4	77.9
9	15	$14.89 \pm 1.0$	7.8	78.5	72.4
10	17.5	$17.98 \pm 0.6$	10.6	84.6	75.7
11	20	$19.55 \pm 3.2$	12.9	86.4	75.2
12	30	$28.53 \pm 1.5$	19.4	83.0	66.9
13	40	$43.68 \pm 2.7$	35.5	77.2	49.8

<sup>a</sup>) First cycle rehydration conversion <sup>b</sup>) Conversion adjusted for inactive  $\text{Ca}(\text{OH})_2$

- [1] T. Degen, M. Sadki, E. Bron, U. König, G. Nénert, Powder Diffraction 2014, 29, S13.  
[2] <http://www.icdd.com>.  
[3] K. S. Peter Blaha, Georg Madsen, Dieter Kvasnicka, Joachim Luitz, ISBN 3-9501031-1-2 2016, TU Wien.  
[4] J. P. Perdew, K. Burke, M. Ernzerhof, Physical review letters 1996, 77, 3865.  
[5] H. J. Monkhorst, J. D. Pack, Physical Review B 1976, 13, 5188.  
[6] X. L. Hu, J. Carrasco, J. Klimeš, A. Michaelides, Physical Chemistry Chemical Physics 2011, 13, 12447.  
[7] K. Okhotnikov, T. Charpentier, S. Cadars, Journal of Cheminformatics 2016, 8.  
[8] H. Peelaers, D. Steiauf, J. B. Varley, A. Janotti, C. G. Van de Walle, Physical Review B 2015, 92.

# An *in-situ* powder X-Ray diffraction study on the rehydration-reactivity of low temperature calcined Mg(OH)<sub>2</sub>

Danny Müller<sup>a,\*</sup>, Christian Knoll<sup>a,b</sup>, Werner Artner<sup>c</sup>, Jan M. Welch<sup>d</sup>, Norbert Freiberger<sup>e</sup>, Roland Nilica<sup>e</sup>, Manfred Schreiner<sup>f</sup>, Michael Harasek<sup>b</sup>, Klaudia Hradil<sup>c</sup>, Andreas Werner<sup>g</sup>, Peter Weinberger<sup>a</sup>

<sup>a</sup> Institute of Applied Synthetic Chemistry, TU Wien, Getreidemarkt 9, 1060 Vienna, Austria.

<sup>b</sup> Institute of Chemical, Environmental & Biological Engineering, TU Wien, Getreidemarkt 9, 1060 Vienna, Austria.

<sup>c</sup> X-Ray Center, TU Wien, Getreidemarkt 9, 1060 Vienna, Austria

<sup>d</sup> Atominstitut, TU Wien, Stadionallee 2, 1020 Vienna, Austria.

<sup>e</sup> RHI-AG, Magnesitstraße 2, 8700 Leoben, Austria.

<sup>f</sup> Institute for Natural Sciences and Technology in the Arts, Academy of Fine Arts, Schillerplatz 3, 1010 Vienna, Austria

<sup>g</sup> Institute for Energy Systems and Thermodynamics, TU Wien, Getreidemarkt 9, 1060 Vienna, Austria.

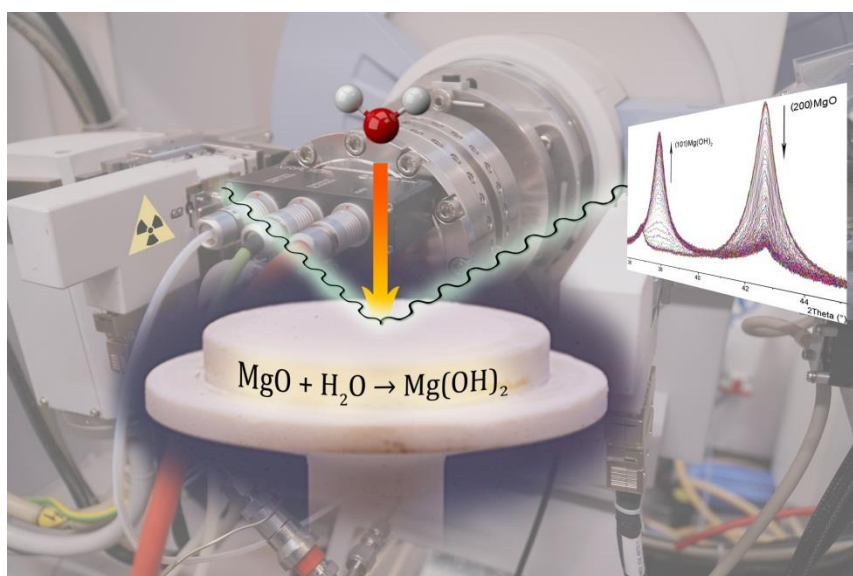
\*Corresponding author      [danny.mueller@tuwien.ac.at](mailto:danny.mueller@tuwien.ac.at)

## Highlights:

- Key parameters affecting the rehydration reactivity of MgO (calcination temperature, specific surface, water vapour concentration and rehydration setup) are identified and compared
- Rehydration reactivity of MgO was determined using an *in-situ* X-ray diffraction setup, correlating calcination conditions, water vapour concentration and reaction rates
- Mg(OH)<sub>2</sub> yield on rehydration varies depending on calcination and rehydration conditions between 65.5 % (furnace-calcination and P-XRD rehydration), 89.5 % (furnace calcination and fluidized-bed rehydration) and 98.5 % (direct calcination and rehydration in the P-XRD)

**Keywords:** low-temperature calcination, magnesium oxide, rehydration reactivity, *in-situ* X-Ray powder diffraction, thermochemistry

## Graphical Abstract



## Abstract

Highly active MgO was investigated as a thermochemical energy storage (TCES) material. Special focus was given to the effects of thermal dehydration of Mg(OH)<sub>2</sub> to MgO: High calcination temperatures and long dwell times notably affect the reactivity of MgO towards rehydration due to sintering processes. A detailed comparative study of the factors governing the rehydration reactivity, including calcination temperature and duration, resulting particle size, morphology and specific surface area and rehydration conditions, is presented. To obtain a correlation between calcination temperature, time and reactivity, sample rehydration was combined with an *in-situ* powder X-ray diffraction (P-XRD) setup. The best results and conversion rates were obtained by calcination of Mg(OH)<sub>2</sub> for 4 hours at 375 °C and subsequent rehydration in the P-XRD using 1 g min<sup>-1</sup> steam. *In-situ* calcined and rehydrated samples in the P-XRD setup showed remarkably higher rehydration reactivity, revealing ageing effects on prolonged storage of the calcined material. Experiments applying the optimized calcination and rehydration conditions in a laboratory-scale fluidized bed reactor were promising for a targeted TCES-cycle: After an initial peak-temperature of 71.5 °C, for more than 50 minutes a reaction temperature between 50-60 °C was achieved.

### 1. Introduction

Thermochemical energy storage (TCES) is a promising technology for the utilization of waste heat and reduction of heat loss by heat storage. Although storage of heat is possible by several different approaches, the concept of TCES, transforming and storing energy by means of a chemical reaction, offers distinctive advantages like high storage density, long-term loss-less storage ability and cost efficiency.<sup>1-3</sup> TCES systems are based on a reversible chemical reaction, during which heat is stored by an endothermic decomposition reaction. On recombination of the products an exothermic reaction occurs, releasing the previously stored heat. The direction of the reaction is temperature dependent as given by the definition of Gibbs' free energy:

$$\Delta G = \Delta H - T \Delta S \quad (1)$$

$$\Delta G_{T_{eq}} = 0 \quad (2)$$

Considering the decomposition of  $\text{Mg}(\text{OH})_2$  into  $\text{MgO}$  and  $\text{H}_2\text{O}$ , in the case that  $T > T_{eq}$ , the reaction will occur spontaneously because  $\Delta G$  becomes negative (charging reaction of the storage material). In contrast, for  $T < T_{eq}$  the back-reaction, in this case the hydration of  $\text{MgO}$  to  $\text{Mg}(\text{OH})_2$  is favoured (discharging of the storage material with concomitant release of heat).

Complementary approaches to the concept of thermochemical energy storage focus on the concepts for thermal energy storage by the application of phase change materials (PCM),<sup>4,5</sup> as well as latent or sensible heat storage materials.<sup>6-8</sup> In comparison to TCES systems, these systems feature disadvantages affecting the cost-value ratio.<sup>9,10</sup> For example, sufficient insulation of the reservoir is needed to decrease heat losses, as the storage material is warmed during the loading process. Due to the inherent lower storage capacity, larger volumes of the storage material are needed. Finally, the operational temperature window is smaller in comparison to TCES-based systems.

The calcination and subsequent rehydration of magnesium oxide (with a storage density of  $1.39 \text{ MJ kg}^{-1}$ ) has been the subject of several experimental studies.<sup>2,11-13</sup> The main reason for the scientific interest in the  $\text{Mg}(\text{OH})_2 / \text{MgO}$  reaction couple is the industrial-scale availability of both materials, allowing for very reasonable material investment costs.<sup>14</sup> Nonetheless, most studies of the  $\text{Mg}(\text{OH})_2 / \text{MgO}$  reaction couple reported so far, focus on kinetic issues, mechanism and process of the thermal decomposition, forming  $\text{MgO}$  from  $\text{Mg}(\text{OH})_2$  under various conditions.<sup>15,16</sup> Due to the principally industrial interest in the calcination reaction, only relatively few efforts have focused on the rehydration process, which is technologically relevant to development of a chemical heat pump, for example.<sup>13,17-19</sup> The major obstacle to the technological use of the  $\text{Mg}(\text{OH})_2 / \text{MgO}$  couple for TCES purposes is the slow and limited reactivity during rehydration. Recently, modifications of the  $\text{Mg}(\text{OH})_2$  with  $\text{LiCl}$ <sup>20</sup> or  $\text{LiBr}$ <sup>21,22</sup> were reported as effective method to enhance the reactivity and energy release during rehydration. To improve the limited thermal conductivity of  $\text{Mg}(\text{OH})_2$ , different composite materials with expanded graphite have been investigated.<sup>16,23-26</sup>

A fundamental investigation regarding the physicochemical background of sluggish rehydration reactivity and correlating the calcination process with the resulting reactivity is still lacking. Nevertheless, from industrial processes it is known that three forms of  $\text{MgO}$  can be distinguished regarding the rehydration reactivity: Dead-burned  $\text{MgO}$ , a very unreactive form used as refractory (formed at temperatures between  $1500\text{-}2000 \text{ }^\circ\text{C}$ ),<sup>27</sup> hard-burned  $\text{MgO}$ , a material of limited reactivity (formed at temperatures between  $1000\text{-}1500 \text{ }^\circ\text{C}$ ) and finally light-burned  $\text{MgO}$ , a more reactive species (formed at temperatures between  $700\text{-}1000 \text{ }^\circ\text{C}$ ).<sup>28</sup> On this basis, the kinetics of the  $\text{MgO}$  rehydration have been shown to be highly dependent on the porous structure and thus surface-area, developed during thermal dehydration.<sup>29</sup> A high surface area facilitates diffusion of water to the reactive sites, resulting in high conversion and reaction rates. An extended thermal treatment of the already dehydrated material or calcination at higher temperatures results in sintering of the material. Thereby, loss of porosity and decrease of reactive surface area results in decreased reactivity of the material.

Herein, we report the first systematic investigation on the rehydration reactivity of  $\text{MgO}$ , obtained by thermal dehydration at temperatures between  $300 \text{ }^\circ\text{C}$  and  $600 \text{ }^\circ\text{C}$ . Samples obtained under different calcination conditions (time and temperature) were investigated regarding their specific surface area, morphology and rehydration behavior, followed by *in-situ* rehydration in a powder X-ray diffraction setup. The results presented allow for scalable identification of the optimum calcination and rehydration conditions, leading to a highly active material suitable for thermochemical energy storage.

## 2. Experimental Methodology

### 2.1 Material

The material, unless otherwise stated, used for all experiments is commercially available  $\text{Mg}(\text{OH})_2$  powder with a particle size of  $\leq 5 \mu\text{m}$ , supplied by RHI-AG. The material used originates from serpentinite, which is industrially treated with dilute hydrochloric acid, followed by a thermal degradation of the resulting magnesium chloride. The obtained  $\text{MgO}$  is then hydrated, yielding  $\text{Mg}(\text{OH})_2$  with a purity of 99 %. Additionally, nano-crystalline  $\text{MgO}$  was purchased from US-Nano.

### 2.2 Thermal analysis

Thermal dehydration data were obtained using a Netzsch STA 449 F1 Jupiter® system equipped with an automatic sample changer and heating rates of 2, 5 and  $10 \text{ }^\circ\text{C min}^{-1}$  under  $\text{N}_2$  atmosphere between  $50 \text{ }^\circ\text{C}$  and  $450 \text{ }^\circ\text{C}$ .

### 2.3 X-Ray Powder Diffraction

The powder X-ray diffraction measurements were carried out on a PANalytical X'Pert Pro diffractometer in Bragg-Brentano geometry using  $\text{Cu K}_{\alpha 1,2}$  radiation and an X'Celerator linear detector with a Ni-filter. For *in-situ* monitoring of experiments an Anton Paar XRK 900 reaction chamber was used. The sample was mounted on a hollow ceramic powder sample holder, allowing for complete perfusion of the sample with the reactive gas. The sample temperature is controlled directly via a NiCr-NiAl thermocouple and direct environmental heating. The reactive gas flow was set to  $0.2 \text{ L min}^{-1}$ , unless otherwise stated. The diffractograms were evaluated using the PANalytical program suite HighScorePlus v3.0d. A background correction and a  $\text{K}_{\alpha 2}$  strip were performed. Phase assignment is based on the ICDD-PDF4+ database, the exact phase composition was obtained via Rietveld-refinement in the program suite HighScorePlus v3.0d. All quantifications based on P-XRD are accurate within of  $\pm 5 \%$ .

### 2.4 *In-situ* rehydration setup for the P-XRD

To follow the rehydration reaction *in-situ*, an Anton Paar XRK 900 sample chamber was equipped with a moisturiser, allowing for X-ray diffraction under an atmosphere with controlled humidity. A 4 mm thick layer of  $\text{MgO}$ -powder, having a diameter of 10 mm flushed with  $0.2 \text{ L min}^{-1}$  a flow of helium, moistened before contacting the sample in a 20 cm high water tank (see figure S1). At the entry of the reaction chamber the gas had a dew-point temperature of  $23.2 \text{ }^\circ\text{C}$ . Considering the gas temperature of  $25 \text{ }^\circ\text{C}$ , this corresponds to a water vapour loading of  $0.25 \text{ g h}^{-1}$ . For higher water concentrations  $1 \text{ ml min}^{-1}$  water (provided by a HPLC-pump) was passed through an evaporation coil kept at  $300 \text{ }^\circ\text{C}$  (see figure S2a). The resulting  $1 \text{ g min}^{-1}$  steam was mixed with  $0.2 \text{ L min}^{-1}$  helium as carrier gas ( $\text{H}_2\text{O}$  partial pressure equals 0.87 bar) and passed from the top through the sample (see figure S2b). The carrier gas is necessary to avoid condensation of water. During rehydration the sample warmed to around  $65 \text{ }^\circ\text{C}$ . As the sample is completely penetrated by the X-rays, the obtained diffractograms are an average through the complete sample.

### 2.5 Scanning electron microscopy (SEM)

A JEOL JSM-5410 analogue scanning electron microscope equipped with a Bruker AXS digitalizing signal processing unit was used to obtain 2D images of the particles of the powder samples. The samples were mounted on carbon pellets on top of the sample holder and plasma



vacuum deposition was used to coat the samples with a thin layer of gold to ensure conductivity. The gold coating was performed using a Baltec Med020 sputtering system. The sample was evacuated for 10 minutes at  $7 \cdot 10^{-4}$  mbar, followed by adjustment of an argon pressure of  $2 \cdot 10^{-2}$  mbar. For the evaporation of the gold target a current of 150 mA for 150 seconds was used.

## 2.6 BET-specific surface area analyzer

The specific surface of the samples was determined by nitrogen sorption measurements, which were performed on an ASAP 2020 (Micromeritics) instrument. The samples (amounts between 100-200 mg) were degassed under vacuum at 80 °C overnight prior to measurement. The surface area was calculated according to Brunauer, Emmett and Teller (BET).<sup>34</sup>

## 2.7 Thermal dehydration in the furnace

For systematic evaluation of the impact of temperature and calcination time on the rehydration reactivity of MgO, Mg(OH)<sub>2</sub> samples were calcined under air and static atmosphere from 2 to 12 hours at 300 °C, 350 °C, 375 °C, 400 °C, 450 °C and 600 °C in an electric muffle furnace. The samples were transferred immediately to a desiccator for cooling after calcination and were afterwards stored in sealed containers.

## 2.8 Fluidized bed reactor

45 g of MgO calcined for 4 hours at 375 °C were fluidized in a 105 cm high reactor with an inner diameter of 3.6 cm in a flow of 20 L min<sup>-1</sup> nitrogen (see figure S3). The reactant was introduced in form of steam, evaporating 1 g min<sup>-1</sup> water at 300 °C and mixed below the glass-sinter bottom with the fluidizing gas stream. The temperature in the reactor was monitored by three K-type thermocouples 10, 20 and 30 cm above the glass-sinter bottom. The heating caused by the steam was determined to result in a temperature increase of 10 °C, which was subsequently corrected in all experiments.

# 3. Results and Discussion

## 3.1 Formation of MgO by calcination of Mg(OH)<sub>2</sub>

To better understand the rehydration reactivity of MgO its formation by calcination of Mg(OH)<sub>2</sub> was studied in detail and the properties (particle size, texture and specific surface area) of materials formed under various conditions were investigated. Information about reaction parameters including temperature (onset of dehydration), rate and degree of conversion (efficiency) were obtained by TG, DSC (thermal analysis) and in situ P-XRD. The dependence of MgO texture on calcination conditions was gleaned from P-XRD data and more detailed information was acquired by BET-surface analysis and SEM.

The thermoanalytical measurements were made to determine the minimum temperature necessary for the thermal decomposition (dehydration) of Mg(OH)<sub>2</sub> to MgO and the efficiency of this process. These experiments (DSC, figure 1 and TG figure S4; parameters summarized in table 1) show that dehydration begins at temperatures between 341 and 374 °C, depending on the heating rate applied.

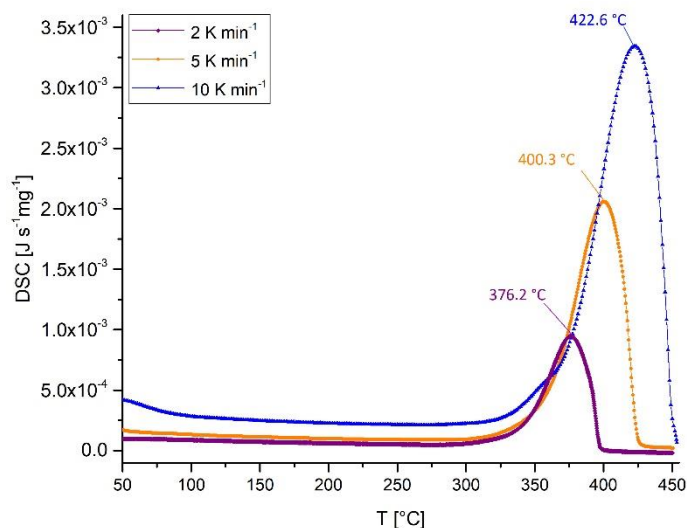


**Figure 1.** Heat flow during the dehydration of  $\text{Mg}(\text{OH})_2$  at different sample heating rates.

A final mass-loss of  $27.77 \pm 0.19$  % is reached between 354 °C and 390 °C depending on the applied heating rate. The theoretical mass-loss should be 30.91 % and, assuming that the observed mass-loss corresponds to the formal removal of one water molecule per magnesium center,  $\sim 90$  % of the theoretical amount of  $\text{MgO}$  is formed. The residual undecomposed material may be attributed to a mixed  $\text{Mg}_2\text{O}(\text{OH})_2$  oxyhydroxide phase that is stable up to 600 °C.<sup>29</sup> The presence of crystalline impurities was excluded by P-XRD analysis (see below).

**Table 1.** DSC and TG data from Figure 1 and Figure S4

	2 °C min <sup>-1</sup>	5 °C min <sup>-1</sup>	10 °C min <sup>-1</sup>
DSC onset [°C]	341.1	358.9	374.8
DSC peak <sub>max</sub> [°C]	376.2	400.3	422.6
heat flow [J g <sup>-1</sup> ]	1072	1065	1053
TG onset [°C]	354.1	370.8	390.6
mass loss [%]	27.59	27.76	27.96

Thermal dehydration of  $\text{Mg}(\text{OH})_2$  was monitored by P-XRD primarily to establish the kinetics of the calcination reaction. An  $\text{Mg}(\text{OH})_2$  sample was heated in the XRD chamber from 25 °C to 400 °C, collecting diffraction data once per minute. The data collected agree well with those obtained previously by DSC/TG. Above 330 °C, the formation of  $\text{MgO}$  and consumption of  $\text{Mg}(\text{OH})_2$  is observed (figure 2,  $\text{MgO}$  peaks marked by asterisks). Above 360 °C a single crystalline  $\text{MgO}$  phase without any secondary phase is observed. The conversion rate data (see figure S5) have an intrinsic uncertainty of less than 1 %, limited only by the accuracy of the P-XRD method.

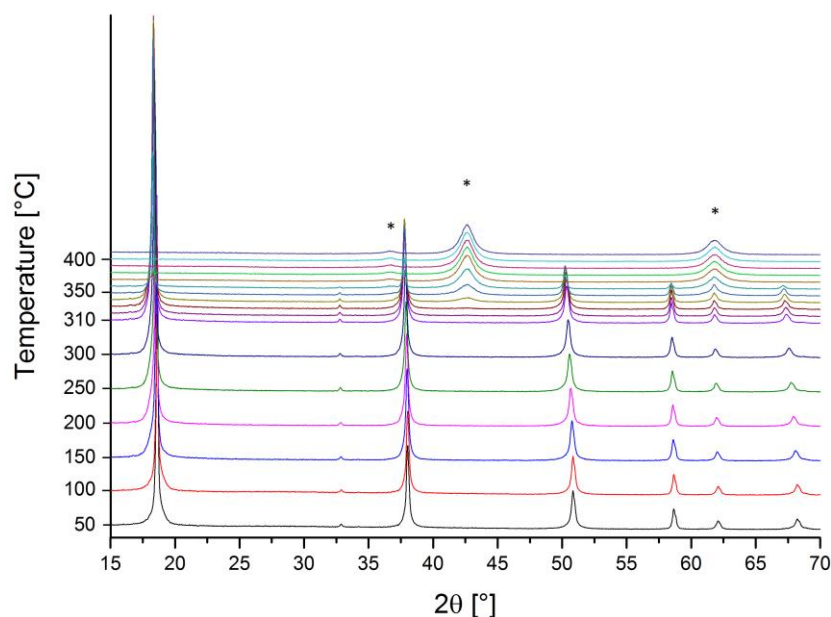


**Figure 2.** Variable temperature powder XRD patterns showing the thermal dehydration of  $\text{Mg}(\text{OH})_2$  to  $\text{MgO}$  ( $\text{MgO}$  peaks marked by asterisks).

In addition to dehydration reactivity information (reaction kinetics), P-XRD also provides insight into the texture and morphology of the particles formed by the reaction. To exploit this information and better understand the effects of calcination temperature and duration on the resulting  $\text{MgO}$ , samples were calcined isothermally at different temperatures between 330-600 °C for up to 10 h while monitoring by P-XRD. Comparing the (111) and (200) reflections for  $\text{MgO}$  samples calcined for 10 hours, both reflections are slightly narrower for samples treated at higher temperatures (see figure S6). This indicates the formation of larger primary crystallites at these temperatures. This effect becomes especially prominent for the  $\text{MgO}$  (200) reflection of the sample treated at 330 °C (red) as compared to that treated at 600 °C (magenta). The mean diffractive crystallite diameters were calculated by Rietveld-analysis for the different calcination temperatures. Diameters of 65.8, 71.8, 82.5 and 111.1 Å were found for samples treated at 330, 350, 400 and 600 °C, respectively after 10 hours calcination time. The primary crystallite sizes of the material during calcination at different temperatures as determined by P-XRD are plotted in figure 3. Quantitatively, during calcination at 330 °C, the primary crystallite size increases by about 5.9 % over the 10 hours dwell time, whereas at 600 °C an increase in crystallite size of 17.3 % is observed over 10 hours.

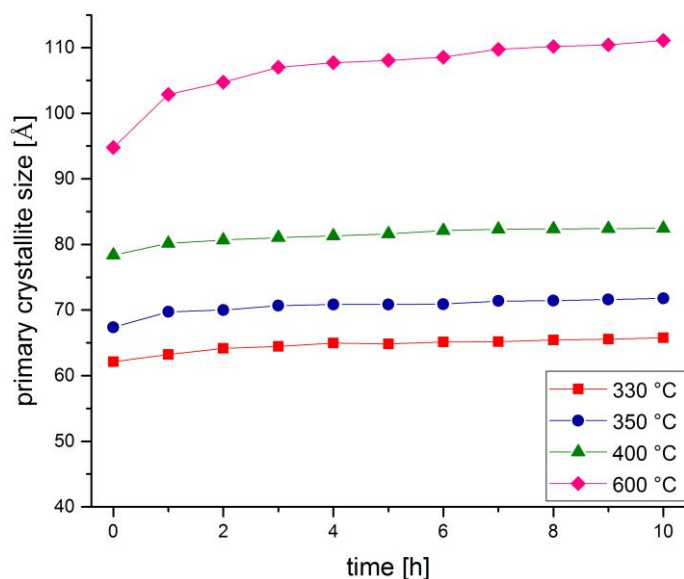


**Figure 3.** Temperature dependent primary crystallite size increase during calcination, shown for the (200) reflection of the material (initially  $\text{Mg}(\text{OH})_2$ , then  $\text{MgO}$ )

Since calcination conditions have a clear effect on the size of the  $\text{MgO}$  particles produced and it is well-known that the first step in the rehydration of  $\text{MgO}$  to  $\text{Mg}(\text{OH})_2$  is the adsorption of water on the particle surface,<sup>29-31</sup> the rehydration of  $\text{MgO}$  should be strongly affected by particle size and porosity (specific surface area). Therefore, the Brunauer, Emmett and Teller method was used to investigate the specific surface area of  $\text{MgO}$  formed by  $\text{Mg}(\text{OH})_2$  calcined under various conditions. In figure 4, the specific surface areas found for material calcined at different temperatures for various lengths of time are plotted (numerical values are tabulated in table S1).

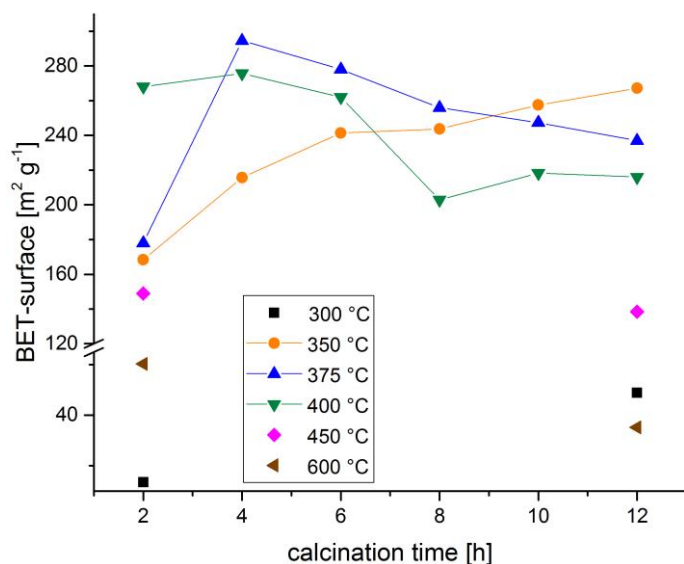


**Figure 4.** Specific surface area of  $\text{MgO}$  samples calcined under different conditions. The specific surface area of untreated  $\text{Mg}(\text{OH})_2$  was determined to be  $4.21 \text{ m}^2\text{g}^{-1}$ , in agreement with the literature value.<sup>29</sup>

As expected, increased sintering on prolonged calcination at higher temperatures is observed as a decrease in the specific surface area. For temperatures above  $375 \text{ °C}$  and dwell times longer

than 4 hours, the specific surface declines steadily. In contrast, the specific surface area of the sample treated at 350 °C – the lower temperature limit for thermal dehydration of Mg(OH)<sub>2</sub> as determined by DSC/TG and P-XRD measurements – was still growing after 12 hours. For the sample treated at 300 °C only a slight increase in the specific surface is observed and for that treated at 600 °C only a small surface area is obtained after only 2 hours. Therefore, the BET surface measurements suggest that the optimal calcination is achieved after 4 hours furnace dwell time at 375 °C, yielding MgO with a specific surface area of 294.51 m<sup>2</sup>g<sup>-1</sup>.

Given the influence of calcination temperature and furnace dwell time on the texture of the resulting MgO and to complement the BET-surface analyses, the particle morphology of MgO formed under various calcination conditions was examined by SEM. In figure 5 and figure S7 representative images of Mg(OH)<sub>2</sub> calcined for 2 and 12 hours at different temperatures are compared. The hexagonal morphology of the MgO platelets, originating from the parent Mg(OH)<sub>2</sub> structure, is preserved in all cases due to the low calcination temperatures applied. For the images obtained from the samples at temperatures below 400 °C, hardly any difference between samples treated for 2 hours or 12 hours is observed. For the samples treated at 600 °C the particle edges become rounded and a concomitant decrease in particle size is observed. The macroscopic particle size modification and decrease with concomitant growth of the primary crystallites corresponds to the thermal sintering process resulting in the loss of hexagonal morphology and formation of the thermodynamically favorable cubic form of MgO.<sup>29</sup>

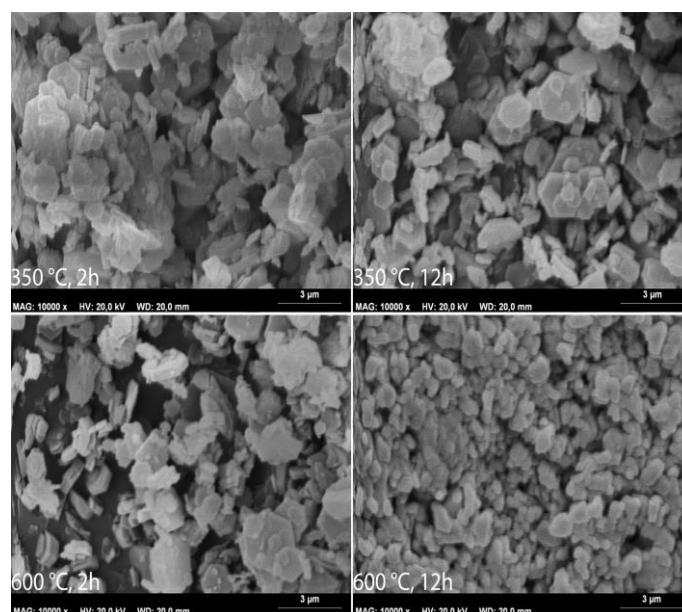


**Figure 5.** SEM-images of the time- and temperature-dependent calcination experiments, 10,000 fold magnification.

These images show the macroscopic aspects of the MgO formed by calcination. The inner structure (including particle porosity) – which is not resolved in figure 5 – is affected by thermal treatment to a far greater extent than MgO particle morphology. Long before a visual change is observed, the nm-sized crystallites of MgO formed during the calcination process that are responsible for the high specific surface area grow and sinter thermally (figure 3). A recent study details the behavior of the inner surface of MgO particles on heating.<sup>29</sup>



### 3.2 Rehydration of MgO monitored by *in situ* P-XRD

Since the calcination process (temperature and duration) affects both the specific surface area and particle morphology of the resulting MgO, the rehydration of MgO produced under different conditions was carefully studied by *in situ* P-XRD. In figure 6, a time-dependent series of diffractograms obtained during rehydration of MgO with  $0.25 \text{ g h}^{-1} \text{ H}_2\text{O}$  ( $\text{Mg}(\text{OH})_2$  calcined at  $375 \text{ }^\circ\text{C}$  for 4h, specific rehydration conditions are described in the experimental) is shown.

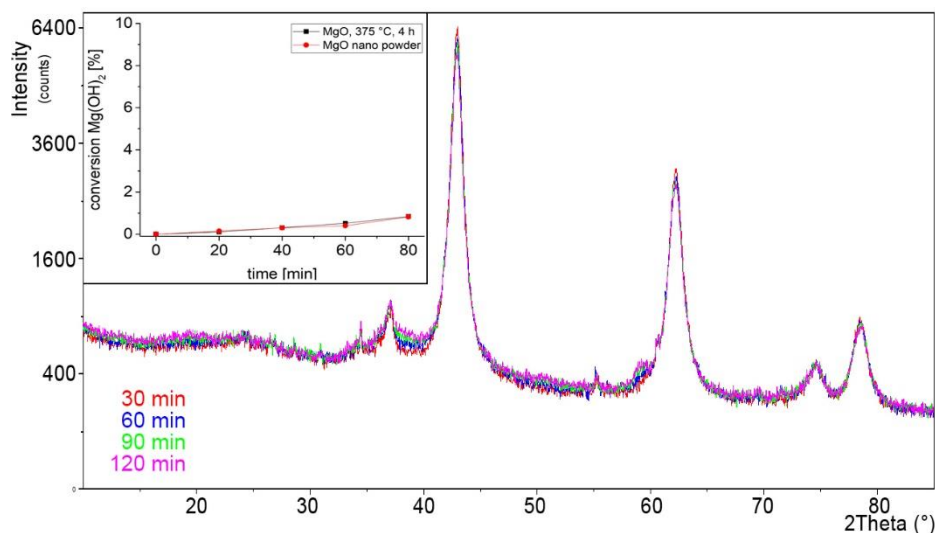


**Figure 6.** Time-dependent rehydration of MgO with  $0.25 \text{ g h}^{-1} \text{ H}_2\text{O}$  ( $25 \text{ }^\circ\text{C}$  and a flow of  $0.2 \text{ L min}^{-1} \text{ He}$ ), shown for a sample generated by calcination of  $\text{Mg}(\text{OH})_2$  at  $375 \text{ }^\circ\text{C}$  for 4 hours. Insert: Conversion rate, calculated from the powder patterns.

Comparing the diffractograms of the initial MgO sample and that obtained after 120 minutes rehydration time, it becomes evident, that nearly no reaction occurs. The insert shows minimal conversion (0.8% over 120 minutes), calculated by Rietveld-analysis of the MgO and  $\text{Mg}(\text{OH})_2$ -phase. The low conversion rate leads to the conclusion that a higher water vapour loading is likely necessary to increase reaction rate. For comparison, the experiment was repeated with a sample of commercially available MgO nano-powder known to be highly active toward rehydration. In the insert, conversion of the nano-powder is shown in red and nearly identical results to those for the sample calcined at  $375 \text{ }^\circ\text{C}$  for 4 hours can be observed.

To enhance the reaction rate, a steam generator was used to introduce  $1 \text{ g min}^{-1}$  of water vapour mixed with  $0.2 \text{ L min}^{-1} \text{ He}$  as carrier gas to the reaction chamber. The results of time-dependent diffraction measurements for rehydration with a greater atmospheric moisture content are shown in figure 7. Clearly, the presence of a large excess of water increases the reaction rate, leading to 65.5 % conversion within the first 2 hours for a sample of MgO generated by calcination of  $\text{Mg}(\text{OH})_2$  for 4 hours at  $375 \text{ }^\circ\text{C}$ . The commercial nano powder was once again analyzed for comparison and shows similar rehydration behavior aside from an initial induction period of approximately 30 minutes, followed by steady conversion at a similar rate to the calcination derived sample.

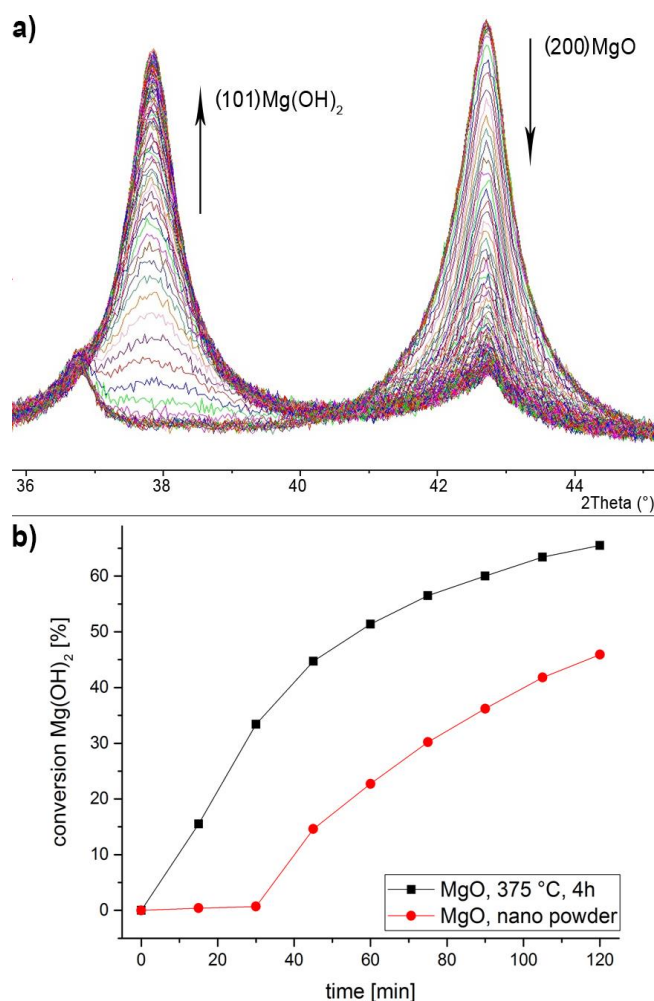


**Figure 7** a) Decreasing intensity of the MgO (200) reflection with concomitant increase in Mg(OH)<sub>2</sub> (101) reflection intensity during rehydration of a sample calcined at 375 °C for 4h. b) Conversion of MgO in a helium-water vapour atmosphere versus time.

The observed acceleration of rehydration by increasing water concentration is in keeping with the known kinetic hindrance of H<sub>2</sub>O-dissociation on the MgO surface. Increasing sample temperature has no impact on the reaction rate, but an excess of reagent (H<sub>2</sub>O) pushes the reaction equilibrium towards the product side. This observation also agrees with previously published theoretical calculations.<sup>32</sup>

To correlate the results from the BET specific surface area analysis of MgO formed by calcination with the *in-situ* P-XRD studies of MgO rehydration, the rehydration of a selection of MgO samples formed by calcination of Mg(OH)<sub>2</sub> under different conditions, were analyzed by P-XRD (figure 8).

As expected for particles with smaller specific surface areas, the MgO samples produced by calcination at higher temperatures feature notably lower rehydration reactivity and incomplete reconversion to Mg(OH)<sub>2</sub> over the two hour reaction time (Figure 8). For samples generated at higher calcination temperatures (and for increased furnace dwell times) an induction period for the rehydration reaction is observed. The sample calcined at 450 °C shows nearly no rehydration within the first 15 minutes, whereas for a calcination temperature of 600 °C this period extends to nearly 90 minutes. A slight trend toward this reduced initial reactivity is also observed for the sample calcined 4 hours at 375 °C, which, nevertheless, shows the greatest

conversion after 120 minutes. The rehydration reaction progress for different samples after 120 minutes is summarized in Table 2.

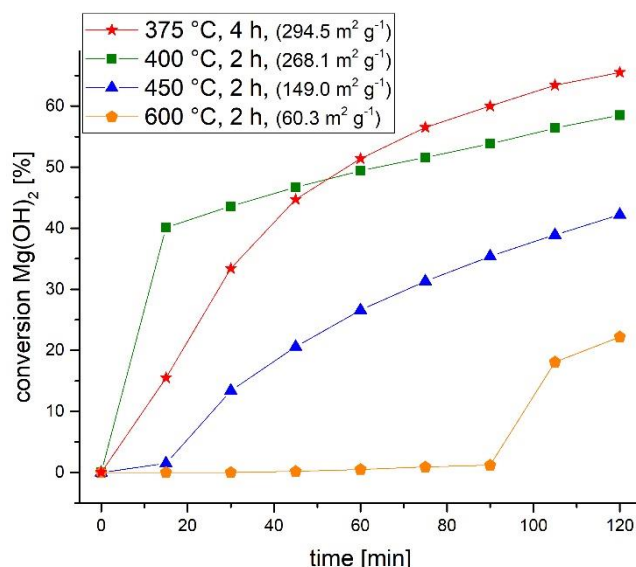


**Figure 8.** Comparison of rehydration rates determined for MgO-samples calcined at different conditions by *in-situ* P-XRD. (Rehydration conditions: 1 g min<sup>-1</sup> H<sub>2</sub>O-vapour, 0.2 L min<sup>-1</sup> He) The diffractograms for the final conversion are shown in figure S8.

As outlined above, higher temperatures and longer calcination times promote particle sintering and the accompanying partial loss of the interior pore structure. This process begins at the particle surface, clogging the pores and thus preventing water molecules from entering the pore structure. Once the sintered outer layers of MgO are rehydrated, platelet growth of Mg(OH)<sub>2</sub> reopens access to the residual interior pore structure.<sup>33</sup> This observation may explain the induction period on rehydration reaction for sintered samples.

**Table 2.** Rehydration of different MgO samples to Mg(OH)<sub>2</sub> after 120 minutes

Sample / calcination temperature	88.7 % moisture	1 g min <sup>-1</sup> H <sub>2</sub> O <sub>(g)</sub> / 0.2 L min <sup>-1</sup> He
MgO US-nano	0.8 %	45.9 %
MgO, 375 °C, 4h	0.8 %	65.5 %
MgO, 400 °C, 2h	---	58.5 %
MgO, 450 °C, 2h	---	42.2 %
MgO, 600 °C, 2h	---	22.2 %

Given these effects of specific surface area and particle morphology on the rehydration reactivity of MgO, the influence of particle size was also studied. To investigate the impact of particle size on reactivity, coarse Mg(OH)<sub>2</sub> was calcined for 4 hours at 375 °C and then fractionated using a vibrating sieve into ≤100 μm, 100-250 μm, 250-350 μm and 350-500 μm particles. Similarly to the SEM-images shown in figure 5, the sieved material consists of small

platelets of  $\leq 5 \mu\text{m}$  size, some of which form larger aggregates along the basal plane of the hexagonal platelets (figure S8). In the bulk material, aggregates and platelets form more or less stable agglomerates. After a few seconds in the vibrating sieve, fractionation was already achieved, the larger agglomerates removed and all four fractions collected and investigated regarding their specific surface and rehydration reactivity. Prolonged sieving should be avoided, as this results in milling of the coarse material and a skew toward the smallest particle sizes. All four fractions have a very similar appearance in the SEM (see figure S10). Only for the 350-500  $\mu\text{m}$  fraction are a slightly increased number of larger particles found. Aside from this, no significant difference is observed in the SEM-images. To investigate the influence of agglomerate size on the reactivity, BET-surface (figure S11) and *in-situ* rehydration rates were determined (figure 10).

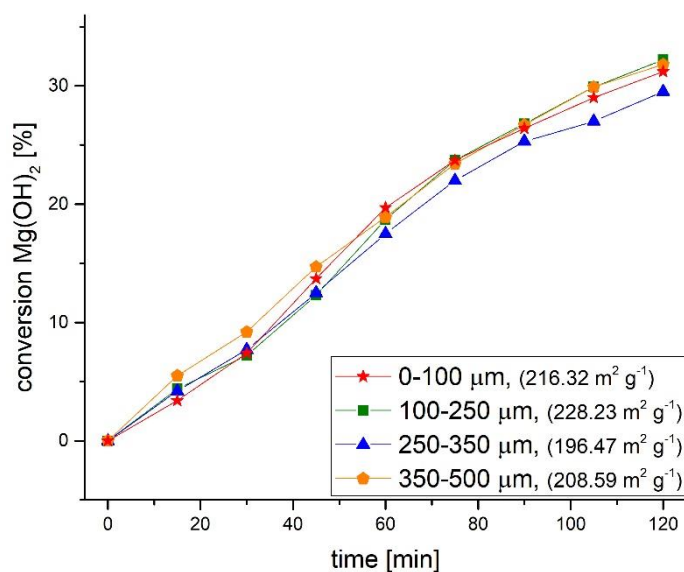


**Figure 10.** Conversion rate of sieved MgO fractions during *in-situ* rehydration in the P-XRD (calcined at 375 °C for 4 hours, Rehydration conditions: 1 g min<sup>-1</sup> H<sub>2</sub>O-vapour, 0.2 L min<sup>-1</sup> He) The diffractograms for the final conversion are shown in figure S12.

The BET specific surface area analyses, as well as the rehydration rates and final conversions are comparable for all four sieved fractions (figure S9). This result fits with the prior findings, especially the SEM-measurements. The MgO samples used for all experiments consist of the finest primary particles in the range of 0-5  $\mu\text{m}$ , forming larger aggregates along their basal planes. But for the rehydration reaction, the formation of these aggregates and agglomerates is not limiting, as the reaction occurs at the surface of the primary particles.

Regarding BET-surface and final conversion a notable discrepancy is observed between the sieved samples and those discussed above. Whereas for the MgO formed by calcination for 4 h at 375 °C without prior sizing a specific surface of 294.5 m<sup>2</sup>g<sup>-1</sup> and a final Mg(OH)<sub>2</sub> conversion of 65.5 % was observed, in the case of the sieved MgO fractions only a surface area around 220 m<sup>2</sup>g<sup>-1</sup> and final conversions of 30 % were evidenced. All applied analytical methods revealed no significant difference between these two groups of samples. Therefore, the only reason for the observed discrepancy in specific surface and reactivity is found in the mechanical treatment of the agglomerates / particles during the sieve analysis. It seems, that the mechanical abrasion during the separation notably affects the reactivity of the material. Further detailed investigations on the impact of mechanical stress on the properties of the Mg(OH)<sub>2</sub> / MgO

particles currently ongoing in our group may provide an in depth explanation for this observation.

### 3.3 MgO-Mg(OH)<sub>2</sub> TCES optimization by *in-situ* P-XRD

To establish the viability of a TCES cycle based on MgO hydration and Mg(OH)<sub>2</sub> dehydration and the nature of any ageing effects occurring either during calcination, another set of experiments was performed in the P-XRD reaction chamber. First, a sample of Mg(OH)<sub>2</sub> was dehydrated under an inert-gas atmosphere while monitored by *in-situ* P-XRD. After complete dehydration was established from the diffraction pattern, the sample was immediately cooled in a nitrogen atmosphere and subsequently rehydrated using the steam generator with He carrier gas. In figure 9 the conversion curves obtained by P-XRD monitoring of rehydration reaction progress are shown.

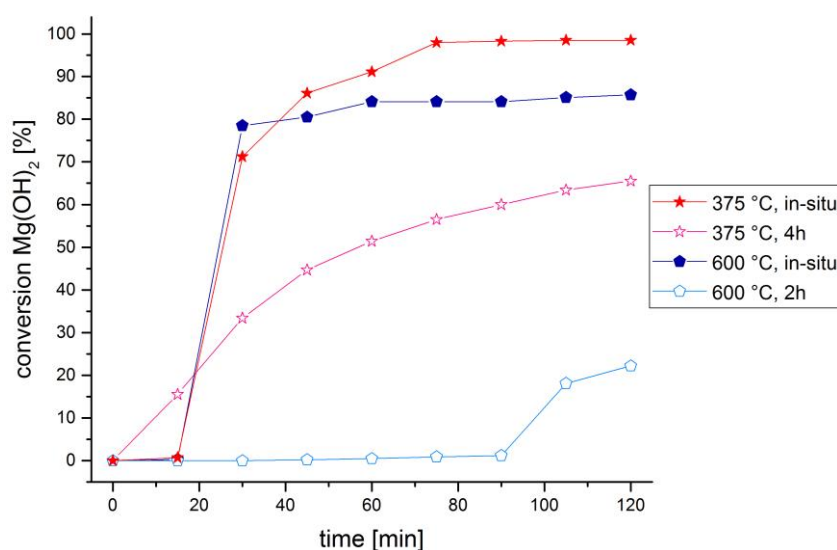


**Figure 9.** Rehydration rates of MgO-samples decomposed *in-situ* (filled symbols) and samples decomposed in the furnace prior to rehydration (unfilled symbols). The initial inhibition in the case of the *in-situ* dehydrated samples may be explained by the dead-volume of the P-XRD setup, as, unlike to prior experiments, the steam generator was connected from the beginning of the rehydration experiment. Threefold repetition of the *in-situ* experiments resulted in highly comparable final conversions. (Rehydration conditions: 1 g min<sup>-1</sup> H<sub>2</sub>O-vapour, 0.2 L min<sup>-1</sup> He) The diffractograms for the final conversion are shown in figure S9.

The final conversion to Mg(OH)<sub>2</sub> of the samples represented in figure 9 after 120 minutes is summarized in table 3.

**Table 3.** Rehydration of different MgO samples to Mg(OH)<sub>2</sub> after 120 minutes

Sample / calcination temperature	1 g min <sup>-1</sup> H <sub>2</sub> O <sub>(g)</sub> / 0.2 L min <sup>-1</sup> He
MgO, 375 °C, 4h	65.5 %
MgO, 375 °C <i>in-situ</i> calcined	98.5 %
MgO, 600 °C, 2h	22.2 %



Upon initial inspection, the results shown in figure 9 were quite unexpected. Samples dehydrated at the same temperature should have nearly identical rehydration reactivity. Samples calcined at 600 °C should also be rehydrated to a much lesser degree due to sintering processes occurring during dehydration. However, the notable differences in the rehydration rate can be explained by the calcination time. For the samples treated in the furnace the dwell time was set *a priori*, whereas for samples treated in the P-XRD chamber the thermal treatment was aborted as soon as complete dehydration was observed. Therefore, although a calcination temperature of 600 °C was applied, the sample experienced only 2 minutes at this temperature. The slightly lower final rehydration conversion achieved in the furnace as compared to the P-XRD cell at 375 °C demonstrates, that Mg(OH)<sub>2</sub> decomposition and sintering occur simultaneously.

For both *in-situ* calcined samples a very high initial reactivity is found, leading to 71.5 % (375 °C) and 78.5 % (600 °C) conversion within 30 minutes. The subsequent flattening of the conversion curve may be attributed to the growth of Mg(OH)<sub>2</sub>-platelets at the particle surface, decelerating the transport of water to the unreacted inner surfaces.<sup>33</sup> Once the rate of rehydration has plateaued, the majority of the MgO has already been rehydrated along a reaction front progressing from the surface of the particles to the inner areas. Diffusion contributes notably to the water transport to the unreacted areas, thus limiting the reaction rate. After 75 minutes the reaction ceases with conversions of 98.5 % (375 °C) and 85.7 % (600 °C).

### 3.4 Rehydration in a laboratory-scale fluidized bed reactor

Experiments to this point have utilized only the very small quantities of material which can be analyzed by *in-situ* P-XRD (~ 0.5 g MgO) due to the geometry of the sample holder. In this configuration, steam was passed through the sample from the top forming a linearly progressing reaction zone. To enable a greater contact between reactants, experiments using a lab-scale fluidized bed reactor (45 g MgO) were performed (figure S3).

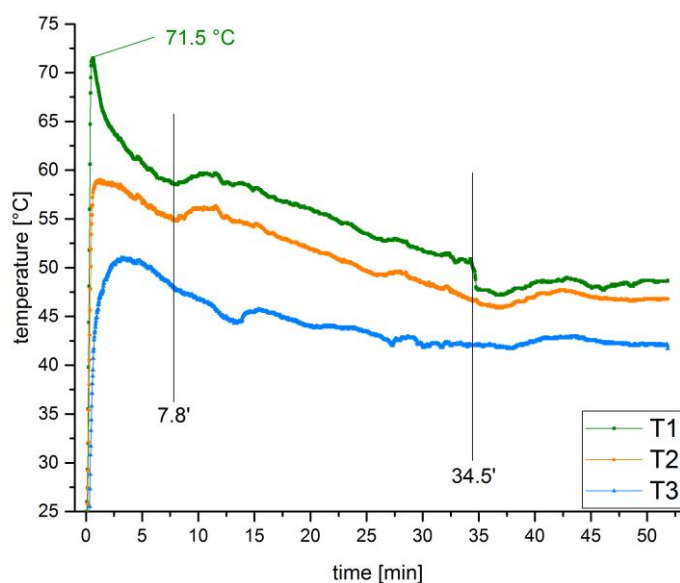


**Figure 11.** Temperature increase during rehydration in the fluidized bed reactor measured by thermocouples T1 – T3. The diffractogram for the final conversion is shown in figure S13.

During the rehydration of 45 g MgO (calcined for 4 hours at 375 °C), a peak-temperature of 71.5 °C (corresponding to a corrected temperature increase of 36 °C was observed (figure 11). The maximum temperature was reached after only 37 seconds, followed by a continuous decrease. In figure 11 three different temperature profiles are plotted, corresponding to the three thermocouples in the fluidized bed reactor. Whereas T1 was in direct contact with the fluidized bed 10 cm above the sintered glass base, T2 and T3 mounted at heights of 20 and 30 cm only had contact to those particles swirling in the reactor and the warmed fluidizing gas stream. The temperature plot demonstrates that under these rehydration conditions the material first yields a rapid temperature increase to the maximal peak temperature, which is followed by a slow decrease to temperatures between 50 °C and 60 °C within the next 40 minutes. The two sudden temperature drops marked in the graph at 7.8 and 34.5 minutes were caused by a short interruption in the steam supply to check the reaction progress. After a reaction time of 53 minutes a conversion of 89.5 % was determined by P-XRD measurement of a sample of material. Compared to the *in-situ* P-XRD rehydration, rehydration in the fluidized bed for 60 minutes led to a higher overall conversion of MgO to Mg(OH)<sub>2</sub>. This is attributed to the higher contact surface between MgO and steam, avoiding the top-down reaction front. Additionally, a certain amount by abrasion and mechanical stress on the particles in the fluidized bed facilitates removal of Mg(OH)<sub>2</sub> growths formed on the particles during rehydration, restoring the reactive MgO surface. A quantification of abrasion and mechanical stress during MgO rehydration in the fluidized bed reactor is ongoing.

Further experiments optimizing this setup, as well as determining the necessary thermodynamic data for the material (thermal conductivity, specific heat capacity, etc.) are currently in progress. Even higher conversions may be obtained using longer rehydration times or an optimized fluidized bed. The current particle size of < 5 µm is not optimal for a fluidized bed reactor and therefore, further experiments regarding agglomeration for fluidization are ongoing.

#### 4. Conclusion

Highly reactive samples of MgO were obtained by calcination at temperatures below 450 °C. The reported systematic approach towards an optimized calcination process of Mg(OH)<sub>2</sub>, offers a simple and cost-effective alternative to the addition of hygroscopic and expensive lithium salts to increase the rehydration reactivity of MgO. The specific surface area (and thus rehydration reactivity) of the samples treated at various temperatures and furnace dwell-times reached a maximum for the sample calcined at 375 °C for 4 hours. Lower temperatures led to lower specific surface areas due to incomplete calcination of the Mg(OH)<sub>2</sub> and longer calcination times or higher temperatures also result in smaller specific surfaces due to sintering of the samples and decrease of their interior porosity as observed in the SEM images. However, particle / agglomerate size does not affect the reactivity of the MgO produced under the conditions of this study. The hydration reactivity of the MgO samples was also found to be dependent on the water concentration as well as the calcination process used to produce them, with higher moisture contents favoring more rapid and complete conversion. Finally, preliminary experiments in a laboratory-scale fluidized bed reactor demonstrate that intimate contact between the reactants leads to higher conversion of furnace-calcined MgO to Mg(OH)<sub>2</sub>. The high degree of conversion (89.5 % within 53 minutes) was attributed not only to the enhanced contact surface, but also to a certain amount to abrasion and mechanical stress on the particles, and thereby restoring a reactive surface during the rehydration process. Further investigations focusing on cycle stability of the material, correlation of particle morphology and reactivity, as well as studies on fluidization and abrasion for a larger-scale fluidized bed setup are ongoing.

## Conflict of interest

The authors declare no conflict of interest

## Acknowledgement

This work was financially supported by the Austrian Research Promotion Agency (FFG-Forschungsförderungsgesellschaft), project 845020, 841150 and 848876.

The X-Ray center (XRC) of TU Wien provided access to the powder X-Ray diffractometer. Finally, we want to acknowledge Prof. Hermann Kronberger from the Institute of Chemical Technologies and Analytics, TU Wien for providing access to the scanning electron microscope and Udo Starzacher for technical support.

## References

- (1)J. Xu, R. Z. W., Y. Li *Solar Energy* **2014**, 610.
- (2)T. Yan, R. Z. W., T. X. Li, L.W.Wang, Ishugah T. Fred *Renewable and Sustainable Energy Reviews* **2015**, 43, 13.
- (3)Ali H. Abedin, M. A. R. *The Open Renewable Energy Journal* **2011**, 4, 42.
- (4)Cabeza, L. F.; Castell, A.; Barreneche, C.; de Gracia, A.; Fernández, A. I. *Renewable and Sustainable Energy Reviews* **2011**, 15, 1675.
- (5)Tian, Y.; Zhao, C. Y. *Energy* **2011**, 36, 5539.
- (6)Dinker, A.; Agarwal, M.; Agarwal, G. D. *Journal of the Energy Institute* **2015**.
- (7)Hasnain, S. M. *Energy Conversion and Management* **1998**, 39, 1127.
- (8)Zalba, B.; Marín, J. M.; Cabeza, L. F.; Mehling, H. *Applied Thermal Engineering* **2003**, 23, 251.
- (9)Cot-Gores, J.; Castell, A.; Cabeza, L. F. *Renewable and Sustainable Energy Reviews* **2012**, 16, 5207.
- (10)Prieto, C.; Cooper, P.; Fernández, A. I.; Cabeza, L. F. *Renewable and Sustainable Energy Reviews* **2016**, 60, 909.
- (11)Shkatulov, A.; Ryu, J.; Kato, Y.; Aristov, Y. *Energy* **2012**, 44, 1028.
- (12)Pan, Z.; Zhao, C. Y. *Energy* **2015**, 82, 611.
- (13)Kato, Y.; Takahashi, F.-u.; Watanabe, A.; Yoshizawa, Y. *Applied Thermal Engineering* **2001**, 21, 1067.
- (14)Green, J. *Journal of Materials Science* **1983**, 18, 637.
- (15)Kato, Y.; Nakahata, J.; Yoshizawa, Y. *Journal of Materials Science* **1999**, 34, 475.
- (16)Kato, Y.; Sasaki, Y.; Yoshizawa, Y. *Energy* **2005**, 30, 2144.
- (17)Kato, Y.; Yoshizawa, Y. *International Journal of Energy Research* **2001**, 25, 129.
- (18)Kato, Y.; Kobayashi, K.; Yoshizawa, Y. *Applied Thermal Engineering* **1998**, 18, 85.
- (19)Kato, Y.; Takahashi, F.; Watanabe, A.; Yoshizawa, Y. *Chemical Engineering Research and Design* **2000**, 78, 745.
- (20)Ishitobi, H.; Hirao, N.; Ryu, J.; Kato, Y. *Industrial & Engineering Chemistry Research* **2013**, 52, 5321.
- (21)Myagmarjav, O.; Ryu, J.; Kato, Y. *Applied Thermal Engineering* **2014**, 63, 170.
- (22)Myagmarjav, O.; Ryu, J.; Kato, Y. *Progress in Nuclear Energy* **2015**, 82, 153.
- (23)Mastronardo, E.; Bonaccorsi, L.; Kato, Y.; Piperopoulos, E.; Milone, C. *Applied Energy* **2016**, 162, 31.
- (24)Zamengo, M.; Ryu, J.; Kato, Y. *Applied Thermal Engineering* **2014**, 64, 339.
- (25)Zamengo, M.; Ryu, J.; Kato, Y. *Applied Thermal Engineering* **2014**, 69, 29.

- (26) Zamengo, M.; Ryu, J.; Kato, Y. *Energy Procedia* **2015**, *71*, 293.
- (27) Zhou, S. *PhD-thesis* **2004**.
- (28) Shand, M. A. *John Wiley & Sons Inc., Hoboken, New Jersey* **2006**.
- (29) Pimminger, H.; Habler, G.; Freiburger, N.; Abart, R. *Physics and Chemistry of Minerals* **2016**, *43*, 59.
- (30) Birchal, V. S.; Rocha, S. D. F.; Mansur, M. B.; Ciminelli, V. S. T. *The Canadian Journal of Chemical Engineering* **2001**, *79*, 507.
- (31) Almeida, A. L.; Martins, J. B. L.; Longo, E.; Taft, C. A.; Murgich, J.; Jalbout, A. F. *Journal of Molecular Structure: THEOCHEM* **2003**, *664-665*, 111.
- (32) Hu, X. L.; Carrasco, J.; Klimeš, J.; Michaelides, A. *Physical Chemistry Chemical Physics* **2011**, *13*, 12447.
- (33) Kuleci, H.; Schmidt, C.; Rybacki, E.; Petrishcheva, E.; Abart, R. *Mineralogy and Petrology* **2016**, *110*, 1.
- (34) Brunauer, S.; Emmett, P. H.; Teller, E. *Journal of the American Chemical Society* **1938**, *60*, 309.

## Appendix A – Supporting Information

### An *in-situ* powder X-Ray diffraction study on the rehydration-reactivity of low temperature calcined MgO

Danny Müller<sup>a,\*</sup>, Christian Knoll<sup>a,b</sup>, Werner Artner<sup>c</sup>, Jan M. Welch<sup>d</sup>, Norbert Freiberger<sup>e</sup>, Roland Nilica<sup>e</sup>, Manfred Schreiner<sup>f</sup>, Michael Harasek<sup>b</sup>, Klaudia Hradil<sup>c</sup>, Andreas Werner<sup>g</sup>, Peter Weinberger<sup>a</sup>

<sup>a</sup> Institute of Applied Synthetic Chemistry, TU Wien, Getreidemarkt 9, 1060 Vienna, Austria.

<sup>b</sup> Institute of Chemical, Environmental & Biological Engineering, TU Wien, Getreidemarkt 9, 1060 Vienna, Austria.

<sup>c</sup> X-Ray Center, TU Wien, Getreidemarkt 9, 1060 Vienna, Austria

<sup>d</sup> Atominstitut, TU Wien, Stadionallee 2, 1020 Vienna, Austria.

<sup>e</sup> RHI-AG, Magnesitstraße 2, 8700 Leoben, Austria.

<sup>f</sup> Institute for Natural Sciences and Technology in the Arts, Academy of Fine Arts, Schillerplatz 3, 1010 Vienna, Austria

<sup>g</sup> Institute for Energy Systems and Thermodynamics, TU Wien, Getreidemarkt 9, 1060 Vienna, Austria.

\*Corresponding author      [danny.mueller@tuwien.ac.at](mailto:danny.mueller@tuwien.ac.at)



**Figure S1.** Moisturiser for the *in-situ* P-XRD setup.

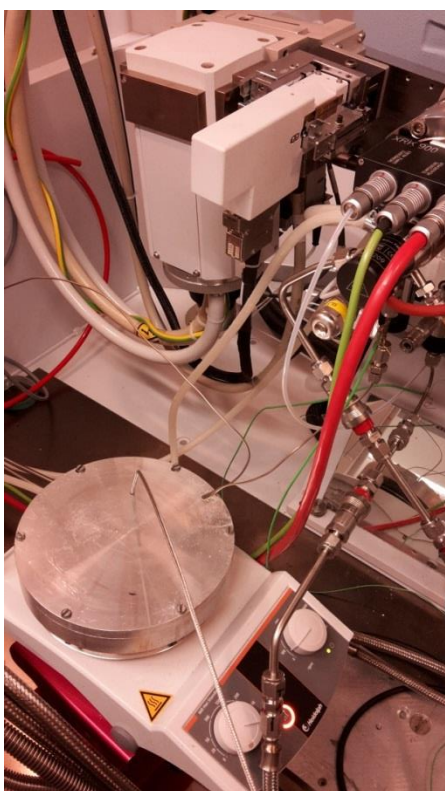


**Figure S2a.** Evaporation coil and steam-supply for the reaction chamber





**Figure S2b.** Sample holder in the reaction chamber. The carrier gas passes the water vapour from the top through the sample.



**Figure S3.** Fluidized bed reactor in laboratory scale.

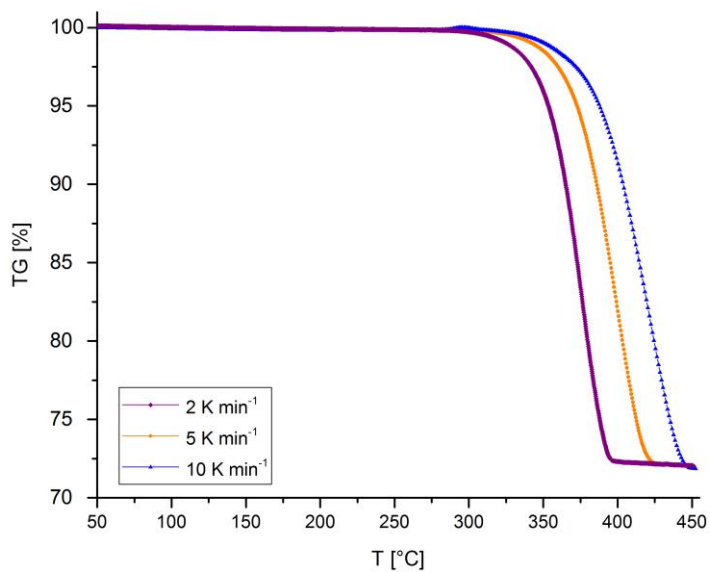


**Figure S4.** Thermogravimetric dehydration of  $\text{Mg}(\text{OH})_2$  at different sample heating rates.

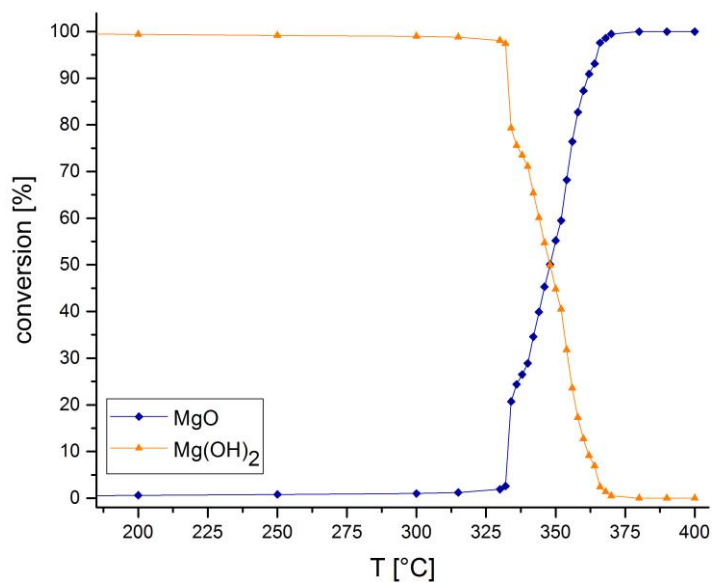


**Figure S5.** Thermal dehydration of  $\text{Mg}(\text{OH})_2$  monitored *in-situ* by P-XRD.

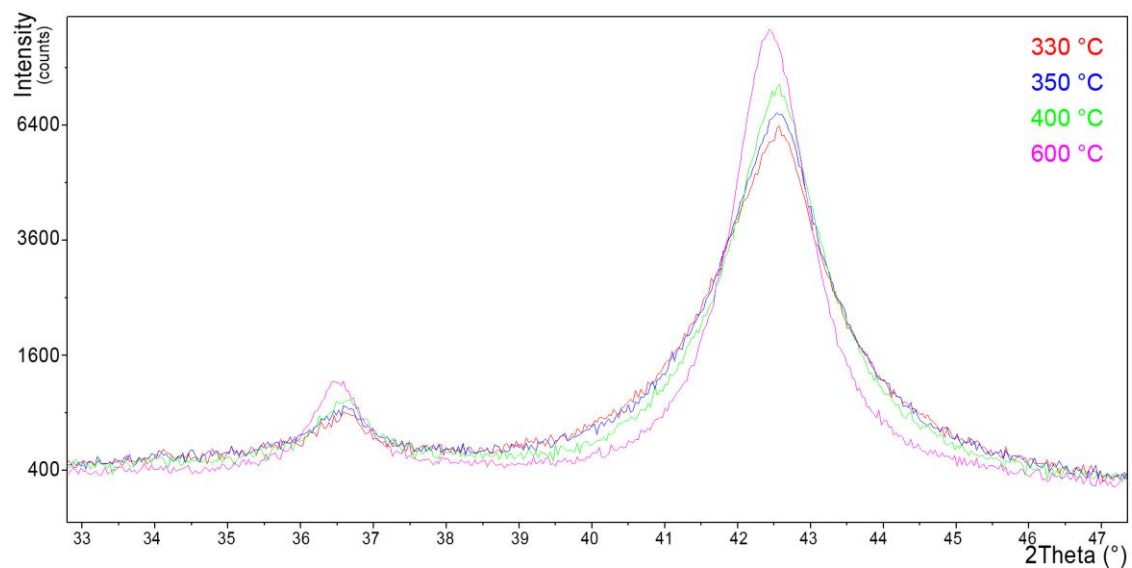


**Figure S6.** (111) and (200) P-XRD reflections of MgO samples calcined at temperatures between 330 - 600 °C after 10 hours of thermal treatment.

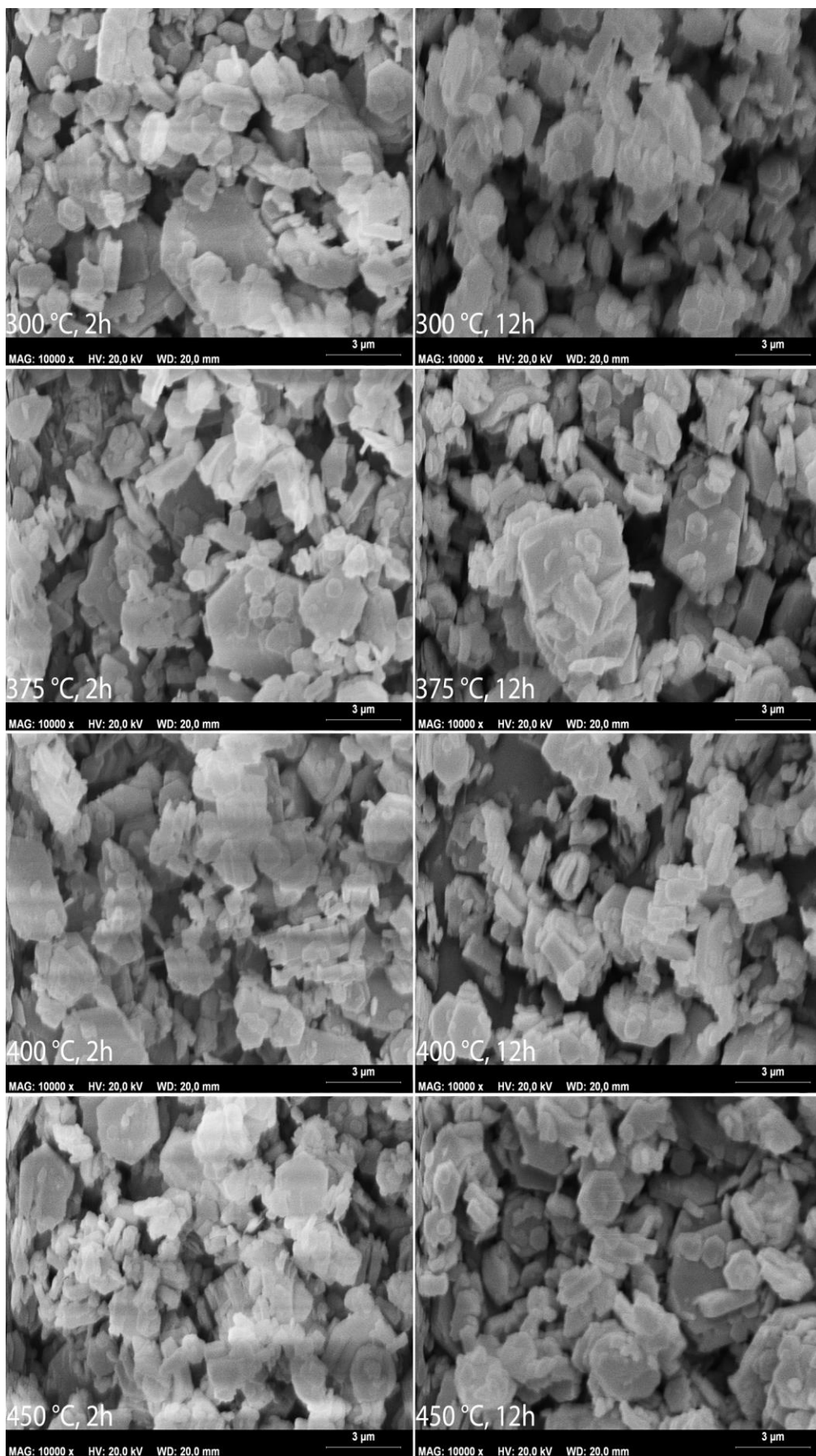


**Figure S7.** SEM-images of the time- and temperature dependent calcination experiments, 10.000 fold magnification.

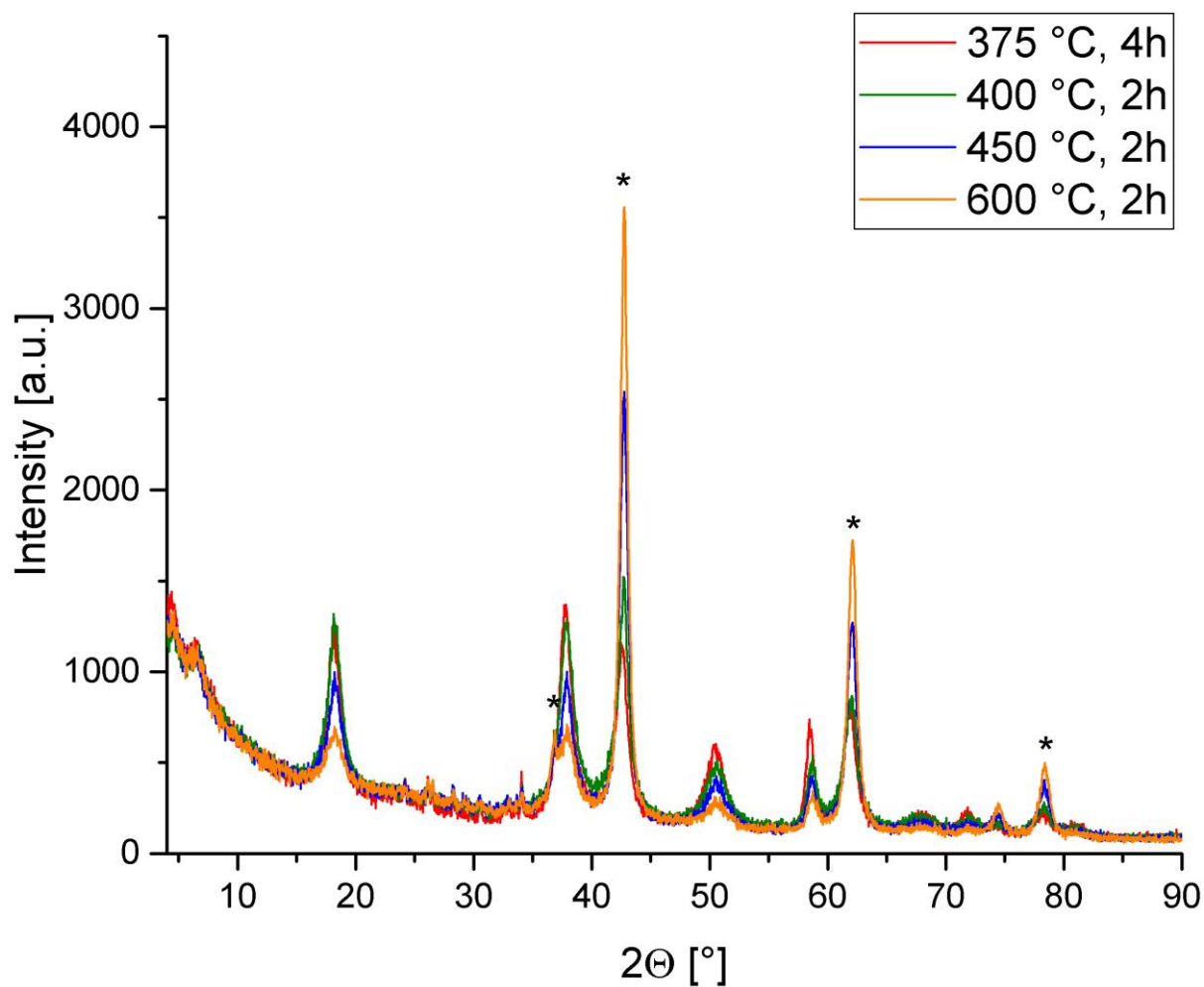


**Figure S8.** Diffractograms showing the final conversion of the different samples described in figure 8. Asterisks mark the isolated MgO-peaks.

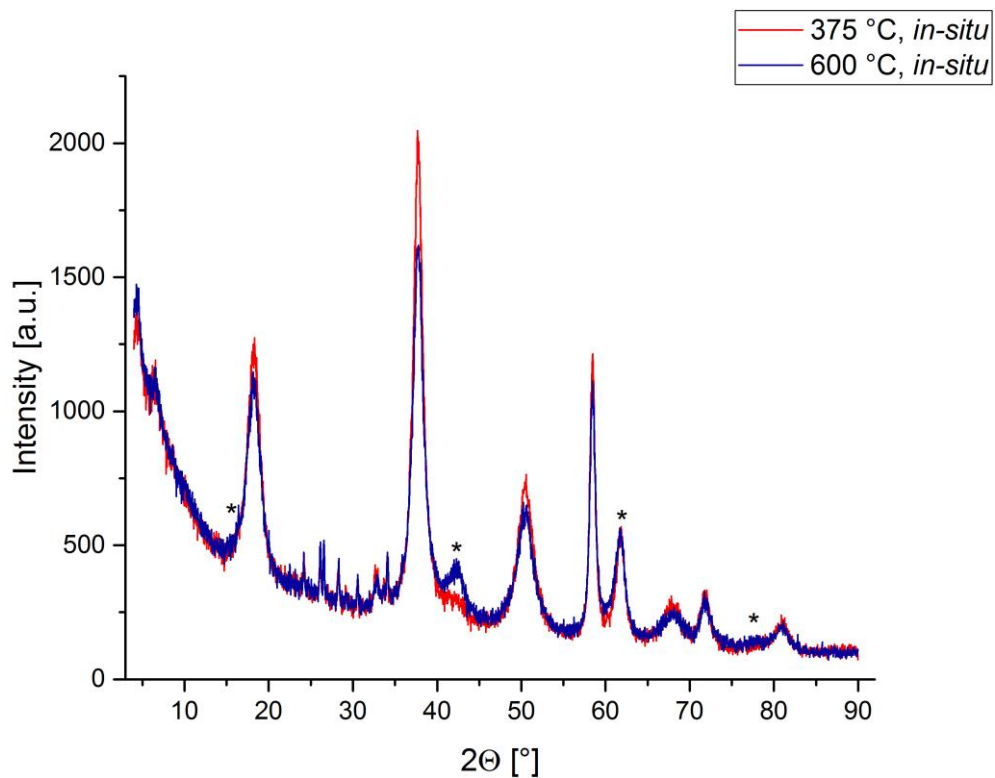


**Figure S9.** Diffractograms showing the final conversion of the different samples described in figure 9. Asterisks mark the isolated MgO-peaks.

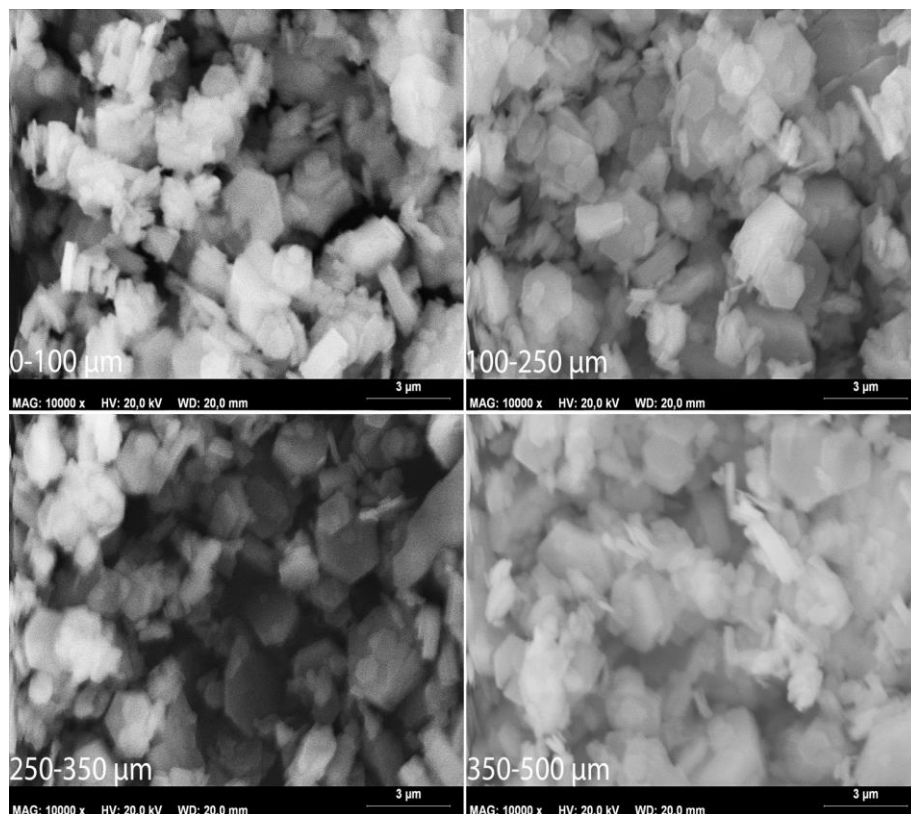


**Figure S10.** SEM-images of sieve-fractions. MgO calcinated for 4 hours at 375 °C, 10.000 fold magnification.



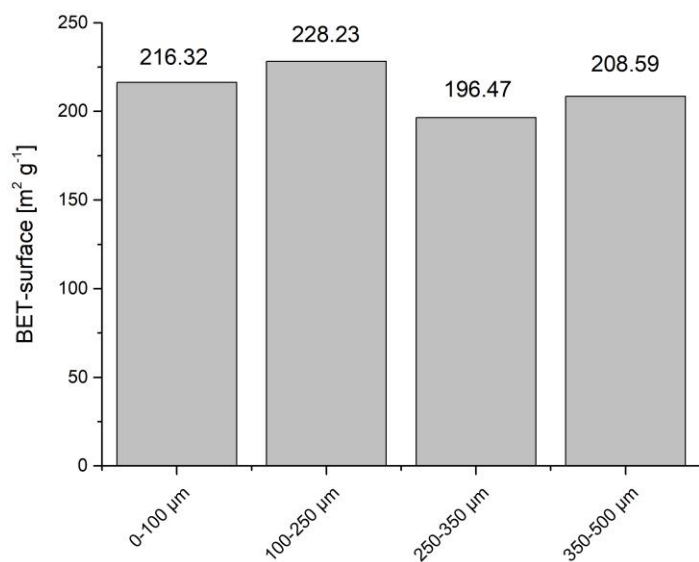


**Figure S11.** BET-surface of the different MgO-sieve fractions.

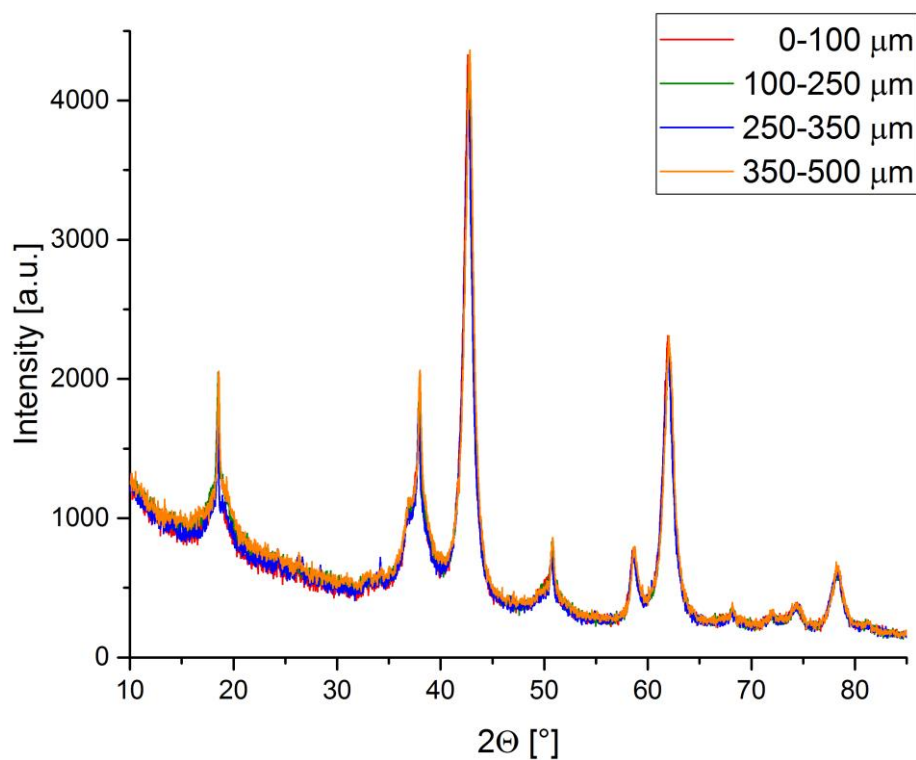


**Figure S12.** Diffractograms showing the final conversion of the different samples described in figure 10.

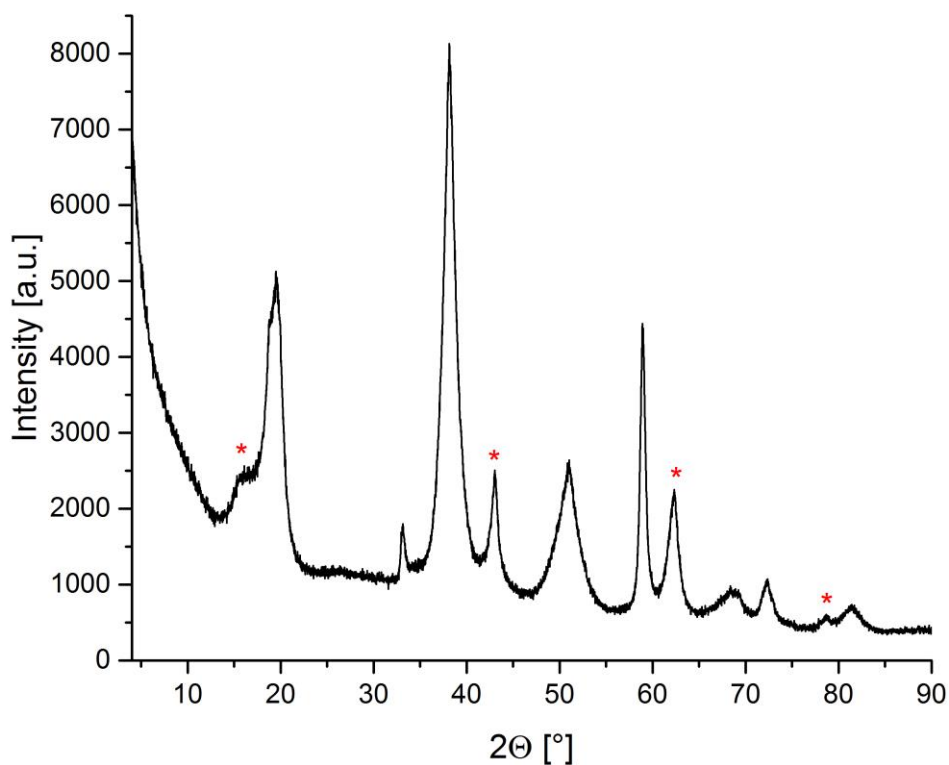


**Figure S13.** Diffractogram showing the final conversion of the fluidized bed experiment. Asterisks mark the isolated MgO-peaks.

**Table S1.** Specific surface areas for the MgO samples, obtained for various calcination times and temperatures. Surface of untreated Mg(OH)<sub>2</sub>: 4.21 m<sup>2</sup>g<sup>-1</sup>

Calcination time [h]	300 °C [m <sup>2</sup> g <sup>-1</sup> ]	350 °C [m <sup>2</sup> g <sup>-1</sup> ]	375 °C [m <sup>2</sup> g <sup>-1</sup> ]	400 °C [m <sup>2</sup> g <sup>-1</sup> ]	450 °C [m <sup>2</sup> g <sup>-1</sup> ]	600 °C [m <sup>2</sup> g <sup>-1</sup> ]
2	13.4	168.4	178.0	268.1	149.0	60.3
4		215.6	294.5	275.7		
6		241.3	278.0	262.0		
8		243.8	255.9	202.8		
10		257.5	247.3	218.3		
12	48.8	267.2	237.0	216.0	138.4	35.2

# Influence of the Particle Morphology on Cycle Stability and Hydration Behavior of Magnesium Oxide

Danny Müller,<sup>\*a</sup> Christian Knoll,<sup>a,b</sup> Werner Artner,<sup>c</sup> Jan M. Welch,<sup>d</sup> Norbert Freiberger,<sup>e</sup> Roland Nilica,<sup>e</sup> Elisabeth Eitenberger,<sup>f</sup> Gernot Friedbacher,<sup>f</sup> Michael Harasek,<sup>b</sup> Klaudia Hradil,<sup>c</sup> Andreas Werner,<sup>g</sup> Herwig Peterlik,<sup>h</sup> Peter Weinberger<sup>a</sup>

<sup>a</sup> Institute of Applied Synthetic Chemistry, TU Wien, Getreidemarkt 9, 1060 Vienna, Austria.

<sup>b</sup> Institute of Chemical, Environmental & Biological Engineering, TU Wien, Getreidemarkt 9, 1060 Vienna, Austria.

<sup>c</sup> X-Ray Center, TU Wien, Getreidemarkt 9, 1060 Vienna, Austria

<sup>d</sup> Atominstitut, TU Wien, Stadionallee 2, 1020 Vienna, Austria.

<sup>e</sup> RHI-AG, Magnesitstraße 2, 8700 Leoben, Austria.

<sup>f</sup> Institute of Chemical Technologies and Analytics, TU Wien, Getreidemarkt 9, 1060 Vienna, Austria

<sup>g</sup> Institute for Energy Systems and Thermodynamics, TU Wien, Getreidemarkt 9, 1060 Vienna, Austria.

<sup>h</sup> Faculty of Physics, University of Vienna, Boltzmannngasse 5, 1090 Vienna, Austria

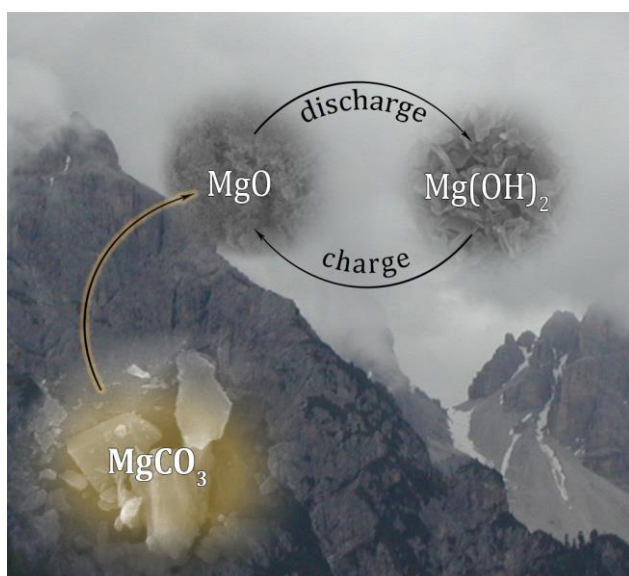
\*Corresponding author      [danny.mueller@tuwien.ac.at](mailto:danny.mueller@tuwien.ac.at)

## Highlights:

- Aerobic calcination of  $\text{Mg}(\text{OH})_2$ ,  $\text{MgCO}_3$  and  $\text{MgC}_2\text{O}_4 \cdot 2\text{H}_2\text{O}$  results in MgO of different particle morphology.
- A correlation between rehydration reactivity of MgO and its particle morphology was established.
- A regeneration process for spent MgO, restoring the initial reactivity, was developed.

**Keywords:** particle morphology, magnesium, cycle stability, hydration reactivity, thermochemistry

## Graphical Abstract



## Abstract

Magnesium oxide ( $\text{MgO}$ ) is a promising material for thermochemical energy storage of medium temperature waste heat. The modest calcination temperature of  $\text{Mg(OH)}_2$  ( $350\text{ }^\circ\text{C} - 450\text{ }^\circ\text{C}$ ) complements a broad variety of waste heat sources in various industrial production processes perfectly. So far, the main obstacle to application of the material in energy storage systems is its limited cycle stability. To overcome this issue,  $\text{Mg(OH)}_2$ ,  $\text{MgCO}_3$  and  $\text{MgC}_2\text{O}_4 \cdot 2\text{H}_2\text{O}$  were compared as precursor materials for  $\text{MgO}$ -production. Depending on the precursor, the particle morphology of the resulting  $\text{MgO}$  changes, resulting in different hydration behavior and cycle stability. A regeneration step developed during the study, leading to decomposition of agglomerates after repeated calcination / hydration cycles, restores the initial reactivity of the material. The herein presented variation of particle morphology and regeneration of spent material overcome the major obstacles of the  $\text{Mg(OH)}_2$  /  $\text{MgO}$  energy storage process.

## 1. Introduction

Energy management is a major challenge for our society, requiring equal measures of political and scientific involvement.[1] Energy supply, sustainable, environmentally benign energy production and efficient utilization are key issues in managing global energy use.[2]

Energy management may, in many cases, be better expressed as ‘heat management,’ as heat is the most ubiquitous form of energy. In nearly all types of electrical power plants, as well as in most industrial processes, heat is used as the driving force and operating medium. Within this context, the utilization of waste heat, accounting for 2/3 of overall global energy production, is an extensively investigated field.[3] The use of waste heat flows includes several aspects, one of them being temporal decoupling of waste heat availability and demand, as the two are not necessarily correlated. The necessary storage may be realized using materials for sensible, latent

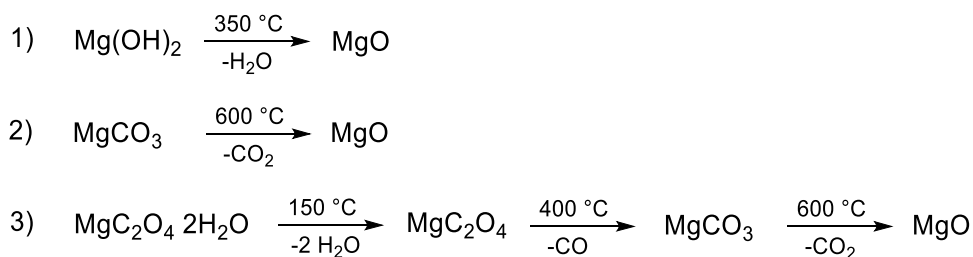
or thermochemical storage of energy (heat).[4-9] All three energy storage concepts offer advantages in specific areas of application.[6, 9, 10]

Thermochemical energy storage (TCES) features long-term storage, a wide range of compatible temperatures, applicability as a heat pump system and finally, high energy storage densities.[10-13] Based on these aspects, medium-temperature waste heat (up to 450 °C and extensively available from industrial processes) is perfectly suitable for TCES-systems.

An attractive TCES-material for medium-temperature applications is the system Mg(OH)<sub>2</sub> / MgO with a storage temperature around 350 °C.[14] Both Mg(OH)<sub>2</sub> and MgO are industrial base materials and are therefore available in large quantities at low prices.

Mg(OH)<sub>2</sub> / MgO as TCES-material is well known for this purpose, with many aspects related to its application in energy storage already investigated in literature. Kinetic investigations of dehydration and rehydration,[15, 16] mechanistic aspects,[17, 18] modification of the material by additions of lithium salts[16, 19, 20] or as composite material,[21, 22] as well as applicability in form of a chemical heat pump[23] were reported. Nonetheless, two key-issues preventing industrial application remain unaddressed: First, rehydration reactivity (completeness) and second, the cycle stability. Whereas for the limited cyclability observed thus far no satisfying solution has been found, the rehydration reactivity is addressed by the addition of lithium salts,[16, 19, 20] which are, however, quite expensive.

Although, on an industrial scale, MgO is produced by calcination of Mg(OH)<sub>2</sub> or MgCO<sub>3</sub>,[24]\* aerobic calcination of any other suitable Mg-compound may result in formation of MgO by stepwise decomposition. In scheme 1 this is demonstrated at the example of three inorganic magnesium salts:



**Scheme 1.** Thermal decomposition of various MgO-precursors: 1) Mg(OH)<sub>2</sub> 2) MgCO<sub>3</sub> 3) MgC<sub>2</sub>O<sub>4</sub>·2H<sub>2</sub>O

So far, investigations of the rehydration of MgO for thermochemical energy storage have largely neglected material history. As Mg(OH)<sub>2</sub>, MgCO<sub>3</sub>, MgC<sub>2</sub>O<sub>4</sub>·2H<sub>2</sub>O and MgO crystallize in different crystal systems (table 1) and feature notably different particle morphologies, MgO samples originating from different precursors should not necessarily show the same rehydration behavior and cycle stability. This assumption is supported by previous studies, showing that the lower rehydration reactivity of MgO[26] compared to *e.g.* CaO[27] is mainly caused by the

---

\* Both precursors are found in natural deposits, but whereas MgCO<sub>3</sub> is won industrially by mining, in the case of Mg(OH)<sub>2</sub> the industrial production occurs via the serpentinite- or seawater process.[25] Shand MA. The Chemistry and Technology of Magnesia. John Wiley & Sons Inc, Hoboken, New Jersey. 2006.

kinetic barrier of the water dissociation on the surface.[28] The disfavored H<sub>2</sub>O-dissociation as first step in formation of Mg(OH)<sub>2</sub> occurs mainly at surface defects, edges, step edges, or corner sites, exhibiting a lower dissociation energy barrier.[29] Therefore, a variation of the particle morphology and history of the material is expected to affect the rehydration behavior. Although, all precursors result in compositionally indistinguishable MgO samples, the particle morphology, crystallographic orientation and thus orientation of the reactive surface of the material are not necessarily the same.

**Table 1.** Crystallographic comparison of selected MgO-precursors and MgO

	Mg(OH) <sub>2</sub> [30]	MgCO <sub>3</sub> [31]	MgC <sub>2</sub> O <sub>4</sub> ·2H <sub>2</sub> O[32]	MgO[33]
Crystal system	Hexagonal	Rhombohedral	Orthorhombic	Cubic
Space group	P $\bar{3}m1$ (164)	R $\bar{3}c$ (167)	Fddd (70)	Fm $\bar{3}m$ (225)
a [Å]	3.1486(1)	4.637(1)	5.3940(11)	4.2113(5)
b [Å]	3.1486(1)	4.637(1)	12.691(3)	4.2113(5)
c [Å]	4.7713(1)	15.023(3)	15.399(3)	4.2113(5)
$\alpha$ [°]	90	90	90	90
$\gamma$ [°]	120	120	90	90
V [Å <sup>3</sup> ]	40.96	279.74	1054.14	74.69

To verify the hypothesis of the from materials' chemical history influenced reactivity of the material and thereby identify novel attractive and more economic approaches to an enhanced cyclability and rehydration rate, MgO from different chemical precursors including Mg(OH)<sub>2</sub>, MgCO<sub>3</sub> and MgC<sub>2</sub>O<sub>4</sub>·2H<sub>2</sub>O has been studied.

## 2. Experimental Methodology

### 2.1 Material

Mg(OH)<sub>2</sub> powder (particle size  $\leq 5 \mu\text{m}$ ) and MgCO<sub>3</sub> (particle size  $\leq 200 \mu\text{m}$ ) were supplied by RHI-AG. MgC<sub>2</sub>O<sub>4</sub>·2H<sub>2</sub>O was purchased from abcr and the particle fraction  $\leq 200 \mu\text{m}$  was used as supplied. The materials were calcined in an electric furnace under air and a static atmosphere for 4h at variable temperatures (Mg(OH)<sub>2</sub>: 375 °C; MgCO<sub>3</sub>: 550 °C, 600 °C, 650 °C;



MgC<sub>2</sub>O<sub>4</sub>·2H<sub>2</sub>O: 650 °C). For regeneration, the *in-situ* calcined material from the P-XRD measurement was kept for 24 h in liquid water under ambient conditions.

## 2.2 BET-surface

The specific surface of the samples was determined by nitrogen sorption measurements, which were performed on an ASAP 2020 (Micromeritics) instrument. The samples (amounts between 100-200 mg) were degassed under vacuum at 80 °C overnight prior to measurement. The surface area was calculated according to Brunauer, Emmett and Teller (BET) and t-plot methods.

## 2.3 Powder X-Ray diffraction with in-situ hydration

Hydration of calcined samples was performed in an Anton Paar XRK 900 sample chamber, connected to an evaporation coil kept at 300 °C. Using an HPLC-pump, 3 ml min<sup>-1</sup> water was evaporated and the resulting 3.72 L min<sup>-1</sup> steam were passed through the sample (4 mm thickness) with 0.2 L min<sup>-1</sup> nitrogen as carrier gas. As the sample is completely penetrated by the X-rays, the obtained diffractograms are an average through the complete sample. The diffractograms were evaluated using the PANalytical program suite HighScorePlus v3.0d. A background correction and a K<sub>α2</sub> strip were performed. Phase assignment is based on the ICDD-PDF4+ database, the exact phase composition, shown in the conversion plots, was obtained via Rietveld-refinement in the program suite HighScorePlus v3.0d. All quantifications based on P-XRD are accurate within of ±5 %.

## 2.4 Scanning electron microscopy

SEM images were recorded on gold coated samples with a Quanta 200 SEM instrument from FEI under low-vacuum at a water vapor pressure of 80 Pa to prevent electrostatic charging.

## 2.5 Small-angle X-Ray Scattering

The samples were prepared either as powder between two pieces of tape or in a sealed capillary. Patterns were recorded using a microsource with X-rays from a copper target (Incoatec High Brilliance, wavelength 0.1542 nm, CuK<sub>α</sub>), a point focus (Nanostar from Bruker AXS) and a 2D detector (VÅNTEC 2000). The X-ray patterns were radially averaged and background corrected to obtain scattering intensities in dependence on the scattering vector  $q=(4\pi/\lambda) \sin\theta$ , with  $2\theta$  being the scattering angle.

The fit function from *Beaucage*[34] to describe scattering intensities of complex systems with a broad size distribution consists of a power law and Guinier's exponential form,

$$I(q) \propto G \exp\left(\frac{-q^2 R_g^2}{3}\right) + B \left[ \frac{(\text{erf}(qR_g/\sqrt{6}))^3}{q} \right]^{d_f} \quad (1)$$

where  $G$  and  $B$  are the numerical prefactors,  $d_f$  is the fractal dimension,  $R_g$  is the radius of gyration and  $erf(x)$  is the error function. To describe the particle interference and thus the tendency of particles to agglomerate, additionally a structure factor from a hard sphere model was used,[35, 36]

$$I(q) \propto \left( G \exp\left(\frac{-q^2 R_g^2}{3}\right) + B \left[ \frac{(\text{erf}(qR_g/\sqrt{6}))^3}{q} \right]^{d_f} \right) S(q)$$

with  $S(q) = 1/(1 + 24\eta G_{int}(2qR_{HS})/(2qR_{HS}))$  (2)

and  $R_{HS}$  being the hard sphere radius describing a typical distance of objects,  $\eta$  the hard sphere volume factor for characterizing the amount of agglomeration, and  $G_{int}$  a function derived in Kinning *et al.*[35]

### 3. Results and Discussion

The different crystallography of the three investigated materials described in table 1 is also observed in the SEM-images of its untreated and calcined samples. In figure 1 a comparison of SEM-pictures of the various MgO-precursors and the resulting MgO-samples, obtained after thermal decomposition, is shown. Whereas  $\text{Mg}(\text{OH})_2$  particles feature a characteristic hexagonal shape and are comparably flat, both  $\text{MgCO}_3$  and  $\text{MgC}_2\text{O}_4 \cdot 2\text{H}_2\text{O}$  consist of irregularly shaped particles. In the case of  $\text{MgC}_2\text{O}_4 \cdot 2\text{H}_2\text{O}$ , a layered structure within the spherical particles is observed.

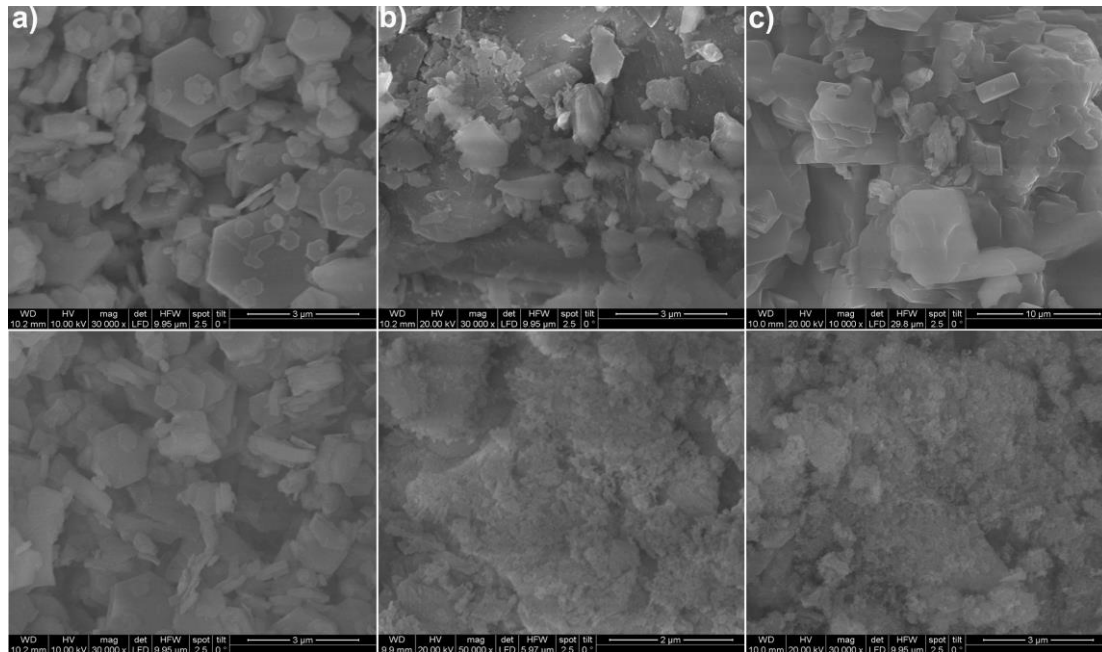


**Figure 1.** SEM-pictures of a)  $\text{Mg}(\text{OH})_2$ , b)  $\text{MgCO}_3$ , c)  $\text{MgC}_2\text{O}_4 \cdot 2\text{H}_2\text{O}$  before calcination (first row) and after calcination (second row)

The particle morphology of the materials changes during calcination (figure 1, second row), leading to three differently textured MgO-samples. Whereas for Mg(OH)<sub>2</sub> (figure 1a) calcination results in an unchanged particle shape, both for MgCO<sub>3</sub> (figure 1b) and MgC<sub>2</sub>O<sub>4</sub>·2H<sub>2</sub>O (figure 1c) surface fragmentation attributed to the release of gas and the structural transformation takes place. Nevertheless, larger particles resulting from the initial texture of the starting material are still present.

On the nanoscale, small-angle X-ray scattering (SAXS) reveals transition of the material from a dense solid to a highly porous material on calcination (see figure S1). We modelled the nanostructured MgO by a unified Guinier/power law[34] resulting in a radius of gyration for the size of the particles and an agglomeration with a structure factor from a hard sphere model describing the agglomeration of particles with a typical distance  $2R_{HS}$  and the packing density with a hard sphere volume ratio  $\eta$ . [35, 36] The detailed fit parameters are found in the supporting information (table S1). In general, the gyration radius of MgO particles calcined from MgCO<sub>3</sub> and MgC<sub>2</sub>O<sub>4</sub>·2H<sub>2</sub>O is about 6.6 and 5.1 nm, respectively, in comparison to about 2 nm if calcined from Mg(OH)<sub>2</sub>. In contrast, the values of  $\eta=0.18$  and a fractal dimension of  $d_f=2.8$  indicate that MgO from Mg(OH)<sub>2</sub> consists of small, agglomerated particles with a wide size distribution, whereas MgO from other precursors is built up of larger, denser nanoparticles ( $\eta$  close to zero,  $d_f=4$ )

To correlate particle morphology with rehydration reactivity and cycle stability for the different MgO samples, rehydration experiments were monitored by *in-situ* powder X-ray diffraction (P-XRD) to quantify the reaction progress. As in previous experiments, the rehydration reactivity of the MgO produced from Mg(OH)<sub>2</sub> was found quite limited.[26] In a first step, the amount of water vapour introduced into the reaction chamber was varied. Increasing the vapour flow from 1 g min<sup>-1</sup> to 3 g min<sup>-1</sup> enhanced the rehydration conversion of MgO to 67 % from 44 % (figure 2a). To assess the cycle stability for the increased vapour flow, five consecutive rehydration - calcination cycles were performed (figure 2b). Similarly, to previous experiments with lower vapour flows, the rehydration yield decreased over 5 cycles, to a final Mg(OH)<sub>2</sub> conversion of only 14 %. Even after the first cycle the rehydration conversion was depleted to 43 %.

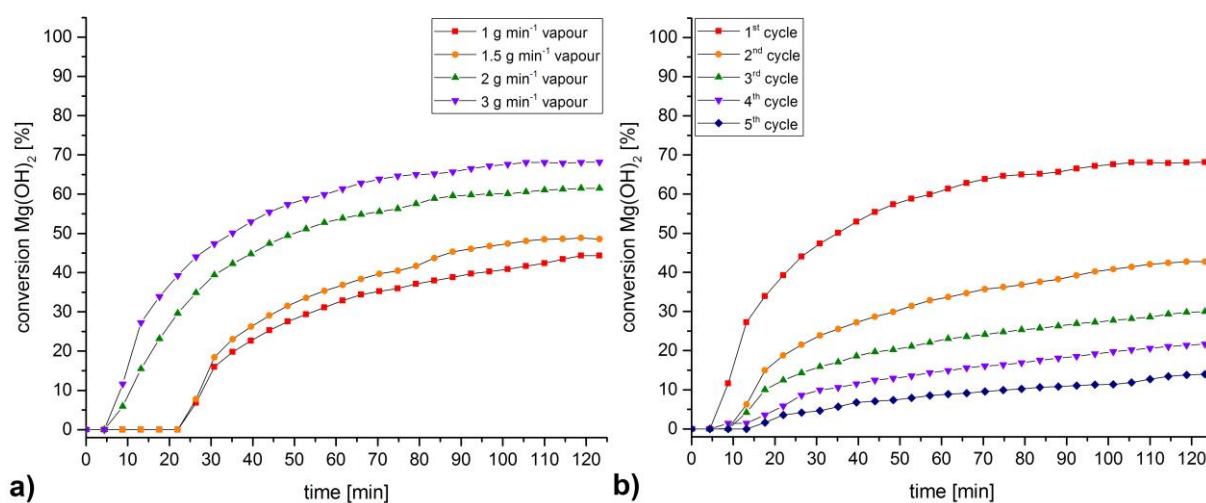


**Figure 2.** a) Rehydration of Mg(OH)<sub>2</sub>-originating MgO with various vapour flow rates. b) Cycle stability of Mg(OH)<sub>2</sub>-originating MgO

For MgO produced by calcination of Mg(OH)<sub>2</sub> a strong correlation between reactivity, accessible surface area and calcination temperature has been established.[26] Higher calcination temperatures promote sintering of the particles, leading to a decreased porosity, increased MgO crystal size and decreased rehydration yield.

To assess the possibility of a similar effect for MgO originating from MgCO<sub>3</sub>, initial studies of the correlation between calcination temperature, BET-surface and rehydration reactivity were made. For this purpose, samples of MgCO<sub>3</sub> were calcined at 550 °C, 600 °C and 650 °C for 3, 6, 9 and 12 hours. The MgO formed from MgCO<sub>3</sub> calcined for 6 h at 600 °C had the highest surface area (figure S2). Nevertheless, attempted rehydration of all samples by water vapor in the P-XRD failed, showing no Mg(OH)<sub>2</sub> formation within 120 minutes. This finding was quite unexpected, but supported the hypothesis that materials of different origin will show different rehydration behavior.

It should be emphasized, that on prolonged exposure to water vapour, very slow conversion to Mg(OH)<sub>2</sub> is observed for the samples obtained by direct calcination of MgCO<sub>3</sub>. To ascertain whether rehydration of this material could be driven by longer exposure to a vast excess of reactant, the samples were stored in liquid water. After 24 h reaction time in water at room-temperature, according to P-XRD measurements the material had been completely transformed to Mg(OH)<sub>2</sub>. After calcination, the BET-surface of those samples was found to be slightly higher than for the MgO originating directly from MgCO<sub>3</sub> (figure S3). The rehydration experiments in the P-XRD were repeated successfully for all materials (for detailed rehydration rates see figure S4). Ranked according to their final conversion to Mg(OH)<sub>2</sub>, the most reactive material within this series was obtained by calcination of MgCO<sub>3</sub> at 600 °C for 6 h (figure 3) and subsequent rehydration in liquid water. A final conversion to 84 % Mg(OH)<sub>2</sub> was not only by far the highest yield for the MgCO<sub>3</sub>-originating series, but also notably more than for MgO originating from Mg(OH)<sub>2</sub> (67 % final conversion).

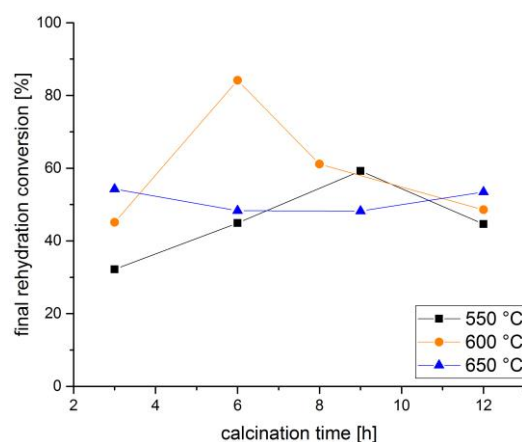


**Figure 3.** Final conversion for rehydration of the various MgCO<sub>3</sub>-originating MgO samples in the P-XRD.

SEM images demonstrate, that the particle morphology of  $\text{MgCO}_3$  (figure 4a) is retained after calcination, although the formerly distinct edges and surfaces are now covered by smaller scales (figure 4b). During the hydration of the calcined material in liquid water the large particles disintegrate into smaller platelets (figure 4c) that do not feature the characteristic hexagonal morphology observed for  $\text{Mg}(\text{OH})_2$  (see figure 1). A subsequent calcination of material rehydrated in liquid water retains the aforementioned platelet morphology (figure 4d).

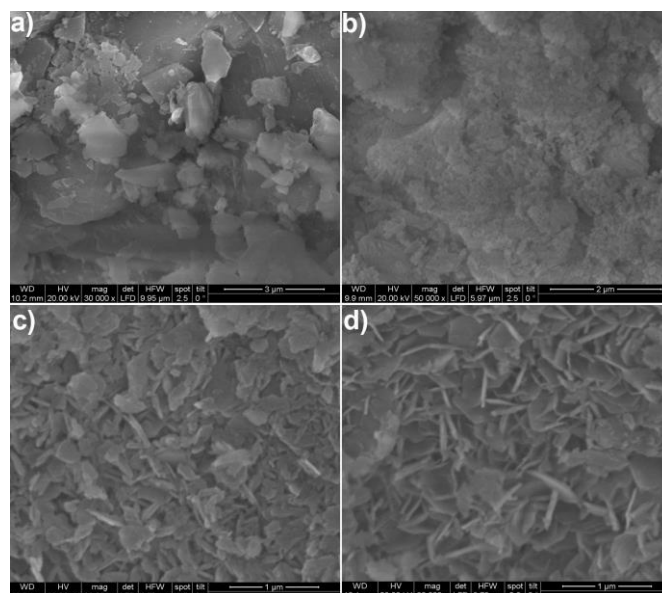


**Figure 4.** SEM images of a)  $\text{MgCO}_3$  b) calcined  $\text{MgCO}_3$  c) calcined  $\text{MgCO}_3$ , rehydrated for 24 h in liquid water d) material from image c after calcination

The inactive  $\text{MgO}$  obtained after calcination of  $\text{MgCO}_3$  undergoes a notable transformation in particle shape, as can be seen in the SEM images, which may be attributed to the volume work on  $\text{Mg}(\text{OH})_2$  formation. Liquid water seems necessary to assist the rehydration-related rearrangement of the material. SAXS intensities (figure S5) show that on each rehydration of the  $\text{MgO}$ -intermediates the particle morphology is unchanged to a large extent. From the larger scattering intensity, a highly porous nanostructure, retained during rehydration, may be extrapolated. At the same time, a general decrease in particle size was also observed in the SEM images (figure 4).

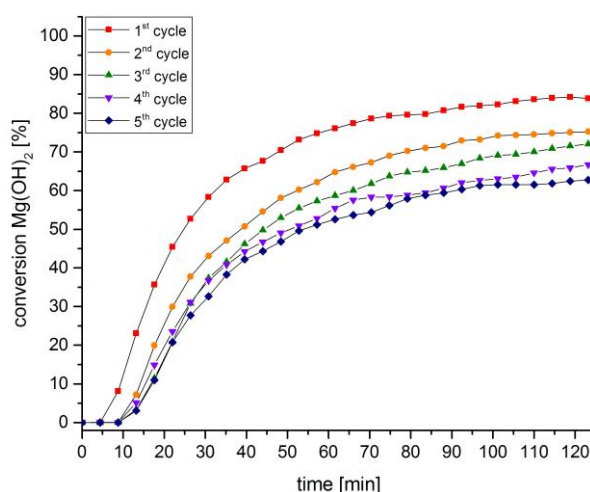




**Figure 5.** Cycle stability of MgCO<sub>3</sub>-originating MgO (after rehydration in liquid water and subsequent calcination)

The carbonate-derived MgO (originating from MgCO<sub>3</sub>, subsequently activated by 24 h rehydration in liquid water, followed by calcination) was also investigated in terms of cycle stability (figure 5). For the carbonate-derived MgO a decrease in rehydration reactivity was also detected, although to a lesser extent than was observed for material originating from Mg(OH)<sub>2</sub>. Over five cycles the rehydration conversion drops to 57 % (84 % in the 1<sup>st</sup>, 75 % in the 2<sup>nd</sup> cycle).

As a third precursor for preparation of reactive MgO, MgC<sub>2</sub>O<sub>4</sub>·2H<sub>2</sub>O was investigated. Since MgC<sub>2</sub>O<sub>4</sub>·2H<sub>2</sub>O decomposes in a stepwise fashion via MgCO<sub>3</sub> (see scheme 1), only samples calcined in the furnace at 600 °C for 6 h were investigated. A comparison of the SEM-images in figure 6, presenting the morphology of the different intermediates (initial oxalate material [figure 6a], calcined material [figure 6b], MgO after rehydration in liquid water [figure 6c], freshly calcined material [figure 6d]) reveals similar behavior as for MgCO<sub>3</sub>. Calcination of the initial material resulted in partial fragmentation, whereas subsequent treatment with liquid water and re-calcination forced the material to adopt a lamellar structure. In contrast to the MgO originating from MgCO<sub>3</sub>, thinner platelets were formed, the structure of which is preserved after calcination. The typical hexagonal shape of MgO derived from Mg(OH)<sub>2</sub> was not observed.

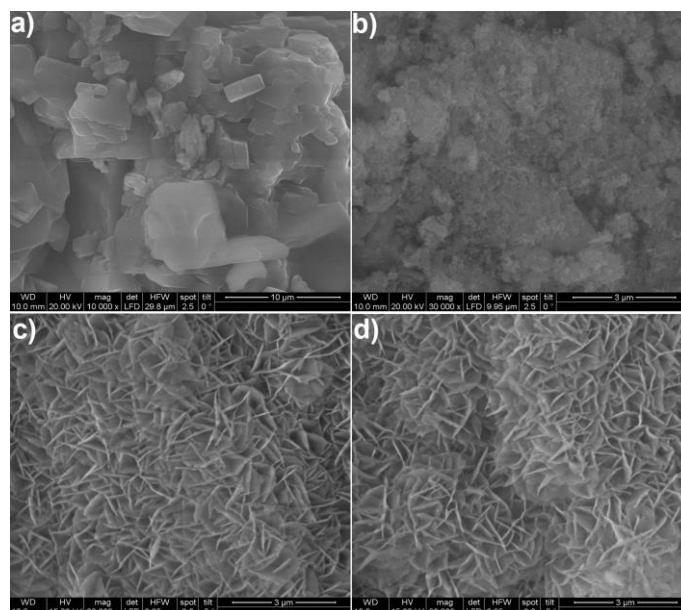


**Figure 6.** SEM images of a) MgC<sub>2</sub>O<sub>4</sub>·2H<sub>2</sub>O b) calcined MgC<sub>2</sub>O<sub>4</sub>·2H<sub>2</sub>O c) calcined MgC<sub>2</sub>O<sub>4</sub>·2H<sub>2</sub>O, rehydrated for 24 h in liquid water d) material from image c after calcination

Not only SEM, but also interpretation of the SAXS data results yields a similar understanding as for MgCO<sub>3</sub>. Rehydration of MgO originating from MgC<sub>2</sub>O<sub>4</sub>·2H<sub>2</sub>O in liquid water results in conservation of the original particle morphology to a wide extent (figure S6). The porous nanostructure formed is preserved during rehydration. Accordingly, the increased SAXS-intensities observed for the rehydrated material seem to arise from the formation of smaller particles (SEM images, Fig. 6).



To determine the reactivity of the  $\text{MgC}_2\text{O}_4 \cdot 2\text{H}_2\text{O}$ -based  $\text{MgO}$ , both the material obtained by direct calcination of  $\text{MgC}_2\text{O}_4 \cdot 2\text{H}_2\text{O}$  and that resulting from the rehydration / calcination sequence was subject to rehydration in the P-XRD. Unlike the case of  $\text{MgCO}_3$ , the directly calcined material was found to be reactive to rehydration, resulting in a final conversion of 68 % (figure 7a).

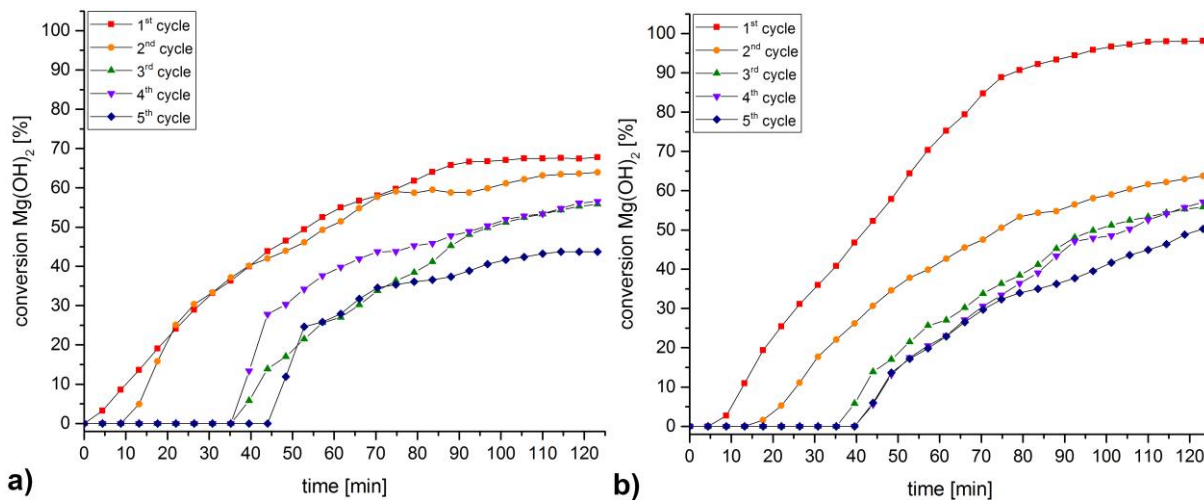


**Figure 7.** a) Direct rehydration and cycle stability of  $\text{MgC}_2\text{O}_4$ -originating  $\text{MgO}$ . b) Rehydration and cycle stability of  $\text{MgC}_2\text{O}_4$ -originating  $\text{MgO}$  after rehydration in liquid water and subsequent calcination

The sample previously rehydrated in liquid  $\text{H}_2\text{O}$  and subsequently calcined could be fully rehydrated in the 1<sup>st</sup> cycle, but in the 2<sup>nd</sup> cycle the rehydration conversion decreased to 64 % (figure 7b). After five cycles both samples gave a comparable final conversion of slightly less than 50 %  $\text{Mg(OH)}_2$ . Although, initial treatment with liquid water led to full rehydration of the  $\text{MgO}$  during the first cycle, due to a large decrease in conversion rate, modest overall-performance and a higher price compared to the other materials studied,  $\text{MgC}_2\text{O}_4 \cdot 2\text{H}_2\text{O}$  is probably not suitable as a competitive  $\text{MgO}$  precursor. A summarizing overview of the calcination and rehydration conditions for various  $\text{MgO}$ -precursor materials is given in scheme S1.

Based on the conversion-enhancing effect of rehydrating calcined material in liquid water, both a sample of spent  $\text{MgO}$  originating from  $\text{Mg(OH)}_2$  and one from  $\text{MgCO}_3$  after the 5<sup>th</sup> rehydration cycle was calcined one more time and then rehydrated for 24 h in liquid water. At that point, P-XRD analysis showed complete transformation to  $\text{Mg(OH)}_2$  for both samples originating from different. Both  $\text{Mg(OH)}_2$ -samples were now subjected further 5 subsequent rehydration / calcination cycles in the P-XRD, followed by a further regeneration in liquid water and another 5 subsequent rehydration / calcination cycles in the P-XRD. Applying this sequence, for both a  $\text{MgO}$ -sample originating from  $\text{Mg(OH)}_2$  and  $\text{MgCO}_3$  the performance and conversion rates for 15 consecutive cycles, including two regeneration steps after 5 cycles each was determined (figure 8).

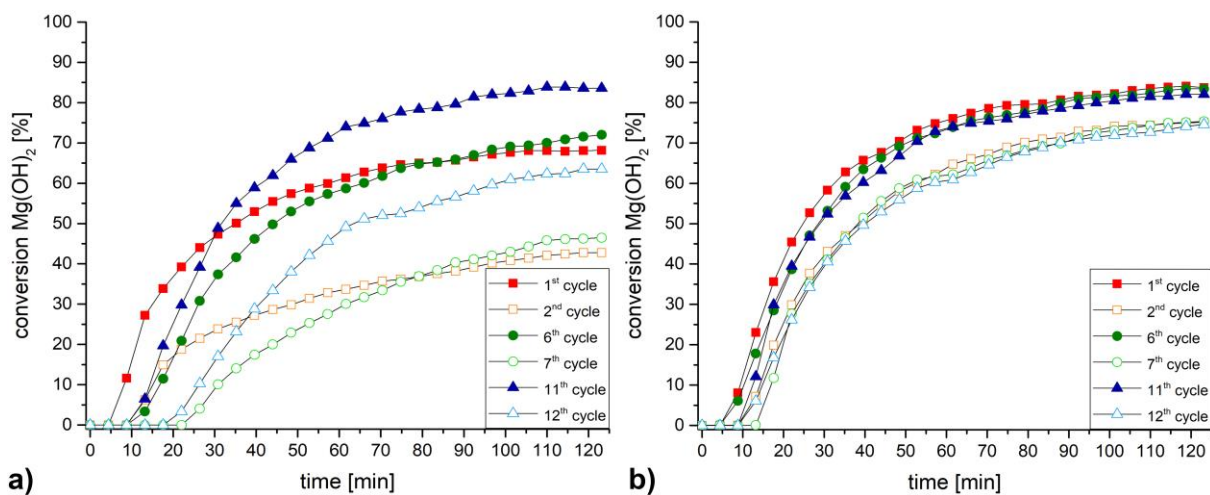


**Figure 8.** Selected conversion rates from a series of 15 consecutive calcination / hydration cycles, including two regeneration steps in liquid water after the 5<sup>th</sup> and the 10<sup>th</sup> cycle. a) Mg(OH)<sub>2</sub>-originating MgO after regeneration b) MgCO<sub>3</sub>-originating MgO after regeneration

In figure 8a the rehydration reactivity for the 15 subsequent cycles for MgO originating from Mg(OH)<sub>2</sub> is shown. Surprisingly, after the first regeneration (cycle 6) the rehydration reactivity was slightly enhanced compared to the very 1<sup>st</sup> cycle, after the second regeneration (cycle 10) the reactivity increased further. Nevertheless, the depletion evidenced in the second cycle was retained even after the second cycles after regeneration, as observed for cycles 6 and 12.

In the case of MgO derived from MgCO<sub>3</sub>, a different but even more promising effect was observed: The spent material could be completely regenerated to reproduce the reactivity observed for the first cycle. Even the second cycle after each regeneration process (cycle 7 and 12) was comparable to the ‘first’ second cycle.

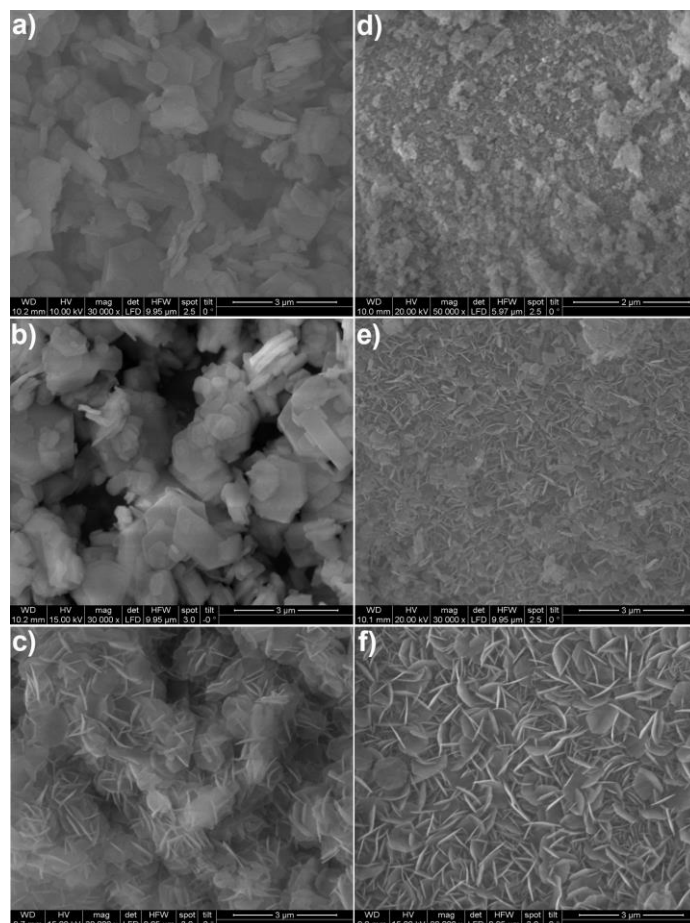


**Figure 9.** SEM-images of various intermediates during calcination / rehydration / regeneration for Mg(OH)<sub>2</sub>- (left) and MgCO<sub>3</sub>-originating MgO (right)  
 a) Mg(OH)<sub>2</sub>-originating MgO b) Mg(OH)<sub>2</sub>-originating MgO after 5 rehydration / calcination cycles c) material of image b after regeneration for 24 h in liquid H<sub>2</sub>O d) MgCO<sub>3</sub>-originating MgO e) MgCO<sub>3</sub>-originating MgO after 5 rehydration / calcination cycles f) material of image e after regeneration for 24 h in liquid H<sub>2</sub>O

To better understand the physical processes during regeneration, SEM-images of material during several stages of regeneration and cycling were compared. Despite differences in initial particle morphology (figure 9a and 9d), MgO originating from Mg(OH)<sub>2</sub> or MgCO<sub>3</sub> shows similar evolution of reactivity during repeated calcination / rehydration cycles. After five consecutive cycles, resulting in aged material of depleted rehydration reactivity (see figure 2 and figure 5), the particle morphology of Mg(OH)<sub>2</sub>-derived MgO (figure 9b) seems nearly unaffected. In contrast, for material originating from MgCO<sub>3</sub>, formation of larger spherical aggregates is observed (figure 9e). After regeneration for 24 h in liquid water both materials reveal a lamellar, platelet morphology devoid of the characteristic hexagonal brucite particle shape (figure 9c and 9f).

To directly monitor the rehydration / regeneration process, both a sample of MgO originating from Mg(OH)<sub>2</sub> and from MgCO<sub>3</sub> were observed during rehydration in liquid water by *in-situ* SAXS (figure S7, S8). Initial SAXS curves (black) and final SAXS curves (red) are highlighted to better visualize the data and clearly show the change in the inner structure of the particles. The main difference is the time required for structural recovery, which is about three-fold

shorter for  $\text{Mg}(\text{OH})_2$ -derived material compared to that from  $\text{MgCO}_3$  (figure S8), most likely due to the considerably larger particle sizes favored by the latter.

Within various repeated experiments the regeneration process described for spent MgO was found to be reproducible – on the one hand for the material of the same origin, on the other for materials of different origins. During the regeneration process, due to the comparably long reaction time and the vast excess of water, a complete conversion to  $\text{Mg}(\text{OH})_2$  as well as a regeneration of the particle morphology seems to occur. Both effects complement each other, restoring the original reactivity of the material.

The possibility of a regeneration of spent material is of utmost importance for assessing the economic feasibility of a TCES-material and energy storage process, as by prolonging the lifetime the materials investment costs are minimized. Additionally, by implementation of a continuous regeneration step into the process, regenerating after each discharging / charging cycle a defined amount of material, permanent high activity of the TCES-material circumventing efficiency losses by ageing would be ensured.

#### 4. Conclusion

MgO obtained by calcination of  $\text{Mg}(\text{OH})_2$ ,  $\text{MgCO}_3$  and  $\text{MgC}_2\text{O}_4 \cdot 2\text{H}_2\text{O}$  was compared regarding its rehydration reactivity and cycle stability to assess its applicability in thermochemical energy storage. The three different MgO-precursors led to three MgO samples featuring different particle morphologies with identical chemical compositions. Whereas  $\text{Mg}(\text{OH})_2$ - and  $\text{MgC}_2\text{O}_4 \cdot 2\text{H}_2\text{O}$  resulted in reactive MgO that could be rehydrated by water vapour to  $\text{Mg}(\text{OH})_2$  directly following calcination, material originating from  $\text{MgCO}_3$  resulted in no conversion on contact with water vapour. Only after rehydration in liquid water and subsequent calcination of the thus formed  $\text{Mg}(\text{OH})_2$ , 84 % of the resulting material could be rehydrated by water vapour. All materials investigated showed decreased rehydration reactivity during consecutive calcination / rehydration cycles, with  $\text{MgCO}_3$  derived MgO showing the smallest decline in reactivity. A regeneration step, consisting of rehydration of the spent material in liquid water over 24 h, restored the initial reactivity allowing for recycling of the material. In the case of  $\text{Mg}(\text{OH})_2$  derived material, the initial reactivity could even be improved by repeated regeneration of the material in liquid water.

The results reported herein confirm, that the reactivity of MgO towards rehydration is strongly correlated to origin and physicochemical history of the material. A detailed knowledge of ongoing processes and key parameters of material performance are crucial for its application in a thermochemical storage process.

#### Conflict of interest

The authors declare no conflict of interest

#### Acknowledgement

This work was financially supported by the Austrian Research Promotion Agency (FFG Forschungsförderungsgesellschaft), project 845020, 841150 and project 848876. The X-Ray center (XRC) of the Vienna University of Technology provided access to the powder X-Ray diffractometer.

## References

- [1] Rahm D. Sustainable Energy and the States, Essay on Politics Markets and Leadership. McFarland, North Carolina. 2002;1st ed.
- [2] IEA. Heating without global warming: Market developments and policy considerations for renewable heat. 2014.
- [3] IEA. Co-generation and Renewables. Solutions for a low-carbon energy future. <https://www.iea.org/publications/freepublications/publication/co-generation-and-renewables-solutions-for-a-low-carbon-energy-future.html>. 2011.
- [4] Bauer T, Steinmann W.D, Laing D, Tamme R. Thermal Energy Storage Materials and Systems. Annual Review of Heat Transfer. 2012;15:131-77.
- [5] Hasnain S.M. Review on sustainable thermal energy storage technologies, Part I: heat storage materials and techniques. Energy Conversion and Management. 1998;39:1127-38.
- [6] Xu J, Wang RZ, Li Y, A review of available technologies for seasonal thermal energy storage. Solar Energy. 2014;610-38.
- [7] Zhang H, Baeyens J, Cáceres G, Degève J, Lv Y. Thermal energy storage: Recent developments and practical aspects. Progress in Energy and Combustion Science. 2016;53:1-40.
- [8] Cabeza LF, Castell A, Barreneche C, de Gracia A, Fernández AI. Materials used as PCM in thermal energy storage in buildings: A review. Renewable and Sustainable Energy Reviews. 2011;15:1675-95.
- [9] Dinker A, Agarwal M, Agarwal GD. Heat storage materials, geometry and applications: A review. Journal of the Energy Institute. 2015.
- [10] Abedin AH, Rosen MA, A Critical Review of Thermochemical Energy Storage Systems. The Open Renewable Energy Journal. 2011;4:42-6.
- [11] Cot-Gores J, Castell A, Cabeza LF. Thermochemical energy storage and conversion: A state-of-the-art review of the experimental research under practical conditions. Renewable and Sustainable Energy Reviews. 2012;16:5207-24.
- [12] Solé A, Fontanet X, Barreneche C, Martorell I, Fernández AI, Cabeza LF. Parameters to take into account when developing a new thermochemical energy storage system. Energy Procedia. 2012;30:380-7.
- [13] Yan T, Wang RZ, Li TZ, Wang TW, Ishugah TF, A review of promising candidate reactions for chemical heat storage. Renewable and Sustainable Energy Reviews. 2015;43:13-31.
- [14] Pan Z, Zhao CY. Dehydration/hydration of MgO/H<sub>2</sub>O chemical thermal storage system. Energy. 2015;82:611-8.
- [15] Kuleci H, Schmidt C, Rybacki E, Petrishcheva E, Abart R. Hydration of periclase at 350 °C to 620 °C and 200 MPa: experimental calibration of reaction rate. Mineralogy and Petrology. 2015;110:1-10.
- [16] Myagmarjav O, Ryu J, Kato Y. Dehydration kinetic study of a chemical heat storage material with lithium bromide for a magnesium oxide/water chemical heat pump. Progress in Nuclear Energy. 2015;82:153-8.
- [17] Birchal VS, Rocha SDF, Mansur MB, Ciminelli VST. A simplified mechanistic analysis of the hydration of magnesia. The Canadian Journal of Chemical Engineering. 2001;79:507-11.



- [18] Zhou S. Hydration mechanisms of magnesia-based refractory bricks. PhD-thesis. 2004.
- [19] Ishitobi H, Hirao N, Ryu J, Kato Y. Evaluation of Heat Output Densities of Lithium Chloride-Modified Magnesium Hydroxide for Thermochemical Energy Storage. *Industrial & Engineering Chemistry Research*. 2013;52:5321-5.
- [20] Myagmarjav O, Ryu J, Kato Y. Lithium bromide-mediated reaction performance enhancement of a chemical heat-storage material for magnesium oxide/water chemical heat pumps. *Applied Thermal Engineering*. 2014;63:170-6.
- [21] Shkatulov A, Ryu J, Kato Y, Aristov Y. Composite material “Mg(OH)<sub>2</sub>/vermiculite”: A promising new candidate for storage of middle temperature heat. *Energy*. 2012;44:1028-34.
- [22] Zamengo M, Ryu J, Kato Y. Composite block of magnesium hydroxide – Expanded graphite for chemical heat storage and heat pump. *Applied Thermal Engineering*. 2014;69:29-38.
- [23] Kato Y, Sasaki Y, Yoshizawa Y. Magnesium oxide/water chemical heat pump to enhance energy utilization of a cogeneration system. *Energy*. 2005;30:2144-55.
- [24] Morozov SA. Synthesis of Porous Magnesium Oxide by Thermal Decomposition of Basic Magnesium Carbonate. *Russian Journal of General Chemistry*. 2003;73:37-42.
- [25] Shand MA. *The Chemistry and Technology of Magnesia*. John Wiley & Sons Inc, Hoboken, New Jersey. 2006.
- [26] Müller D, Knoll C, Artner W, Welch JM, Freiburger N, Nilica R, et al. Influence of the Particle Morphology on Cycle Stability and Hydration Behavior of Magnesium Oxide. *Applied Energy*. 2017;submitted.
- [27] Criado YA, Alonso M, Abanades JC. Kinetics of the CaO/Ca(OH)<sub>2</sub> Hydration/Dehydration Reaction for Thermochemical Energy Storage Applications. *Industrial & Engineering Chemistry Research*. 2014;53:12594-601.
- [28] Hu XL, Carrasco J, Klimeš J, Michaelides A. Trends in water monomer adsorption and dissociation on flat insulating surfaces. *Physical Chemistry Chemical Physics*. 2011;13:12447.
- [29] Stankic S, Bernardi J, Diwald O, Knözinger E. Optical Surface Properties and Morphology of MgO and CaO Nanocrystals. *The Journal of Physical Chemistry B*. 2006;110:13866-71.
- [30] Kazimirov VY, Smirnov MB, Bourgeois L, Guerlou-Demourgues L, Servant L, Balagurov AM, et al. Atomic structure and lattice dynamics of Ni and Mg hydroxides. *Solid State Ionics*. 2010;181:1764-70.
- [31] Effenberger H, Mereiter K, Zemann J. Crystal structure refinements of magnesite, calcite, rhodochrosite, siderite, smithonite, and dolomite, with discussion of some aspects of the stereochemistry of calcite type carbonates. *Zeitschrift für Kristallographie - Crystalline Materials*. 1981;156.
- [32] Chen X-A, Song F-P, Chang X-A, Zang H-G, Xiao W-Q. A new polymorph of magnesium oxalate dihydrate. *Acta Crystallographica Section E Structure Reports Online*. 2008;64:m863-m.
- [33] Boiocchi M, Caucia F, Merli M, Prella D, Ungaretti L. Crystal-chemical reasons for the immiscibility of periclase and wüstite under lithospheric P,T conditions. *European Journal of Mineralogy*. 2001;13:871-81.
- [34] Beaucage G. Approximations Leading to a Unified Exponential/Power-Law Approach to Small-Angle Scattering. *Journal of Applied Crystallography*. 1995;28:717-28.
- [35] Kinning DJ, Thomas EL. Hard-sphere interactions between spherical domains in diblock copolymers. *Macromolecules*. 1984;17:1712-8.
- [36] Pabisch S, Feichtenschlager B, Kickelbick G, Peterlik H. Effect of interparticle interactions on size determination of zirconia and silica based systems – A comparison of SAXS, DLS, BET, XRD and TEM. *Chemical Physics Letters*. 2012;521:91-7.



## Supporting Information

### Influence of the Particle Morphology on Cycle Stability and Hydration Behavior of Magnesium Oxide

Danny Müller,<sup>\*a</sup> Christian Knoll,<sup>a,b</sup> Werner Artner,<sup>c</sup> Jan M. Welch,<sup>d</sup> Norbert Freiberger,<sup>e</sup> Roland Nilica,<sup>e</sup> Elisabeth Eitenberger,<sup>f</sup> Gernot Friedbacher,<sup>f</sup> Michael Harasek,<sup>b</sup> Klaudia Hradil,<sup>c</sup> Andreas Werner,<sup>g</sup> Herwig Peterlik,<sup>h</sup> Peter Weinberger<sup>a</sup>

<sup>a</sup> Institute of Applied Synthetic Chemistry, TU Wien, Getreidemarkt 9, 1060 Vienna, Austria.

<sup>b</sup> Institute of Chemical, Environmental & Biological Engineering, TU Wien, Getreidemarkt 9, 1060 Vienna, Austria.

<sup>c</sup> X-Ray Center, TU Wien, Getreidemarkt 9, 1060 Vienna, Austria

<sup>d</sup> Atominstitut, TU Wien, Stadionallee 2, 1020 Vienna, Austria.

<sup>e</sup> RHI-AG, Magnesitstraße 2, 8700 Leoben, Austria.

<sup>f</sup> Institute of Chemical Technologies and Analytics, TU Wien, Getreidemarkt 9, 1060 Vienna, Austria

<sup>g</sup> Institute for Energy Systems and Thermodynamics, TU Wien, Getreidemarkt 9, 1060 Vienna, Austria.

<sup>h</sup> Faculty of Physics, University of Vienna, Boltzmannngasse 5, 1090 Vienna, Austria

\*Corresponding author      [danny.mueller@tuwien.ac.at](mailto:danny.mueller@tuwien.ac.at)

---

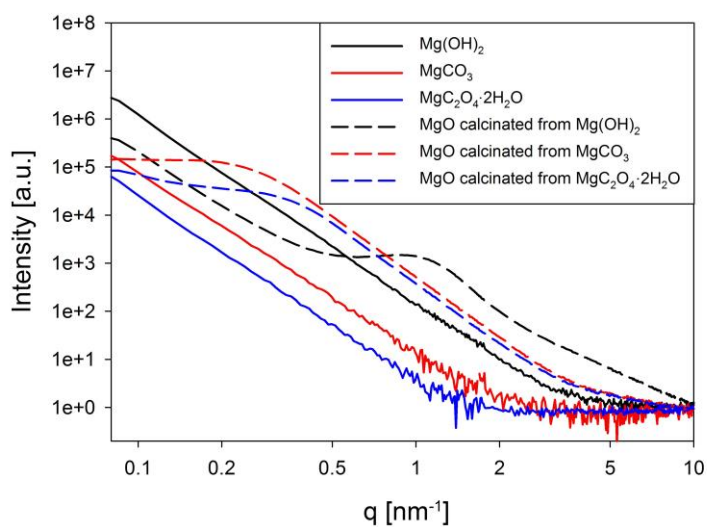


**Figure S1.** SAXS intensities of starting materials and materials after calcination. The considerably higher scattering intensity after calcination shows the development into a porous material consisting of particles in the nanometer size.

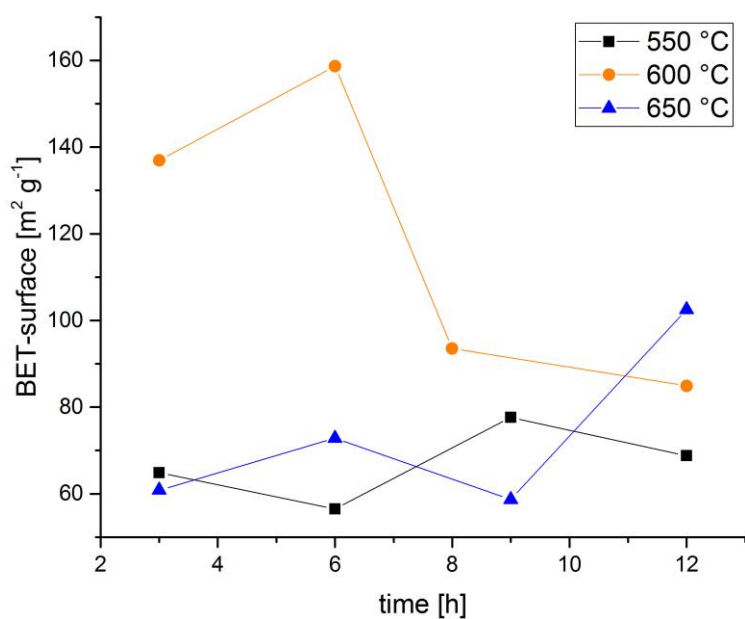


**Figure S2.** BET-surfaces of the  $\text{MgCO}_3$ -originating  $\text{MgO}$ -samples

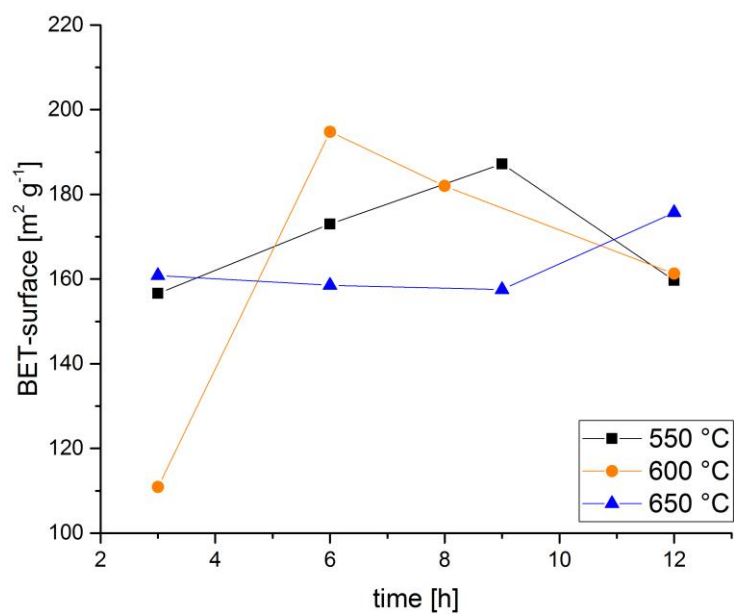


**Figure S3.** BET-surfaces of the  $\text{MgCO}_3$ -originating  $\text{MgO}$ -samples after rehydration for 24 h in liquid water and subsequent calcination

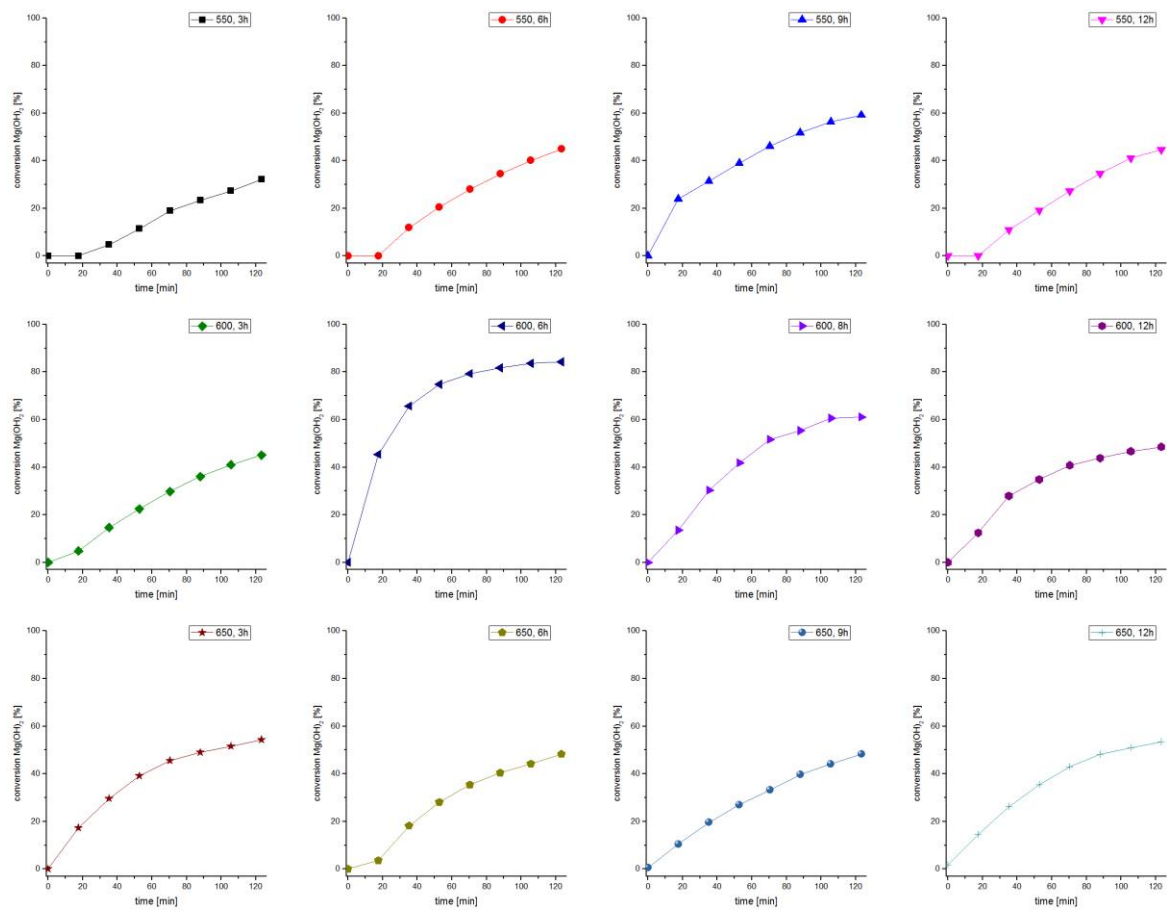


**Figure S4.** Rehydration rates of  $\text{MgCO}_3$ -originating MgO-samples in the P-XRD after rehydration for 24 h in liquid water and subsequent calcination

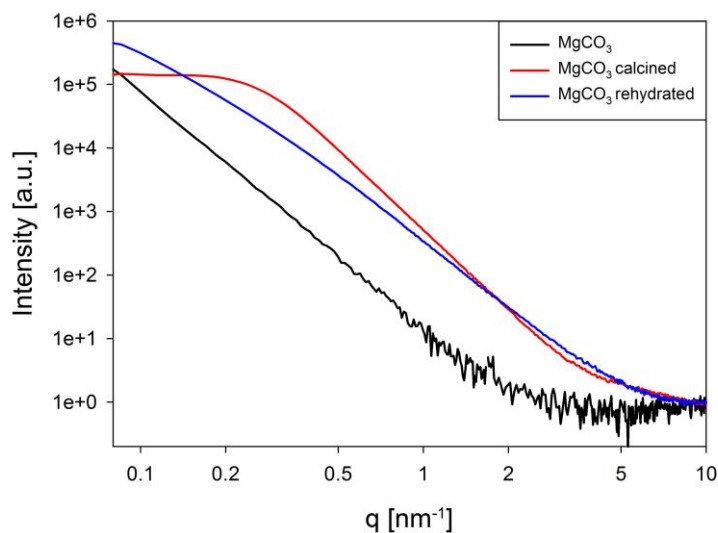


**Figure S5.** SAXS intensities of materials from  $\text{MgCO}_3$  precursor. The original structure is recovered to a wide extent after rehydration. The porosity is, however, is much higher after calcination and rehydration, visible by the higher scattering intensity.

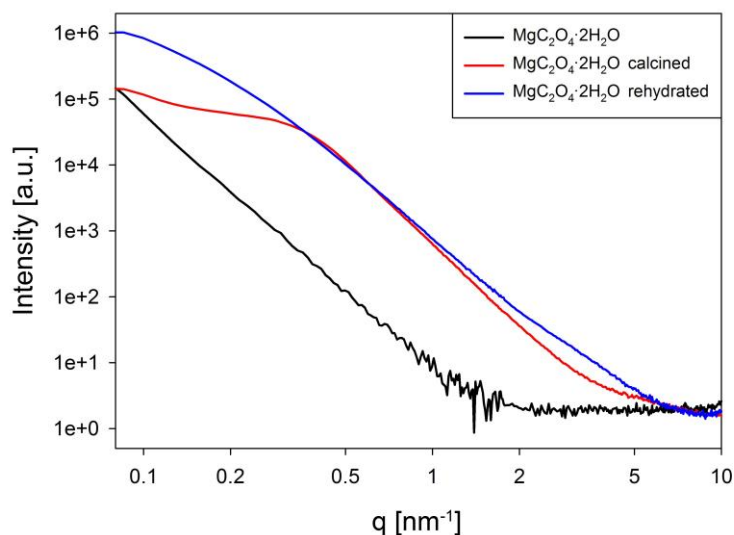


**Figure S6.** SAXS intensities of materials from  $\text{Mg}_2\text{C}_2\text{O}_4 \cdot 2\text{H}_2\text{O}$  precursor. The original structure is recovered to a wide extent after rehydration. The porosity, however, is much higher after calcination and rehydration, visible by the higher scattering intensity.

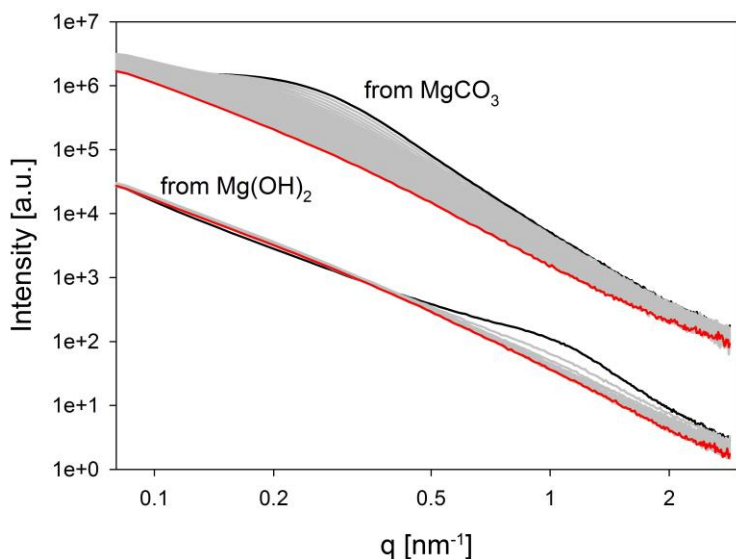


**Figure S7.** *In-situ* SAXS intensities during regeneration in liquid water for 24 h. SAXS curve at the beginning in black, then grey lines for measurements taken each half an hour and final measurement (red line). The  $\text{MgCO}_3$  lines vertically shifted for better visibility. A considerable difference is the much faster kinetics for the  $\text{Mg(OH)}_2$  derived material.

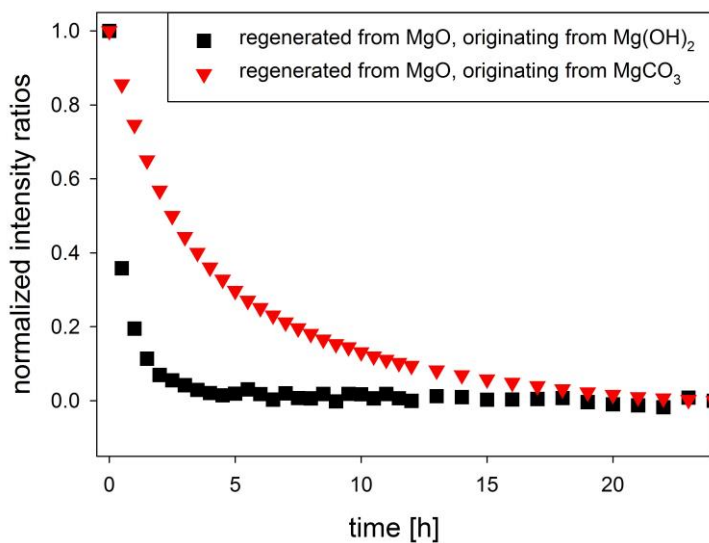
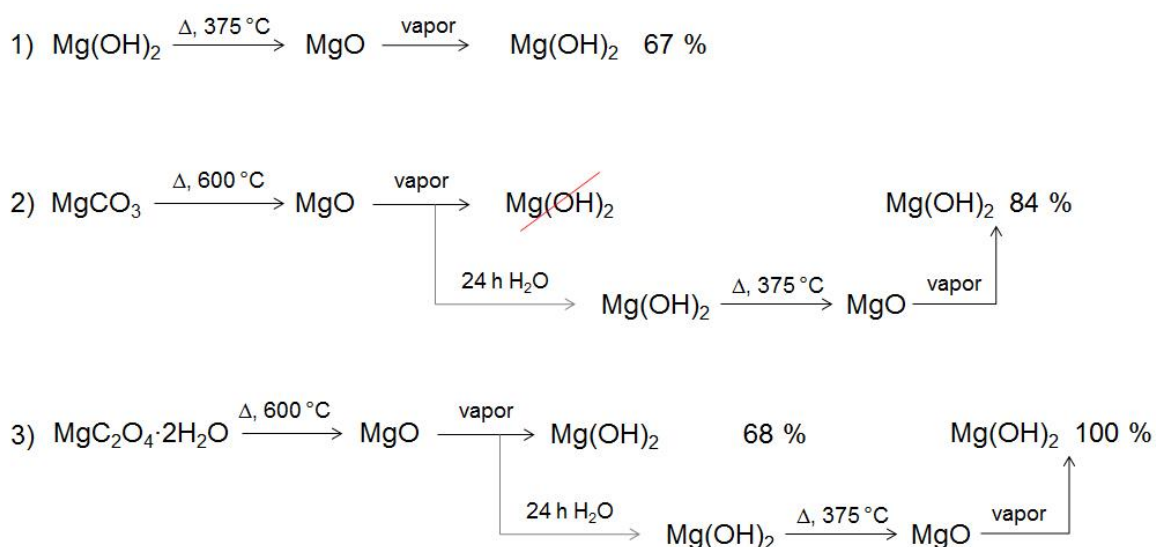


**Figure S8.** Kinetics of conversion to hydroxide during regeneration in liquid water, evaluated from the decrease of the intensity difference between starting (calcined) and finally transformed hydroxide material from *in-situ* SAXS intensity data in Fig S1d, normalized to the initial difference. Regeneration kinetics is about three times slower for  $\text{MgCO}_3$  than for  $\text{Mg(OH)}_2$  originating material.



**Scheme S1.** Overview on conditions for calcination and rehydration of MgO obtained from various precursors 1)  $\text{Mg(OH)}_2$  2)  $\text{MgCO}_3$  3)  $\text{MgC}_2\text{O}_4 \cdot 2\text{H}_2\text{O}$

**Table S1.** Fit data for calcined materials using a model combining the unified scattering function of Beaucage /1/ (resulting in a radius of gyration  $R_g$  and a fractal dimension  $d_f$ ) together with a packing factor from a hard sphere model /2,3/ describing the agglomeration of units (distance  $R_{HS}$  and hard sphere volume ratio  $\eta$ ).

Material MgO	$R_g$ / nm	$d_f$	$R_{HS}$ / nm	$\eta$
calcined from $\text{Mg(OH)}_2$	1.8	2.8	2.6	0.18
calcined from $\text{MgCO}_3$	6.6	4.0	12	0.06
calcined from $\text{Mg}_2\text{C}_2\text{O}_4 \cdot 2\text{H}_2\text{O}$	5.1	4.0	7.0	0.04



# Magnesium oxide from natural magnesite samples as thermochemical energy storage material

Christian Knoll<sup>a,b</sup>, Danny Müller<sup>a,\*</sup>, Werner Artner<sup>c</sup>, Jan M. Welch<sup>d</sup>, Norbert Freiberger<sup>e</sup>, Roland Nilica<sup>e</sup>, Elisabeth Eitenberger<sup>f</sup>, Gernot Friedbacher<sup>f</sup>, Andreas Werner<sup>g</sup>, Peter Weinberger,<sup>a</sup> Michael Harasek<sup>b</sup>

<sup>a</sup> Institute of Applied Synthetic Chemistry, TU Wien, Getreidemarkt 9, 1060 Vienna, Austria.

<sup>b</sup> Institute of Chemical, Environmental & Biological Engineering, TU Wien, Getreidemarkt 9, 1060 Vienna, Austria.

<sup>c</sup> X-Ray Center, TU Wien, Getreidemarkt 9, 1060 Vienna, Austria

<sup>d</sup> Atominstitut, TU Wien, Stadionallee 2, 1020 Vienna, Austria.

<sup>e</sup> RHI-AG, Magnesitstraße 2, 8700 Leoben, Austria.

<sup>f</sup> Institute of Chemical Technologies and Analytics, TU Wien, Getreidemarkt 9/164, 1060 Vienna, Austria

<sup>g</sup> Institute for Energy Systems and Thermodynamics, TU Wien, Getreidemarkt 9, 1060 Vienna, Austria.

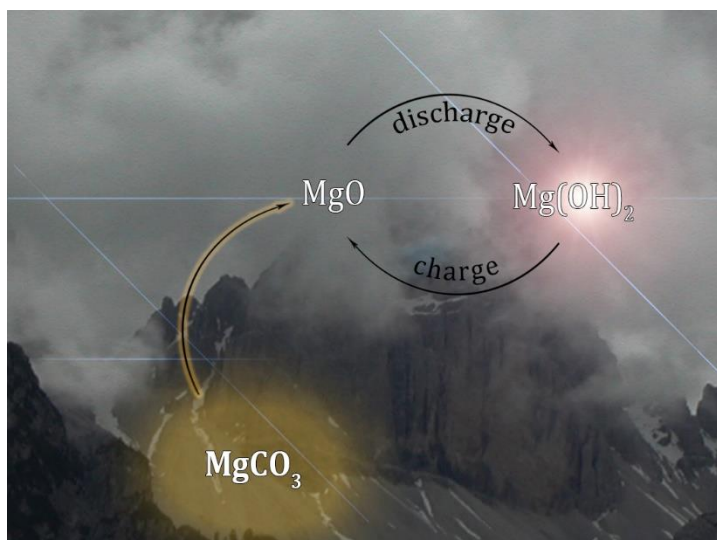
\*Corresponding author      danny.mueller@tuwien.ac.at

## Highlights:

- Three industrially available magnesites were used as MgO-precursor, aiming for a Mg(OH)<sub>2</sub> / MgO thermochemical storage cycle
- Various amounts of Ca<sup>2+</sup> and Fe<sup>2+</sup> as major impurities did not notably affect the reactivity / cycle stability within the series
- MgO-samples containing foreign ions reveal a notably decreased performance compared to analytically pure material

**Keywords:** magnesite, magnesium oxide, hydration reactivity, *in-situ* X-Ray powder diffraction, thermochemical energy storage

## Graphical Abstract



Natural magnesite-derived samples of  $\text{MgO}$  are investigated for their reactivity in a  $\text{Mg(OH)}_2$  /  $\text{MgO}$  thermochemical energy storage cycle.

## Abstract

Thermochemical energy storage based on the  $\text{Mg(OH)}_2$  /  $\text{MgO}$  cycle is considered as attractive process for recycling of industrial waste heat between 350-400 °C. Based on a recent study, revealing  $\text{MgCO}_3$ -derived  $\text{MgO}$  as highly attractive starting material for such a storage cycle, three different natural magnesites were investigated to analyze the process-performance using industrially available raw-materials. Whereas, the varying amounts of  $\text{Ca}^{2+}$  and  $\text{Fe}^{2+}$  as major impurities did not notably affect the reactivity / cycle stability within the series, compared to the analytically pure reference material a notable decrease of performance was evidenced.

## 1. Introduction

A variety of inorganic materials is reversibly decomposed above their equilibrium temperature forming a solid residue and a gaseous by-product. As the reaction is reversible, an exothermic back reaction occurs below the decomposition temperature in the presence of the formerly released gas. Due to the inherent consumption of energy / heat on decomposition, and its release during recombination, such reversible chemical reactions attracted scientific interest for their application in thermal energy storage. [1, 2]

Although, latent [3] or sensible [4] heat storage is already a commercialized technology for thermal energy storage, a thermochemical energy storage (TCES) approach using reversible chemical reactions to store excess / waste heat, could be attractive for complementary purposes, where latent or sensible heat storage are less efficient, or even unsuitable. [5] The major advantage of TCES-materials compared to the so far established thermal energy storage systems is on the one hand a notably higher storage density and a loss-less storage (in the absence of the

reactive gas no backreaction, thus discharging occurs), but even more the large operable temperature window. [6]

Depending on the selected material, categorized according to the involved reactive gas as *e.g.* H<sub>2</sub>O, NH<sub>3</sub>, H<sub>2</sub>, CO<sub>2</sub>, O<sub>2</sub>, waste heat levels between approximately 50 – 1200 °C may be addressed. The lower limits are realized by salt hydrates, suitable for energy-efficient smart housing concepts, [7, 8] whereas on the other end carbonates and oxides allow for *e.g.* combination with concentrating solar power plants (CSP) to bridge non-operational times. [9, 10] In the medium-temperature level between 250-500 °C a variety of industrial waste heat sources is compatible with *e.g.* hydroxide / oxide equilibria. [11, 12] One major criterion for application of a TCES-process on an industrial scale is the availability of the involved raw-material in massive quantities to an attractive price. In this context, especially Mg(OH)<sub>2</sub> / MgO used on industrial scales as raw-material for refractories or cement [13] would be an attractive candidate. The operational temperature of the Mg(OH)<sub>2</sub> / MgO couple with 350-400 °C would also perfectly fit the industrial demands. [12, 14]

Considering these boundary conditions, several studies focused on various aspects of the rehydration reaction of MgO, as *e.g.* fundamental reactivity [15] and kinetics, [16, 17] a suitable reactor setup, [18] application as a heat pump, [19-22] and last but not least an enhancement of the materials' reactivity. Especially the aim for a higher reactivity of the material is crucial for its application in TCES, as compared to the homologous Ca(OH)<sub>2</sub> / CaO system [11] the performance in regard of reaction rate and completeness is worse.\* Composite materials for a better thermal conductivity, [23, 24] the addition of lithium salts [25-27] or even a dotation of MgO with Ca<sup>2+</sup> [28] were reported to enhance the performance. Scientifically valid and highly interesting, nevertheless all these modifications must be considered as pure academic approach, as the correlated costs outweigh the advantage of Mg(OH)<sub>2</sub> / MgO as cost-efficient TCES-material and thereby impede an application of those modified materials on an industrial scale.

Recently it was demonstrated, [29] that the reactivity of the MgO is notably affected by the chemical history / particle morphology of the precursor material, thus a Mg(OH)<sub>2</sub>- based MgO reacts differently than a MgO derived from MgC<sub>2</sub>O<sub>4</sub>·2H<sub>2</sub>O or MgCO<sub>3</sub>. Especially MgCO<sub>3</sub>-based MgO has a higher reactivity and much better cycle stability than the Mg(OH)<sub>2</sub>-based MgO. As magnesite (MgCO<sub>3</sub>) is also industrially used as raw-material for the preparation of MgO, this could direct to an industrial feasibility of the process.

To prevent any interfering effects of impurities or naturally present secondary phases and thus simplify the characterization, so far most studies used analytically pure materials. On an industrial scale only naturally occurring material, in this case naturally abundant magnesite, could be used as raw-material in a TCES-process. Therefore, herein three different naturally occurring magnesite samples, used in industrial processes for cement or refractory production, were investigated regarding their performance in a thermochemical energy storage process and compared to the previously obtained results for analytically pure MgCO<sub>3</sub>.

---

\* The application of Ca(OH)<sub>2</sub> / CaO instead of Mg(OH)<sub>2</sub> / MgO is hampered for many purposes due to the notably higher decomposition temperature of Ca(OH)<sub>2</sub> around 600 °C.

## 2. Experimental Methodology

### 2.1 Material

Three natural magnesite samples **A1**, **B1** and **C1**, having a particle size below 65 $\mu$ m, were provided by the RHI-AG, being typical raw-materials used for the industrial production of refractories and, therefore available in massive quantities at low costs.

Most common foreign ions are Ca<sup>2+</sup> and Fe<sup>2+</sup>, so the three samples were selected to cover both a variable range of Ca<sup>2+</sup>- and Fe<sup>2+</sup> content:

- Magnesite **A1**: crypto crystalline, 2.05 % CaO, 0.31 % Fe<sub>2</sub>O<sub>3</sub>
- Magnesite **B1**: coarse crystalline, 1.95 % CaO, 6.57 % Fe<sub>2</sub>O<sub>3</sub>
- Magnesite **C1**: coarse crystalline, 11.06 % CaO, 5.95 % Fe<sub>2</sub>O<sub>3</sub>

A complete quantification of the elemental composition of the samples **A1**, **B1** and **C1** by X-Ray fluorescence analysis is given in the electronic supplement in table S1.

### 2.3 X-Ray Powder Diffraction

The powder X-ray diffraction measurements were carried out on a PANalytical X'Pert Pro diffractometer in Bragg-Brentano geometry using Cu K <sub>$\alpha$ 1,2</sub> radiation and an X'Celerator linear detector with a Ni-filter. For *in-situ* monitoring of experiments an Anton Paar XRK 900 reaction chamber was used. The sample was mounted on a hollow ceramic powder sample holder, allowing for complete perfusion of the sample with the reactive gas. The sample temperature is controlled directly via a NiCr-NiAl thermocouple and direct environmental heating. The reactive gas flow was set to 0.2 L min<sup>-1</sup>, unless otherwise stated. For the *in-situ* observation of the rehydration reactivity 3 ml min<sup>-1</sup> water (provided by a HPLC-pump) was passed through an evaporation coil kept at 300 °C. The resulting 3 g min<sup>-1</sup> steam were mixed with 0.2 L min<sup>-1</sup> helium as carrier gas (H<sub>2</sub>O partial pressure equals 0.96 bar) and passed from the top through the sample. The carrier gas is necessary to force the steam transfer through the system. During rehydration the sample warmed to around 65 °C. Between the consecutive rehydration cycles the *in-situ* formed Mg(OH)<sub>2</sub> was calcined at 375 °C for 15 minutes directly in the reaction chamber of the P-XRD. As the sample is completely penetrated by the X-rays, the obtained diffractograms are an average through the complete sample. The diffractograms were evaluated using the PANalytical program suite HighScorePlus v3.0d. A background correction and a K <sub>$\alpha$ 2</sub> strip were performed. Phase assignment is based on the ICDD-PDF4+ database, the exact phase composition was obtained via Rietveld-refinement in the program suite HighScorePlus v3.0d. All quantifications based on P-XRD are accurate within of  $\pm 5$  %.

### 2.4 Scanning electron microscopy (SEM)

SEM images were recorded on gold coated samples with a Quanta 200 SEM instrument from FEI under low-vacuum at a water vapor pressure of 80 Pa to prevent electrostatic charging.

### 2.5 BET-specific surface area analyzer

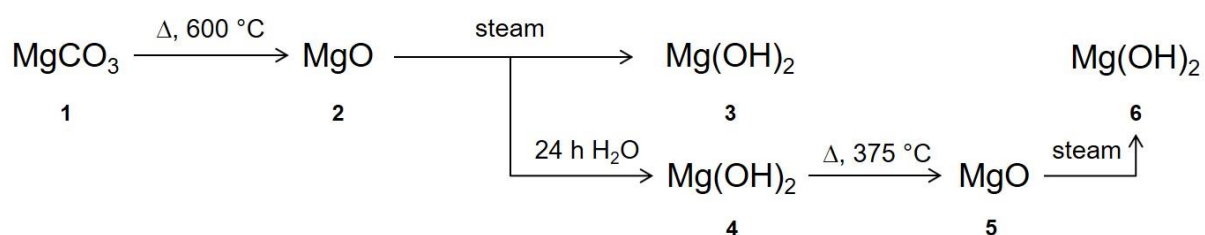
The specific surface of the samples was determined by nitrogen sorption measurements, which were performed on an ASAP 2020 (Micromeritics) instrument. The samples (amounts between 100-200 mg) were degassed under vacuum at 80 °C overnight prior to measurement. The surface area was calculated according to Brunauer, Emmett and Teller (BET). [30]

## 2.5 X-Ray fluorescence analysis

X-Ray fluorescence analysis was performed on a Bruker S8 TIGER instrument. The sample was heated together with LiBF<sub>4</sub> to 1050 °C, yielding the beads for the analysis.

## 3. Results and Discussion

Based on former experience with calcination of MgCO<sub>3</sub> the natural samples (scheme 1, **A1-C1**) were calcined at 600 °C under a static atmosphere of air for 4 h, resulting the corresponding samples of MgO (scheme 1, **A2-C2**). The increased Fe<sup>2+</sup>-content in magnesite B and C is also evidenced from the slight orange shade of the samples **B2** and **C2** after calcination (see figure S1).



**Scheme 1.** Calcination / rehydration flow-chart applied for the characterization of the natural magnesite samples.

From previous work on MgCO<sub>3</sub>-derived MgO it was already known, [29] that directly calcined MgO (MgO **2** in scheme 1) would exhibit no, or only a very limited reactivity towards steam during attempted rehydration to Mg(OH)<sub>2</sub>. Therefore, MgO **2** was rehydrated in liquid water for 24 h and afterwards calcined for 4 h at 375 °C. [15]

The BET-surfaces of the magnesite-precursors (**A1-C1**) and of the different MgO samples **A2-C2** and **A5-C5** were compared to anticipate the rehydration reactivity. [31]

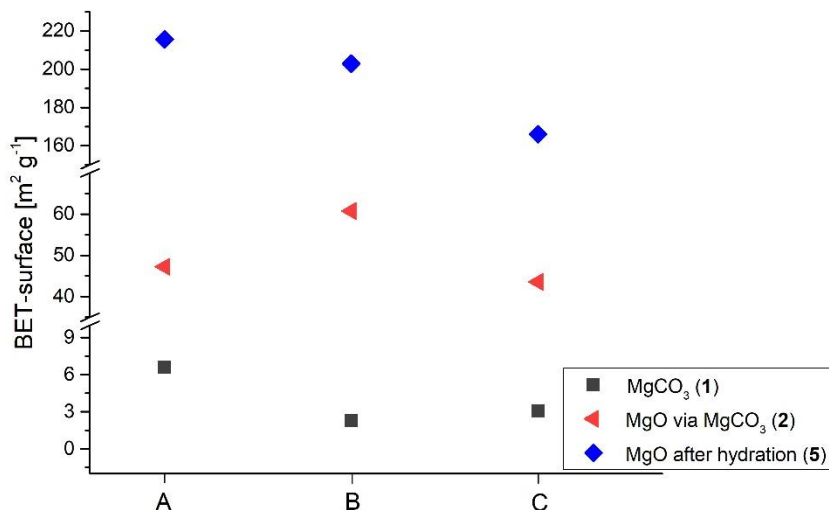


**Figure 1.** Specific surfaces of the different MgO-species derived from magnesite samples **A**, **B** and **C**. Numerical values are given in table S2.

The surface area for highly reactive MgO species obtained by calcination of Mg(OH)<sub>2</sub> varies between 250 – 300 m<sup>2</sup> g<sup>-1</sup>, [31] whereas, using analytically pure MgCO<sub>3</sub> for the resulting MgO values up to 160 m<sup>2</sup> g<sup>-1</sup> were reported. [29] Using the natural magnesites, for the directly calcined MgO notably lower values – indicating a poor reactivity – were obtained (red symbols in figure 1). In contrast, after hydration in liquid water and subsequent calcination (blue symbols) the found specific surfaces were found even higher than for identically treated MgO originating from analytically pure MgCO<sub>3</sub>. [29]

To correlate the specific surface of the various samples to the rehydration reactivity, MgO was reacted in the P-XRD, allowing for *in-situ* observation of the Mg(OH)<sub>2</sub> formation. In figure 2 the rehydration behavior for the MgO samples **A2-C2** is compared.

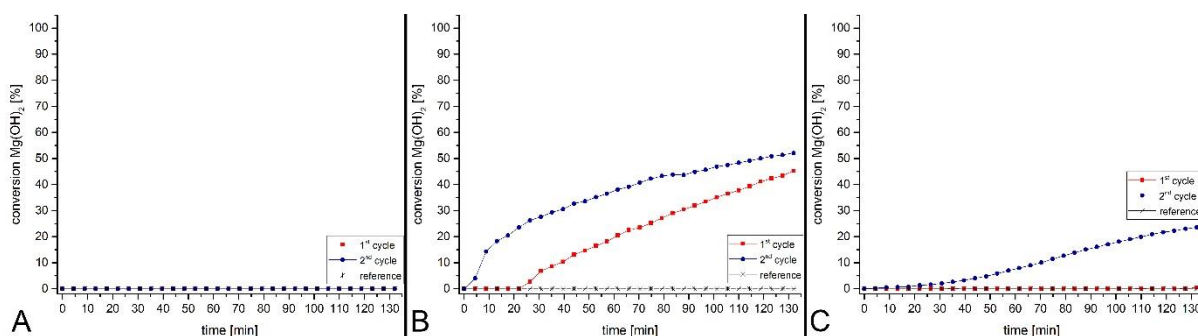


**Figure 2.** Conversion plots derived from the *in-situ* powder X-Ray diffraction during hydration of samples **A2** (left), **B2** (middle) and **C2** (right). The typical conversion for an equivalent sample, derived from analytically pure MgCO<sub>3</sub> is given as reference. (Rehydration conditions: 3 g min<sup>-1</sup> steam, 0.2 L min<sup>-1</sup> He)

The rehydration reactivity of samples **B2** and **C2** was quite unexpected, as from the BET-data and the previous experience with MgCO<sub>3</sub>-derived MgO for all three samples no conversion to the hydroxide was expected at this stage. So far, all MgCO<sub>3</sub>-derived MgO samples needed a prior rehydration step in liquid water, before the anew calcined material would be reactive



towards steam, forming the hydroxide. In the actual case this assumption was only partially confirmed by displaying a higher reactivity towards steam in the second rehydration cycle. As most reactive material was identified **B2**, resulting a conversion of 52.1 % for the second cycle.

From a chemical point of view the presence of 6.57 %  $\text{Fe}^{2+}$  in sample **B2** does not really explain this unexpected reactivity. Therefore, for a possible explanation the morphology of the three materials was compared in the SEM.

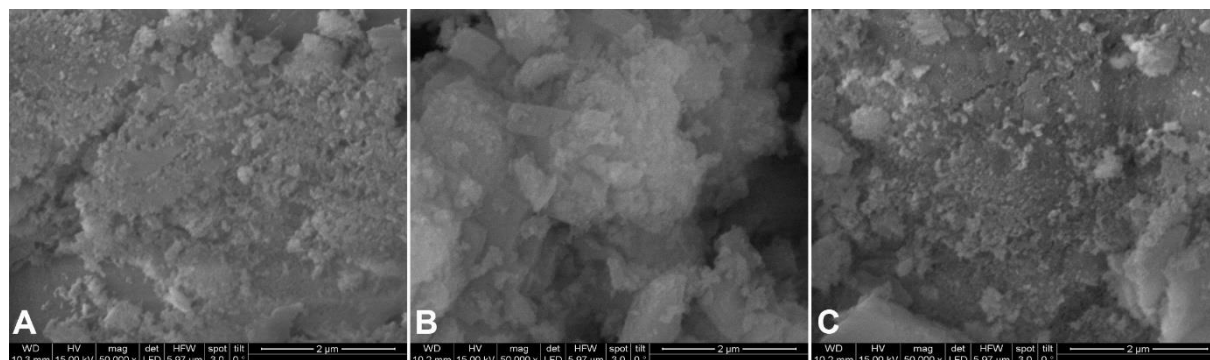


**Figure 3.** SEM-images of the MgO samples **A2** (left), **B2** (middle) and **C2** (right).

The SEM-images for the three freshly calcined magnesite samples revealed, that the original particle morphology of the magnesites **A1**, **B1** and **C1** (figure S2) had been mostly retained during calcination. Calcination had caused a further decrease of the particle size for sample **A1** – the crypto crystalline magnesite –, whereas, for **B1** and **C1** (with an increased fraction of smaller particles) still the coarse crystalline structure was retained. Based on the SEM-images, the reason for the unexpected reactivity of **B1** most likely was attributed to the structured particle morphology, whereas for **A1** completely, and for **C1** to a major extent a fragmentation of the particles had occurred.

A notably different picture was obtained when analyzing the SEM-images of the samples after 24 h rehydration in water (**A3-C3**).

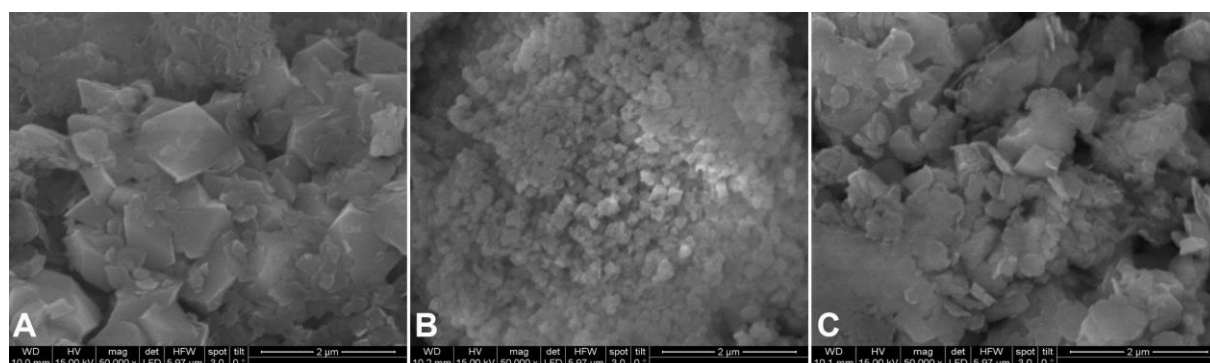


**Figure 4.** SEM-images of the magnesite samples **A3** (left), **B3** (middle) and **C3** (right).

The liquid water treatment over 24 h resulted in a notable reorganization of the particle morphology for all three samples, inverting the prior observation: Whereas especially in **A3**, but also in **C3** well-shaped crystallites had formed, **B3** had converted to tiny agglomerates of

smallest particles. Particularly interesting and unprecedented may be considered the particle shape of the materials:  $\text{Mg}(\text{OH})_2$  adopts a very characteristic morphology, consisting of hexagonal brucite platelets aggregating along their basal plane. The morphology observed in figure 4 is notably different for all three samples, consisting of spherical particles with clearly shaped edges. Thermal treatment during calcination of the material at 375 °C for 4 h, leading to the MgO-samples **A4-C4**, even promoted the initiated process, as derived from the SEM-images shown in figure 5.

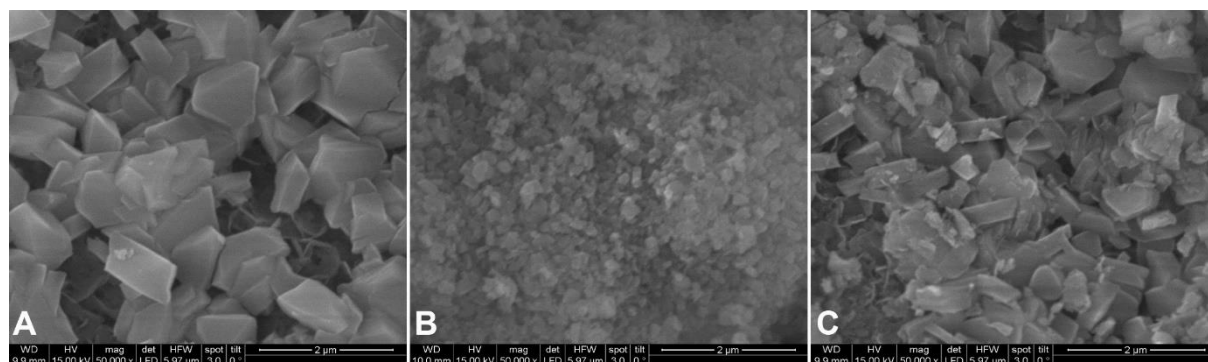


**Figure 5.** SEM-images of the magnesite samples **A5** (left), **B5** (middle) and **C5** (right).

Although, according to the SEM-images in figure 5 the MgO-samples **A5-C5** feature a notably different particle morphology, the BET-surfaces (figure 1, table S2) between 165  $\text{m}^2 \text{g}^{-1}$  (**C5**) and 215  $\text{m}^2 \text{g}^{-1}$  (**A5**) direct for all three samples towards a promising rehydration reactivity in the presence of steam. To investigate also the cycle stability of the materials, the MgO-samples **A5-C5** were subjected 5 consecutive rehydration / calcination cycles with *in-situ* determination of the phase-composition in the P-XRD setup. The intermediate calcination steps were realized directly in the reaction chamber of the P-XRD, heating the sample for 15 minutes to 375 °C in a stream of 0.2  $\text{L min}^{-1}$  helium without introduction of moisture.

A comparison of rehydration reactivity and cycle stability of the three MgO samples **A5-C5** is shown in figure 6.

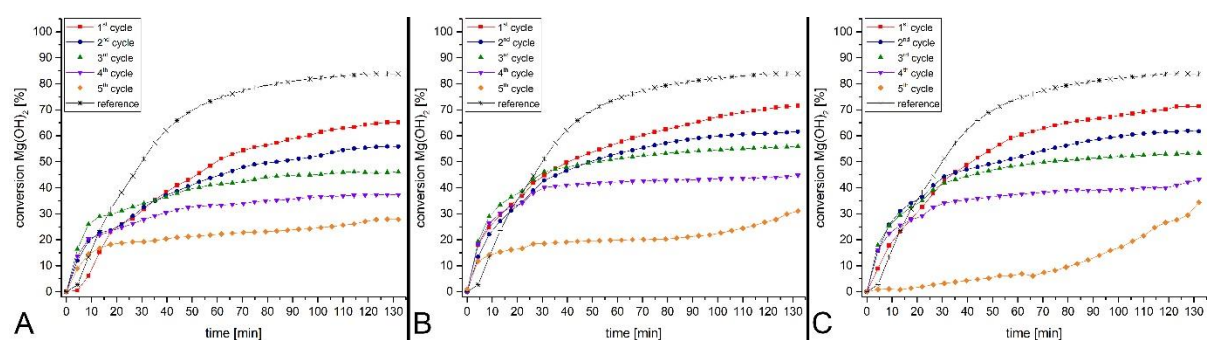


**Figure 6.** Conversion plots derived from the *in-situ* powder X-Ray diffraction during hydration of samples **A5** (left), **B5** (middle) and **C5** (right) for 5 consecutive cycles. The typical conversion for an equivalent sample, derived from analytically pure  $\text{MgCO}_3$  is given as reference. (Rehydration conditions: 3  $\text{g min}^{-1}$  steam, 0.2  $\text{L min}^{-1}$  He)

Comparing the results shown in figure 6, a quite comparable and very similar rehydration reactivity and cycle stability is evidenced for the samples **A5-C5**. All of them feature a notable decrease of overall-conversion from the 1<sup>st</sup> to the 5<sup>th</sup> cycle, **C5** having an anomalous strong decrease of reactivity between the 4<sup>th</sup> and 5<sup>th</sup> cycle. For all three samples after rehydration (A6-C6) in the SEM a platelet type morphology – still lacking the characteristic hexagonal brucite shape – is observed (figure S6).

Compared to the reference, resulting 84 % formed Mg(OH)<sub>2</sub> within the first cycle, the maximum conversion for the natural magnesite derived MgO samples is lower, **B5** and **C5** yielding both 71.5 %, **A5** only 65.5 % Mg(OH)<sub>2</sub>. The decrease during the 5 cycles to around 30 % is for the natural samples by far more pronounced than in the case of the reference material (62.7 %). In figure 7 each 1<sup>st</sup> and 5<sup>th</sup> cycle for the samples **A5-C5**, including the reference material is given for a better visualization.

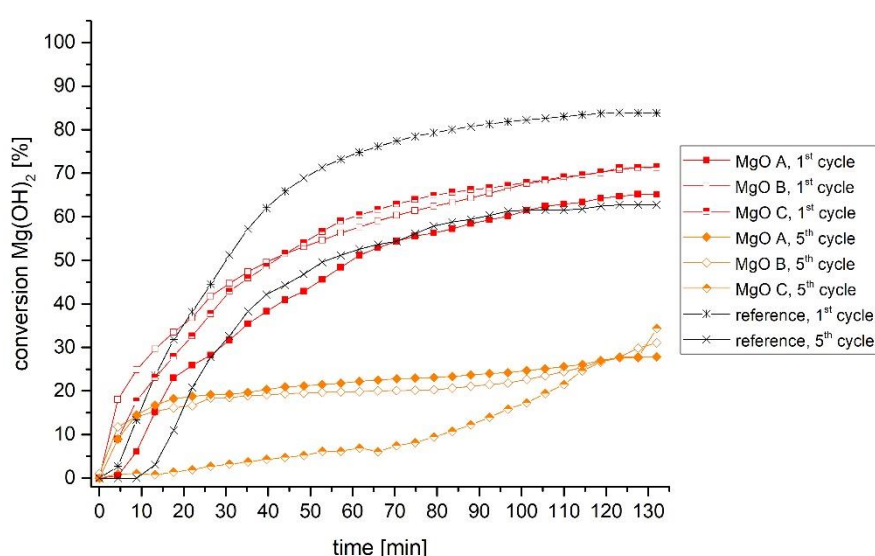


**Figure 7.** Conversion plots derived from the *in-situ* powder X-Ray diffraction for the 1<sup>st</sup> and 5<sup>th</sup> cycles of the three magnesite-derived MgO samples **A5-C5** and the corresponding reference material from analytically pure MgCO<sub>3</sub>

The outcome of the conversion and especially cycle-stability tests of the natural magnesite-derived MgO material summarized in figure 7 reveals sobering regarding the performance of the materials suitable for a TCES-process based on Mg(OH)<sub>2</sub> / MgO on a technological scale. Whereas, the initial reactivity of the materials was slightly worse than for an analytically pure MgCO<sub>3</sub>-based MgO sample, the poor cycle stability over 5 consecutive rehydration / calcination cycles is a major issue. A process with a lower overall-conversion may be feasible under properly selected boundary conditions, but not in combination to a material degradation within 5 cycles to 50 % of the initial activity. MgCO<sub>3</sub> was selected as precursor for the MgO used in the Mg(OH)<sub>2</sub> / MgO TCES-cycle as previous studies revealed, that the thereby obtained MgO displayed a much higher reactivity than a Mg(OH)<sub>2</sub>-derived material. In the case of the natural magnesites this effect could not be confirmed based on the present experimental data.

An interesting finding of this comparative study is the observation, that the reactivity / conversion of the various samples is only minorly affected by the increased amounts of

unreactive  $\text{CaCO}_3$  and  $\text{Fe}^{2+}$ -impurities within the series.<sup>†</sup> Nevertheless, as based on the specific surface of the samples' and their among each other comparable morphology no real explanation for the inferior performance in rehydration reactivity compared to a  $\text{MgO}$ -sample derived from analytically pure  $\text{MgCO}_3$  is found, the source of the different performance may be located in the secondary phases of the magnesite-derived samples. As the series with  $\text{CaCO}_3$ -contents between 1.95 – 11.06 % and  $\text{Fe}^{2+}$ -contents between 0.31 – 6.57 % provides similar performance, even low amounts of foreign ions seem to deteriorate the reactivity of the material.

#### 4. Conclusion

Natural crypto-crystalline and coarse-crystalline magnesite samples, containing as major impurities  $\text{Ca}^{2+}$  (1.95 – 11.06 %) and  $\text{Fe}^{2+}$  (0.31 – 6.57 %), were thermally decomposed to  $\text{MgO}$ , which was investigated for its performance in a  $\text{Mg}(\text{OH})_2$  /  $\text{MgO}$  thermochemical energy storage (TCES) cycle. The reaction conditions during calcination / rehydration of the samples were the same as for a recent study using analytically pure  $\text{MgCO}_3$  as  $\text{MgO}$ -precursor, revealing a notable improvement rehydration reactivity of the material compared to a  $\text{Mg}(\text{OH})_2$ -derived  $\text{MgO}$ .

Comparison of the rehydration reactivity, cycle stability and particle morphology of the magnesite-derived  $\text{MgO}$  resulted in following key-findings:

- The reactivity of the magnesite-derived  $\text{MgO}$  samples is comparable within the series (between 65-75 %  $\text{Mg}(\text{OH})_2$ -formation), but lower than for the reference sample from analytically pure  $\text{MgCO}_3$  with 84 % conversion.
- Also the cycle stability is comparable within the series, again inferior than for the reference sample (conversion depletes within the series to about 30 %, for the reference to 63 %).
- The natural magnesite-derived  $\text{MgO}$ -samples form during rehydration in liquid water after the initial calcination a  $\text{Mg}(\text{OH})_2$ -phase with well-shaped crystallites, lacking the typical brucite-type hexagonal platelet morphology. The shape is retained during anew calcination.
- As from the specific surface, chemical behavior and particle morphology no sound explanation for the inferior reactivity towards an analytically pure reference material is found, the reason is found in the present impurities. It appears, as even impurities below 2 %  $\text{Ca}^{2+}$  and 0.3 %  $\text{Fe}^{2+}$  notably hamper the rehydration reactivity and cycle stability of magnesite-derived  $\text{MgO}$ .

The aim of the herein reported work was a feasibility study on the application of natural magnesites, used in industrial processes, for thermochemical energy storage purposes based on the  $\text{Mg}(\text{OH})_2$  /  $\text{MgO}$  cycle. Based on the obtained results it may be concluded, that only pure materials are feasible for a successful application in TCES, which derogates attractiveness and financial rentability of such a process on industrial scales.

---

<sup>†</sup> The conversion curves displayed within this study are so far uncorrected for the amount of inactive material, so by its consideration the final yields of  $\text{Mg}(\text{OH})_2$  would be slightly higher.



## Conflict of interest

The authors declare no conflict of interest. The RHI-AG as industrial research partner provided the natural magnesite samples, but had no influence on the realization or methodology of the herein reported study.

## Acknowledgement

This work was financially supported by the Austrian Research Promotion Agency (FFG Forschungsförderungsgesellschaft), project 845020, 841150 and project 848876. The X-Ray center (XRC) of the Vienna University of Technology provided access to the powder X-Ray diffractometer.

## References

- [1] Bauer T, Steinmann W-D, Laing D, Tamme R. Thermal Energy Storage Materials and Systems. *Annual Review of Heat Transfer*. 2012;15:131-77.
- [2] Zhang H, Baeyens J, Cáceres G, Degrève J, Lv Y. Thermal energy storage: Recent developments and practical aspects. *Progress in Energy and Combustion Science*. 2016;53:1-40.
- [3] Zalba B, Marín JM, Cabeza LF, Mehling H. Review on thermal energy storage with phase change: materials, heat transfer analysis and applications. *Applied Thermal Engineering*. 2003;23:251-83.
- [4] J. Xu RZW, Y. Li. A review of available technologies for seasonal thermal energy storage. *Solar Energy*. 2014:610-38.
- [5] Dinker A, Agarwal M, Agarwal GD. Heat storage materials, geometry and applications: A review. *Journal of the Energy Institute*. 2015.
- [6] Ali H. Abedin MAR. A Critical Review of Thermochemical Energy Storage Systems. *The Open Renewable Energy Journal*. 2011;4:42-6.
- [7] van Essen VM, Cot Gores J, Bleijendaal LPJ, Zondag HA, Schuitema R, Bakker M, et al. Characterization of Salt Hydrates for Compact Seasonal Thermochemical Storage. 2009:825-30.
- [8] Knoll C, Müller D, Artner W, Welch JM, Werner A, Harasek M, et al. Probing cycle stability and reversibility in thermochemical energy storage – CaC<sub>2</sub>O<sub>4</sub>·H<sub>2</sub>O as perfect match? *Applied Energy*. 2017;187:1-9.
- [9] Ervin G. Solar heat storage using chemical reactions. *Journal of Solid State Chemistry*. 1977;22:51-61.
- [10] Kuravi S, Goswami Y, Stefanakos EK, Ram M, Jotshi C, Pendyala S, et al. Thermal Energy Storage for Concentrating Solar Power Plants. *Technology & Innovation*. 2012;14:81-91.
- [11] Linder M, Roßkopf C, Schmidt M, Wörner A. Thermochemical Energy Storage in kW-scale based on CaO/Ca(OH)<sub>2</sub>. *Energy Procedia*. 2014;49:888-97.
- [12] Kato Y, Takahashi R, Sekiguchi T, Ryu J. Study on medium-temperature chemical heat storage using mixed hydroxides. *International Journal of Refrigeration*. 2009;32:661-6.
- [13] Shand MA. *The Chemistry and Technology of Magnesite*. John Wiley & Sons Inc, Hoboken, New Jersey. 2006.
- [14] Pan Z, Zhao CY. Dehydration/hydration of MgO/H<sub>2</sub>O chemical thermal storage system. *Energy*. 2015;82:611-8.
- [15] Müller D, Knoll C, Artner W, Welch JM, Freiburger N, Nilica R, et al. An in-situ powder X-Ray diffraction study on the rehydration-reactivity of low temperature calcined Mg(OH)<sub>2</sub>. *Applied Energy*. 2017;submitted.
- [16] Birchal VS, Rocha SDF, Mansur MB, Ciminelli VST. A simplified mechanistic analysis of the hydration of magnesite. *The Canadian Journal of Chemical Engineering*. 2001;79:507-11.

- [17] Kuleci H, Schmidt C, Rybacki E, Petrishcheva E, Abart R. Hydration of periclase at 350 °C to 620 °C and 200 MPa: experimental calibration of reaction rate. *Mineralogy and Petrology*. 2016;110:1-10.
- [18] Kato Y, Takahashi F, Watanabe A, Yoshizawa Y. Thermal Performance of a Packed Bed Reactor of a Chemical Heat Pump for Cogeneration. *Chemical Engineering Research and Design*. 2000;78:745-8.
- [19] Kato Y, Kobayashi K, Yoshizawa Y. Durability to repetitive reaction of magnesium oxide/water reaction system for a heat pump. *Applied Thermal Engineering*. 1998;18:85-92.
- [20] Kato Y, Sasaki Y, Yoshizawa Y. Magnesium oxide/water chemical heat pump to enhance energy utilization of a cogeneration system. *Energy*. 2005;30:2144-55.
- [21] Mastrorardo E, Bonaccorsi L, Kato Y, Piperopoulos E, Milone C. Efficiency improvement of heat storage materials for MgO/H<sub>2</sub>O/Mg(OH)<sub>2</sub> chemical heat pumps. *Applied Energy*. 2016;162:31-9.
- [22] Zamengo M, Ryu J, Kato Y. Thermochemical performance of magnesium hydroxide–expanded graphite pellets for chemical heat pump. *Applied Thermal Engineering*. 2014;64:339-47.
- [23] Shkatulov A, Ryu J, Kato Y, Aristov Y. Composite material “Mg(OH)<sub>2</sub>/vermiculite”: A promising new candidate for storage of middle temperature heat. *Energy*. 2012;44:1028-34.
- [24] Zamengo M, Ryu J, Kato Y. Composite block of magnesium hydroxide – Expanded graphite for chemical heat storage and heat pump. *Applied Thermal Engineering*. 2014;69:29-38.
- [25] Ishitobi H, Hirao N, Ryu J, Kato Y. Evaluation of Heat Output Densities of Lithium Chloride-Modified Magnesium Hydroxide for Thermochemical Energy Storage. *Industrial & Engineering Chemistry Research*. 2013;52:5321-5.
- [26] Myagmarjav O, Ryu J, Kato Y. Lithium bromide-mediated reaction performance enhancement of a chemical heat-storage material for magnesium oxide/water chemical heat pumps. *Applied Thermal Engineering*. 2014;63:170-6.
- [27] Myagmarjav O, Ryu J, Kato Y. Dehydration kinetic study of a chemical heat storage material with lithium bromide for a magnesium oxide/water chemical heat pump. *Progress in Nuclear Energy*. 2015;82:153-8.
- [28] Müller D, Knoll C, Ruh T, Artner W, Welch JM, Peterlik H, et al. Calcium Dotation Facilitates Water Dissociation in Magnesium Oxide. *Adv Sus Systems*. 2017;submitted.
- [29] Müller D, Knoll C, Artner W, Welch JM, Freiberger N, Nilica R, et al. Influence of the Particle Morphology on Cycle Stability and Hydration Behavior of Magnesium Oxide. *Applied Energy*. 2017;submitted.
- [30] Brunauer S, Emmett PH, Teller E. Adsorption of Gases in Multimolecular Layers. *Journal of the American Chemical Society*. 1938;60:309-19.
- [31] Pimminger H, Habler G, Freiberger N, Abart R. Evolution of nanostructure and specific surface area during thermally driven dehydration of Mg(OH)<sub>2</sub>. *Physics and Chemistry of Minerals*. 2016;43:59-68.



## Supporting information

### Magnesium oxide from natural magnesite samples as thermochemical energy storage material

Christian Knoll<sup>a,b</sup>, Danny Müller<sup>a,\*</sup>, Werner Artner<sup>c</sup>, Jan M. Welch<sup>d</sup>, Norbert Freiberger<sup>e</sup>, Roland Nilica<sup>e</sup>, Elisabeth Eitenberger<sup>f</sup>, Gernot Friedbacher<sup>f</sup>, Andreas Werner<sup>g</sup>, Peter Weinberger,<sup>a</sup> Michael Harasek<sup>b</sup>

<sup>a</sup> Institute of Applied Synthetic Chemistry, TU Wien, Getreidemarkt 9, 1060 Vienna, Austria.

<sup>b</sup> Institute of Chemical, Environmental & Biological Engineering, TU Wien, Getreidemarkt 9, 1060 Vienna, Austria.

<sup>c</sup> X-Ray Center, TU Wien, Getreidemarkt 9, 1060 Vienna, Austria

<sup>d</sup> Atominstitut, TU Wien, Stadionallee 2, 1020 Vienna, Austria.

<sup>e</sup> RHI-AG, Magnesitstraße 2, 8700 Leoben, Austria.

<sup>f</sup> Institute of Chemical Technologies and Analytics, TU Wien, Getreidemarkt 9/164, 1060 Vienna, Austria

<sup>g</sup> Institute for Energy Systems and Thermodynamics, TU Wien, Getreidemarkt 9, 1060 Vienna, Austria.

\*Corresponding author      [danny.mueller@tuwien.ac.at](mailto:danny.mueller@tuwien.ac.at)

---

**Table S1.** Elemental composition of magnesite-samples A, B and C according to X-Ray fluorescence analysis

	Magnesite A	Magnesite B	Magnesite C
MgO	96.01	86.71	79.44
CaO	2.05	1.95	11.06
Fe <sub>2</sub> O <sub>3</sub>	0.31	6.57	5.95
Na <sub>2</sub> O	0.02	0.34	0.26
Al <sub>2</sub> O <sub>3</sub>	0.09	1.73	1.30
SiO <sub>2</sub>	1.47	1.82	1.21
P <sub>2</sub> O <sub>5</sub>	0.00	0.02	0.02
SO <sub>3</sub>	0.00	0.00	0.00
K <sub>2</sub> O	0.00	0.02	0.04
TiO <sub>2</sub>	0.01	0.13	0.03
Cr <sub>2</sub> O <sub>3</sub>	0.00	0.02	0.08
MnO	0.01	0.69	0.63
ZrO <sub>2</sub>	0.03	0.01	0.00

**Table S2.** Specific surfaces of the different MgO-species derived from magnesite samples A, B and C

	Magnesite A	Magnesite B	Magnesite C
MgCO <sub>3</sub> (1)	6.61	2.27	3.08
MgO via MgCO <sub>3</sub> (2)	47.23	60.76	43.55
MgO after hydration (5)	215.61	202.83	165.98

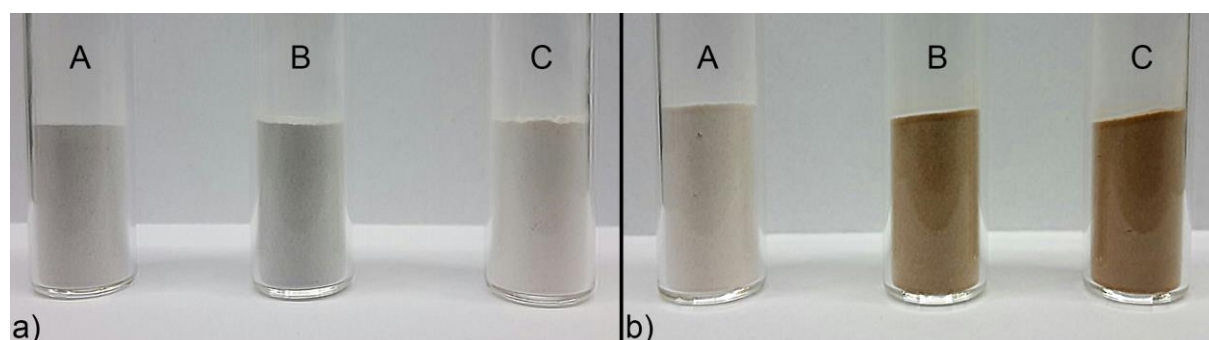


**Figure S1.** Natural magnesite samples A-C a) before calcination b) after calcination

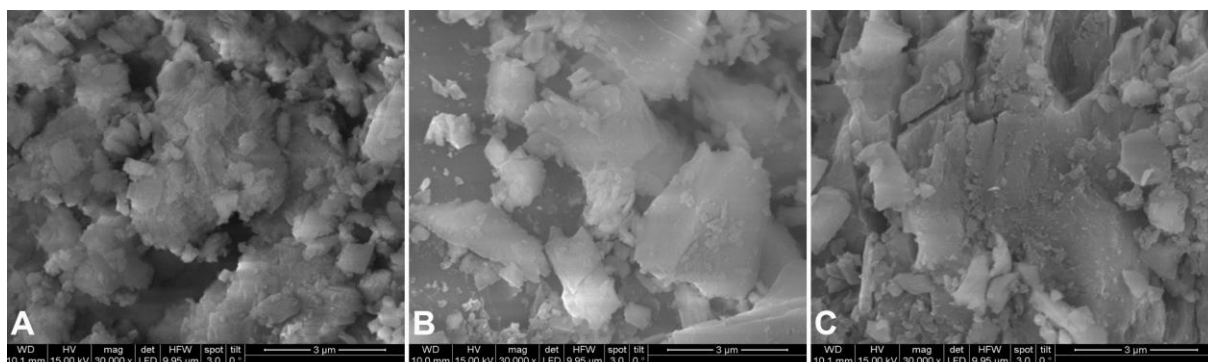


**Figure S2.** SEM-images of the magnesite samples **A1** (left), **B1** (middle) and **C1** (right).

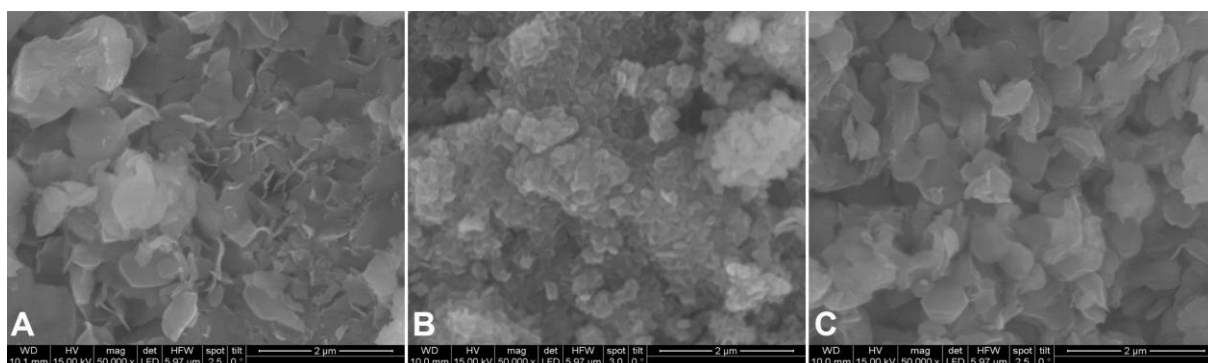


**Figure S2.** SEM-images of the magnesite samples **A6** (left), **B6** (middle) and **C6** (right) after 5 consecutive rehydration / calcination cycles in the P-XRD.

# Metal oxides for thermochemical energy storage – From gas-triggered isothermal cycling to low-temperature applications with increased O<sub>2</sub> pressure

Christian Knoll,<sup>1,2</sup> Georg Gravogl<sup>1,3</sup>, Werner Artner,<sup>4</sup> Elisabeth Eitenberger,<sup>5</sup> Gernot Friedbacher,<sup>5</sup> Andreas Werner,<sup>6</sup> Ronald Miletich,<sup>3</sup> Peter Weinberger,<sup>1</sup> Danny Müller,<sup>1\*</sup> Michael Harasek<sup>2</sup>

<sup>1</sup> Institute of Applied Synthetic Chemistry, TU Wien, Getreidemarkt 9/163-AC, 1060 Vienna, Austria

<sup>2</sup> Institute of Chemical, Environmental & Biological Engineering, TU Wien, Getreidemarkt 9, 1060 Vienna, Austria

<sup>3</sup> Institut für Mineralogie und Kristallographie, University of Vienna, Althanstraße 14, (UZA 2), 1090 Vienna, Austria

<sup>4</sup> X-Ray Center, TU Wien, Getreidemarkt 9, 1060 Vienna, Austria

<sup>5</sup> Institute of Chemical Technologies and Analytics, TU Wien, Getreidemarkt 9/164, 1060 Vienna, Austria

<sup>6</sup> Institute for Energy Systems and Thermodynamics, TU Wien, Getreidemarkt 9/302, 1060 Vienna, Austria

danny.mueller@tuwien.ac.at

## Abstract

Metal oxides providing various, reversibly accessible oxidation states are in the focus as auspicious materials for high-temperature thermochemical energy storage (TCES) materials. Among all principally suitable metal oxides due to equilibrium temperature and, in particular, reaction rate and reversibility, only the couple Co<sub>3</sub>O<sub>4</sub> / CoO and to a smaller extend Mn<sub>2</sub>O<sub>3</sub> / Mn<sub>3</sub>O<sub>4</sub> are considered as suitable candidates. Based on recent studies on isothermal TCES-cycles, the impact of temperature and increased O<sub>2</sub>-pressure on the reaction rate was investigated by varying the O<sub>2</sub>-partial pressure in the low-temperature oxidation of the reduced oxide. Whereas Mn<sub>3</sub>O<sub>4</sub> was found to react too slow for a process at lower temperatures, CoO was found suitable. For an increase of the O<sub>2</sub> pressure to 6 bar between 500 – 550 °C an attractive oxidation behavior was observed. At 900 °C Co<sub>3</sub>O<sub>4</sub> / CoO could be cycled within 4.5 minutes between both oxidation states by changing the atmosphere from N<sub>2</sub> to O<sub>2</sub> and vice versa.

*Keywords: cobalt oxide, manganese oxide, non-ambient pressure, in-situ powder X-Ray diffraction, thermochemical energy storage*

---

## 1. Introduction

The different technologies suitable for thermal energy storage are defined according to the storage process as sensible (Dinker et al., 2015), latent (Zalba et al., 2003) and thermochemical heat storage (Abedin, 2011; Cot-Gores et al., 2012). The latter provides the highest storage densities and has the potential for loss-less storage, once the material was charged. The necessary smaller amounts of material – related to the higher storage densities compared to other techniques, – as well as the enormous applicational flexibility due to the large temperature range being tolerated, are additional advantages of this technique. (Yan, 2015)

The loss-less storage ability of thermochemical energy storage materials (TCES-materials) is an intrinsic feature, as no discharging of the storage occurs in the absence of the reactive gas. The broad operational temperature

profile of TCES-materials is given by the equilibrium temperatures of the applied substance classes. By ranking the materials following to the involved reactive gases such as H<sub>2</sub>O, NH<sub>3</sub>, H<sub>2</sub>, CO<sub>2</sub> or O<sub>2</sub>, the field of application for TCES-materials ranges from low-temperature storage with temperatures below 100 °C (van Essen et al., 2009; Knoll et al., 2017) (mostly hydrated salts for e.g. civil engineering applications as in an energy self-sufficient building) to medium-temperature storage using ammoniates or hydrides and to temperatures between 800-1200 °C (T. Yan, 2015), using carbonates or oxides in combination with e.g. concentrating solar power plants. (Pardo et al., 2014)

Oxides suitable for TCES require several stable oxidation states of the metal, reversibly accessible via redox-reactions. During the charging of the storage material the metal is reduced, while discharging in the presence of O<sub>2</sub> leads to a restorage of the (initial) higher oxidation state (see equation 1).



Although, metal oxides are investigated with respect to their thermochemical properties since the 80's, only a few suitable oxides are known due to the necessary reversibility of the redox-process. Candidate materials promising for application are the couple Co<sub>3</sub>O<sub>4</sub> / CoO, as well as Mn<sub>2</sub>O<sub>3</sub> / Mn<sub>3</sub>O<sub>4</sub> considering reversibility, toxicity issues, temperature range and reaction time. A variety of studies was reported in particular for the cobalt system, covering cycle stability tests (Agrafiotis et al., 2014), composite materials, (Agrafiotis et al., 2016a), (Agrafiotis et al., 2015a; 2015b; Karagiannakis et al., 2016) materials optimization via spinel-phases (Babiniec et al., 2015; Block et al., 2014; LiuPrewitt, 1990), mechanical stress (Karagiannakis et al., 2016), etc. Although, Mn<sub>2</sub>O<sub>3</sub> is also widely known for TCES purposes, (Carrillo, A. J. et al., 2014) due to the slower reaction kinetics, (Alonso et al., 2013; Chen et al., 2013) as well as the minor performance compared to the cobalt-system. Most efforts focussed on the dotation of Mn<sub>2</sub>O<sub>3</sub> with iron (Carrillo, A. J. et al., 2015; Wokon et al., 2017), forming perovskites, or the combination with Co<sub>3</sub>O<sub>4</sub> for a combined system. (Agrafiotis et al., 2016b)

Theoretically suitable metal oxides such as ZnO, (Palumbo, 2001) Fe<sub>2</sub>O<sub>3</sub> or V<sub>2</sub>O<sub>5</sub> feature equilibrium temperatures well above 1500 °C (Pardo et al., 2014), hampering both their routine investigation for storage processes, and their combination with conventional concentrating solar power plants. In order to expand the portfolio of redox-TCES materials, experimental approaches combining TCES with syngas production (Muthusamy et al., 2014), or the application of peroxide / oxide reactions (Carrillo, A. J. et al., 2016) were reported for energy storage in literature.

Apart from their potential of bridging non-operational times in concentrating power plants, the interest in oxidic TCES-materials relates mainly to their high storage density. Recently we could demonstrate (Müller et al., 2017), that between 830 - 930 °C a regime of coexistence between CoO and Co<sub>3</sub>O<sub>4</sub>, depending on the O<sub>2</sub>-concentration, allows for isothermal TCES-cycles. Moreover, both CoO and Mn<sub>3</sub>O<sub>4</sub> start oxidation under O<sub>2</sub>-atmosphere already below 500 °C. Materials of high storage densities would be highly appreciated for applications around these temperatures. To enhance the reaction rate and obtain a material, which would combine fast reaction rates with high energy densities and a broad perspective of applicability, in the present study the impact of temperature on the isothermal redox-cycle, and the effect of an increased oxygen partial pressure on the oxidation rate was investigated by an *in-situ* powder diffraction (P-XRD) study.

## 2. Results and Discussion

### 2.1 Isothermal oxidation of CoO triggered by variation of the reactive gas

Based on the previously identified window of coexistence between CoO and Co<sub>3</sub>O<sub>4</sub>, selected temperatures between 880 °C and 920 °C were chosen to determine the reaction rate by isothermal thermogravimetry / differential scanning calorimetry (TG / DSC). The isothermal reduction of Co<sub>3</sub>O<sub>4</sub> under N<sub>2</sub> with subsequent oxidation by changing the atmosphere to O<sub>2</sub>\* was investigated at five temperature levels for each two cycles

---

\* The redox-reaction of Co<sub>3</sub>O<sub>4</sub> under gas-change conditions was confirmed to be highly comparable for 20 consecutive cycles (figure S1).

(figure 1).

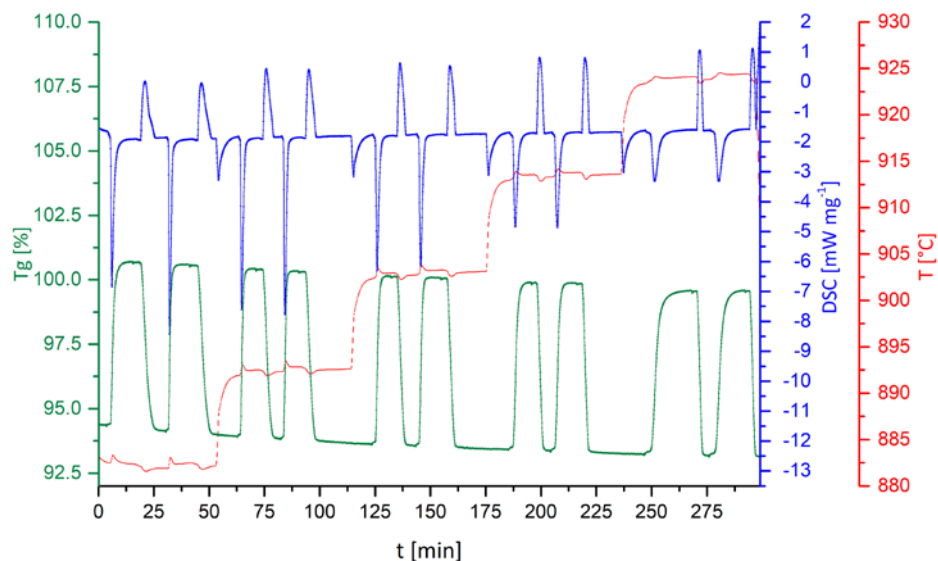


Fig. 1: TG / DSC of isothermal redox-cycles of  $\text{Co}_3\text{O}_4$ , triggered by variation of the atmosphere at 880, 890, 900, 910 and 920 °C

The averaged reaction times for reduction and oxidation, obtained from figure 1, are given in table 1.

Tab. 1: Average reaction times for isothermal reduction and oxidation of  $\text{Co}_3\text{O}_4 / \text{CoO}$ , calculated from the differential scanning calorimetry data

	880 °C	890 °C	900 °C	910 °C	920 °C
Oxidation [min]	$3.92 \pm 0.40$	$3.35 \pm 0.03$	$4.54 \pm 0.11$	$4.95 \pm 0.03$	$6.91 \pm 0.28$
Reduction [min]	$7.07 \pm 0.15$	$5.58 \pm 0.05$	$4.62 \pm 0.08$	$3.96 \pm 0.08$	$3.41 \pm 0.19$

Except the spike for the oxidation time at 890 °C, an apparent linear correlation between reaction time and temperature is obtained. The oxidation time doubles with increased isothermal temperature almost nearly over the whole investigated temperature range, whereas the reduction time is exactly halved. Based on the herein obtained results the most suitable temperature for such an isothermal TCES-process is identified with 900 °C, where oxidation and reduction of the material are taking equal times.

The presented isothermal redox-cycling between 880 - 920 °C with the optimum at 900 °C represents a notable improvement regarding the earlier investigations, where oxidation was accomplished within 10.4 minutes at 848 °C and the complete reduction accounted for 23 minutes. (Müller et al., 2017)

## 2.2 Isothermal oxidation of CoO

The second objective of the current study on isothermal redox-reactions for thermochemical energy storage was the combination of low-temperature oxidation of CoO at around 500 °C under increased  $\text{O}_2$ -pressure. The isothermal oxidation under varied oxygen contents at ambient pressure was selected as a starting point. In order to compare the reactivity towards  $\text{O}_2$  in the desired temperature regime, samples of CoO were oxidized at 500, 520 and 550 °C using an atmosphere with 21 %  $\text{O}_2$  (synthetic air) and 100 %  $\text{O}_2$ .



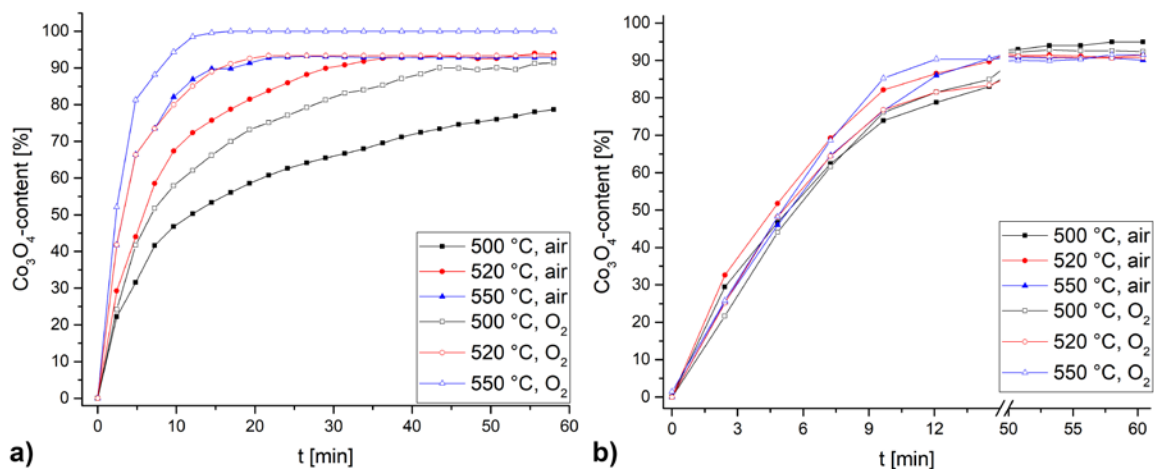


**Fig. 2:** Oxidation rate of CoO at several temperatures and O<sub>2</sub>-concentrations for a) a CoO-sample obtained from thermal decomposition of Co<sub>3</sub>O<sub>4</sub> under N<sub>2</sub> b) a commercial CoO sample

A concentrating plot of the different oxidation rates for CoO – obtained from Co<sub>3</sub>O<sub>4</sub> by thermal reduction of the material under N<sub>2</sub> at 890 °C for 5 minutes – is shown in figure 2a. Especially for the series at 500 °C a notable difference in oxidation rate between the measurement under air and O<sub>2</sub> is found. The impact of the O<sub>2</sub> concentration with increasing temperature is superimposed by the thermal contribution, leading to a nearly identical oxidation rate observed in the experiments at 520 °C under O<sub>2</sub> and 550 °C under air.

In principle both a Co<sub>3</sub>O<sub>4</sub> initially reduced to CoO and a CoO prepared on an industrial scale should be feasible for a Co-based TCES process. For comparison, the same series of oxidation experiments was repeated using a commercial sample of CoO (figure 2b). Interestingly, a completely different picture is observed in this case. The chemically identical sample provides much faster oxidation rates with conversions above 80 % under all applied conditions within the first 15 minutes. The reason for this behavior was found in the SEM-images of both precursors, showing for the Co<sub>3</sub>O<sub>4</sub> (figure 3a) large sintered agglomerates, whereas the CoO (figure 3b) consisted of small, isolated particles. The different O<sub>2</sub>-concentrations, as well as the various temperatures, have no impact on the initial particle morphology (see figure S2).

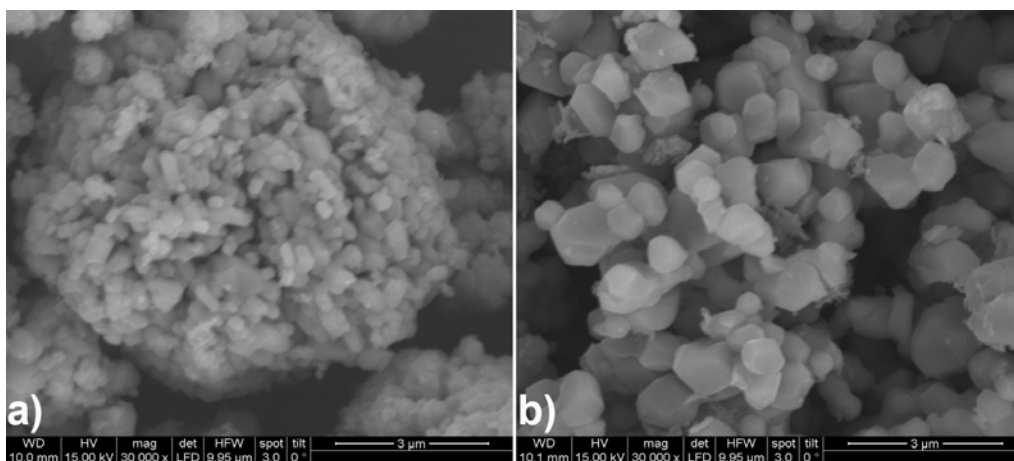


**Fig. 3:** SEM-images of a) commercial Co<sub>3</sub>O<sub>4</sub> b) commercial CoO. Image size 9 x 9 µm

### 2.3 Isothermal oxidation of CoO under elevated O<sub>2</sub> pressure

In order to facilitate investigations on the impact of an increased oxygen pressure, which is higher than the atmospheric one, Co<sub>3</sub>O<sub>4</sub> that has been *in-situ* reduced under N<sub>2</sub> was used for the experimental approach. Although, the commercial CoO sample would provide faster reaction rates, no reliable results would have been obtained even with a high-end laboratory P-XRD setup.<sup>†</sup>

The oxidation rates for the experiments under ambient pressure, 3 bar and 6 bar O<sub>2</sub><sup>‡</sup> are shown in figure 4, which reveals a rate-enhancing effect of the increased O<sub>2</sub> pressure for all three temperature levels. Obviously, the largest influence on the oxidation is observed for 500 °C (figure 4a). By applying 3 bar O<sub>2</sub> the conversion within the first 15 minutes is enhanced about 20 %. 6 bar O<sub>2</sub> result in a quantitative Co<sub>3</sub>O<sub>4</sub> formation after 30 minutes, the reaction rate being only slightly faster than for 3 bar.

In case of the series at 520 °C, O<sub>2</sub> oxidation under ambient pressure and 3 bar O<sub>2</sub> reveal only slight differences in the reaction rate. At 6 bar O<sub>2</sub> an increased oxidation within the first 6 minutes leads to quantitative Co<sub>3</sub>O<sub>4</sub> formation after 15 minutes. Finally, at 550 °C the temperature increase predominates over the increased pressure, as both 3 bar and 6 bar O<sub>2</sub> yield a complete oxidation - 3 bar after 12 minutes, 6 bar after 8 minutes.

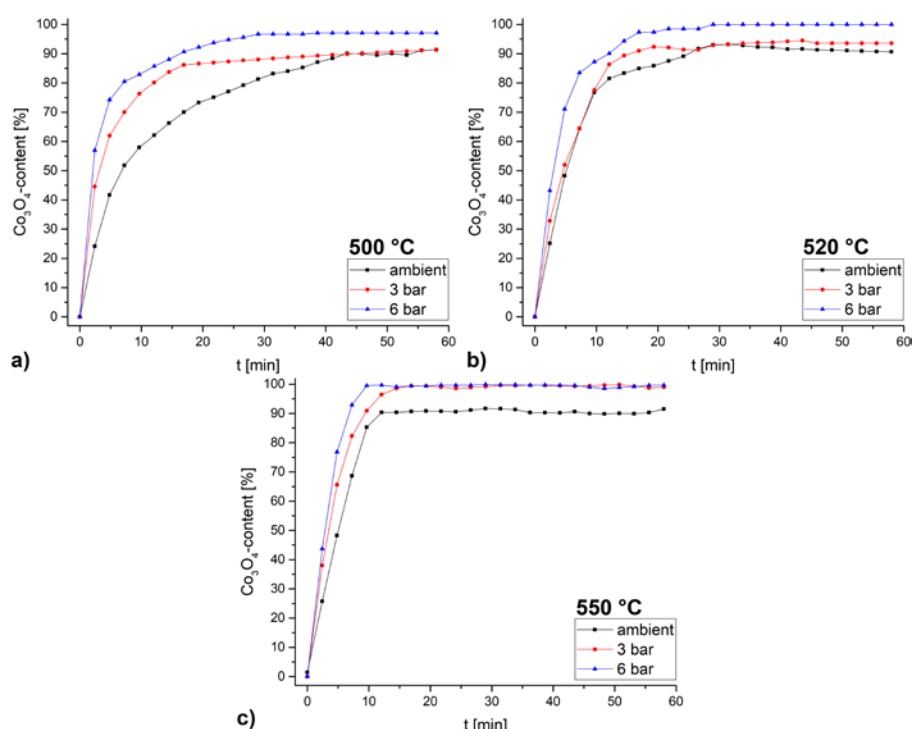


Fig. 4: Oxidation rate of CoO at different pressures and temperatures at a) 500 °C b) 520 °C c) 550 °C

Based on these results a lower oxidation temperature for CoO in a TCES-process seems feasible, increasing the reaction rate by moderately enhanced pressure. For technological processes elevated pressure is always correlated with much higher expenditures regarding the process design. Using only 6 bar O<sub>2</sub> – for all three temperatures yielding a notable enhancement of the conversion rate – may be still worth the efforts aiming for an oxide-based

<sup>†</sup> This limitation – also slightly affecting the accuracy of the phase-determination for the high Co<sub>3</sub>O<sub>4</sub>-contents – is attributed to the overlap of significant peaks in the diffractograms of the two Co-phases, as well as the high fluorescence of the Co-containing samples in combination with the available Cu K<sub>α</sub>-radiation (see figure S3). To ensure the data quality, a minimum measurement time of 2 minutes per diffractogram was necessary.

<sup>‡</sup> Although, the used Anton Paar XRK 900 would tolerate pressures up to 12 bar, applying a higher pressure than 6 bar O<sub>2</sub> extends due to radiation absorption and the fluorescence background the measurement time notably, so within one diffractogram the transformation from CoO to Co<sub>3</sub>O<sub>4</sub> is completed. For similar measurements under higher pressures a different X-Ray source or a synchrotron would be needed.

medium-temperature TCES-process.

The only drawback of the increased pressure is the promoted sintering of the material, which is already evidenced in the SEM-images of the  $\text{Co}_3\text{O}_4$  samples, oxidized at 550 °C and various pressures (see figure 5). Nevertheless, this changed particle morphology so far was not found to decrease the reactivity of the material on repeated cycling.

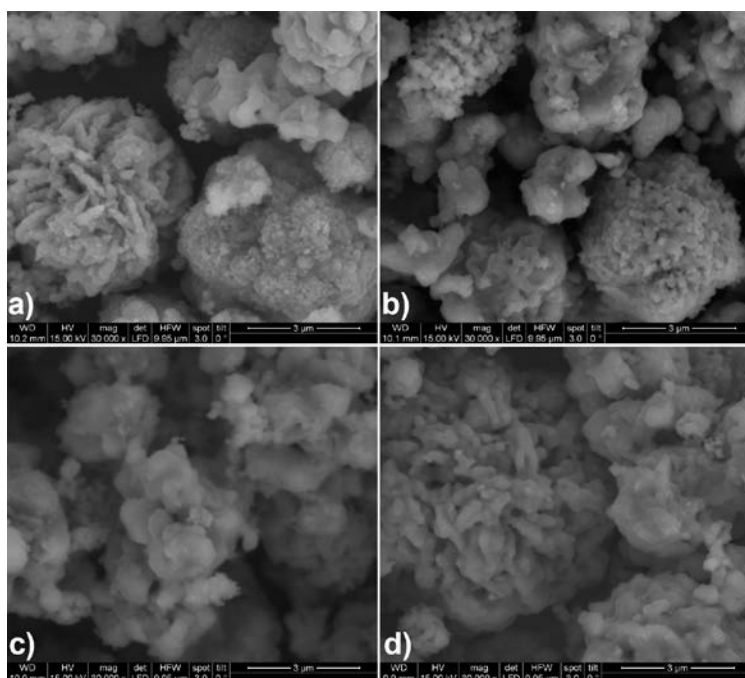


Fig. 5: Particle morphology of  $\text{Co}_3\text{O}_4$  after oxidation at 550 °C and varied  $\text{O}_2$  pressures a)  $\text{Co}_3\text{O}_4$  starting material b) ambient pressure c) 3 bar  $\text{O}_2$  d) 6 bar  $\text{O}_2$ . Image size 9 x 9  $\mu\text{m}$

#### 2.4 Isothermal oxidation of $\text{Mn}_3\text{O}_4$

Similar to the study on the isothermal oxidation of  $\text{CoO}$ , a series was carried out also on  $\text{Mn}_3\text{O}_4$  which was oxidized at different temperatures (470 °C, 500 °C, 520 °C, 550 °C) and ambient pressure under synthetic air and pure oxygen (figure 6).

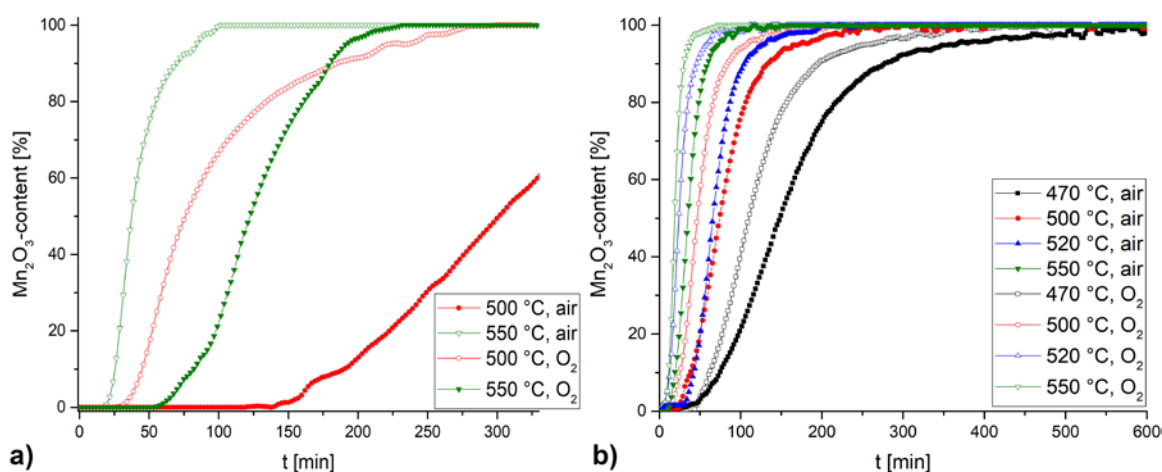


Fig. 6: Oxidation rate of  $\text{Mn}_3\text{O}_4$  at various temperatures and  $\text{O}_2$ -concentrations for a) a  $\text{Mn}_3\text{O}_4$ -sample obtained from thermal decomposition of  $\text{MnO}_2$  under  $\text{N}_2$  b) a commercial  $\text{Mn}_3\text{O}_4$  sample

Similar to the Co-system also for  $\text{Mn}_3\text{O}_4$  a notable difference between the *in-situ* reduced sample under  $\text{N}_2$  (figure 6a) and the commercially obtained  $\text{Mn}_3\text{O}_4$  (figure 6b) was found. For the freshly reduced  $\text{Mn}_3\text{O}_4$  at 500 °C under

air within 330 minutes only 62 % of  $\text{Mn}_2\text{O}_3$  are formed, whereas  $\text{O}_2$  enables complete conversion to  $\text{Mn}_2\text{O}_3$ . Still a notable difference is observed at 550 °C, where both air and  $\text{O}_2$  result in complete re-oxidation.

In the case of the commercial  $\text{Mn}_3\text{O}_4$  a clear trend towards faster oxidation rates, both with increased temperature and  $\text{O}_2$ -content is found. Similar to CoO also for  $\text{Mn}_3\text{O}_4$  temperature increases the oxidation rate more efficiently than a higher  $\text{O}_2$  concentration. Comparable oxidation rates in this case are found at 550 °C under air and 520 °C under  $\text{O}_2$ .

### 3. Conclusion

In the present study the redox-couple  $\text{Co}_3\text{O}_4$  / CoO was investigated with respect to an isothermal redox-cycle, triggered by changing the atmosphere from  $\text{N}_2$  to  $\text{O}_2$  between 880 – 920 °C. A reasonably linear correlation was found between the reduction / oxidation times and the applied temperature. Within the investigated temperature range the best conditions for an isothermal redox-cycle were found at 900 °C, as both reduction and oxidation take place quantitatively within 4.5 minutes. This represents an improvement of the so far reported results on isothermal cycling.

Based on former results an isothermal low-temperature oxidation of CoO between 500-550 °C under increased  $\text{O}_2$ -pressure was attempted, allowing for the application (only discharging) of a TCES-material featuring a high energy density at medium-temperatures. Increasing the  $\text{O}_2$ -pressure during oxidation from ambient conditions to 6 bar resulted in an attractive increase of reaction rate, discharging the CoO (oxidation to  $\text{Co}_3\text{O}_4$ ) quantitatively at 500 °C within 24 minutes, at 550 °C within 8 minutes.

$\text{Mn}_3\text{O}_4$  was found to be too slow in its oxidation under all investigated conditions to be competitive in comparison to CoO.

## 4. Experimental

### 4.1 Material

Cobalt(II,III) oxide (99.995%), cobalt(II) oxide (99.99%), manganese(IV) oxide (99.99%) and manganese(II, III) oxide (97%) were obtained from Sigma-Aldrich and used as supplied.

### 4.2 X-Ray Powder Diffraction

The powder X-ray diffraction measurements were carried out on a PANalytical X'Pert Pro diffractometer in Bragg-Brentano geometry using  $\text{Cu K}_{\alpha 1,2}$  radiation and an X'Celerator linear detector with a Ni-filter. For *in-situ* experiments at elevated pressures an Anton Paar XRK 900 reaction chamber, operable between ambient pressure and 12 bar was used. The sample was mounted on a hollow ceramic powder sample holder, allowing for complete perfusion of the sample with the reactive gas. The sample temperature is controlled directly via a NiCr-NiAl thermocouple and direct environmental heating. For the *in-situ* experiments at ambient pressure an Anton Paar HTK 1200N sample chamber was used. The sample temperature is controlled via a Pt 10 % RhPt thermocouple and direct environmental heating. The diffractograms were evaluated using the PANalytical program suite HighScorePlus v4.6a. (Degen et al., 2014) A background correction and a  $\text{K}_{\alpha 2}$  strip were performed. Phase assignment is based on the ICDD-PDF4+ database (<http://www.icdd.com>), the exact phase composition, shown in the conversion plots, was obtained via Rietveld-refinement incorporated in the program suite HighScorePlus v4.6a. (Degen et al., 2014) All quantifications based on P-XRD are accurate within of  $\pm 5$  %.

### 4.3 Thermal Analysis

For thermal analysis of the redox-reactions a Netzsch TGA/DSC 449 C Jupiter ® equipped with a water vapour furnace including an air-cooled double jacket was used. The oven operates between 25 °C and 1250 °C, regulated by an S-type thermocouple. Oxygen and nitrogen gases were 99.999 % and obtained from Messer. For all measurements under air a mixture of 21 %  $\text{O}_2$  and 79 %  $\text{N}_2$  was applied. The gas flow was set to 25 ml  $\text{min}^{-1}$ ,

controlled and mixed with Vögtlin Instruments “red-y” mass flow controllers. A sample mass of 20 mg in an open  $\text{Al}_2\text{O}_3$  crucible was used for all experiments with heating and cooling rates of  $10\text{ }^\circ\text{C min}^{-1}$ . The DSC was calibrated according to the procedure suggested by Netzsch, using the In, Sn, Bi, Zn, Al and Ag standards provided by the manufacturer.

#### 4.4 Scanning Electron Microscopy

SEM images were recorded on gold coated samples with a Quanta 200 SEM instrument from FEI under low-vacuum at a water vapor pressure of 80 Pa to prevent electrostatic charging.

### 5. References

1. Dinker, A., M. Agarwal, and G.D. Agarwal, 2015. Heat storage materials, geometry and applications: A review. *Journal of the Energy Institute*
2. Zalba, B., et al., 2003. Review on thermal energy storage with phase change: materials, heat transfer analysis and applications. *Applied Thermal Engineering* 3, 251-283.
3. Ali H. Abedin, M.A.R., 2011. A Critical Review of Thermochemical Energy Storage Systems. *The Open Renewable Energy Journal* 42-46.
4. Cot-Gores, J., A. Castell, and L.F. Cabeza, 2012. Thermochemical energy storage and conversion: A state-of-the-art review of the experimental research under practical conditions. *Renewable and Sustainable Energy Reviews* 7, 5207-5224.
5. T. Yan, R.Z.W., T. X. Li, L.W.Wang, Ishugah T. Fred, 2015. A review of promising candidate reactions for chemical heat storage. *Renewable and Sustainable Energy Reviews* 13-31.
6. van Essen, V.M., et al., 2009. Characterization of Salt Hydrates for Compact Seasonal Thermochemical Storage. 825-830.
7. Knoll, C., et al., 2017. Probing cycle stability and reversibility in thermochemical energy storage –  $\text{CaC}_2\text{O}_4\cdot\text{H}_2\text{O}$  as perfect match? *Applied Energy* 1-9.
8. Pardo, P., et al., 2014. A review on high temperature thermochemical heat energy storage. *Renewable and Sustainable Energy Reviews* 591-610.
9. Agrafiotis, C., et al., 2014. Exploitation of thermochemical cycles based on solid oxide redox systems for thermochemical storage of solar heat. Part 1: Testing of cobalt oxide-based powders. *Solar Energy* 189-211.
10. Agrafiotis, C., et al., 2016a. Exploitation of thermochemical cycles based on solid oxide redox systems for thermochemical storage of solar heat. Part 5: Testing of porous ceramic honeycomb and foam cascades based on cobalt and manganese oxides for hybrid sensible/thermochemical heat storage. *Solar Energy* 676-694.
11. Agrafiotis, C., et al., 2015a. Exploitation of thermochemical cycles based on solid oxide redox systems for thermochemical storage of solar heat. Part 2: Redox oxide-coated porous ceramic structures as integrated thermochemical reactors/heat exchangers. *Solar Energy* 440-458.
12. Agrafiotis, C., et al., 2015b. Exploitation of thermochemical cycles based on solid oxide redox systems for thermochemical storage of solar heat. Part 3: Cobalt oxide monolithic porous structures as integrated thermochemical reactors/heat exchangers. *Solar Energy* 459-475.
13. Karagiannakis, G., et al., 2016. Cobalt/cobaltous oxide based honeycombs for thermochemical heat storage in future concentrated solar power installations: Multi-cyclic assessment and semi-quantitative heat effects estimations. *Solar Energy* 394-407.
14. Babiniec, S.M., et al., 2015. Investigation of  $\text{LaxSr}_{1-x}\text{Co}_y\text{M}_{1-y}\text{O}_{3-\delta}$  (M=Mn, Fe) perovskite materials as thermochemical energy storage media. *Solar Energy* 451-459.
15. Block, T., N. Knoblauch, and M. Schmäcker, 2014. The cobalt-oxide/iron-oxide binary system for use as high temperature thermochemical energy storage material. *Thermochemica Acta* 25-32.
16. Liu, X. and C. Prewitt, 1990. High-temperature X-ray diffraction study of  $\text{Co}_3\text{O}_4$ : Transition from normal to disordered spinel. *Physics and Chemistry of Minerals* 2,
17. Carrillo, A.J., et al., 2014. Thermochemical heat storage based on the  $\text{Mn}_2\text{O}_3/\text{Mn}_3\text{O}_4$  redox couple: influence of the initial particle size on the morphological evolution and cyclability. *J. Mater. Chem. A* 45, 19435-19443.
18. Alonso, E., et al., 2013. Kinetics of  $\text{Mn}_2\text{O}_3\text{--Mn}_3\text{O}_4$  and  $\text{Mn}_3\text{O}_4\text{--MnO}$  Redox Reactions Performed under Concentrated Thermal Radiative Flux. *Energy & Fuels* 8, 4884-4890.
19. Chen, S., et al., 2013. Synthesis of  $\text{Mn}_2\text{O}_3$  microstructures and their energy storage ability studies. *Electrochimica Acta* 360-371.
20. Carrillo, A.J., et al., 2015. Improving the Thermochemical Energy Storage Performance of the  $\text{Mn}_2\text{O}_3/\text{Mn}_3\text{O}_4$  Redox Couple by the Incorporation of Iron. *ChemSusChem* 11, 1947-1954.

21. Wokon, M., A. Kohzer, and M. Linder, 2017. Investigations on thermochemical energy storage based on technical grade manganese-iron oxide in a lab-scale packed bed reactor. *Solar Energy* 200-214.
22. Agrafiotis, C., M. Roeb, and C. Sattler, 2016b. Exploitation of thermochemical cycles based on solid oxide redox systems for thermochemical storage of solar heat. Part 4: Screening of oxides for use in cascaded thermochemical storage concepts. *Solar Energy* 695-710.
23. Möller, S. and R. Palumbo, 2001. The Development of a Solar Chemical Reactor for the Direct Thermal Dissociation of Zinc Oxide. *Journal of Solar Energy Engineering* 2, 83.
24. Muthusamy, J.P., N. Calvet, and T. Shamim, 2014. Numerical Investigation of a Metal-oxide Reduction Reactor for Thermochemical Energy Storage and Solar Fuel Production. *Energy Procedia* 2054-2057.
25. Carrillo, A.J., et al., 2016. Revisiting the BaO<sub>2</sub>/BaO redox cycle for solar thermochemical energy storage. *Phys. Chem. Chem. Phys.* 11, 8039-8048.
26. Müller, D., et al., 2017. Combining in-situ X-ray diffraction with thermogravimetry and differential scanning calorimetry – An investigation of Co<sub>3</sub>O<sub>4</sub>, MnO<sub>2</sub> and PbO<sub>2</sub> for thermochemical energy storage. *Solar Energy* 11-24.
27. Degen, T., et al., 2014. The HighScore suite. *Powder Diffraction* S2, S13-S18.
28. <http://www.icdd.com>,



## 6. Appendix

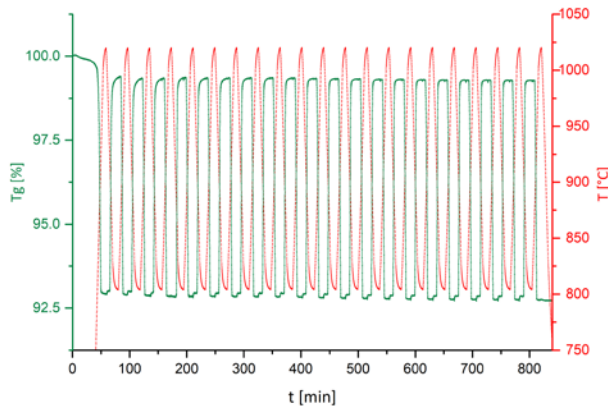


**Fig. S1: 20 consecutive redox-cycles of  $\text{Co}_3\text{O}_4$  under alternating atmosphere ( $\text{N}_2$  vs.  $\text{O}_2$ )**

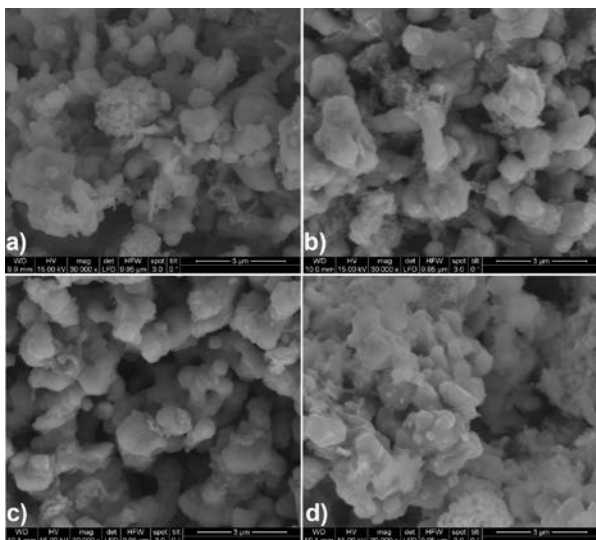


**Fig. S2: SEM images of different  $\text{Co}_3\text{O}_4$  samples after the oxidation in the P-XRD a) CoO after oxidation under air at 500 °C b) CoO after oxidation under air at 550 °C c) CoO after oxidation under  $\text{O}_2$  at 500 °C d) CoO after oxidation under  $\text{O}_2$  at 550 °C. Image size 9 x 9  $\mu\text{m}$**

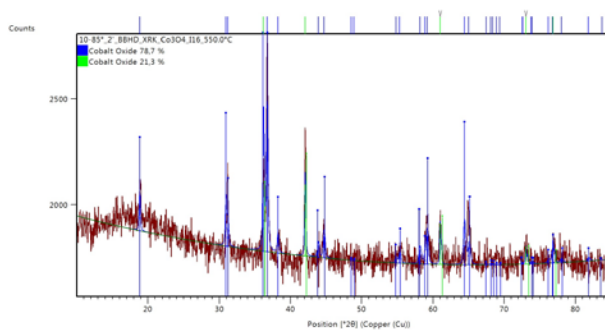


**Fig. S3: P-XRD of a mixed  $\text{CoO} / \text{Co}_3\text{O}_4$  sample, showing the moderate signal-to-noise ratio for the weaker peaks due to the X-Ray fluorescence of Co**

## Transition metal ammoniates for thermochemical energy storage

Danny Müller<sup>a,\*</sup>, Christian Knoll<sup>a,b</sup>, Christian Jordan<sup>b</sup>, Jan M. Welch<sup>c</sup>, Andreas Werner<sup>d</sup>, Michael Harasek<sup>b</sup>, Peter Weinberger<sup>a</sup>

Received 00th January 20xx,  
Accepted 00th January 20xx

DOI: 10.1039/x0xx00000x

[www.rsc.org/](http://www.rsc.org/)

On the quest for novel materials applicable as thermochemical energy storage (TCES) materials at medium-temperature levels between 25 °C - 400 °C, the class of transition metal ammoniates was so far widely neglected. In the present study a series of metal chlorides and sulphates were investigated for their performance as TCES-materials, reversibly forming in the presence of ammonia the corresponding ammine-complexes. Among the investigated materials high storage densities and high cycle stabilities were found. In the case of the chlorides decomposition in the presence of ammonia caused slow degradation. In contrast, sulphates are perfectly stable and reversible under the investigated conditions. Aiming for a combination of high storage densities and complete reversibility, for CuSO<sub>4</sub> the best performance was obtained. According to the presented results, selected transition metal ammoniates are suggested as attractive new materials for high-performance TCES-applications, allowing due to their high storage densities for efficient combination with *e.g.* solar heating to overcome non-operational times.

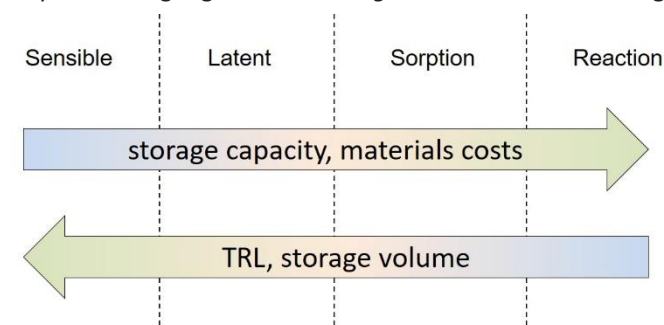
### Introduction

On the road to a more sustainable and renewable energy supply chain a major challenge for integration of renewable energy into existing structures is the compensation of peaks in energy production and energy demand.<sup>1</sup> Especially in combination with fluctuating energy sources as the sun, non-operational times at night or harsh weather conditions, and the temporal mismatch between production and consumption need coverage to ensure the required energy supply.<sup>2,3</sup> For shifting collected solar excess heat to low-production times, efficient thermal storage is necessary.<sup>4</sup> The same issue is also highly relevant for heat recovery systems, recovering so far unused (industrial) waste heat.<sup>1,2</sup> In other words, the success of matching demand and supply is strongly related to the availability and development of efficient heat storage technologies.

Several concepts are known for the storage of heat,<sup>3,5</sup> the most important being sensible,<sup>5</sup> latent<sup>6</sup> and thermochemical<sup>7,8</sup> (sorption and reaction) heat storage are known. Whereas, the storage capacity of the technologies increases from left to right in scheme 1, their technology readiness level is inverted. A very illustrative example of necessary expenditures for a storage capacity of 10 GJ using the various available storage technologies was given by Luo et al., demonstrating, that 1 m<sup>3</sup> of thermochemical storage material can replace 34 m<sup>3</sup> of sensible heat storage medium.<sup>9</sup>

In literature the state of the art for thermal storage systems in combination with solar thermal systems is extensively reviewed revealing, that despite the generally acknowledged potential of thermochemical energy storage (TCES) concepts so far, only sensible, and to a much smaller extent latent storage systems are used.<sup>1-6,9-17</sup>

The experimental concept of thermochemical storage includes charging of the material by its chemical decomposition ( $A + \text{heat} \leftrightarrow B + C$ ), storage of the material and, finally, re-formation of the initial material with concomitant release of the stored energy during the discharging step.<sup>7,8</sup> This concept allows for highest storage capacities, loss-less (long-term) storage without necessity of insulation and a broad range of operational temperatures according to the selected storage reaction.<sup>18</sup> The drawbacks so far preventing an application are the issues of cycle stability, reaction rate and of course the materials investment costs. Many *per se* suitable materials reveal slow decomposition during cycling or very slow reaction rates for the discharging step, therefore, disqualifying them for a thermochemical application. The material costs – obviously in any case being higher than for *e.g.* water as sensible storage



**Scheme 1** Schematic comparison of storage capacity, materials costs, technology readiness level (TRL) and necessary storage volume for the different thermal energy storage concepts.

<sup>a</sup> Institute of Applied Synthetic Chemistry, TU Wien, Getreidemarkt 9/163-AC, 1060 Vienna, Austria E-mail: [danny.mueller@tuwien.ac.at](mailto:danny.mueller@tuwien.ac.at)

<sup>b</sup> Institute of Chemical, Environmental & Biological Engineering, Getreidemarkt 9/166, 1060 Vienna, Austria

<sup>c</sup> Atominstytut, TU Wien, Stadionallee 2, 1020 Vienna, Austria

<sup>d</sup> Institute for Energy Systems and Thermodynamics, TU Wien, Getreidemarkt 9, 1060 Vienna, Austria

Electronic Supplementary Information (ESI) available: [Energy content and thermogravimetry of all investigated materials.] See DOI: 10.1039/x0xx00000x

material – may be relativized putting them into perspective with the storage capacity, faster reaction times during charging and discharging and to reduced overall investment costs due to notably smaller storage systems. Summing up, the ideal thermochemical storage material would provide a preferably high energy storage density at moderate materials costs, perfect cycle stability without any degradation effects and a fast reaction rate for charging and discharging.

A class of TCES-materials which so far found only minor attention in literature are (transition) metal salt ammoniates, using  $\text{NH}_3$  as reactive gas. Based on theoretically calculated values, ammoniates should provide exceptionally high energy storage capacities. Nevertheless, only a few studies with  $\text{NH}_3$  as reactive gas in combination with metal salts were published since their first mentioning in the 80's.<sup>19-22</sup> Many more efforts were put on the thermal dissociation and recombination of ammonia in solar power plants.<sup>23-27</sup>

To derive, whether salt ammoniates could reveal as ideal thermochemical energy storage material according to the above-mentioned criteria, in the herein presented study a systematic survey on the reaction of (transition) metal chlorides and sulphates with  $\text{NH}_3$  was performed, putting special emphasis on the experimental determination of energy storage capacity and reversibility / cycle stability.

## Experimental

### Material

All transition metal salts were commercially obtained and used as supplied. Ammonia (99.98 %) was obtained from Messer.

### Thermal analysis

For thermal analysis a Netzsch TGA/DSC 449 C Jupiter® equipped with a water vapour furnace including an air-cooled double jacket was used. The oven operates between 25 °C and 1250 °C, regulated by an S-type thermocouple. For determination of the energy contents at room-temperature the gas flow was set to 100 ml min<sup>-1</sup>, controlled by Vögtlin Instruments “red-y” mass flow controllers. For decomposition and cycle experiments, a sample mass of approximately 10 mg

in an open alumina crucible was used, applying heating and cooling rates of 10 °C min<sup>-1</sup>. The DSC was calibrated according to the procedure suggested by Netzsch, using the In, Sn, Bi, Zn, Al and Ag standards provided by the manufacturer. Prior to all measurements a correction was performed.

## Results and discussion

The first report of a thermochemical energy storage system utilizing  $\text{NH}_3$  was limited to  $\text{CaCl}_2$  and  $\text{ZnCl}_2$ ,<sup>19</sup> although the  $\text{NH}_3$  coordination chemistry of a variety of other transition metal ions including  $\text{Cu}^{2+}$ ,  $\text{Co}^{2+}$  and  $\text{Ni}^{2+}$  is well-known.<sup>28</sup> Apart from the ammine-complexes of transition metal chlorides featuring textbook examples of complex ion isomerism,<sup>28</sup> the ammine complexes of transition metal sulphates are also known. Based on a systematic analysis of thermochemical database entries, metal salts (e.g.  $\text{Pd}^{2+}$ ,  $\text{Pt}^{2+}$ ,  $\text{Cd}^{2+}$ ,  $\text{Sc}^{3+}$ ,  $\text{Ce}^{3+}$ ) theoretically attractive for TCES with  $\text{NH}_3$  as reactive gas<sup>29</sup> and a variety of transition metal candidates derived from ‘text-book knowledge’ (e.g.  $\text{Mn}^{2+}$ ,  $\text{Fe}^{2+/3+}$ ,  $\text{Co}^{2+}$ ,  $\text{Ni}^{2+}$ ,  $\text{Cu}^{2+}$ ,  $\text{Zn}^{2+}$ ), a variety of (transition) metal chlorides and sulphates were investigated.

Differential scanning calorimetry (DSC) under an  $\text{NH}_3$  atmosphere at 25 °C was used to determine the heat of formation of the ammine-complexes. In figure 1a the energy contents for all investigated anhydrous salts are given. The materials are ranked according to their gravimetric energy contents (kJ/kg; blue) with molar energy content (kJ/mol; green) reported for completeness and convenience. As several of the investigated salts are available both in their anhydrous and variously hydrated forms, the most common hydrate species were also investigated with respect to their reactivity toward  $\text{NH}_3$  (figure 1b). Of the anhydrous materials investigated, the highest energy content was measured for  $\text{NiCl}_2$ , liberating 2464 kJ kg<sup>-1</sup> during amination. This accounts to a storage capacity of 2.43 MWh per m<sup>3</sup> of the material. Of the sulphates investigated,  $\text{CuSO}_4$  (position 5, 1772 kJ kg<sup>-1</sup> [1.72 MWh per m<sup>3</sup>]) was found to have the largest heat of formation for its tetraamine-complex. In figure S1 the entries from figure 1 are ranked according to the molar energy contents, favouring salts with a higher molecular weight, especially in the case of the hydrates. The exact values for both energy content in

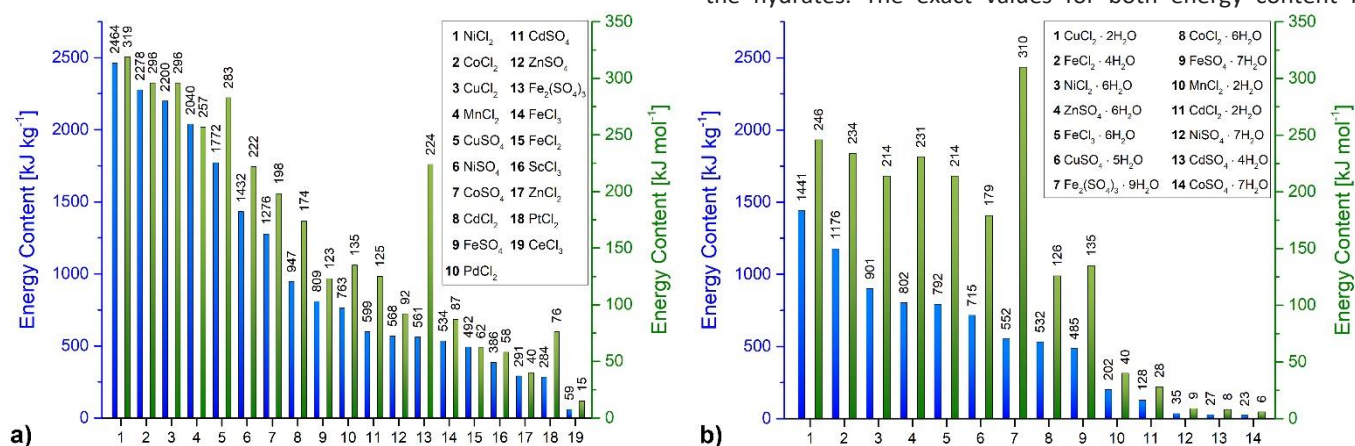
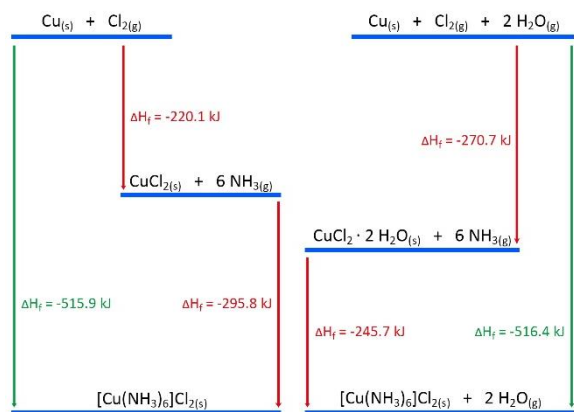


Figure 1 Energy content of selected (transition) metal salts for reaction with  $\text{NH}_3$  at 25 °C. a) Anhydrous form of the salts b) Most common hydrate species



**Figure 3** Schematic comparison of the heats of formation for anhydrous  $\text{CuCl}_2$  and  $\text{CuCl}_2 \cdot 2\text{H}_2\text{O}$  and the further reaction with  $\text{NH}_3$  to the  $[\text{Cu}(\text{NH}_3)_6]\text{Cl}_2$ -complex.  $\Delta H_f$   $\text{CuCl}_2$  /  $\text{CuCl}_2 \cdot 2\text{H}_2\text{O}$ : The NBS tables of chemical thermodynamic properties<sup>32</sup>;  $\Delta H_f$   $[\text{Cu}(\text{NH}_3)_6]\text{Cl}_2$ : This work.

$\text{kJ kg}^{-1}$  and  $\text{kJ mol}^{-1}$ , as well as the energy density in  $\text{MJ m}^{-3}$ , allowing for the technologically important assessment of the volumetric efficiency of a storage material, are given in table S1. Although, according to theoretical data<sup>29</sup> also  $\text{Pd}^{2+}$ ,  $\text{Pt}^{2+}$ ,  $\text{Cd}^{2+}$ ,  $\text{Sc}^{3+}$ ,  $\text{Ce}^{3+}$  should react highly exothermic with  $\text{NH}_3$  to form ammine-complexes, based on the results from figure 1 investigations were limited to the first-row transition metal salts.

The significantly different energy contents determined for sulphates and chlorides of the same cation – the sulphates displaying values between 20 to  $100 \text{ kJ mol}^{-1}$  lower than the chlorides – are attributed to the lower Lewis-acidity of the sulphates, as well as to the impact of the anion. The bivalent sulphate anions promote in the case of *e.g.*  $[\text{Cu}(\text{NH}_3)_4]\text{SO}_4 \cdot \text{H}_2\text{O}$  a square-planar geometry of the  $\text{NH}_3$ -ligands around the  $\text{Cu}^{2+}$ -ion,<sup>30</sup> whereas in the case of the smaller monovalent chloride anions the  $\text{Cu}^{2+}$ -ion is coordinated octahedrally by six  $\text{NH}_3$ -ligands.<sup>31</sup>

In addition to the anion, the initial salt hydration state affects the heat of reaction for the formation of ammine-complexes. In figure 2 a schematic representation of the heats of reaction for  $[\text{Cu}(\text{NH}_3)_6]\text{Cl}_2$  is given, on the left via anhydrous  $\text{CuCl}_2$  as intermediate, on the right via the dihydrate  $\text{CuCl}_2 \cdot 2\text{H}_2\text{O}$ . All involved reaction steps from copper to the final  $[\text{Cu}(\text{NH}_3)_6]\text{Cl}_2$ -complex are exothermic. For the initial formation of  $\text{CuCl}_2$  the coordination of two water molecules results a higher enthalpy of formation. Consequently, for the ligand-exchange reaction during reaction of  $\text{CuCl}_2 \cdot 2\text{H}_2\text{O}$  with  $\text{NH}_3$  a lower enthalpy of reaction is observed than for  $\text{CuCl}_2$ . For both pathways, combining the literature values for the  $\Delta H_f$   $\text{CuCl}_2$  /  $\text{CuCl}_2 \cdot 2\text{H}_2\text{O}$ <sup>32</sup> with the formation enthalpy for  $[\text{Cu}(\text{NH}_3)_6]\text{Cl}_2$  determined in the present work, a perfect agreement for the calculated  $\Delta H_f = -516 \text{ kJ mol}^{-1}$  was found.

The exothermic reaction between the metal salt and  $\text{NH}_3$  corresponds to the discharging reaction of a TCES-material. Charging the storage material through thermal decomposition of the ammine-complex formed results in the anhydrous material, regardless of the used salt precursor. Therefore, on repeated operation of the TCES-process, the lower energy

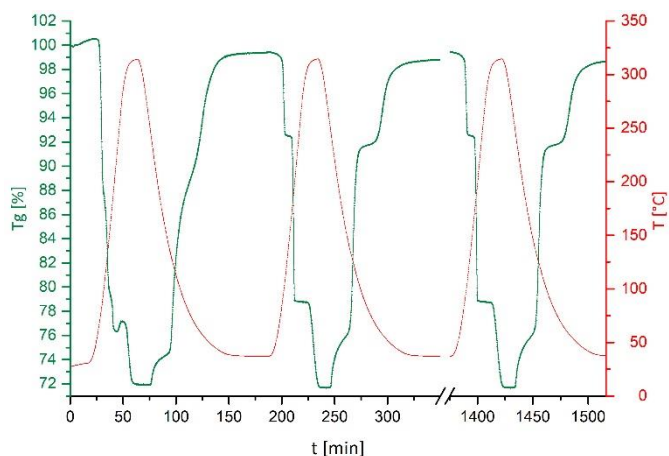


**Figure 2** Cycling experiment with  $\text{CuSO}_4 \cdot 5\text{H}_2\text{O}$ . During the first complete charging / discharging the former hydrate water is removed from the system, resulting a stable and reproducible performance from the second cycle on. For comparison, after the intersection the 10<sup>th</sup> cycle is represented.

capacity of the hydrated salts is observed for only the first cycle, from the second cycle on reproducibly the capacity of the anhydrous material is observed. Once the hydrate water is fully removed after the first charging / discharging cycle, from the second cycle on the performance is fully reversible and unvaried during continuous operation. In figure 3 this behaviour is shown for the case of  $\text{CuSO}_4 \cdot 5\text{H}_2\text{O}$ , for which, after initial formation of the ammine-complex at  $25^\circ\text{C}$  starting from  $\text{CuSO}_4 \cdot 5\text{H}_2\text{O}$ , the hydrate water is removed from the system within the first complete charging / discharging cycle, then leading to a stable energy storage performance of the material.

The key requirement for a TCES-material is not only a high energy storage potential, but more critically, full reversibility, allowing for long-term application of the system. Therefore,  $\text{NiCl}_2$  as transition metal salt with the most attractive energy storage potential was investigated for cycle stability by TG / DSC from  $25$  to  $400^\circ\text{C}$ . Even after the first cycle 5.4 % of the initial  $\text{NiCl}_2$ -mass were lost. This mass-loss continues during cycling and worsens throughout the seven test cycles to 25.2 %.

The reason for this continuous mass-loss of  $\text{NiCl}_2$  is thought to be a combination of transport phenomenon and decomposition

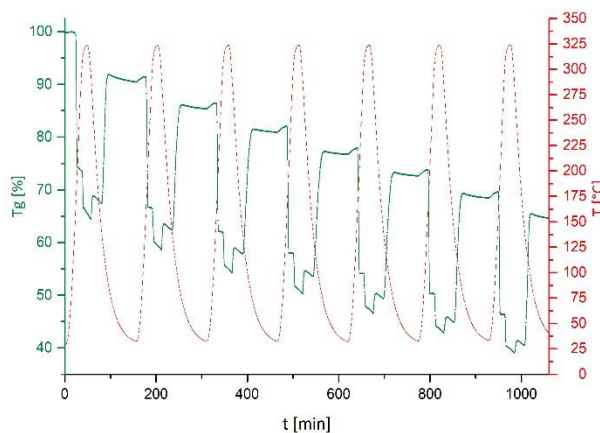


**Figure 4** Mass-loss of  $\text{NiCl}_2$  during cycle-stability tests. Within 7 consecutive cycles % of the initial  $\text{NiCl}_2$  is lost.



of NiCl<sub>2</sub>, heated under an atmosphere of NH<sub>3</sub>. After the 7<sup>th</sup> cycle, the formerly yellow material had darkened and traces of NH<sub>4</sub>Cl could be identified. In addition, on the sample holder of the TG / DSC system, a dark layer had deposited around the crucible. The slow decomposition observed in the case of NiCl<sub>2</sub> was also observed during cycling experiments with CoCl<sub>2</sub> and CuCl<sub>2</sub> shown in figure S2 and S3, although to a notably lesser degree (CoCl<sub>2</sub> 2.1 %, CuCl<sub>2</sub> 3.2 %). For all chlorides, prior to loss of the last NH<sub>3</sub>-ligand, gradual, but continuous decomposition is observed from the TG-curve. In contrast, in the case of the sulphates all steps of NH<sub>3</sub>-release proceed separated clearly by a plateau-phase. Therefore, even ideal temperature control cannot fully prevent slight decomposition in the case of the chlorides. A comparison of the thermal decomposition of [Cu(NH<sub>3</sub>)<sub>6</sub>]Cl<sub>2</sub> and [Cu(NH<sub>3</sub>)<sub>4</sub>]SO<sub>4</sub> is given in figure S4.

Both charging and discharging reaction (thus thermal decomposition and re-formation of the ammine-complex) were investigated under an atmosphere of NH<sub>3</sub>. Purging the system with N<sub>2</sub> to remove the liberated NH<sub>3</sub> during thermal decomposition could most likely prevent the slow degradation of the material. The reason for performing the cycling experiments under a permanent NH<sub>3</sub>-atmosphere is related to applicability, as due to the inherent toxicity of NH<sub>3</sub> the TCES-process on a technological scale will be necessarily performed in a closed system, avoiding release of NH<sub>3</sub> into the ambient.

Under such conditions NH<sub>3</sub> will always be the main-component of the gas-phase.

In contrast to the chlorides, in the case of the transition metal sulphates no decomposition during cycling was observed, as shown in figure S5 for 10 charging / discharging cycles with

**Table 1** Decomposition / formation temperatures and associated energies for the investigated transition metal ammoniates.

	[Ni(NH <sub>3</sub> ) <sub>6</sub> ]Cl <sub>2</sub>		[Co(NH <sub>3</sub> ) <sub>4</sub> ]Cl <sub>2</sub>		[Cu(NH <sub>3</sub> ) <sub>6</sub> ]Cl <sub>2</sub>	
	charging	discharging	charging	discharging	charging	discharging
	T [°C] / E [kJ kg <sup>-1</sup> ]	T [°C] / E [kJ kg <sup>-1</sup> ]	T [°C] / E [kJ kg <sup>-1</sup> ]	T [°C] / E [kJ kg <sup>-1</sup> ]	T [°C] / E [kJ kg <sup>-1</sup> ]	T [°C] / E [kJ kg <sup>-1</sup> ]
1 <sup>st</sup> step	176.3 / 802.4	274.0 / -133	140.0 / 743	56.4 / -807	99.8 / 320	---
2 <sup>nd</sup> step	309.9 / 374.1	139.6 / -1289	---	---	133.5 / 366	---
3 <sup>rd</sup> step	---	---	---	---	296.6 / 1199	---
	[Mn(NH <sub>3</sub> ) <sub>2</sub> ]Cl <sub>2</sub>		[Cu(NH <sub>3</sub> ) <sub>4</sub> ]SO <sub>4</sub>		[Ni(NH <sub>3</sub> ) <sub>4</sub> ]SO <sub>4</sub>	
	charging	discharging	charging	discharging	charging	discharging
	T [°C] / E [kJ kg <sup>-1</sup> ]	T [°C] / E [kJ kg <sup>-1</sup> ]	T [°C] / E [kJ kg <sup>-1</sup> ]	T [°C] / E [kJ kg <sup>-1</sup> ]	T [°C] / E [kJ kg <sup>-1</sup> ]	T [°C] / E [kJ kg <sup>-1</sup> ]
1 <sup>st</sup> step	87.5 / 846	60.8 / -2005	79 / 180	66 / -153	119.3 / 598	127.1 / -378
2 <sup>nd</sup> step	249.3 / 581	---	168 / 444	138 / -479	---	---
3 <sup>rd</sup> step	---	---	307 / 443	248 / -247	---	---
	[Co(NH <sub>3</sub> ) <sub>4</sub> ]SO <sub>4</sub>		[Cd(NH <sub>3</sub> ) <sub>4</sub> ]Cl <sub>2</sub>		[Fe(NH <sub>3</sub> ) <sub>2</sub> ]SO <sub>4</sub>	
	charging	discharging	charging	discharging	charging	discharging
	T [°C] / E [kJ kg <sup>-1</sup> ]	T [°C] / E [kJ kg <sup>-1</sup> ]	T [°C] / E [kJ kg <sup>-1</sup> ]	T [°C] / E [kJ kg <sup>-1</sup> ]	T [°C] / E [kJ kg <sup>-1</sup> ]	T [°C] / E [kJ kg <sup>-1</sup> ]
1 <sup>st</sup> step	101.7 / 268	80.2 / -1026	58.5 / 372	---	79.5 / 441	---
2 <sup>nd</sup> step	132.1 / 332	---	237.9 / 236	---	231.2 / 198	---
3 <sup>rd</sup> step	260.3 / 307.4	---	---	---	---	---
4 <sup>th</sup> step	293.2 / 258	---	---	---	---	---
	[Cd(NH <sub>3</sub> ) <sub>2</sub> ]SO <sub>4</sub>		[Zn(NH <sub>3</sub> ) <sub>4</sub> ]SO <sub>4</sub>		[Zn(NH <sub>3</sub> ) <sub>4</sub> ]Cl <sub>2</sub>	
	charging	discharging	charging	discharging	charging	discharging
	T [°C] / E [kJ kg <sup>-1</sup> ]	T [°C] / E [kJ kg <sup>-1</sup> ]	T [°C] / E [kJ kg <sup>-1</sup> ]	T [°C] / E [kJ kg <sup>-1</sup> ]	T [°C] / E [kJ kg <sup>-1</sup> ]	T [°C] / E [kJ kg <sup>-1</sup> ]
1 <sup>st</sup> step	85.6 / 314	163.5 / -226	79.0 / 27	105 / -761	94.8 / 27	235.0 / -71
2 <sup>nd</sup> step	200.4 / 585	65.1 / -490	108.0 / 202	---	247.0 / 58	---
3 <sup>rd</sup> step	---	---	174.0 / 243	---	---	---
4 <sup>th</sup> step	---	---	215.0 / 343	---	---	---
	[Cu(NH <sub>3</sub> ) <sub>6</sub> ]Cl <sub>2</sub> via CuCl <sub>2</sub> 2H <sub>2</sub> O		[Fe(NH <sub>3</sub> ) <sub>3</sub> ]Cl <sub>2</sub> via FeCl <sub>2</sub> 4H <sub>2</sub> O		[Cu(NH <sub>3</sub> ) <sub>4</sub> ]SO <sub>4</sub> via CuSO <sub>4</sub> 5H <sub>2</sub> O	
	charging	discharging	charging	discharging	charging	discharging
	T [°C] / E [kJ kg <sup>-1</sup> ]	T [°C] / E [kJ kg <sup>-1</sup> ]	T [°C] / E [kJ kg <sup>-1</sup> ]	T [°C] / E [kJ kg <sup>-1</sup> ]	T [°C] / E [kJ kg <sup>-1</sup> ]	T [°C] / E [kJ kg <sup>-1</sup> ]
1 <sup>st</sup> step	103.0 / 265	134.1 / -74	117.3 / 776	127.4 / -1350	98.4 / 200	248.0 / -161
2 <sup>nd</sup> step	137.3 / 299	104.8 / -310	283.1 / 178	---	173.2 / 456	136.0 / -629
3 <sup>rd</sup> step	291.8 / 369	---	---	---	308.4 / 246	66.5 / -175
	[Fe(NH <sub>3</sub> ) <sub>2</sub> ]SO <sub>4</sub> via Fe <sub>2</sub> (SO <sub>4</sub> ) <sub>3</sub> 9H <sub>2</sub> O		[Mn(NH <sub>3</sub> ) <sub>2</sub> ]Cl <sub>2</sub> via MnCl <sub>2</sub> 2H <sub>2</sub> O		[Cd(NH <sub>3</sub> ) <sub>2</sub> ]SO <sub>4</sub> via CdSO <sub>4</sub> 4H <sub>2</sub> O	
	charging	discharging	charging	discharging	charging	discharging
	T [°C] / E [kJ kg <sup>-1</sup> ]	T [°C] / E [kJ kg <sup>-1</sup> ]	T [°C] / E [kJ kg <sup>-1</sup> ]	T [°C] / E [kJ kg <sup>-1</sup> ]	T [°C] / E [kJ kg <sup>-1</sup> ]	T [°C] / E [kJ kg <sup>-1</sup> ]
1 <sup>st</sup> step	137.6 / 88	---	91.2 / 414	61.3 / -949	83.7 / 399	160 / -296
2 <sup>nd</sup> step	---	---	---	---	206.7 / 258	64.3 / -490
3 <sup>rd</sup> step	---	---	---	---	258.4 / 197	---
	[Co(NH <sub>3</sub> ) <sub>4</sub> ]SO <sub>4</sub> via CoSO <sub>4</sub> 7H <sub>2</sub> O					
	charging	discharging				
	T [°C] / E [kJ kg <sup>-1</sup> ]	T [°C] / E [kJ kg <sup>-1</sup> ]				
1 <sup>st</sup> step	111.6 / 678	93.7 / 1048				
2 <sup>nd</sup> step	244.1 / 366	---				
3 <sup>rd</sup> step	---	---				

CuSO<sub>4</sub>. Although, the chlorides could provide higher energy contents, based on the results of the cycle stability tests and the above-mentioned necessity of full reversibility and long-term cycle stability, transition metal chlorides are, under the conditions investigated so far, unsuitable for application as thermochemical energy storage materials. In order to investigate the cycling behaviour of all other materials, two consecutive charging / discharging cycles under an atmosphere of NH<sub>3</sub> were performed in the TG / DSC. The results are detailed in the supporting information figures S6-S15. The decomposition and formation temperatures of the ammine-complexes, as well as the associated energies are reported in table 1.

After excluding the chlorides, the 19 prospective materials shown in figure 1a could be reduced to three final candidates: CuSO<sub>4</sub>, CoSO<sub>4</sub> and ZnSO<sub>4</sub>. Whereas, CoSO<sub>4</sub> was completely stable over the two cycles, ZnSO<sub>4</sub> revealed a slight decrease in mass attributed to a slight loss of hydrate water, as the material used was found to be slightly contaminated with ZnSO<sub>4</sub>·H<sub>2</sub>O. Excluding the chlorides and all non-cycle stable materials, CuSO<sub>4</sub> showed the best performance in the present study, both in terms of reversibility and energy content. Regarding the chlorides investigated, CoCl<sub>2</sub> seems the most promising material, as only a slight decomposition was evidenced. Should a storage cycle avoiding an atmosphere of NH<sub>3</sub> during the thermal decomposition be developed, CoCl<sub>2</sub> or CuCl<sub>2</sub> could also become attractive materials for a TCES system.

## Conclusions

The present study reports the investigation of transition metal ammoniates, a so far widely neglected class of auspicious thermochemical energy storage (TCES) materials. A selection of 19 anhydrous and 14 hydrated metal chlorides and sulphates was reacted with NH<sub>3</sub>, using differential scanning calorimetry to determine the specific energy content. Regarding the energy density and compared to other TCES- materials operated in the temperature window between 25 – 400 °C, transition metal ammoniates are amongst the most attractive energy storage materials reported so far: For the chlorides a maximum of 2.43 MWh m<sup>-3</sup> (NiCl<sub>2</sub>), and for the sulphates of 1.72 MWh m<sup>-3</sup> (CuSO<sub>4</sub>) was observed. Cycle stability investigations demonstrated, that chlorides undergo already within 10 cycles slight decomposition / transport reactions when heated during the charging step in the presence of NH<sub>3</sub>. Assuming, that a technological process will involve a closed cycle having present NH<sub>3</sub> during the decomposition reaction only sulphates would be suitable. Among the investigated sulphates CuSO<sub>4</sub> was identified as most promising material revealing perfect cycle stability. Based on the herein reported results transition metal ammoniates – and especially the reaction couple CuSO<sub>4</sub>/ [Cu(NH<sub>3</sub>)<sub>4</sub>]SO<sub>4</sub> – are of notable interest for the development of TCES-processes combining small scales and high storage densities for combination with *e.g.* solar heating. Continuative studies on ammoniates as TCES-materials will demonstrate, how their potential may be used most efficiently in combination with efficient heat storage technologies.

## Conflicts of interest

There are no conflicts to declare.

## Acknowledgements

This work was financially supported by the Austrian Research Promotion Agency (FFG Forschungsförderungsgesellschaft), projects 845020, 841150 and 848876.

## Notes and References

\* The use of NH<sub>3</sub> may be restricted due to its inherent toxicity. Operation in closed systems as for *e.g.* industrial cooling is a state of the art technology, therefore, also for energy storage purposes using a closed system NH<sub>3</sub> should cause no further issues.

1. M. M. Farid, A. M. Khudhair, S. A. K. Razack and S. Al-Hallaj, *Energy Conversion and Management*, 2004, **45**, 1597-1615.
2. Y. Kato, *Springer, Netherlands*, 2007, 377–391.
3. H. Ibrahim, A. Ilinca and J. Perron, *Renewable and Sustainable Energy Reviews*, 2008, **12**, 1221-1250.
4. M. Thirugnanasambandam, S. Iniyan and R. Goic, *Renewable and Sustainable Energy Reviews*, 2010, **14**, 312-322.
5. L. F. E. Cabeza, *Elsevier*, 2015.
6. F. Agyenim, N. Hewitt, P. Eames and M. Smyth, *Renewable and Sustainable Energy Reviews*, 2010, **14**, 615-628.
7. A. H. Abedin and M. R. Rosen, *The Open Renewable Energy Journal*, 2011, **4**, 42-46.
8. S. M. Hasnain, *Energy Conversion and Management*, 1998, **39**, 1127-1138.
9. K. E. N'Tsoukpoe, H. Liu, N. Le Pierrès and L. Luo, *Renewable and Sustainable Energy Reviews*, 2009, **13**, 2385-2396.
10. M. M. Alkilani, K. Sopian, M. A. Alghoul, M. Sohif and M. H. Ruslan, *Renewable and Sustainable Energy Reviews*, 2011, **15**, 1476-1490.
11. L. F. Cabeza, C. Sole, A. Castell, E. Oro and A. Gil, *Proceedings of the IEEE*, 2012, **100**, 525-538.
12. L. A. Chidambaram, A. S. Ramana, G. Kamaraj and R. Velraj, *Renewable and Sustainable Energy Reviews*, 2011, **15**, 3220-3228.
13. M. Liu, W. Saman and F. Bruno, *Renewable and Sustainable Energy Reviews*, 2012, **16**, 2118-2132.
14. P. Pinel, C. A. Cruickshank, I. Beausoleil-Morrison and A. Wills, *Renewable and Sustainable Energy Reviews*, 2011, **15**, 3341-3359.
15. A. Shukla, D. Buddhi and R. L. Sawhney, *Renewable and Sustainable Energy Reviews*, 2009, **13**, 2119-2125.
16. Y. Tian and C. Y. Zhao, *Applied Energy*, 2013, **104**, 538-553.
17. B. Xu, P. Li and C. Chan, *Applied Energy*, 2015, **160**, 286-307.
18. J. Cot-Gores, A. Castell and L. F. Cabeza, *Renewable and Sustainable Energy Reviews*, 2012, **16**, 5207-5224.
19. R. M. Dunlap, *Journal*, 1982.
20. Z. Aidoun and M. Ternan, *Applied Thermal Engineering*, 2001, **21**, 1019-1034.



21. J. Trudel, S. Hosatte and M. Ternan, *Applied Thermal Engineering*, 1999, **19**, 495-511.
22. L. Jiang, F. Q. Zhu, L. W. Wang, C. Z. Liu and R. Z. Wang, *Renewable Energy*, 2016, **91**, 130-136.
23. R. Dunn, K. Lovegrove and G. Burgess, *Proceedings of the IEEE*, 2012, **100**, 391-400.
24. A. S. Lavine, K. M. Lovegrove, J. Jordan, G. B. Anleu, C. Chen, H. Aryafar and A. Sepulveda, 2016, **1734**, 050028.
25. E. Lepinasse and B. Spinner, *International Journal of Refrigeration*, 1994, **17**, 309-322.
26. K. Lovegrove, H. Kreetz and A. Luzzi, *Le Journal de Physique IV*, 1999, **09**, Pr3-581-Pr583-586.
27. K. Lovegrove, A. Luzzi, I. Soldiani and H. Kreetz, *Solar Energy*, 2004, **76**, 331-337.
28. J. E. Huheey, E. A. Keiter, R. L. Keiter and O. K. Medhi, *Pearson Education, 4th Edt.*, 2006.
29. M. Deutsch, D. Müller, C. Aumeyr, C. Jordan, C. Gierl-Mayer, P. Weinberger, F. Winter and A. Werner, *Applied Energy*, 2016, **183**, 113-120.
30. M. Simerská, *Czechoslovak Journal of Physics*, 1954, **4**, 277-288.
31. K. B. Nilsson, L. Eriksson, V. G. Kessler and I. Persson, *Journal of Molecular Liquids*, 2007, **131-132**, 113-120.
32. D. Wagmann, W. Evans, V. Parker, R. Schumm, I. Halow, S. Bailey, K. Churney and R. Nuttal, *Journal of Physical and Chemical Reference Data*, 1982, **11**.

## Supporting Information

### Transition metal ammoniates for thermochemical energy storage

Danny Müller<sup>a,\*</sup>, Christian Knoll<sup>a,b</sup>, Christian Jordan<sup>b</sup>, Jan M. Welch<sup>c</sup>, Andreas Werner<sup>d</sup>, Michael Harasek<sup>b</sup>, Peter Weinberger<sup>a</sup>

<sup>a</sup> Institute of Applied Synthetic Chemistry, TU Wien, Getreidemarkt 9/163-AC, 1060 Vienna, Austria

E-mail: [danny.mueller@tuwien.ac.at](mailto:danny.mueller@tuwien.ac.at)

<sup>b</sup> Institute of Chemical, Environmental & Biological Engineering, Getreidemarkt 9/166, 1060 Vienna, Austria

<sup>c</sup> Atominstytut, TU Wien, Stadionallee 2, 1020 Vienna, Austria

<sup>d</sup> Institute for Energy Systems and Thermodynamics, TU Wien, Getreidemarkt 9, 1060 Vienna, Austria

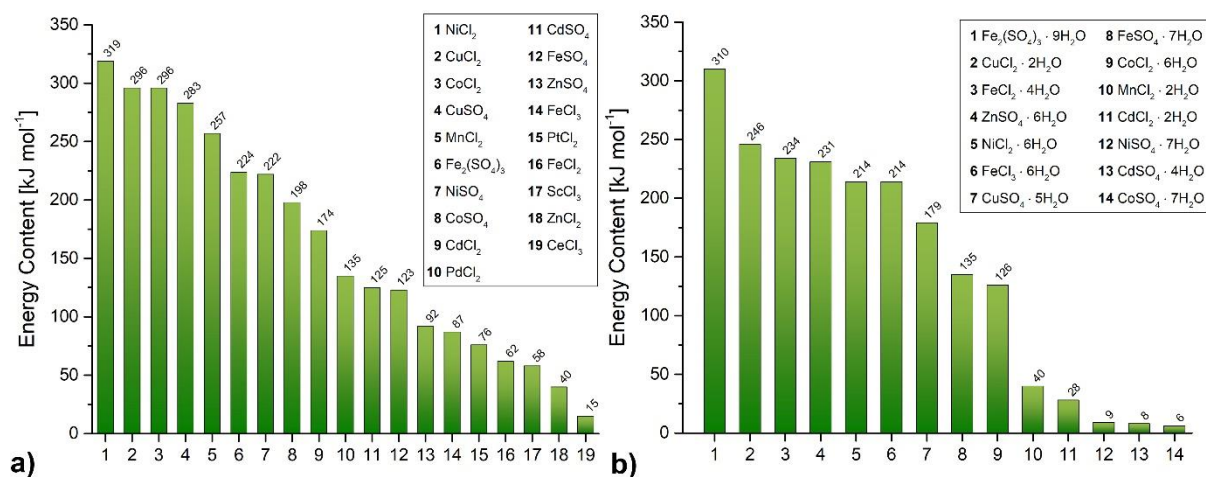


**Figure S1** Energy content of selected (transition) metal salts for reaction with NH<sub>3</sub> at 25 °C, ranked according to the molar energy content. a) Anhydrous form of the salts b) Most common hydrate species

**Table 1** Energy contents of the investigated anhydrous salts in kJ kg<sup>-1</sup>, kJ mol<sup>-1</sup> and energy density in MJ m<sup>-3</sup>

Entry	Salt	kJ kg <sup>-1</sup>	kJ mol <sup>-1</sup>	MJ m <sup>-3</sup>
1	NiCl <sub>2</sub>	2464	319	694
2	CoCl <sub>2</sub>	2278	296	678
3	CuCl <sub>2</sub>	2200	296	649
4	MnCl <sub>2</sub>	2040	257	685
5	CuSO <sub>4</sub>	1772	283	492
6	NiSO <sub>4</sub>	1432	222	357
7	CoSO <sub>4</sub>	1276	198	344
8	CdCl <sub>2</sub>	947	174	234
9	FeSO <sub>4</sub>	809	123	222
10	PdCl <sub>2</sub>	763	135	191
11	CdSO <sub>4</sub>	599	125	128
12	ZnSO <sub>4</sub>	568	92	160
13	Fe <sub>2</sub> (SO <sub>4</sub> ) <sub>3</sub>	561	224	181
14	FeCl <sub>3</sub>	534	87	184
15	FeCl <sub>2</sub>	492	62	156
16	ScCl <sub>3</sub>	386	58	162
17	ZnCl <sub>2</sub>	291	40	100
18	PtCl <sub>2</sub>	284	76	47
19	CeCl <sub>3</sub>	59	15	15

**Table 2** Energy contents of the investigated salt hydrates in  $\text{kJ kg}^{-1}$ ,  $\text{kJ mol}^{-1}$  and energy density in  $\text{MJ m}^{-3}$

Entry	Salt	$\text{kJ kg}^{-1}$	$\text{kJ mol}^{-1}$	$\text{MJ m}^{-3}$
1	$\text{CuCl}_2 \cdot 2\text{H}_2\text{O}$	1441	246	567
2	$\text{FeCl}_2 \cdot 4\text{H}_2\text{O}$	1176	234	609
3	$\text{NiCl}_2 \cdot 6\text{H}_2\text{O}$	901	214	469
4	$\text{ZnSO}_4 \cdot 6\text{H}_2\text{O}$	802	231	387
5	$\text{FeCl}_3 \cdot 6\text{H}_2\text{O}$	792	214	435
6	$\text{CuSO}_4 \cdot 5\text{H}_2\text{O}$	715	179	312
7	$\text{Fe}_2(\text{SO}_4)_3 \cdot 9\text{H}_2\text{O}$	552	310	291
8	$\text{CoCl}_2 \cdot 6\text{H}_2\text{O}$	532	126	277
9	$\text{FeSO}_4 \cdot 7\text{H}_2\text{O}$	485	135	255
10	$\text{MnCl}_2 \cdot 2\text{H}_2\text{O}$	202	40	100
11	$\text{CdCl}_2 \cdot 2\text{H}_2\text{O}$	128	28	38
12	$\text{NiSO}_4 \cdot 7\text{H}_2\text{O}$	35	9	18
13	$\text{CdSO}_4 \cdot 4\text{H}_2\text{O}$	27	8	9
14	$\text{CoSO}_4 \cdot 7\text{H}_2\text{O}$	23	6	12

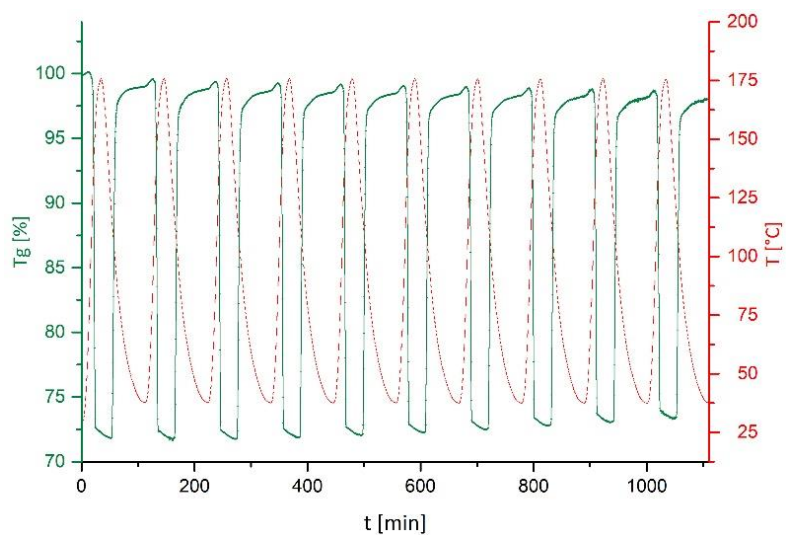


**Figure S2** Cycle stability experiment of the reaction couple  $[\text{Co}(\text{NH}_3)_4]\text{Cl}_2 \rightleftharpoons \text{CoCl}_2$  under  $\text{NH}_3$  atmosphere. Mass-loss during 10 consecutive cycles: 2.1 %

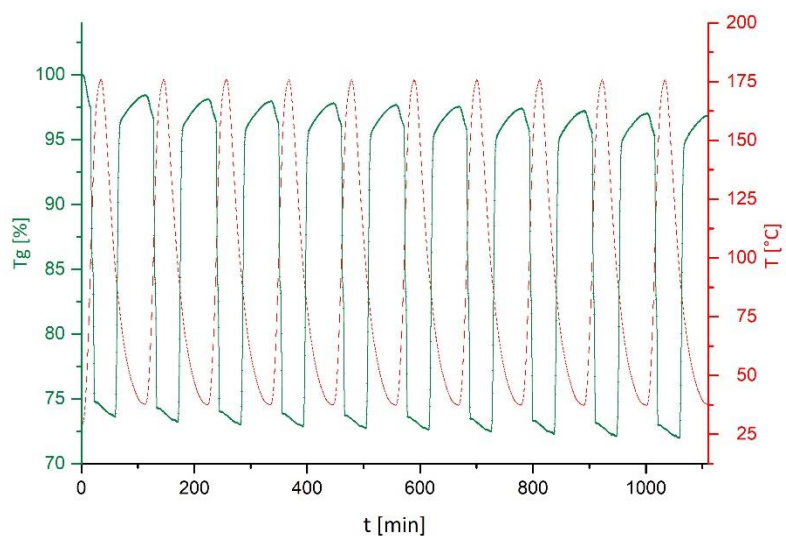


**Figure S3** Cycle stability experiment of the reaction couple  $[\text{Cu}(\text{NH}_3)_6]\text{Cl}_2 \rightleftharpoons \text{CuCl}_2$  under  $\text{NH}_3$  atmosphere. Mass-loss during 10 consecutive cycles: 3.2 %

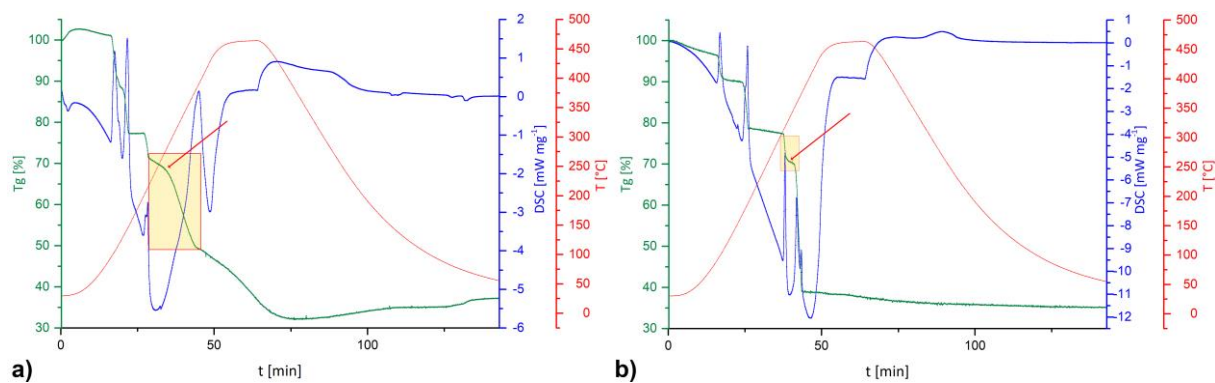


**Figure S4** a) Decomposition of  $[\text{Cu}(\text{NH}_3)_6]\text{Cl}_2$  under  $\text{NH}_3$  atmosphere, continuous gradual mass-loss before and after removal of the last  $\text{NH}_3$ -ligand. b) Decomposition of  $[\text{Cu}(\text{NH}_3)_4]\text{SO}_4$  under  $\text{NH}_3$  atmosphere, plateau-phase during removal of the last  $\text{NH}_3$ -ligand.

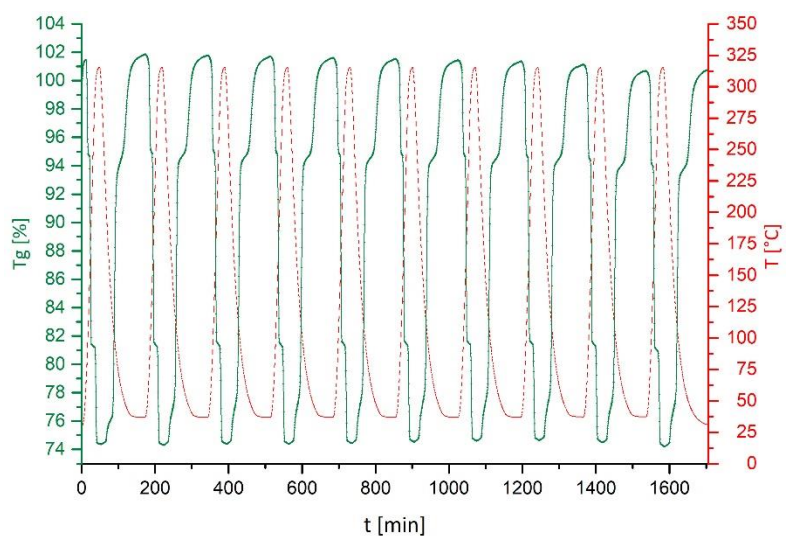


**Figure S5** Cycle stability experiment of the reaction couple  $[\text{Cu}(\text{NH}_3)_4]\text{SO}_4 \rightleftharpoons \text{CuSO}_4$  under  $\text{NH}_3$  atmosphere

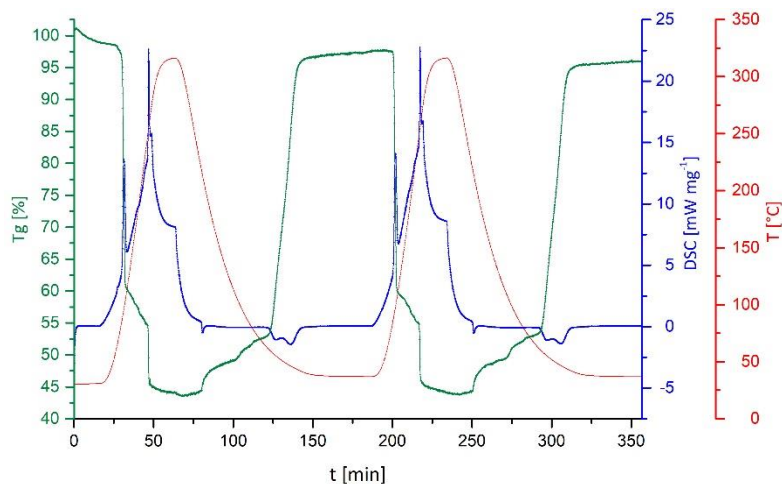


**Figure S6** Two consecutive charging / discharging cycles under  $\text{NH}_3$  atmosphere of the reaction couple  $[\text{Mn}(\text{NH}_3)_2]\text{Cl}_2 \rightleftharpoons \text{MnCl}_2$

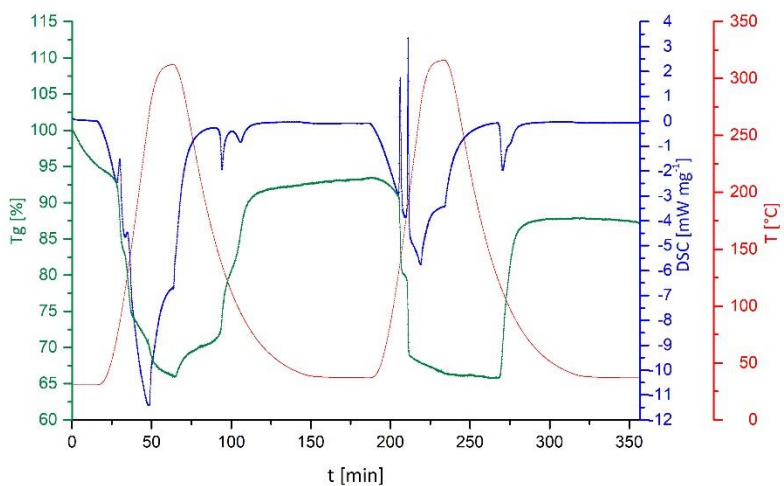


Figure S7 Two consecutive charging / discharging cycles under  $\text{NH}_3$  atmosphere of the reaction couple  $[\text{Ni}(\text{NH}_3)_4]\text{SO}_4 \rightleftharpoons \text{NiSO}_4$

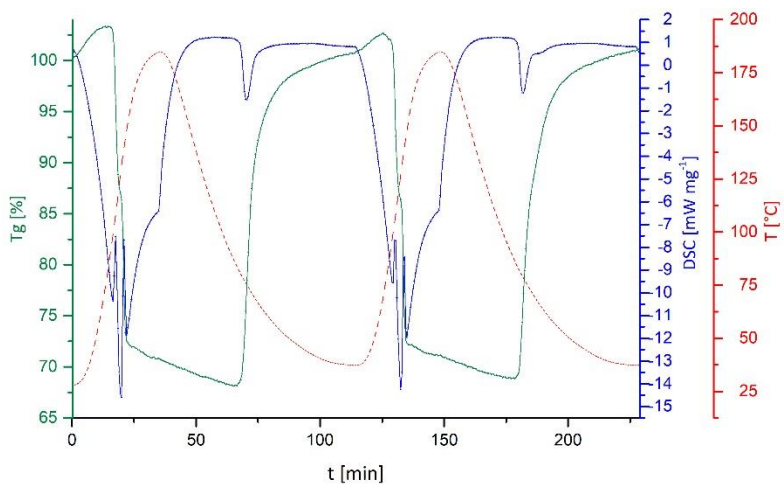


Figure S8 Two consecutive charging / discharging cycles under  $\text{NH}_3$  atmosphere of the reaction couple  $[\text{Co}(\text{NH}_3)_4]\text{SO}_4 \rightleftharpoons \text{CoSO}_4$

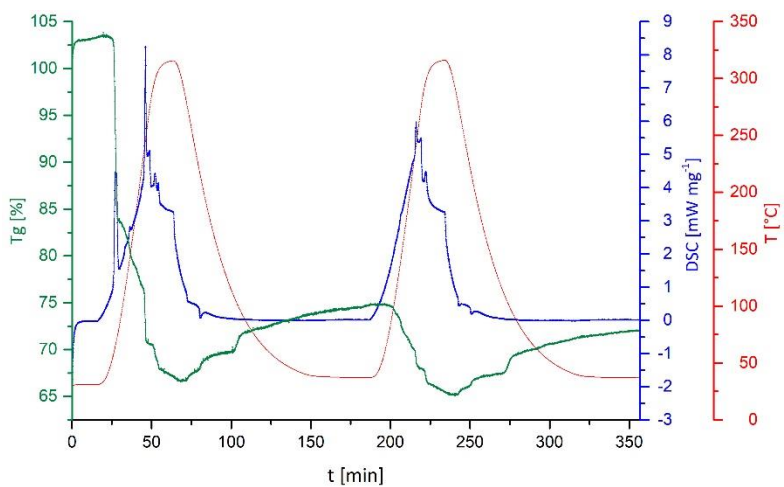


Figure S9 Two consecutive charging / discharging cycles under  $\text{NH}_3$  atmosphere of the reaction couple  $[\text{Cd}(\text{NH}_3)_4]\text{Cl}_2 \rightleftharpoons \text{CdCl}_2$

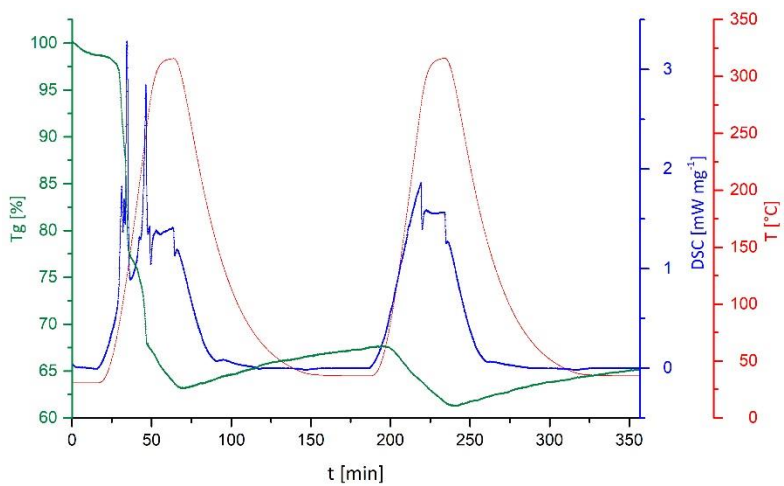


Figure S10 Two consecutive charging / discharging cycles under  $\text{NH}_3$  atmosphere of the reaction couple  $[\text{Fe}(\text{NH}_3)_2]\text{SO}_4 \rightleftharpoons \text{FeSO}_4$

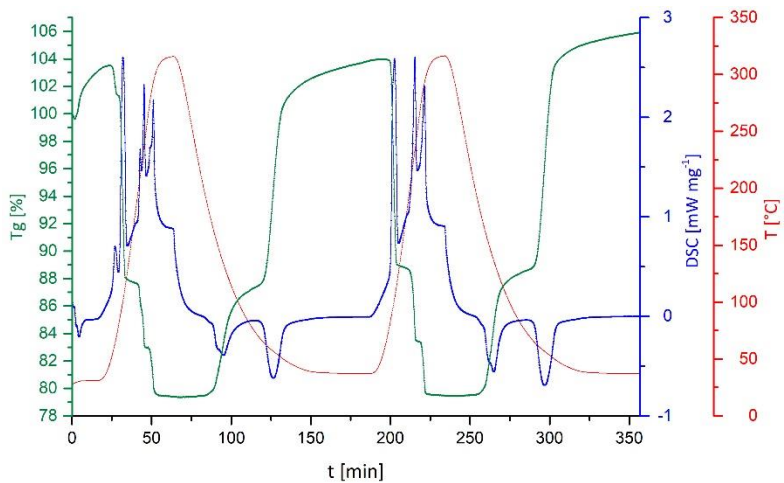


Figure S11 Two consecutive charging / discharging cycles under  $\text{NH}_3$  atmosphere of the reaction couple  $[\text{Cd}(\text{NH}_3)_2]\text{SO}_4 \rightleftharpoons \text{CdSO}_4$

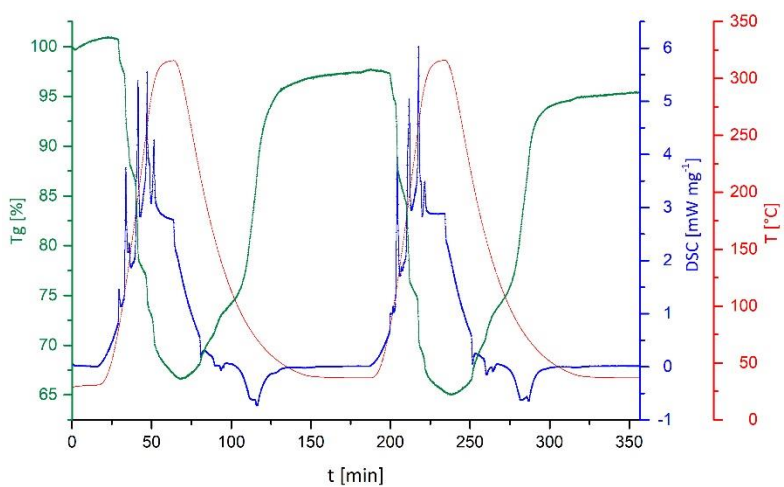


Figure S12 Two consecutive charging / discharging cycles under  $\text{NH}_3$  atmosphere of the reaction couple  $[\text{Zn}(\text{NH}_3)_4]\text{SO}_4 \rightleftharpoons \text{ZnSO}_4$



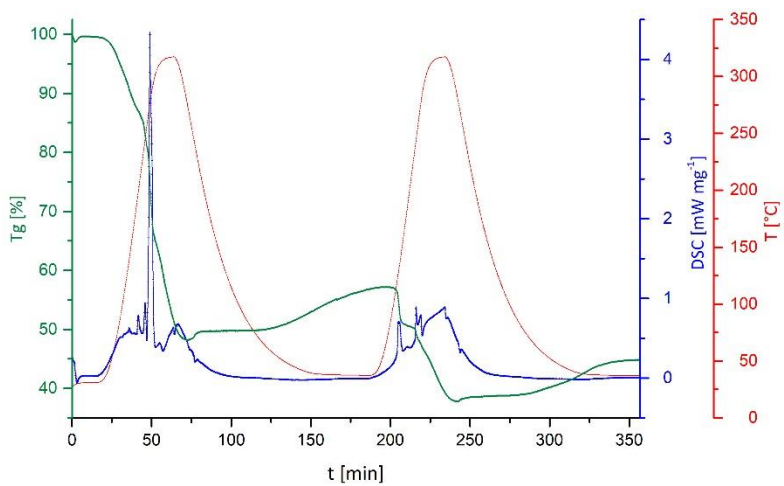


Figure S13 Two consecutive charging / discharging cycles under  $\text{NH}_3$  atmosphere of the reaction couple  $[\text{Fe}(\text{NH}_3)_3]\text{Cl}_3 \rightleftharpoons \text{FeCl}_3$

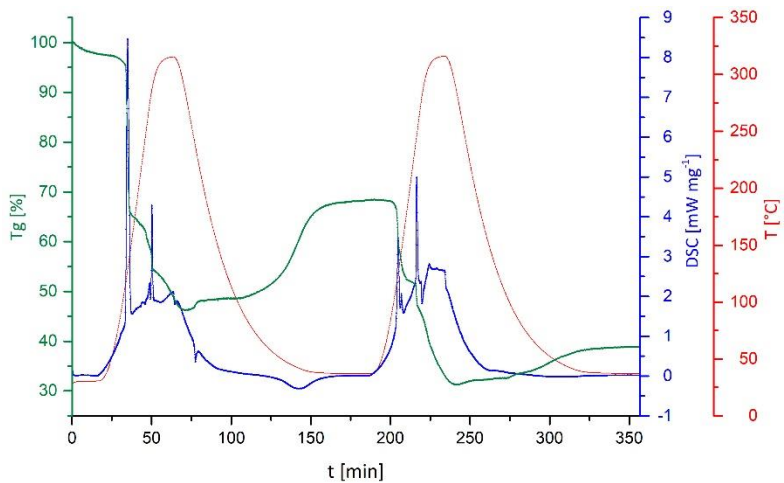


Figure S14 Two consecutive charging / discharging cycles under  $\text{NH}_3$  atmosphere of the reaction couple  $[\text{Fe}(\text{NH}_3)_3]\text{Cl}_2 \rightleftharpoons \text{FeCl}_2$

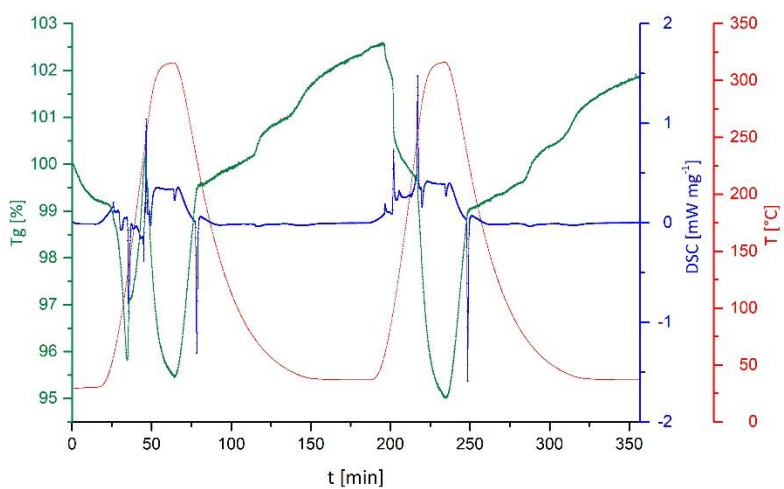


Figure S15 Two consecutive charging / discharging cycles under  $\text{NH}_3$  atmosphere of the reaction couple  $[\text{Zn}(\text{NH}_3)_4]\text{Cl}_2 \rightleftharpoons \text{ZnCl}_2$

# Lab-scale demonstration of thermochemical energy storage with NH<sub>3</sub> and impregnated-loaded zeolites

Danny Müller,<sup>1\*</sup> Christian Knoll,<sup>1,2</sup> Georg Gravogl,<sup>1,3</sup> Andreas Werner,<sup>4</sup> Michael Harasek,<sup>2</sup>  
Ronald Miletich,<sup>3</sup> Peter Weinberger<sup>1</sup>

<sup>1</sup> Institute of Applied Synthetic Chemistry, TU Wien, Getreidemarkt 9/163-AC, 1060 Vienna, Austria

<sup>2</sup> Institute of Chemical, Environmental & Biological Engineering, TU Wien, Getreidemarkt 9, 1060 Vienna, Austria

<sup>3</sup> Institut für Mineralogie und Kristallographie, University of Vienna, Althanstraße 14, 1090 Vienna, Austria

<sup>4</sup> Institute for Energy Systems and Thermodynamics, TU Wien, Getreidemarkt 9/302, 1060 Vienna, Austria

danny.mueller@tuwien.ac.at

## Abstract

High energy densities are one key-feature of thermochemical energy storage materials. Among the substance classes featuring the highest energy densities are oxides and carbonates, having both operational temperature profiles between 800 °C - 1200 °C. Comparable high energy contents are provided by the reaction between ammonia and (transition) metal salts, operable in a medium-temperature range between 150 °C - 450 °C. Due to the toxicity of ammonia a closed cycle preventing the release of ammonia to the surrounding environment would be necessary.

Herein, CuSO<sub>4</sub> and CuCl<sub>2</sub> are investigated in a laboratory scale reactor for their application in thermochemical energy storage with ammonia as reactive gas. In the current setup after 80 seconds peak temperatures of 312 °C and 238 °C respectively were measured. To circumvent the notable volume expansion during the reaction with ammonia, both copper salts were loaded on zeolite 13X, yielding matrix-supported composite materials. Operation of those materials in the laboratory scale reactor under ammonia revealed, that the rapid temperature increase and the high peak temperatures could be retained, simultaneously simplifying the handling of the materials.

*Keywords: copper salts, copper ammoniates, laboratory scale reactor, thermochemical energy storage*

---

## 1. Introduction

Increased awareness of a necessary reduction of greenhouse gasses in relation to energy production stimulated an ongoing reorientation of the energy market. (IEA, 2014, Paris agreement, 2015) Environmentally benign energy production with increasing percentages of renewable energy, a sustainable energy management and a responsible use of the produced energy led to a multiplicity of innovative approaches, complying the climate targets. (Keith Shine, 2005) Related to this development are also the increase of energy efficiency, especially in context of electricity production, as according to the IEA about 2/3 of the therefore used energy are lost in form of waste heat. (IEA, 2011)

Optimizing the waste heat management encouraged research to develop recycling methods for so far lost waste heat. (Bauer et al., 2012; Hasnain, 1998) One auspicious approach due to its broad application profile is the thermal storage of waste heat by sensible, (Zhang et al., 2016) latent (Zalba et al., 2003) or thermochemical energy storage materials. (Abedin; A.H. 2011; Cot-Gores et al.; 2012, T. Yan, 2015) Thermochemical energy storage (TCES) takes a very prominent position amongst these approaches, as highest storage densities, loss-less storage, a broad

operational temperature profile and fast reaction times allow for a flexible application in domestic and industrial environments, compatible with waste heat temperatures between 30 °C and above 1200 °C.(T. Yan, 2015)

Depending on the available waste heat source, the suitable materials may be selected from an ample catalogue of principally suitable reactions, ranked according to their storage density and application temperature.(Deutsch et al., 2016) On the lower end of the temperature spectrum are located salt hydrates for *e.g.* application in energy efficient housing projects,(van Essen et al., 2009) whereas the high temperature end around 800 °C - 1200 °C is covered by carbonates and oxides, complementing *e.g.* concentrating solar power plants (CSP) during non-operational times. (Pardo et al., 2014) For the medium temperature region between 150 °C - 450 °C so far mainly hydroxide / oxide reactions (Criado et al., 2014) or metal hydrides were considered. (T. Yan, 2015)

A so far widely neglected class of TCES-materials operating in this temperature range are (transition) metal salt ammoniates, featuring notably high storage densities, comparable to redox-active metal oxides. Although, first reports on reactions of NH<sub>3</sub> with salts for energy storage purposes date back to the 80's, (Dunlap, 1982) until today only a handful of publications dealing with the reaction between CoCl<sub>2</sub>, (AidounTernan, 2001; Trudel et al., 1999) MnCl<sub>2</sub> (Jiang et al., 2016) or ZnCl<sub>2</sub> and NH<sub>3</sub> (Dunlap, 1982) is known. Concepts for NH<sub>3</sub> in energy storage technology relate mainly on the NH<sub>3</sub> formation / splitting in combination with solar power. (Dunn et al., 2012; Lavine et al., 2016; Lepinasse-Spinner, 1994; Lovegrove et al., 1999; 2004)

One major obstacle of NH<sub>3</sub> is its inherent toxicity. Therefore, to enable thermochemical energy storage based on NH<sub>3</sub>-metal salt reactions, a closed reactor design, avoiding any release of NH<sub>3</sub>, would be necessary. For this purpose, in the present work a feasibility study of a NH<sub>3</sub>-based storage reaction, using CuSO<sub>4</sub> / CuCl<sub>2</sub> loaded on zeolite 13X in a hermetically closed laboratory scale reactor, is presented.

## 2. Results and Discussion

### 2.1 Reaction between NH<sub>3</sub> and CuSO<sub>4</sub> / CuCl<sub>2</sub>

The reaction between NH<sub>3</sub> and CuSO<sub>4</sub> / CuCl<sub>2</sub> – although, mainly in aqueous solutions – is a well-known, colorful reaction for demonstration of simple coordination chemistry in undergraduate-laboratories. Even in the case of mixing the aqueous solutions of NH<sub>3</sub> and CuSO<sub>4</sub> an increase of the reaction temperature is observed.

For the gas-solid reaction between NH<sub>3</sub> and CuSO<sub>4</sub> / CuCl<sub>2</sub> energy-densities of 1.77 MJ kg<sup>-1</sup> and 2.20 MJ kg<sup>-1</sup> were obtained by differential scanning calorimetry. These values are highly comparable to the benchmark of metal-oxide redox-reactions, featuring the highest energy densities among the various TCES-materials. Even more important for a potential TCES-material, thermogravimetry evidenced a full reversibility of the NH<sub>3</sub>- coordination, thus by heating the formed ammine-complexes to 350 °C the initial copper salts are restored (see figure S1). Based on the decomposition of the copper-ammine complexes their composition was determined as [Cu(NH<sub>3</sub>)<sub>4</sub>]SO<sub>4</sub> and [Cu(NH<sub>3</sub>)<sub>6</sub>]Cl<sub>2</sub>, thus CuSO<sub>4</sub> reacting with 4 equivalents of NH<sub>3</sub>, CuCl<sub>2</sub> with 6.

The experimental setup selected for the gas-solid reaction between NH<sub>3</sub> and the anhydrous copper salts on a laboratory scale is shown in figure 1.

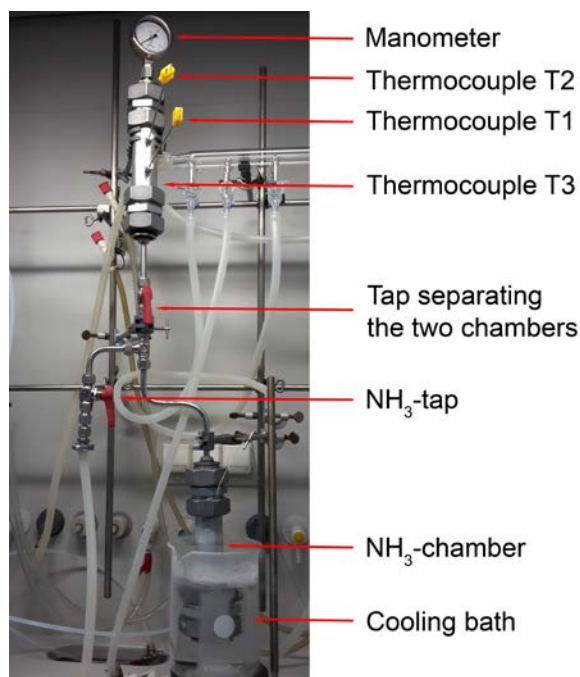


**Fig. 1: Laboratory scale reactor for the gas-solid reaction between  $\text{NH}_3$  and copper salts in a closed system**

Based on the necessity of a closed system preventing the release of  $\text{NH}_3$ , a reactor with two chambers, separated by a tap, was selected. The copper salt is situated in the reaction chamber (upper part). After evacuation of the complete system the tap between the two chambers is closed and  $\text{NH}_3$  is condensed into the precooled  $\text{NH}_3$ -chamber. Once the  $\text{NH}_3$ -tap is closed, the  $\text{NH}_3$ -chamber is warmed to room-temperature and the reaction is started by opening the tap between the two chambers. The temperature gradient during the reaction was monitored by the 3 thermocouples T1-T3, T1 and T2 placed inside, in the middle of the reactor, T3 on the outside to follow the heat conductance. Due to the  $\text{NH}_3$ -excess used, through all experiments a constant pressure around 6 bar was obtained.

In figure 2 the temperature plots for the formation of  $[\text{Cu}(\text{NH}_3)_4]\text{SO}_4$  (figure 2a) and  $[\text{Cu}(\text{NH}_3)_6]\text{Cl}_2$  (figure 2b) are given.

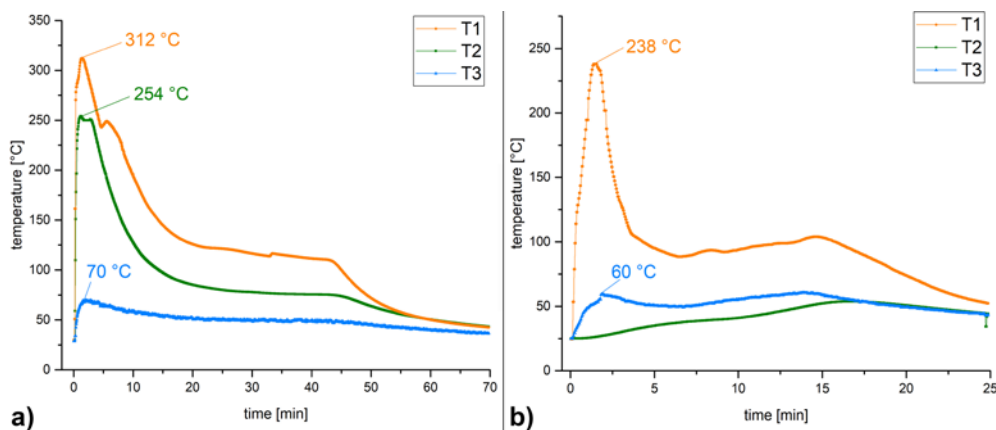


**Fig. 2: Temperature plots for the formation of a)  $[\text{Cu}(\text{NH}_3)_4]\text{SO}_4$  and b)  $[\text{Cu}(\text{NH}_3)_6]\text{Cl}_2$  in the reactor**

For both experiments starting with the opening of the tap between the two chambers an extremely fast increase of the internal temperature is observed. For  $\text{CuSO}_4$  the peak temperature of  $312\text{ °C}^*$  is reached after 80 seconds, after 10 seconds T1 exceeds already  $160\text{ °C}$ . In the case of  $\text{CuCl}_2$  a peak temperature of  $238\text{ °C}$  was reached after 90 seconds.

Both experiments are highly encouraging, as such extremely fast reactions with concomitant high temperature

\* The difference between T1 and T2 is attributed to the linear progression of the reaction zone and sintering of the material, notably affecting permeability of the packed bed.

differences are notably rare for thermochemical energy storage materials. Nevertheless, the packed bed using the pure metal salts in the reaction chamber cannot be considered ideal, as due to the extreme volume work during the reaction a compacting / sintering process of the material occurs, deteriorating permeability of the packed bed and thus hampering the completeness of the reaction. In the case of  $\text{CuSO}_4$  after the reaction the former loose powder had turned into a solid brick, which had to be removed mechanically from the reaction chamber. Additionally, from the bottom to the top of the packed bed the completeness of reaction was notably affected: Whereas, in the bottom the dark blue  $[\text{Cu}(\text{NH}_3)_4]\text{SO}_4$  was formed, on the top only a slight blue color of the former white material was observed. The kinks and sudden increases in the temperature profile are attributed to the volume work of the material, varying permeability of the continuously expanding packed bed.

In the case of  $\text{CuCl}_2$ , although with the observed peak temperature of  $238\text{ }^\circ\text{C}$  the melting point of  $[\text{Cu}(\text{NH}_3)_6]\text{Cl}_2$  was not exceeded, due to partial overheating near to the bottom of the reaction chamber a dark black-bluish molten residue in the reactor was formed immediately. As the thermocouple T1 was above this molten mass, the observed peak temperature was lower than in the case of  $\text{CuSO}_4$  (see figure S2). Additional, nearly 2/3 of the reactors' content did not react, as the  $\text{NH}_3$  could not pass the molten salt / ammoniate mass. Therefore, also thermocouple T2 featured only very low temperatures and the temperature in the reactor had dropped within 25 minutes significantly.

The slow decrease of the temperature profile, retaining for some extended period temperatures above  $100\text{ }^\circ\text{C}$ , followed by a sudden decrease of the temperature is caused by the stepwise reaction of the copper salts with  $\text{NH}_3$ . As seen from the thermogravimetric decomposition in figure S1, for the consecutive addition or removal of each of the  $\text{NH}_3$ -ligands different equilibrium / decomposition temperatures are found. Therefore, with the initial temperature rise the reaction temperature is too high to allow for complete reaction. Coming to lower temperatures, the further coordination of  $\text{NH}_3$  is enabled, still releasing notable heat and thus keeping the temperature almost constant unless the reactant is consumed.

In figure 3 a time-dependent series of infrared-images, visualizing the temperature increase and slow decrease during the reaction of  $\text{NH}_3$  with  $\text{CuSO}_4$  at the outside of the reactor is shown.

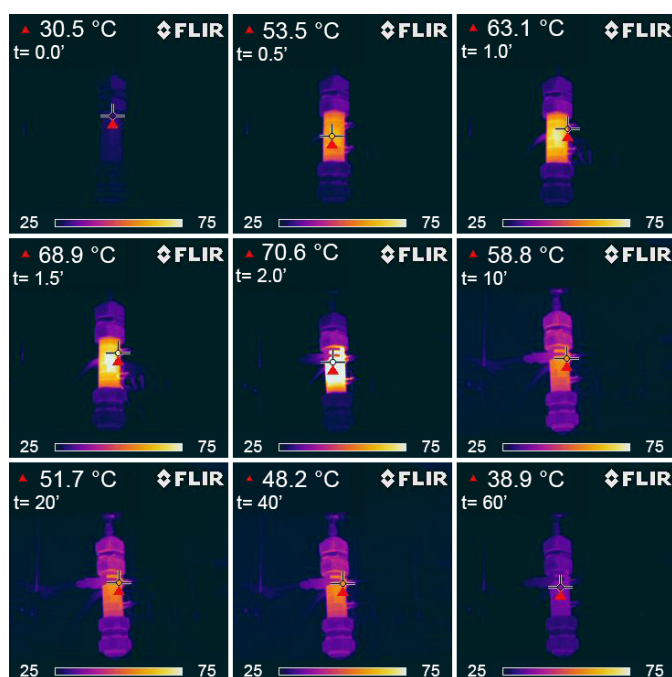


Fig. 3: Infrared-images of the reactor during the reaction of  $\text{NH}_3$  with  $\text{CuSO}_4$  at different time steps as indicated

Already after 30 seconds the temperature of the reactor walls had increased about  $23\text{ }^\circ\text{C}$ , reaching its maximum of  $70.6\text{ }^\circ\text{C}$  after 120 seconds. For the next 50 minutes a nearly constant temperature of  $50\text{ }^\circ\text{C}$  was observed. The temperature distribution in the IR-image after 40 minutes clearly shows, that the reaction was still ongoing.

The extreme volume work occurring on coordination of  $\text{NH}_3$  to both copper salts becomes evident comparing the crystallographic parameters for the four different materials in table 1 (although, for  $[\text{Cu}(\text{NH}_3)_4]\text{SO}_4$  only the

monohydrate is found in the ICSD-database).

**Tab. 1: Crystallographic parameters for CuSO<sub>4</sub>, CuCl<sub>2</sub> and the corresponding NH<sub>3</sub>-complexes**

	<b>CuSO<sub>4</sub></b>	<b>CuCl<sub>2</sub></b>	<b>[Cu(NH<sub>3</sub>)<sub>4</sub>]SO<sub>4</sub>·H<sub>2</sub>O</b>	<b>[Cu(NH<sub>3</sub>)<sub>6</sub>]Cl<sub>2</sub></b>
	orthorhombic	monoclinic	orthorhombic	tetragonal
Space group	<i>P n m a</i>	<i>C 1 2/m 1</i>	<i>P b n m</i>	<i>F 4/m m m</i>
Nr°	62	12	62	139
Z	4	2	4	4
a [Å]	8.3976(1)	6.9038(9)	12.12	10.375(7)
b [Å]	6.70382(9)	3.2995(4)	10.66	10.375(7)
c [Å]	4.82443(8)	6.824(1)	7.07	9.481(11)
α [°]	90	90	90	90
β [°]	90	122.197(8)	90	90
γ [°]	90	90	90	90
V [Å <sup>3</sup> ]	271.6	131.54	913.44	1020.54

Based on the unit-cell volumes given in table 1, for CuSO<sub>4</sub> a 3.4-fold, for CuCl<sub>2</sub> a 3.9-fold volume expansion during the reaction with NH<sub>3</sub> is obtained.

To circumvent, or at least decrease the expansion of the material, causing considerable issues on larger (or applicational) scale, allow for a better permeability of the packed bed and control the temperature release during the reaction, the impregnation of zeolite 13X with CuSO<sub>4</sub> and CuCl<sub>2</sub> was chosen.

## 2.2 Reaction between NH<sub>3</sub> and matrix-supported CuSO<sub>4</sub> / CuCl<sub>2</sub>

The CuSO<sub>4</sub> / CuCl<sub>2</sub> loaded zeolite samples (**13X-SO<sub>4</sub>** and **13X-Cl**) were obtained as described in the experimental section, having a greenish-brown color after drying in the furnace (see figure S3). The copper-loading was determined gravimetrically and by X-Ray fluorescence spectroscopy with 0.16 g CuSO<sub>4</sub>, and 0.09 g CuCl<sub>2</sub> per gram of zeolite.

Of course, the better handling and limited volume expansion goes to the expense of a much lower copper content compared to the pure salts, relating to a lower energy content and thus decreased reaction temperature. Due to the matrix-support also the heat transfer is affected. Therefore, externally copper-coated samples were prepared by reducing the external layer of copper-salts on the zeolite by hydrazine hydrate (see experimental), which should improve the thermal conductivity of the material.

To compare the performance of the various matrix-supported copper salts in the reactor, the same approach as described for the pure copper salts was chosen. In figure 3 the temperature plots of the experiments using **13X-SO<sub>4</sub>** (figure 4a) and **13X-Cl** (figure 4b), and their partially reduced equivalents **13X-SO<sub>4</sub>\_Cu** (figure 4c) and **13X-Cl\_Cu** (figure 4d) are shown.



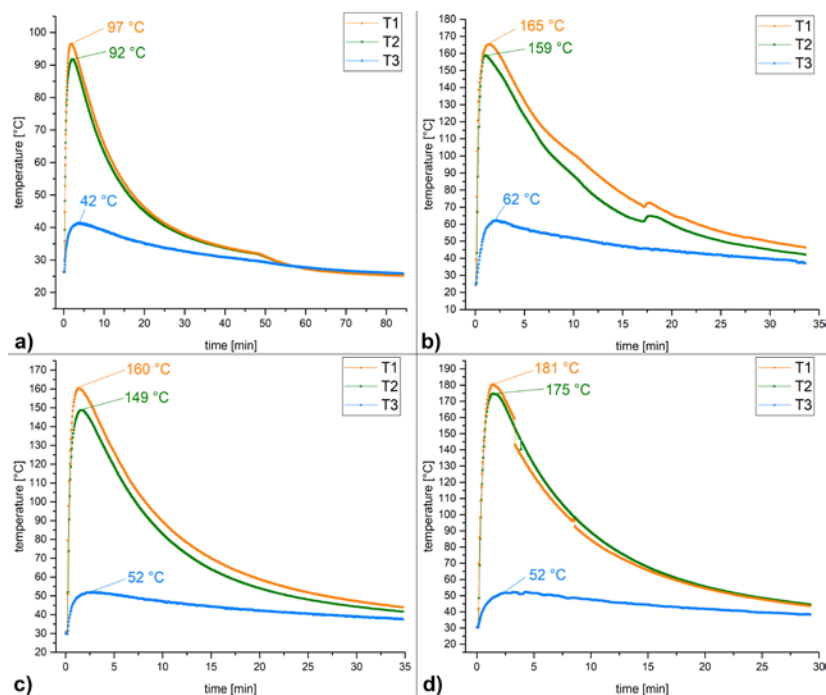


Fig. 4: Temperature plots for the reaction of  $\text{NH}_3$  with a)  $13\text{X-SO}_4$  b)  $13\text{X-Cl}$  c)  $13\text{X-SO}_4\text{-Cu}$  d)  $13\text{X-Cl-Cu}$  in the reactor

The prior observed temperature rise after opening the tap between the two chambers was also found in the present experiments, in all cases reaching the maximal temperature within 90 seconds. This finding is very promising, stating, that although the copper salts was heavily ‘diluted’ by loading on the matrix, its performance is still outstanding for a TCES-material. In these experiments also the temperature difference between T1 and T2 was reduced, as a notably better permeability of the packed bed was achieved. It should be emphasized, that due to the particle shape of the zeolite the contact between thermocouple and material was less efficient as in the previous experiments. In this respect, the partial reduction of the copper salts on the zeolite matrix, yielding a better thermal conductivity was found quite efficient, as in the experiments with  $13\text{X-SO}_4\text{-Cu}$  (figure 4c) and  $13\text{X-Cl-Cu}$  (figure 4d) notably higher peak temperatures were observed. Especially, in the case of  $13\text{X-SO}_4\text{-Cu}$  (figure 4c) the impact of the external Cu-coating increased the measured temperature about 60 °C. The discontinuities in the temperature plots of  $13\text{X-Cl}$  and  $13\text{X-Cl-Cu}$  are attributed to slight movements of the packed bed, affecting the contact between thermocouple and zeolite particles.

A control experiment with a mixed packed bed loading of  $13\text{X-Cl}$  and 10 % copper turnings (figure S4) showed a decreased temperature output (figure S5) even compared to the experiment using unmodified  $13\text{X-Cl}$ . It seems, that in the case of the matrix-loaded copper salts even a further 10 % dilution has a negative impact on the highest achievable reaction temperature.

The use of matrix-supported copper salts in the reactor experiments turned out to be quite promising, as still the fast temperature increase and notably high peak temperature was retained, at the same time avoiding the volume expansion of the material during the reaction.

### 3. Conclusion

The reaction between  $\text{NH}_3$  and  $\text{CuSO}_4 / \text{CuCl}_2$  was investigated for their feasibility as thermochemical energy storage process. Initial requirement was the operation in a closed system to prevent release of  $\text{NH}_3$  to the surrounding environment due to its toxicity. For this purpose, a two-chamber reactor setup with the reaction chamber and the  $\text{NH}_3$ -chamber – loaded by condensation of  $\text{NH}_3$  at  $-50\text{ °C}$  – was chosen.

For the pure copper salts 80 seconds after beginning of the reaction the peak temperatures of  $312\text{ °C}$  ( $\text{CuSO}_4$ ) and  $238\text{ °C}$  ( $\text{CuCl}_2$ ) were obtained. Such an abrupt and remarkable temperature increase is quite outstanding and very promising for a high-end technological applicability of thermochemical storage materials. The reaction temperature is kept for about 40 minutes around  $100\text{ °C}$ , as the stepwise coordination of  $\text{NH}_3$ -ligands to the copper

salts continuously releases heat until the reaction is complete. The only and major drawback of such an operation is the extreme volume work during the reaction accounting up to a 3.9-fold volume expansion in the case of  $\text{CuCl}_2$ . This causes a sintering and condensing of the packed bed, affecting completeness of the reaction due to very limited permeability of the bed and complicates the handling, as the reacted material needs mechanical force to be removed from the reactor. In the case of  $\text{CuCl}_2$  due to initial high reaction temperatures, exceeding locally the melting point of the  $[\text{Cu}(\text{NH}_3)_6]\text{Cl}_2$  the reaction product is obtained as massive solid.

To allow for a better handling, but retain the promising reactivity, both  $\text{CuSO}_4$  and  $\text{CuCl}_2$  were loaded on zeolite 13X, resulting in matrix-supported copper salts. In this case the volume expansion during the reaction is nearly eliminated, concomitantly retaining high initial peak temperatures and fast energy release on reaction with  $\text{NH}_3$ . To ensure a better heat conductivity, partial reduction of the copper on the outside of the zeolite particles was accomplished by treatment of the composite materials with hydrazine hydrate. The thereby obtained externally copper coated, copper salt loaded materials revealed a much better thermal conductivity, leading to the observation of higher peak temperatures.

As the main objective of the present work was a feasibility study on the reaction of  $\text{NH}_3$  with copper salts, respectively matrix-supported copper salts, the main subject of continuative studies will be the optimization of the heat output / heat transfer. Design and operation of the reactor / process will need some improvement to efficiently use and transfer the released heat.

## 4. Experimental

### 4.1 Material

CuSO<sub>4</sub> was obtained by drying CuSO<sub>4</sub>·5H<sub>2</sub>O for 3 h at 400 °C in an electric furnace. All other materials were commercially obtained and used as supplied.

The copper-loaded zeolites **13X-SO<sub>4</sub>** and **13X-Cl** were prepared by soaking zeolite 13X for 30 minutes in a saturated solution of CuSO<sub>4</sub>·5H<sub>2</sub>O or CuCl<sub>2</sub>·2H<sub>2</sub>O. The zeolite was rinsed with water and dried for 2 h at 150 °C under vacuum, before the soaking procedure was repeated. After rinsing with water, the loaded zeolite was dried for 2 h at 400 °C and stored after cooling in a desiccator. The Cu-loading was determined gravimetrically and by X-Ray fluorescence spectroscopy with 0.16 g CuSO<sub>4</sub>, and 0.09 g CuCl<sub>2</sub> per gram of zeolite.

For preparation of the partially reduced copper-loaded zeolites, dried samples of **13X-SO<sub>4</sub>** and **13X-Cl** were soaked for 15 minutes in a 10 % aqueous solution of N<sub>2</sub>H<sub>4</sub>·H<sub>2</sub>O. Due to the exothermic reaction no additional heating was necessary to keep the reaction constantly at 65 °C.

### 4.2 Thermal Analysis

For thermal analysis a Netzsch TGA/DSC 449 C Jupiter ® equipped with a water vapour furnace including an air-cooled double jacket was used. The oven operates between 25 °C and 1250 °C, regulated by an S-type thermocouple. NH<sub>3</sub> gas was 99.98 % and obtained from Messer. The gas flow was set to 100 ml min<sup>-1</sup>, controlled and mixed with Vögtlin Instruments “red-y” mass flow controllers. A sample mass of 10 mg in an open aluminum crucible was used for all experiments with heating and cooling rates of 10 °C min<sup>-1</sup>. The DSC was calibrated according to the procedure suggested by Netzsch, using the In, Sn, Bi, Zn, Al and Ag standards provided by the manufacturer.

### 4.3 Reactor-setup

For the experiments in a closed system a reactor consisting of two separated chambers connected via a tap was used. Both chambers had an inner diameter of 40 mm and a length of 200 mm. The reaction chamber was fitted with a manometer to monitor the internal pressure, as well with two K-type thermocouples positioned in the middle of the chamber (T1 and T2) and a further K-type thermocouple on the outside (T3). The reaction chamber was loaded with the dried copper salt / copper-loaded zeolite and the whole system was evacuated for 10 minutes. The tap between reaction chamber and NH<sub>3</sub>-chamber was closed, and NH<sub>3</sub> liquified in the NH<sub>3</sub>-chamber being cooled down to – 50 °C. After 10 minutes the tap to the NH<sub>3</sub> cylinder was closed and the NH<sub>3</sub>-chamber warmed to room-temperature. Once the reactor had established a thermal equilibrium with the surrounding, the tap between NH<sub>3</sub>-chamber and reaction chamber was opened to start the reaction (discharging of the storage material). Due to the excess of NH<sub>3</sub> during all experiments a pressure of 6 bar was obtained in the system.

For all experiments 250 ml of material were charged to the reactor.

### 4.4 Scanning Electron Microscopy

SEM images were recorded on gold coated samples with a Quanta 200 SEM instrument from FEI under low-vacuum at a water vapor pressure of 80 Pa to prevent electrostatic charging.

## 5. References

1. IEA, 2014. Heating without global warming: Market developments and policy considerations for renewable heat.
2. Treatie, U.N., 2015. Paris agreement, No. 54113,
3. Keith Shine, J.F., Kinfe Hailemariam, Nicola Stuber, 2005. Alternatives to the Global Warming Potential for Comparing Climate Impacts of Emissions of Greenhouse Gases. *climatic change* 3, 281-302.

4. IEA, 2011. Co-generation and Renewables. Solutions for a low-carbon energy future. <https://www.iea.org/publications/freepublications/publication/co-generation-and-renewables-solutions-for-a-low-carbon-energy-future.html>
5. Bauer, T., et al., 2012. Thermal Energy Storage Materials and Systems. *Annual Review of Heat Transfer* 15, 131-177.
6. Hasnain, S.M., 1998. Review on sustainable thermal energy storage technologies, Part I: heat storage materials and techniques. *Energy Conversion and Management* 11, 1127-1138.
7. Zhang, H., et al., 2016. Thermal energy storage: Recent developments and practical aspects. *Progress in Energy and Combustion Science* 1-40.
8. Zalba, B., et al., 2003. Review on thermal energy storage with phase change: materials, heat transfer analysis and applications. *Applied Thermal Engineering* 3, 251-283.
9. Ali H. Abedin, M.A.R., 2011. A Critical Review of Thermochemical Energy Storage Systems. *The Open Renewable Energy Journal* 42-46.
10. Cot-Gores, J., A. Castell, and L.F. Cabeza, 2012. Thermochemical energy storage and conversion: A state-of-the-art review of the experimental research under practical conditions. *Renewable and Sustainable Energy Reviews* 7, 5207-5224.
11. T. Yan, R.Z.W., T. X. Li, L.W.Wang, Ishugah T. Fred, 2015. A review of promising candidate reactions for chemical heat storage. *Renewable and Sustainable Energy Reviews* 13-31.
12. Deutsch, M., et al., 2016. Systematic search algorithm for potential thermochemical energy storage systems. *Applied Energy* 113-120.
13. van Essen, V.M., et al., 2009. Characterization of Salt Hydrates for Compact Seasonal Thermochemical Storage. 825-830.
14. Pardo, P., et al., 2014. A review on high temperature thermochemical heat energy storage. *Renewable and Sustainable Energy Reviews* 591-610.
15. Criado, Y.A., M. Alonso, and J.C. Abanades, 2014. Kinetics of the CaO/Ca(OH)<sub>2</sub> Hydration/Dehydration Reaction for Thermochemical Energy Storage Applications. *Industrial & Engineering Chemistry Research* 32, 12594-12601.
16. Dunlap, R.M., *Thermochemical energy storage and mechanical energy converter system*. 1982, Google Patents.
17. Aidoun, Z. and M. Ternan, 2001. Pseudo-stable transitions and instability in chemical heat pumps: the NH<sub>3</sub>-CoCl<sub>2</sub> system. *Applied Thermal Engineering* 10, 1019-1034.
18. Trudel, J., S. Hosatte, and M. Ternan, 1999. Solid-gas equilibrium in chemical heat pumps: the NH<sub>3</sub>-CoCl<sub>2</sub> system. *Applied Thermal Engineering* 5, 495-511.
19. Jiang, L., et al., 2016. Experimental investigation on a MnCl<sub>2</sub>-CaCl<sub>2</sub>-NH<sub>3</sub> thermal energy storage system. *Renewable Energy* 130-136.
20. Dunn, R., K. Lovegrove, and G. Burgess, 2012. A Review of Ammonia-Based Thermochemical Energy Storage for Concentrating Solar Power. *Proceedings of the IEEE* 2, 391-400.
21. Lavine, A.S., et al., 2016. Thermochemical energy storage with ammonia: Aiming for the sunshot cost target. 050028.
22. Lepinasse, E. and B. Spinner, 1994. Production de froid par couplage de réacteurs solide-gaz I: Analyse des performances de tels systèmes. *International Journal of Refrigeration* 5, 309-322.
23. Lovegrove, K., H. Kretz, and A. Luzzi, 1999. The first ammonia based solar thermochemical energy storage demonstration. *Le Journal de Physique IV PR3*, Pr3-581-Pr3-586.
24. Lovegrove, K., et al., 2004. Developing ammonia based thermochemical energy storage for dish power plants. *Solar Energy* 1-3, 331-337.

## 6. Appendix

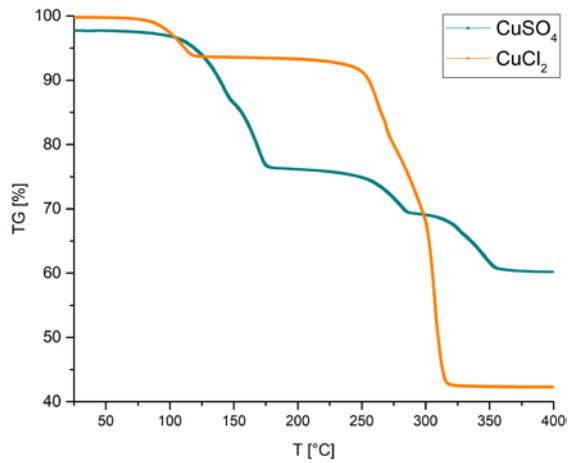


Fig. S1: Thermogravimetric decomposition of  $[\text{Cu}(\text{NH}_3)_4]\text{SO}_4$  and  $[\text{Cu}(\text{NH}_3)_5]\text{Cl}_2$



Fig. S4: A mixed packed bed loading of 13X-Cl and Cu-turnings

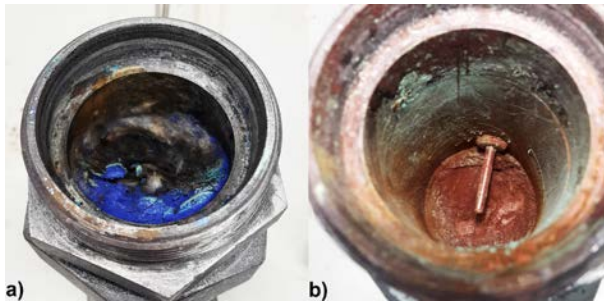


Fig. S2: Molten residue of  $[\text{Cu}(\text{NH}_3)_6]\text{Cl}_2$  after the reaction a) molten residue on the bottom b) unreacted  $\text{CuCl}_2$  on the top with thermocouple T2

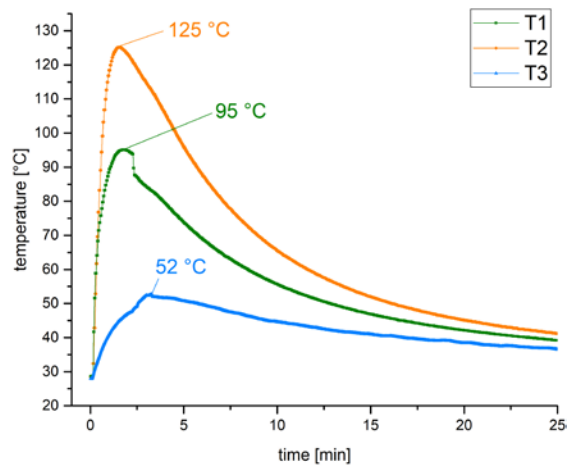


Fig. S5: Temperature plot for the reaction of  $\text{NH}_3$  with a mixed packed bed loading of 13X-Cl and Cu-turnings

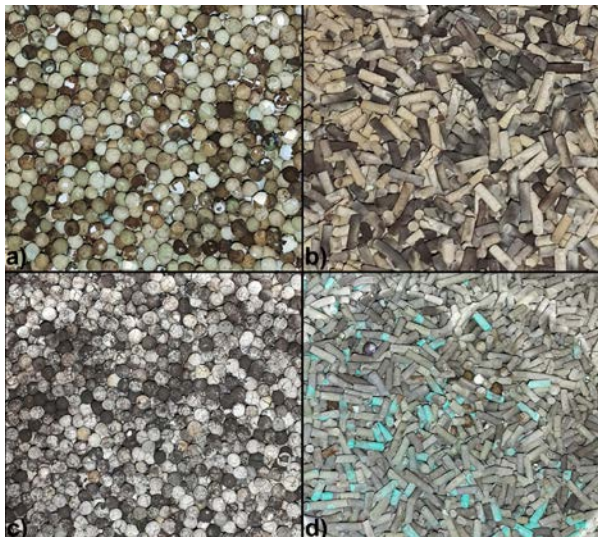


Fig. S3: Images of copper-impregnated zeolite 13X a) 13X- $\text{SO}_4$  b) 13X-Cl, c) 13X- $\text{SO}_4$  after reaction with  $\text{NH}_3$ , c) 13X- $\text{Cl}_2$  after reaction with  $\text{NH}_3$



## Publications in Scientific Journals

1. Jan Welch, D. Müller, C. Knoll, M. Wilkovitsch, G. Giester, J. Ofner, B. Lendl, P. Weinberger, G. Steinhauser:  
"Picomolar Traces of Americium(III) Introduce Drastic Changes in the Structural Chemistry of Terbium(III): A Break in the "Gadolinium Break"";  
Angewandte Chemie International Edition, **56** (2017), 13264 - 13269.
2. M. Deutsch, F. Birkelbach, C. Knoll, M. Harasek, A. Werner, F. Winter:  
"An extension of the NPK method to include the pressure dependency of solid state reactions";  
Thermochimica Acta, **654** (2017), 168 - 178.
3. D. Müller, C. Knoll, W. Artner, M. Harasek, C. Gierl-Mayer, Jan Welch, A. Werner, P. Weinberger:  
"Combining in-situ X-ray diffraction with thermogravimetry and differential scanning calorimetry - An investigation of  $\text{Co}_3\text{O}_4$ ,  $\text{MnO}_2$  and  $\text{PbO}_2$  for thermochemical energy storage";  
Solar Energy, **153** (2017), 11 - 24.
4. M. Seifried, C. Knoll, G. Giester, Jan Welch, D. Müller, P. Weinberger:  
"Aryl and Heteroaryl N1-Tetrazoles through Ligand-Free Suzuki-Reaction under Aerobic, Aqueous Conditions";  
European Journal of Organic Chemistry, **17** (2017), 2416 - 2424.
5. M. Deutsch, F. Horvath, C. Knoll, D. Lager, C. Gierl-Mayer, P. Weinberger, F. Winter:  
"High-Temperature Energy Storage: Kinetic Investigations of the  $\text{CuO}/\text{Cu}_2\text{O}$  Reaction Cycle";  
Energy & Fuels, **31** (2017), 3; 2324 - 2334.
6. D. Müller, C. Knoll, P. Weinberger:  
"Microwave alkylation of lithium tetrazolate";  
Monatshefte für Chemie, **148** (2017), 131 - 137.
7. C. Knoll, D. Müller, W. Artner, Jan Welch, A. Werner, M. Harasek, P. Weinberger:  
"Probing cycle stability and reversibility in thermochemical energy storage -  $\text{CaC}_2\text{O}_4 \cdot \text{H}_2\text{O}$  as perfect match?";  
Applied Energy, **187** (2017), 1 - 9.
8. D. Müller, C. Knoll, M. Seifried, P. Weinberger:  
"ATR or Transmission – A variable temperature study comparing both techniques using  $[\text{Fe}(\text{3ditz})_3](\text{BF}_4)_2$  as model system";  
Vibrational Spectroscopy, **86** (2016), 198 - 205.
9. M. Seifried, C. Knoll, G. Giester, M. Reissner, D. Müller, P. Weinberger:  
"Hexakis (propargyl-1H-tetrazole) Iron(II)  $\text{X}_2$  [ $\text{X} = \text{BF}_4, \text{ClO}_4$ ] - Spin Switchable Complexes with Functionalization Potential and the Myth of the Explosive SCO Compound";  
Magnetochemistry, **2** (2016), 1; 1 - 13.
10. C. Knoll, D. Müller, G. Giester, J. Ofner, B. Lendl, P. Weinberger, G. Steinhauser:  
"An unusually water-poor 5,5'-azobistetrazolate of dysprosium: stabilization of a nitrogen-rich heterocycle by a minimum of hydrogen bonds";  
New Journal of Chemistry, **37** (2013), 3840 - 3844.
11. D. Müller, C. Knoll, B. Stöger, W. Artner, M. Reissner, P. Weinberger:  
"A Modified Synthetic Pathway for the Synthesis of so far Inaccessible N1-Functionalized Tetrazole Ligands - Synthesis and Characterization of the 1D Chain-Type Spin Crossover Compound  $[\text{Fe}(\text{3ditz})_3](\text{BF}_4)_2$ ";  
European Journal of Inorganic Chemistry (invited), **cluster issue** (2013), 984 - 991.



## Talks and Poster Presentations (with Proceedings-Entry)

1. M. Seifried, C. Knoll, D. Müller, G. Giester, M. Reissner, P. Weinberger:  
*"Aryl spaced bis-(1H)-tetrazoles as rigid bridging ligand systems for iron(II) spin crossover polymers"*;  
Poster: 27th International Conference on Organometallic Chemistry (ICOMC) 2016, Melbourne (Australia); 2016-07-17 - 2016-07-22; in: "Program", (2016).
2. M. Seifried, D. Müller, C. Knoll, P. Weinberger:  
*"Green Suzuki cross coupling of 4-bromobenzyl-(1H)-tetrazole under atmospheric conditions"*;  
Poster: 27th International Conference on Organometallic Chemistry (ICOMC) 2016, Melbourne (Australia); 2016-07-17 - 2016-07-22; in: "Program", (2016).
3. M. Seifried, C. Knoll, D. Müller, P. Weinberger, M. Reissner, G. Giester:  
*"New Synthetic Protocols for aryl-substituted tetrazoles for Fe(II) Spin-Crossover Complexes"*;  
Poster: ECOSTBio: Sixth scientific workshop, Lissabon; 2017-03-30 - 2017-03-31; in: "Book of Abstracts", R. Louro, P. Martinho (ed.); (2017), 49.
4. D. Müller, C. Knoll, A. Werner, P. Weinberger:  
*"Novel materials for thermochemical energy storage - from hydroxides to ammoniates"*;  
Talk: 27th International Conference on Organometallic Chemistry (ICOMC) 2016, Melbourne (Australia); 2016-07-17 - 2016-07-22; in: "Book of abstracts", (2016), 45.
5. C. Knoll, D. Müller, M. Deutsch, C. Jordan, M. Harasek, A. Werner, P. Weinberger:  
*"Oxalate and carbonate based thermochemical energy storage materials - reaction kinetics and material optimization"*;  
Talk: 27th International Conference on Organometallic Chemistry (ICOMC) 2016, Melbourne (Australia); 2016-07-17 - 2016-07-22; in: "Book of abstracts", (2016), 43.
6. D. Müller, C. Knoll, M. Seifried, G. Giester, M. Reissner, P. Weinberger:  
*"Porous spin crossover networks for multifunctional materials"*;  
Poster: 42nd International Conference on Coordination Chemistry (ICCC), Brest (Frankreich); 2016-07-03 - 2016-07-08; in: "Programme Book", (2016).
7. M. Seifried, D. Müller, C. Knoll, G. Giester, M. Reissner, P. Weinberger:  
*"Propargyl-1H-tetrazole as promising ligand for post-functionalization of spin switchable iron(II) complexes"*;  
Talk: 42nd International Conference on Coordination Chemistry (ICCC), Brest (Frankreich); 2016-07-03 - 2016-07-08; in: "Programme Book", (2016).
8. C. Knoll, D. Müller, M. Seifried, G. Giester, M. Reissner, P. Weinberger:  
*"Rigidity in iron (II) tetrazole spin crossover chains"*;  
Talk: 42nd International Conference on Coordination Chemistry (ICCC), Brest (Frankreich); 2016-07-03 - 2016-07-08; in: "Programme Book", (2016).
9. D. Müller, C. Knoll, M. Seifried, G. Giester, M. Reissner, P. Weinberger:  
*"Zero- to three-dimensional iron(II) spin crossover coordination compounds - from ligand design to tunable spin switching behaviour"*;  
Talk: 42nd International Conference on Coordination Chemistry (ICCC), Brest (Frankreich); 2016-07-03 - 2016-07-08; in: "Programme Book", (2016).
10. C. Knoll, M. Seifried, D. Müller, P. Weinberger:  
*"Variable Temperature ATR-IR Spectroscopy as a Valuable Tool for the in situ Spin State Detection of Iron(II) Spin Crossover Complexes"*;  
Talk: ECOSTBio: Fourth scientific workshop, Prague; 2016-04-13 - 2016-04-15; in: "Book of abstracts", (2016), 29.
11. C. Knoll, D. Müller, M. Seifried, P. Weinberger:  
*"Elucidating structural features of rigid spin crossover coordination polymers using HPC"*;  
Talk: AHPC16, Grundlsee; 2016-02-22 - 2016-02-24; in: "Austrian HPC Meeting 2016 - AHPC16", VSC - Vienna Scientific Cluster (ed.); (2016), 50.

12. D. Müller, C. Knoll, M. Seifried, P. Weinberger, M. Reissner:  
*"Using Mössbauer studies and various other methods for the determination of the spin transition properties of Iron(II) Spin-Crossover Compounds"*;  
 Poster: ICAME 2015 - The 33rd International Conference on the Application of the Mössbauer Effect, Hamburg; 2015-09-13 - 2015-09-18; in: *"Conference Programme"*, Hamburg (2015), 108.
13. C. Knoll, D. Müller, P. Weinberger:  
*"The interpretation of experimental spectroscopic data in coordination chemistry using high performance computing"*;  
 Poster: ICAVS 8, Wien; 2015-07-12 - 2015-07-17; in: *"ICAVS8 Abstracts Poster"*, (2015), ISBN: 978-3-200-04205-6; 632 - 633.
14. C. Knoll, M. Seifried, D. Müller, P. Weinberger:  
*"Variable Temperature ATR-IR Spectroscopy as a Valuable Tool for the In Situ Spin-State Detection of Iron(II) Spin Crossover Complexes"*;  
 Talk: ICAVS 8, Wien; 2015-07-12 - 2015-07-17; in: *"ICAVS8 Abstracts Oral"*, (2015), ISBN: 978-3-200-04205-6; 164 - 165.
15. C. Knoll, D. Müller, G. Giester, P. Weinberger:  
*"CNC-Tetrazolylidene Complexes of Group 8 Metals"*;  
 Poster: The XXVI International Conference on Organometallic Chemistry ICOMC 2014, Sapporo (Japan); 2014-07-13 - 2014-07-18; in: *"Program"*, (2014), 29.
16. C. Knoll, D. Müller, G. Giester, P. Weinberger, G. Steinhauser:  
*"Supercritical CO<sub>2</sub> as Unusual Desiccant for 5,5'-Azobistetrazolate Compounds of Dysprosium"*;  
 Poster: XLI International Conference on Coordination Chemistry ICC 41, Singapur; 2014-07-24 - 2014-07-25; in: *"Programme"*, Singapore National Institute of Chemistry, (2014), 138.
17. D. Müller, C. Knoll, M. Reissner, P. Weinberger:  
*"Group 14 Metallated Tetrazoles and their Fe(II) SCO Complexes"*;  
 Poster: XLI International Conference on Coordination Chemistry ICC 41, Singapur; 2014-07-24 - 2014-07-25; in: *"Programme"*, Singapore National Institute of Chemistry, (2014), 121.
18. D. Müller, C. Knoll, M. Reissner, G. Giester, P. Weinberger:  
*"Switchable Coordination Polymers - Novel Hosts Meet Their Guests"*;  
 Talk: XLI International Conference on Coordination Chemistry ICC 41, Singapur; 2014-07-24 - 2014-07-25; in: *"Programme"*, Singapore National Institute of Chemistry, (2014), 38.
19. P. Weinberger, C. Knoll, D. Müller, W. Artner, B. Stöger, M. Reissner:  
*"The influence of steric and electronic factors on the spin transition behaviour of Fe(II) spin-crossover compounds"*;  
 Talk: XLI International Conference on Coordination Chemistry ICC 41, Singapur; 2014-07-24 - 2014-07-25; in: *"Programme"*, Singapore National Institute of Chemistry, (2014), 78.
20. D. Müller, C. Holzhaecker, C. Knoll, K. Kirchner, P. Weinberger:  
*"PN - Fe(II) Spin Crossover Complexes - Insights into Spin State and Coordination"*;  
 Poster: IRDG Spring Meeting Vienna, Wien; 2014-04-24 - 2014-04-25; in: *"Program & Poster Abstracts"*, (2014), 15.
21. C. Knoll, D. Müller, P. Weinberger:  
*"Temperature-dependent ATR-IR spectroscopy for in situ spin state detection of Iron(II) Spin Crossover complexes"*;  
 Poster: IRDG Spring Meeting Vienna, Wien; 2014-04-24 - 2014-04-25; in: *"Program & Poster Abstracts"*, (2014), 12.
22. C. Knoll, D. Müller, G. Steinhauser, P. Weinberger:  
*"Fremdioneninduzierte Anomalien in der f-Element Koordinationschemie"*;  
 Talk: 8. Workshop Anorganische Chemie in Österreich (WACÖ), Salzburg; 2014-04-14 - 2014-04-15; in: *"Book of abstracts"*, (2014).
23. D. Müller, C. Knoll, M. Reissner, P. Weinberger:  
*"Spin crossover beyond room-temperature - A matter of substitution"*;

Talk: 8. Workshop Anorganische Chemie in Österreich (WACÖ), Salzburg; 2014-04-14 - 2014-04-15; in: "Book of abstracts", (2014).

24. C. Knoll, D. Müller, P. Weinberger:  
"HPC as valuable tool for the interpretation of experimental spectroscopic data in coordination chemistry";  
Poster: 3rd Vienna Scientific Cluster User Workshop, Neusiedl am See; 2014-02-24 - 2014-02-25; in: "book of abstracts", (2014), 12.
25. C. Knoll, P. Weinberger:  
"Tetrazole - carboxylic acids as bifunctional ligands for Iron - Lanthanide complexes";  
Poster: 14<sup>th</sup> Blue Danube Symposium on Heterocyclic Chemistry, Podbanské, SK; 2011-11-26 - 2011-11-29; in: "Book of Abstracts - 14th Blue Danube Symposium on Heterocyclic Chemistry", Vydavateľstvo STU - Publishing House of Slovak University of Technology, Bratislava, Slovakia (2011), ISBN: 978-80-227-3529-2; 76.

## Talks and Poster Presentations (without Proceedings-Entry)

1. T. Ruh, C. Knoll, D. Müller, P. Weinberger, P. Blaha:  
"DFT Study of Water Adsorption on Alkaline-Earth-Oxide Surfaces";  
Poster: Solids4Fun Summerschool 2017, Waidhofen a.d.Ybbs; 2017-07-03 - 2017-07-07.
2. T. Ruh, C. Knoll, D. Müller, P. Weinberger, P. Blaha:  
"DFT Study of Water Adsorption on Ca-Doped (001)-MgO Surfaces";  
Poster: Joint Annual Meeting of SPS and ÖPG, Geneva, Switzerland; 2017-08-21 - 2017-08-25.
3. C. Knoll, D. Müller, W. Artner, Jan Welch, A. Werner, M. Harasek, P. Weinberger:  
"Oxalate-hydrates in thermochemical energy storage - a so far neglected class of salt hydrates";  
Talk: The International Symposium on Energy 7, Manchester; 2017-08-13 - 2017-08-17.
4. D. Müller, C. Knoll, G. Gravogl, M. Deutsch, S. Flegkas, M. Harasek, F. Winter, D. Lager, R. Miletich, P. Weinberger, A. Werner:  
"Solid Heat - Materials for Thermochemical Energy Storage";  
Talk: SHC ECES Task58/Annex33 Kick-Off Experts Meeting, Lyon (Frankreich); 2017-04-05 - 2017-04-07.
5. T. Ruh, C. Knoll, D. Müller, P. Weinberger, P. Blaha:  
"DFT Study of Water Adsorption on Cation Doped (001)-MgO Surfaces";  
Talk: DPG Frühjahrstagung 2017, Dresden, Germany; 2017-03-19 - 2017-03-24.
6. T. Ruh, C. Knoll, D. Müller, P. Weinberger, P. Blaha:  
"Alkaline-Earth-Doped MgO-Surfaces";  
Poster: AHCP17, Grundlsee; 2017-03-01 - 2017-03-03.
7. C. Knoll, D. Müller, M. Harasek, P. Weinberger:  
"Transition Metal Oxide Redox Couples for High Temperature Thermochemical Energy Storage";  
Poster: 32. Workshop Novel Materials and Superconductivity, Obertraun; 2017-02-12 - 2017-02-18.
8. G. Gravogl, D. Müller, C. Knoll, P. Weinberger, R. Miletich, A. Werner:  
"Pressure Dependence of Thermochemical Energy Storage Materials";  
Poster: 32. Workshop Novel Materials and Superconductivity, Obertraun; 2017-02-12 - 2017-02-18.
9. D. Müller, C. Knoll, M. Seifried, M. Reissner, G. Giester, P. Weinberger:  
"The Spin Crossover Phenomenon and its Possible Application - Challenges and Chances";  
Keynote Lecture: 32. Workshop Novel Materials and Superconductivity, Obertraun (invited); 2017-02-12 - 2017-02-18.
10. T. Ruh, C. Knoll, D. Müller, P. Weinberger, P. Blaha:

- "DFT study of water adsorption on alkaline-earth-oxide surfaces"*;  
Poster: 32. Workshop Novel Materials and Superconductivity, Obertraun; 2017-02-12 - 2017-02-18.
11. T. Ruh, C. Knoll, D. Müller, P. Weinberger, P. Blaha:  
*"DFT study of water adsorption on mixed (Mg,Ca)-Oxide surfaces"*;  
Poster: ICAMM2016, Rennes, France; 2016-09-05 - 2016-09-07.
  12. C. Knoll, D. Müller, M. Harasek, P. Weinberger:  
*"Thermochemical energy storage materials - earth alkali oxalate hydration/dehydration as promising process"*;  
Poster: 31. Workshop on Novel Materials and Superconductivity, Obertraun; 2016-02-07 - 2016-02-13.
  13. P. Weinberger, D. Müller, C. Knoll, M. Seifried, G. Giester, M. Reissner:  
*"Zero- to three-dimensional iron(II) spin crossover coordination compounds: from ligand design to tunable spin switching behavior"*;  
Talk: 31. Workshop on Novel Materials and Superconductivity, Obertraun; 2016-02-07 - 2016-02-13.
  14. M. Seifried, C. Knoll, G. Giester, M. Reissner, D. Müller, P. Weinberger:  
*"Insights in phase transitions of coordination compounds by  $\Delta T$  MIR/FIR spectroscopy"*;  
Poster: 30. Workshop on Novel Materials and Superconductivity, Obertraun, Austria; 2015-02-08 - 2015-02-14.
  15. C. Knoll, D. Müller, G. Giester, P. Weinberger:  
*"Tetrazole-substituted polycyclic hydrocarbons for rigid Fe(II) spin crossover coordinated polymers"*;  
Poster: 30. Workshop on Novel Materials and Superconductivity, Obertraun, Austria; 2015-02-08 - 2015-02-14.
  16. D. Müller, C. Knoll, M. Seifried, W. Artner, G. Giester, M. Reissner, P. Weinberger:  
*"Iron(II) spin crossover facing applicability"*;  
Talk: 30. Workshop on Novel Materials and Superconductivity, Obertraun, Austria; 2015-02-08 - 2015-02-14.
  17. D. Müller, C. Knoll, G. Giester, M. Reissner, P. Weinberger:  
*"Fe(II) SCO chains tuned by solvent and anion"*;  
Poster: 2nd Scientific Workshop of ECOSTBio, Marseille; 2015-01-12 - 2015-01-13.
  18. D. Müller, C. Knoll, M. Reissner, G. Giester, P. Weinberger:  
*"Fe(II) spin crossover complexes: Using 1-substituted tetrazole ligands to tune the spin transition properties"*;  
Talk: 2nd Scientific Workshop of ECOSTBio, Marseille (invited); 2015-01-12 - 2015-01-13.
  19. D. Müller, C. Knoll, M. Reissner, P. Weinberger:  
*"Main group (IV) substituted tetrazoles in Fe(II) spin-crossover"*;  
Poster: 29. Workshop on Novel Materials and Superconductivity, Obertraun; 2014-02-09 - 2014-02-15.
  20. C. Knoll, D. Müller, G. Giester, J. Ofner, P. Weinberger, G. Steinhäuser:  
*"An unusual water-poor 5,5'-azobistetrazolate of dysprosium"*;  
Poster: 29. Workshop on Novel Materials and Superconductivity, Obertraun; 2014-02-09 - 2014-02-15.
  21. P. Weinberger, C. Knoll, D. Müller, W. Artner, M. Reissner:  
*"Impact of electronic and steric factors on iron(II) spin-crossover behaviour"*;  
Talk: 29. Workshop on Novel Materials and Superconductivity, Obertraun; 2014-02-09 - 2014-02-15.
  22. D. Müller, C. Knoll, B. Stöger, W. Artner, M. Reissner, P. Weinberger:  
*"[Fe(3ditz)3](BF4)2: A rare example of a strongly cooperative spin transition behavior of a 1D - chain-type coordination polymer using a per se flexible ligand"*;

Poster: 28. Workshop on "Novel materials and superconductivity", Planneralm, 8953  
Donnersbach; 2013-02-09 - 2013-02-16.

23. C. Knoll, D. Müller, G. Steinhauser, B. Stöger, P. Weinberger:  
"Am(III) doped Tb(III) complexes of 5,5'-azobis[tetrazolide] as an example for overcoming the Gd-break in lanthanide coordination chemistry";  
Poster: 28. Workshop on "Novel materials and superconductivity", Planneralm, 8953  
Donnersbach; 2013-02-09 - 2013-02-16.

24. C. Knoll, D. Müller, P. Weinberger, B. Stöger:  
"New tetrazole compounds as asymmetric ligands for mixed iron(II) lanthanide complexes";  
Poster: 27. Workshop on Novel Materials and superconductors, Universitätssportheim  
Planneralm; 2012-02-11 - 2012-02-18.

## Patents

1. D. Müller, C. Knoll, P. Weinberger, A. Werner, M. Harasek:  
"Verfahren zur thermochemischen Energiespeicherung";  
Patent: Österreich, No. A345/2017; submitted: 2017-08-29.
2. D. Müller, C. Knoll, P. Weinberger, A. Werner:  
"Verfahren zur thermochemischen Energiespeicherung";  
Patent: Europäisches Patentamt, No. PCT/EP2017/066753; submitted: 2017-07-05.
3. D. Müller, C. Knoll, P. Weinberger, A. Werner:  
"Verfahren zur thermochemischen Energiespeicherung";  
Patent: Österreich, No. A 327/2016; submitted: 2016-07-11.

## Diploma and Master Theses (authored and supervised)

1. C. Knoll:  
"Rigidity enhanced bridging tetrazoles for iron(II) spin crossover polymers";  
Supervisor: P. Weinberger; Institut für Angewandte Synthesechemie, 2015; final examination:  
2015-09-10.

# Curriculum Vitae

## Personal Details

Name Dipl.-Ing. Christian Knoll, BSc  
Birthdate, -place 22.8.1989, Vienna, Austria  
Address Fernkorngasse 9-13/2/4/20, 1100 Wien  
Phone number 01/58801-163700  
E-Mail christian.knoll@tuwien.ac.at  
Nationality Austrian  
Language skills German (mother language)  
English (fluent)

## Education

11/2017 TU Wien: Continuing Education Center: MBA-studies: General Management  
10/2015 - TU Wien: Doctoral program in Engineering Sciences: Technical Chemistry,  
Dissertation: „Investigations of the reaction kinetics of thermochemical energy  
storage materials”  
2012-2015 TU Wien: Master's program Technical Chemistry, Diploma thesis: „Rigidity  
enhanced bridging tetrazoles for iron(II) spin crossover polymers“  
2008-2012 TU Wien: Bachelor's program Technical Chemistry, Bachelor thesis:  
„Asymmetrische Brückenliganden für 3d-4f Komplexe“  
11/2007-07/2008 Regular civil service: Arbeiter Samariterbund Österreichs, 1220 Vienna  
06/2007 Matura: Gymnasium und Realgymnasium Kollegium Kalksburg, 1230 Vienna

## Prizes & Awards

12/2017 35. Laureate of Dr. Ernst Fehrer-Preis of TU Wien 2017

## University Occupation

09/2015 - TU Wien: Project assistant: Institute for Applied Synthetic Chemistry and  
Institute of Chemical, Environmental & Biological Engineering  
2011 - 2015 TU Wien: Member of working group Priv.-Doz. Dr. Peter Weinberger:  
Magneto and Thermochemistry

## Teaching

2015 - TU Wien: Lab course instructor for Synthesis Laboratory Course, Advanced  
Laboratory Course in Synthetic Chemistry, Preparative Laboratory for  
Chemical Engineers  
2011-2014 TU Wien: Tutor for Lab courses: Preparative Laboratory for Chemical  
Engineers, General Chemistry Introductory Laboratory, Synthesis Laboratory  
Course

## Internships

08/2010 G.L. Pharma GmbH: Department of Pharmaceutical Development, Analytics  
u. Stability studies of development batches  
08-09/2009 OMV AG: Competence Center Lubricants, Product Development and  
Analytics

## Voluntary Activities

10/2008 - Notfallsanitäter NKV (Emergency paramedic) at the ASBÖ group Floridsdorf-  
Donaustadt, Volunteer in the emergency rescue for “Wiener Berufsrettung”  
02/2011 - Instructor for first aid courses